COMPUTER AIDED ANALYSIS AND DESIGN

OF

A SINGLE PHASE TUBULAR INDUCTION ACTUATOR

GONGFAN HU

A thesis submitted in partial fulfillment of the
requirements of Dundee Institute of Technology
for the degree of Doctor of Philosophy

July 1993

I certify that this thesis is the true and accurate version of the thesis approved by the examiners.

Signed .... [redacted] (Director of Studies) Date 26/10/93

DECLARATION

I declare that while registered as a candidate for the degree for which this thesis is presented I have not been a candidate for any other award. I further declare that except where stated the work contained in this thesis is original and was performed by the author.

Signed 

Gongfan Hu

In addition to the original research reported in this thesis the author attended or presented papers in following conferences:

[1] G. Hu & C.B. Rajanathan, 'Some Design Aspects of the Rotor Tube in a Linear Induction Actuator', Proc. of the 18th University Power Engineering Conference, UPEC'93, pp. 429 - 432.

[2] C.B. Rajanathan & G. Hu, 'A Novel Tubular Linear Induction Actuator', Intern. Conf. on Electrical Machines, ICEM'92, Manchester, U.K. 15-17th September, 1992, pp. 137 - 140.

[3] C.B. Rajanathan & G. Hu, 'Electromechanical Transient Characteristics of an Induction Actuator by Finite Element Analysis', (Invited paper), The 5th IEEE BIENNIAL Conference on Electromagnetic Field Computation, Claremont, California, U.S.A. 3rd-5th Aug. 1992.

[4] G. Hu & C.B. Rajanathan, 'Dynamic Analysis of Voltage Excited Tubular Linear Induction Actuators', Proc. of IEE International Conference on Computation in Electromagnetics, IEE Savoy Place, London, U.K. 25-27 Nov. 1991, pp. 319 - 322.

ACKNOWLEDGEMENTS

The work presented in this thesis was carried out at the Dundee Institute of Technology, under the supervision of Dr. C.B. Rajanathan. I am extremely grateful for his advice and encouragement throughout the project.

I am indebted to my two external supervisors Prof. D. Rodger and J.F. Eastham for their interest and invaluable advice, especially to Prof. Rodger for his many creative suggestions and constructive criticism.

The author also wishes to thank the following, without whose help this work would not have been possible:

Mr. W. Harper, Mr. S. Murray, Mr. W. Butter and J. Mason for their advice and assistance concerning the technical aspects of the investigation.

The staff of the Computer Center for their patience and considerable help in VAX/VMS system.

The Scottish Education Department and Dundee Institute of Technology for providing the financial assistance which made this work possible.

My colleagues in Shanghai University of Technology have supported my study overseas in a variety of ways, and I express my gratitude to them particularly to Prof. Chen Hao, the head of my Dept., for being deeply concerned about my research.

Finally, I wish to express my sincere thanks to my wife and family for their forbearance over the last three years.

ABSTRACT

This thesis introduces a novel tubular linear induction actuator (TLIA) which makes use of eddy currents to produce useful thrust. Compared with normal DC or AC solenoids, it possesses advantages of long thrust, large starting force and low starting current. Unlike linear motors, it is much simpler in structure and cheaper.

In order to investigate the principle of operation, design and dynamic performance of this TLIA, a time-stepping computer program named COUPV has been developed. Based on the finite element method, it couples the axisymmetric 3-D internal electromagnetic field containing eddy currents and non-linear materials with external electric circuits, involving power electronics and a moving mechanical load. The power supply can be of any kind of voltage or current waveform, such as sine wave, square wave, PWM wave or phase controlled wave. The simulated results in both steady and dynamic states are found to be in very good agreement with the measurements obtained from existing models.

Two special features of the TLIA defined as the shielding effect and the inner end effect are studied. These two effects dominate its performance and make its analysis different from conventional magnets, solenoids and linear motors. With the help of the COUPV, special attention is paid to the design and control of the TLIA. Its basic construction, slot shape and materials of stator and plunger are studied. Both bang-bang and position control strategies are investigated. It is evident that COUPV can find application for many types of electromechanical devices such as magnetic bearings, fuel injectors, various electric motors and even θ guns.

LIST OF PRINCIPAL SYMBOLS

$\mathbf{A}$	magnetic vector potential, (Wb/m)
A_s	area of the cross section of the stator winding, (m^2)
$\mathbf{B}$	magnet flux density, (Tesla)
B_r	magnet flux density in the radial direction, (Tesla)
B_z	magnet flux density in the axial direction, (Tesla)
D	displacement in the axial direction, (m)
	viscous damping coefficient, (N·s/m)
$\mathbf{E}$	electric field strength, (V/m)
E_1	back electromotive force of the stator winding, (V)
E_m	mechanical energy, (Joule)
f	body force per unit volume, (N/m^3)
f_p	preload force, (N)
f_m	total magnetic force of the plunger, (N)
F_1	magnetomotive force, (A·Turns)
F_m	mechanical force (N)
F_r	force in the radial direction, (N)
F_z	force in the axial direction, (N)
g	length of the airgap, (m); gravitation constant, (m/s^2)
$\mathbf{H}$	magnetic field strength, (A/m)
I_1	stator current, (A)
I_e	eddy current in the plunger, (A)
i,j,k	integers denoting the position of a finite element node,
J_e	induced eddy current density, (A/m^2)

K	spring constant, (m/N)
l	length of circle line for integration, (m)
m	mass, (kg)
N_1	number of turns of the stator winding, (Turns)
P_e	eddy current loss, (W)
R_e	equivalent resistance, (Ω)
X_e	equivalent reactance, (Ω)
X_σ	leakage reluctance, (Ω)
u	transient voltage, (V)
V_z	velocity in the axial direction, (m/s)
α_a	accelerating convergence factor,
α_r, α_θ, α_z	unit vectors of the cylindrical coordinate
δ	thickness of the plunger wall, (m)
μ_0	permeability of free space, (H/m)
μ_r	relative permeability,
ρ	resistivity, (Ω·m)
Λ	permeance of the magnetic circuit, (H)
σ	conductivity, $(\Omega \cdot m)^{-1}$
ω	angular frequency, (rad/s)
Δ	penetration depth, (m); area of an element (mm^2)
Ψ	flux linkage, (Wb·Turns)
ϕ	flux, (Wb)
ν	reluctivity, (m/H)
ε	error

TABLE OF CONTENTS

CHAPTER 1 INTRODUCTION

1.1 Object of Thesis

The work described in this thesis is aimed at introducing and studying a novel single phase tubular linear induction actuator (TLIA) and developing an associated computer program. This developed computer program can be used not only for the analysis, simulation and design of the TLIA but also for simulating the dynamic characteristics of various other electromechanical devices.

1.2 A Novel Actuator & Its Topology

The electromagnetic actuator is an electromechanical device in which electric energy is absorbed from the power supply, stored as magnetic energy and changed into mechanical force or torque to drive the mechanical load. The difference between an actuator and a conventional electrical motor, in the author's viewpoint, is that the former performs more of a control or servo function than the latter, whose major task is simply to drive its load in continuous rotary or linear motion at constant speed. This is why most servo motors, magnets or solenoids are called actuators in the literature. In other words, whether or not magnets, solenoids and various kind of motors are called actuators depends on their applications and output performance.

In this thesis, a novel actuator is introduced and studied, which makes use of induced eddy currents to produce its thrust. A review of all the electromagnetic linear actuators in current industrial use reveals that they can be classified into three main groups. They are magnets, solenoids

and linear motors.[1] The former two belong to the class of magnetic devices, since they utilize the flux density in the magnetic circuit directly to produce force. They have a simple construction. Their operating principles are based on the variation of reluctance of their main magnetic circuits. Generally they can be used only in bang-bang control involving short strokes. On the other hand, linear motors are electromagnetic devices, since they must couple the impressed and induced currents in their secondary sides with the main magnetic field to produce the output force. They possess the advantages of long stroke, high efficiency and smooth output force. Nevertheless, their construction is complicated and the cost is high. They are the counterparts of rotating machines. Therefore, like the rotating machine, they can be classified into AC, DC or pulse powered according to the nature of the power supply. They can be further divided into induction, synchronous or reluctance types depending upon their operating principles. In this thesis, the author will only use the linear induction motor to compare the TLIA with, since both of them are induction devices producing linear motion. The TLIA has distinct properties such as longer thrust and higher starting force, than magnetic and solenoid actuators. It can be used in both bang-bang and position control. Its construction is similar to the solenoid but is much simpler than the linear motor. It is an electromagnetic machine as its secondary is a hollow conducting cylinder in which induced currents flow. Its output force depends on induced eddy currents interacting with the magnetic field.

Because this is a new machine, there will be a number of questions arising. What is its topology and what does it look like? What are its operating principles? What are its applications? Compared to the conventional linear actuators, what are its advantages and disadvantages? Where did this idea come from? All these will be answered in this section.

1.2.1 Basic Model & Its Operating Principle

The basic topology of the TLIA is illustrated in Fig. 1.1. It is composed of four parts. Starting from the outside, the first is the stator which needs to be laminated to limit the eddy currents. The second is the stator winding, which consists of one or more coils. The third is a hollow plunger which could be made of copper or aluminum with high conductivity. The last one is a mandrel which provides the return magnetic path so that it must be made of a material with high permeability and low conductivity. Like all electromagnetic devices, there must be an airgap to allow movement and electromechanical energy conversion. The TLIA has three airgaps as shown in Fig. 1.2a. One is located between the plunger and the stator. The second is between the plunger and the mandrel. The third is located beside the inner end of the plunger. When the plunger moves, all these airgaps will change their length or width.

In order to design this machine and analyze its performance, it is necessary to investigate and understand its basic operating principles. The production of axial thrust can be explained in two different ways.

The first explanation is based on Lorentz law:

$$\mathbf{f} = q\cdot\mathbf{E} + \mathbf{J}\times\mathbf{B}$$

As there is no stationary electric charge in the TLIA, the body force per unit volume can be simply written as

$$\mathbf{f} = \mathbf{J}\times\mathbf{B}$$

If it is assumed that the positive direction of the stator current faces towards the paper, the positive direction of the flux will follow the path and the direction as shown in Fig. 1.2a in accordance with the right-hand

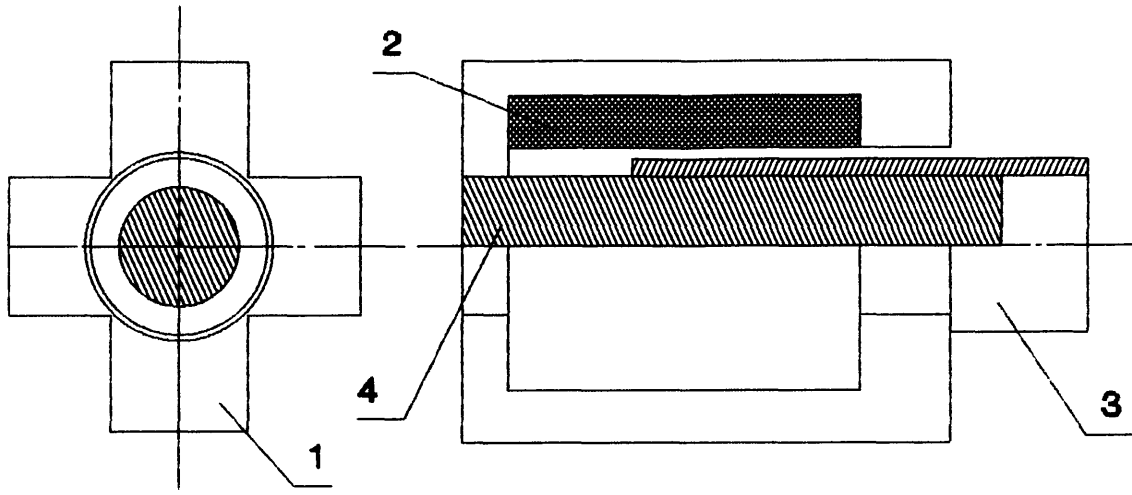

Fig. 1.1 Basic Model of the TLIA

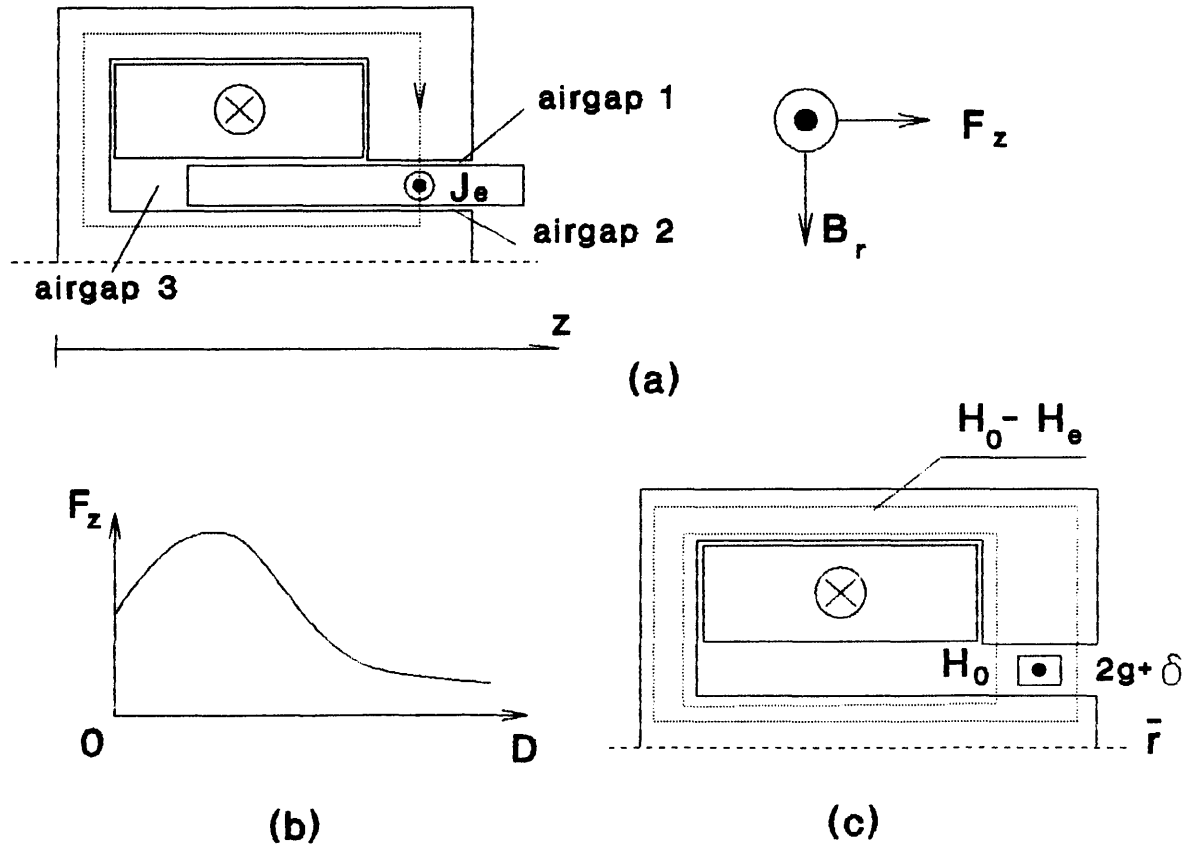

Fig. 1.2 Operating Principle

rule. The eddy currents induced in the plunger will thus have their directions opposite to the stator current, outwards from the paper. The axial force in the Z direction will be produced in terms of Lorentz law:

$$F_z = \int J_e \cdot B_r \cdot dv,$$

which is in the direction to the right as shown in Fig. 1.2a. A typical force-stroke curve will have the shape shown in Fig. 1.2b.

If the plunger is separated into a number of small filaments with the eddy currents producing an opposite magnetic field to the one produced by the stator current, this axial force can also be explained by the Maxwell stress summation along a closed contour surrounding a single filament as shown in the Fig. 1.2c. If the permeability of the stator and mandrel is considered infinite, the whole system becomes linear and the superposition principle can be applied. Let H_0 be the magnetic field strength of a closed contour surrounding only the stator coil so that the magnetic field strength surrounding both stator coil and the filament becomes $H_0 - H_e$ where H_e is the magnetic field strength due to induced eddy current. According to the Maxwell stress law, the axial thrust acting on the filament will be

$$F_z = \frac{1}{2} \cdot \mu_0 \cdot [H_0^2 - (H_0 - H_e)^2] \cdot 2\pi \cdot \bar{r} \cdot (2g+\delta) \qquad \cdots\cdots(1.1)$$

where g is the airgap length, δ is the thickness of the plunger wall and $\bar{r}$ is an average radius of the filament. Consequently, the axial thrust density $F_z > 0$ and acts in the positive Z direction. Both methods lead to the conclusion that the TLIA does produce its thrust in the specified direction.

1.2.2. Previous Work & First Prototype

The idea of this machine[2] was originally conceived by the authors of reference [3], when they studied a transverse flux linear induction motor. During the time of their study on the stability characteristics of the levitator, by experimenting with a single phase E core,[3] the first author believed that its destabilising force could be used to produce useful thrust and the E core levitator itself could become a linear actuator. Later he developed a new machine by wrapping the levitator into a primitive tubular actuator as shown in Fig. 1.3. This development can be described as follows. First, the iron plate of the levitator is changed into a mandrel. Then, the conducting sheet is rolled up to produce a hollow plunger. The destabilising force of the current sheet becomes the useful axial thrust in the tubular actuator. And then the coil of the E core levitator is changed into a pancake coil which surrounds both plunger and mandrel. Finally, the E core is separated into four parts which are arranged as in Fig. 1.1. The first TLIA will be called a Xi-core model as shown in a photograph in Fig. 1.4.

Constructed from transformer laminations, this Xi-core model consists of three windings named B (bottom), M (middle) and T (top) in its three slots. The electrical parameters of these windings are listed in the table 1.1. The middle winding consists of four coils referred to as M_1, M_2, M_3 and M_4 in the table 1.1. There are three different plungers available for the primary study of the plunger materials. The first one, $1^{\#}$, is made of thick wall copper. The second, $2^{\#}$, is made of thin wall hollow copper. The third, $3^{\#}$, is composed of a thin copper tube on the outside and a steel hollow tube inside. All the details are given in Fig. 1.5.

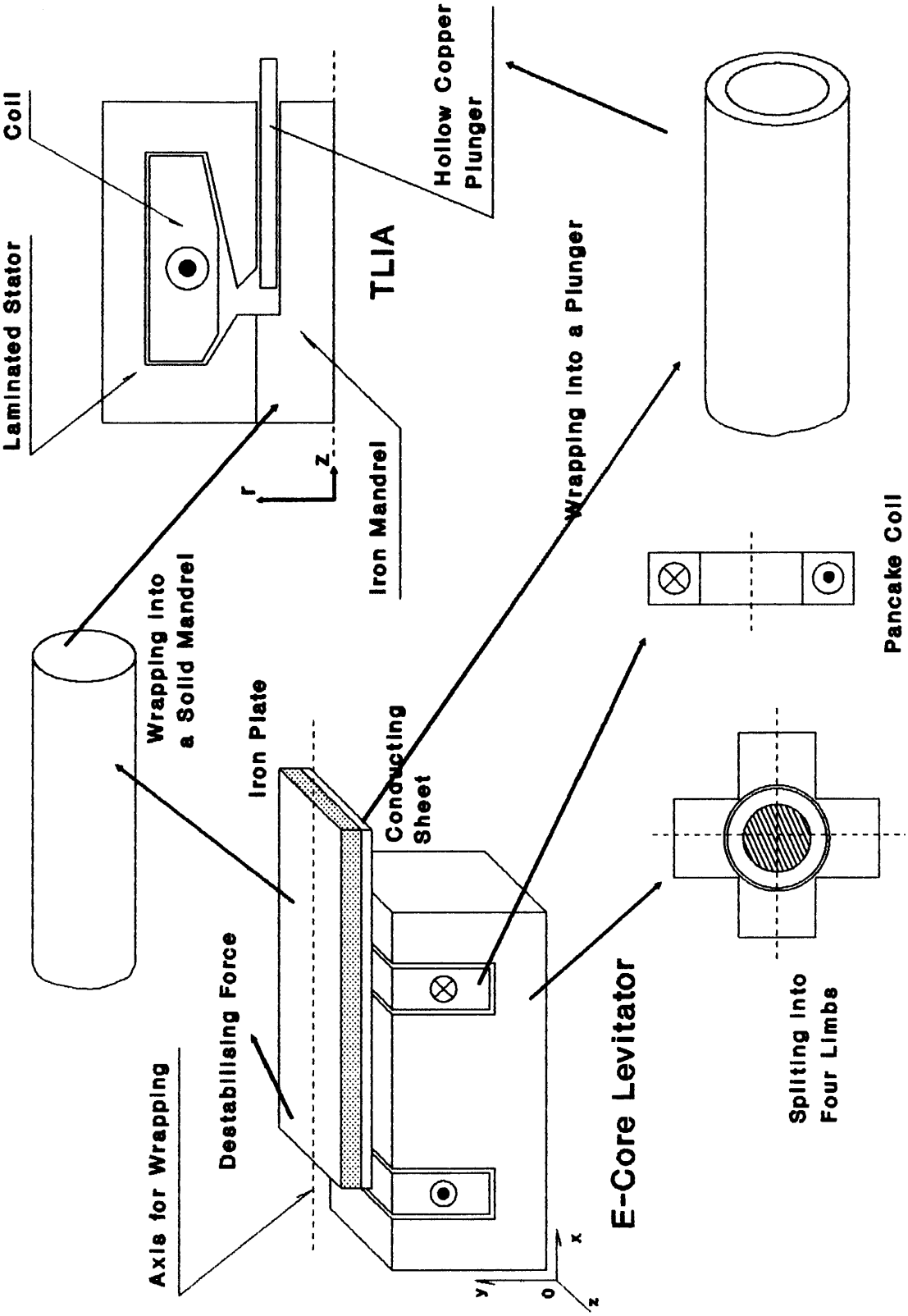

Fig. 1.3 Evolution of the Actuator

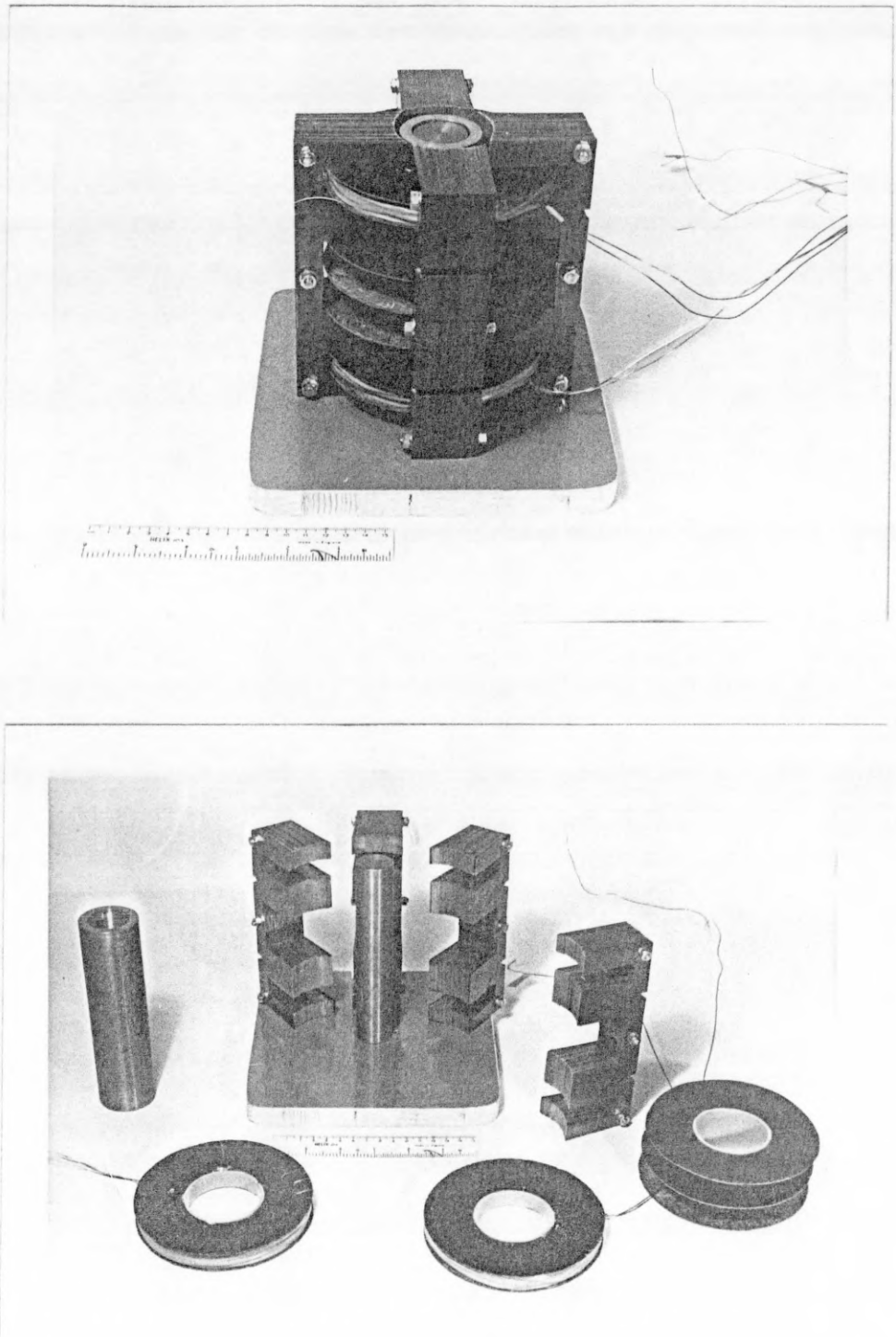

Fig. 1.4 The Xi-core Tubular Linear Induction Actuator

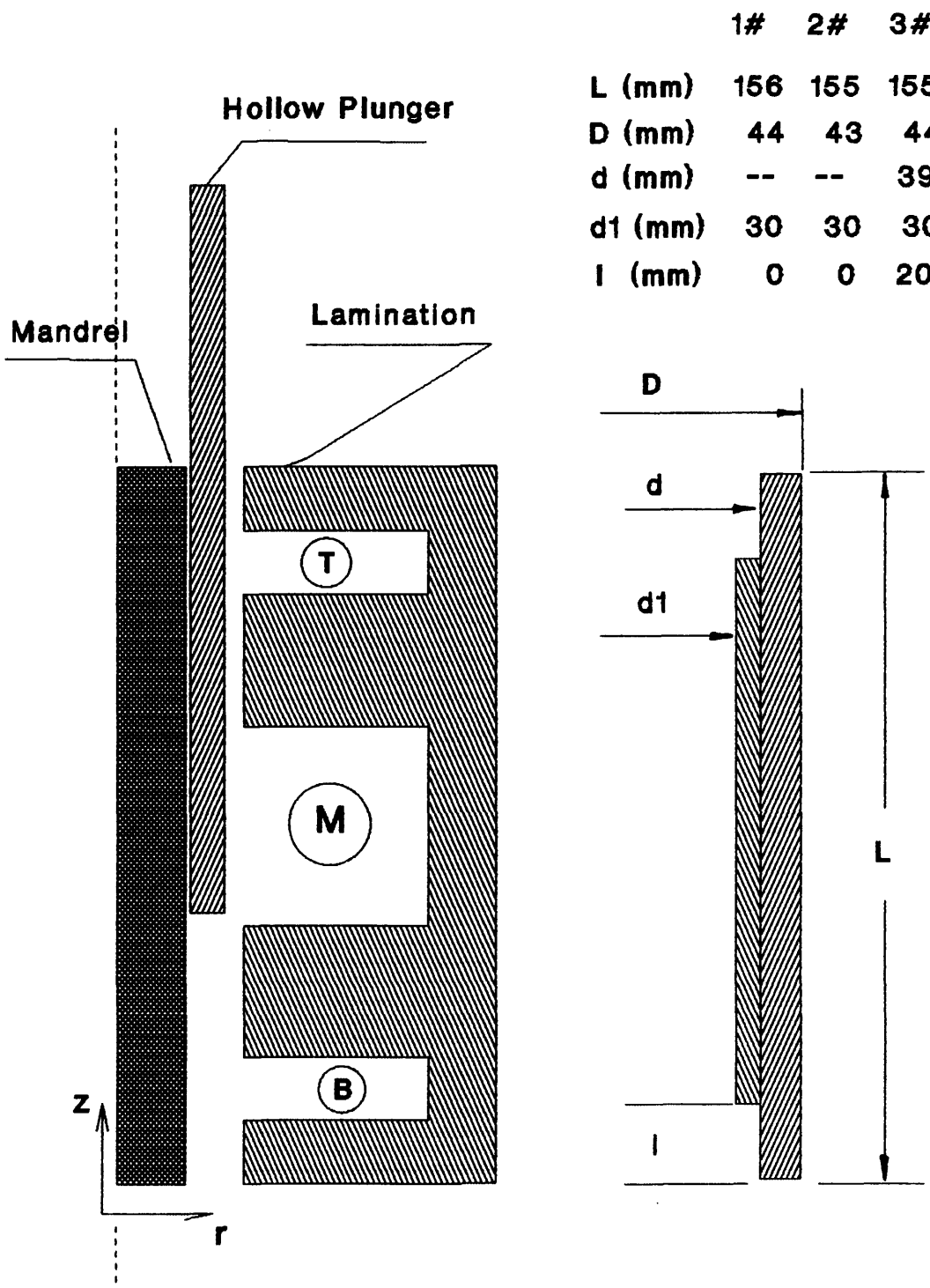

	1#	2#	3#
L (mm)	156	155	155
D (mm)	44	43	44
d (mm)	--	--	39
d1 (mm)	30	30	30
l (mm)	0	0	20

Fig. 1.5 Geometric Data of the Xi-core TLIA

	Turns	Diameter of Wire (m)	Resistance (Ω) 20 C
B	400	0.001	5.0
M_1	250	0.001	3.75
M_2	400	0.001	4.1
M_3	400	0.001	4.6
M_4	250	0.001	3.5
T	400	0.001	4.9

Table 1.1 Coil Parameters of the Xi-core TLIA

This Xi-core TLIA provides some information about its fundamental properties. If the initial plunger position is chosen where the centres of both plunger and coil align with each other, *i.e.* the displacement of the plunger is defined as zero at this point, its force-stroke curve can be plotted as shown in Fig. 1.6a. When the displacement is equal to zero, the output force is zero too. The reason is quite simple since at this position both sides of the plunger center will have the same axial force but in the opposite direction. The total output force thus becomes zero. The maximum output force occurs when the end of the plunger is at the center of the stator coil. Only one half of the Xi-core is useful. If the basic model is modified by closing the airgap at one side, then its force-stroke curve will be similar to that in Fig. 1.2b.

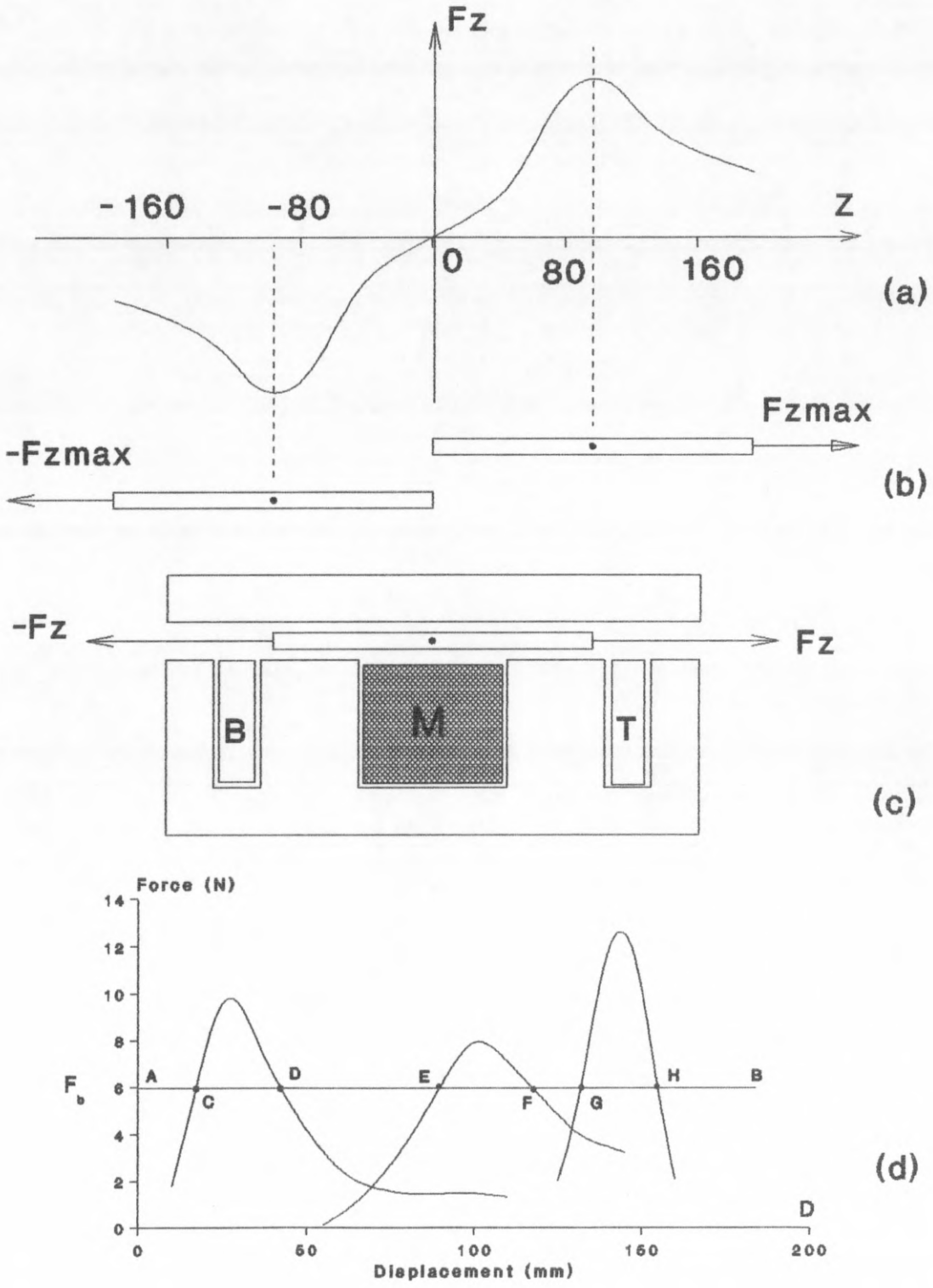

Fig. 1.6 Properties of the Xi-core TLIA

1.2.3. Multi-stage Model & θ Gun

For a linear actuator, important parameters are the output thrust and stroke. These two variables represent its capacity because the product of them is the total mechanical energy output, *i.e.*

$$E_m = \int_0^D F_m \cdot dz \qquad \cdots\cdots(1.2)$$

where E_m and F_m represent mechanical energy and mechanical force obtained from the plunger. If output force is able to remain constant, the expression reduces to

$$E_m = F_m \cdot D \qquad \cdots\cdots(1.3)$$

where D is the total displacement of the plunger.

Naturally, the designer aims to produce an actuator with high output force and long stroke. According to the expression (1.3), to extend the stroke with the same output force means that much electrical energy must be drawn from the power supply. Thus, larger capacity and volume are needed for the TLIA to transform electrical energy to magnetic energy and finally to mechanical energy.

The simplest way to extend the stroke may be to add additional stages. The Xi-core model serves as a ready-made example of multi-stage actuators. When its bottom, middle and top windings are switched on one by one, its output force-stroke characteristics are depicted in Fig. 1.6d. Obviously, if there is no external force acting on the plunger, the plunger will move from the starting point D=0 to the end of the actuator. Each winding pushes it forward when the plunger arrives at a specific position. The plunger will be accelerated at each stage and move faster and faster. This

is similar to the θ gun[4], shown in Fig. 1.7a. One difference is that the θ gun is excited by a series of current pulses while the Xi-core model is excited by sine wave power supply. Their working principles are the same. The plunger in the actuator or the projectile in the θ gun moves forward due to the interaction between the magnetic field and induced eddy current.

Although increasing the number of stages is a good and simple strategy for the TLIA with a free plunger or light load, it has a less obvious shortcoming when a heavy load is carried. For example, if the plunger encounters an opposing force F_b as represented by a straight line *AB* in Fig. 1.6d, the plunger may stop between the points *D* and *E* or *F* and *G*, because F_b is larger than F_z in these areas. This could happen if the plunger is connected to a pull-back spring or if it carries a weight load as shown in Fig. 1.8a. Thus, the multi-stage TLIA poses several new questions. Is it possible to smooth out the concavities in the force/displacement characteristics? What are their causes? Are they related to the slot shape or the excitation arrangement? For example, if the slot mouth is nearly closed, half closed or totally opened, what will happen? All these questions will be studied by a two-stage TLIA with nearly closed slot mouth similar to the model in Fig. 1.7b. The model used not only simulates the TLIA, but is also very useful to study the θ gun. Moreover, one of its contributions is to verify the computer program developed and reported in the thesis.

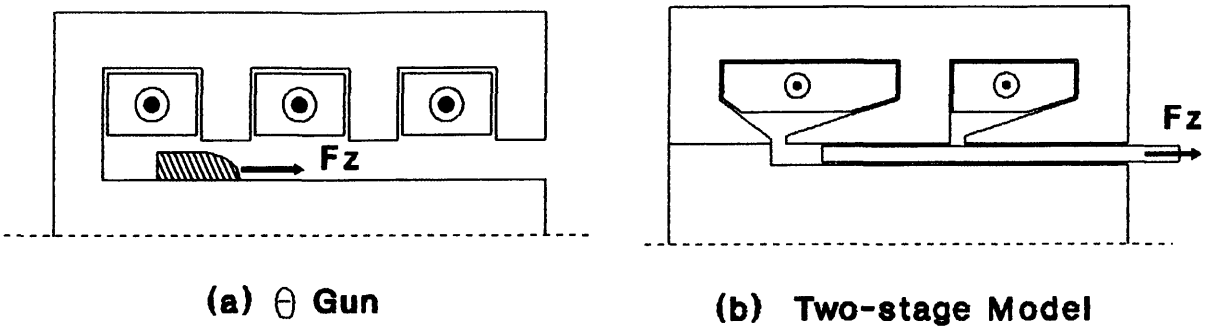

Fig. 1.7 θ Gun and Two-stage TLIA

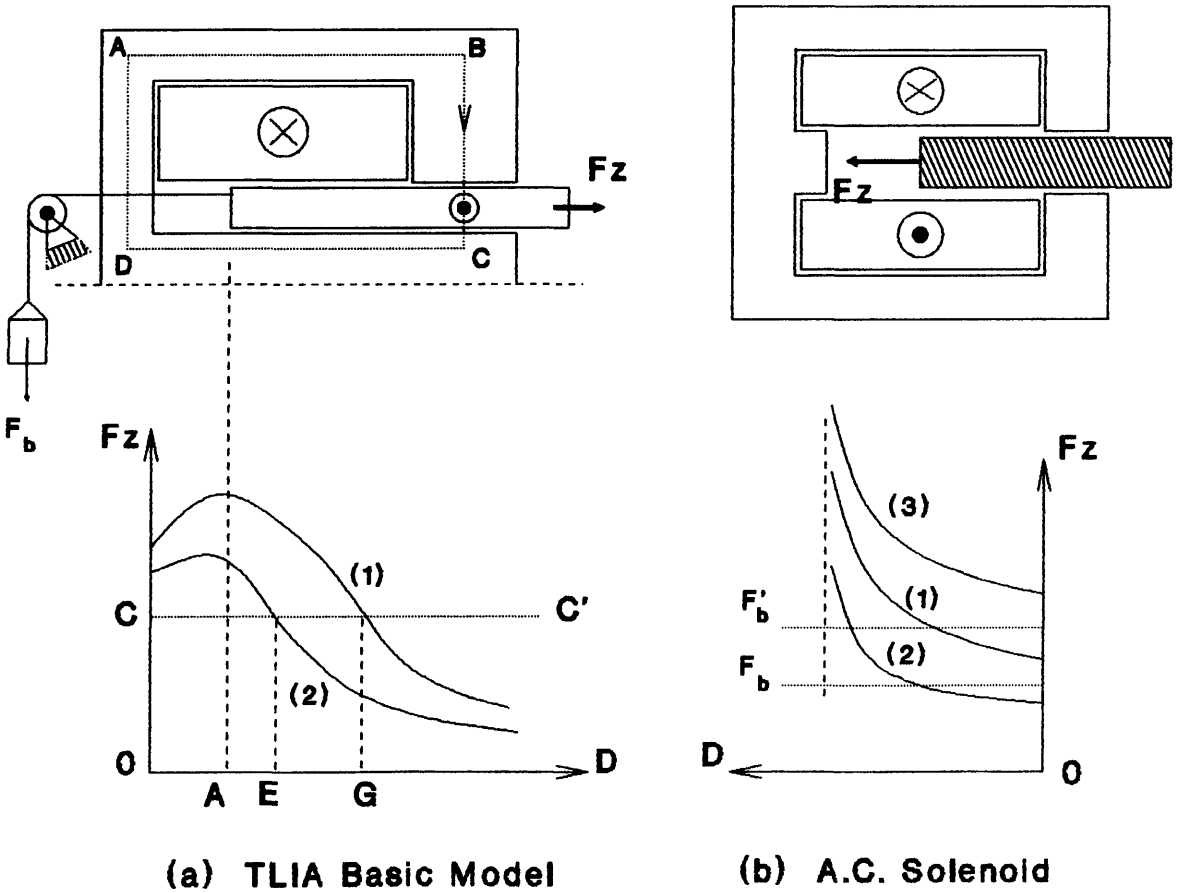

Fig. 1.8 Comparison between the TLIA and AC Solenoid

1.3 Comparison with Other Linear Actuators

As the TLIA is a new machine, it is very important to compare it with other existing actuators and examine what its advantages and disadvantages are. The nearest counterparts of the TLIA are AC solenoids and linear induction motors.

1.3.1. Comparison with AC Solenoids

AC solenoids are well known devices which have been used in various industrial applications for a long period. Its main working principle is based on the fact that the flux always tries to find the way to close on itself. Therefore the free plunger will be attracted in such a direction as to reduce the total reluctance of its magnetic circuit. Its construction is very simple. While the TLIA is composed of four main parts, *i.e.* stator, stator winding, plunger and mandrel, the AC solenoid has only three main parts. They are the stator, the stator winding and the plunger as shown in Fig. 1.8b. Its typical performance characteristics are also shown in Fig. 1.8b.

The comparison between these two machines can be made in respect of the following parameters.

1. Force Direction Due to their different working principles, they have different directions of output axial forces. The TLIA produces pushing force while the AC solenoid produces pulling force.

2. Starting Force The axial starting force of the TLIA is high. It decreases as the displacement increases as shown in Fig. 1.8a. Conversely, the starting force of the AC solenoid is very low because its body force

density is dependent on the flux density B_a in its airgap, *i.e.* $f_z = \frac{B_a^2}{\mu_0}$. The longer the airgap, the lower the force that will be produced.

3. Starting Current The starting current in the AC solenoid is very high and could reach 10 times or more than its rated value, because initially the airgap is long so that the impedance of the magnetic circuit is very small. In order to balance the supply voltage, there must be a large input current to produce enough *mmf* and flux linkage. The starting current of the TLIA is high too, but it is not as high as that of the A.C. solenoid because the causes of the high starting current are different. From Fig. 1.8a, it is clear that the length of the airgap will never change as long as the flux follows the dashed line ABCD. However, in practice, the induced eddy current in the plunger will produce an opposing magnetic field which makes the flux line deviate from the dashed line ABCD. This, in fact, increases the reluctance of the magnetic circuit leading to reduction in the self-inductance of the stator winding, thus increasing the stator current. This will be referred to as the shielding effect and is discussed in Chapter 2. According to the results of the simulation and experiment it is found that the starting current of the TLIA is 4 to 5 times more than its rated value, which is defined as the input current when the plunger reaches its end position.

4. Stroke It is impossible for the AC solenoid to have a long stroke. A long stroke means that it should have a large airgap when it starts. Hence, in general, the stroke of the AC solenoid is limited to about 30 to 50 mm. The stroke of the TLIA can be longer than that of the solenoid but one has to pay the price of the high eddy current losses in the plunger. This will be analysed by a linear finite element package in Chapter 2.

5. Force/Power Ratio Compared with the AC solenoid, the TLIA has to incur additional eddy current loss if it is to produce the same force at the same

stroke. In the AC solenoid the main losses consist of copper loss in stator winding and iron loss in stator and plunger laminations. In the TLIA, there is considerable eddy current loss in its conducting plunger. Therefore, the AC solenoid has higher *Force/Power* ratio than that of the TLIA.

6. Force/Volume Ratio Unlike the solenoid, in which the laminated plunger is also a part of the magnetic circuit, the TLIA should have a mandrel to complete the flux path. In order to obtain the same flux density, the TLIA will have larger volume than that of the solenoid as it has a plunger between the stator and mandrel.

7. Force Pulsation Both an AC solenoid and a TLIA have a double power supply frequency component in their output force. Normally, the AC solenoid is fitted with a shading ring to suppress this oscillation. It can also be used in the TLIA.

8. Control Properties Most AC solenoids are used for two position control, *i.e.* bang-bang control. This is dictated by their inherent characteristics, as shown in Fig. 1.8b. If it carries a constant load F_b, and its force-stroke characteristics is described by the *curve (1)*, the plunger will move from starting point and can not stop until the plunger reaches the end, as F_z is always larger than F_b. If the load is heavier than the starting force, *i.e.* the load F_b', the plunger will not move at all because at the position of $D = 0$, $F_b' > F_z$. Changing the input voltage will move the characteristic up or down, but the plunger will still have only two stable positions. One is the starting point and the other is the end stop. The performance of the TLIA is different. In Fig. 1.8a, the vertical line through *A* splits the force-stroke curve into two parts. The left part is called the unstable region and the right part is the stable one. In the stable region the TLIA can be used for position control. If

the load is constant and represented by a straight line CC', the stable point is at the displacement G. If the force-stroke curve is adjusted to the position represented by the *curve (2)*, the stable operating point will move to the displacement E. Actually, the TLIA is a force machine. It can move at very low speed, or even achieve zero speed.

9. Time Response The time response is an important specification of the actuator. With regard to these two machines, mechanical time constant will dominate the time response because electromagnetic time constants are comparatively small. For a linear machine the mechanical time constant is determined mainly by the mass of its moving member. Because the plunger of the AC solenoid is made of laminations its mass is large. In contrast, the plunger of the TLIA is hollow, and it can be made of a light conductor such as aluminum. So, one can conclude that the TLIA can have a faster response than the AC solenoid. Combined with its good control properties, the former can find several applications in position control.

10. Construction and Cost The main difference in the construction is that instead of a laminated plunger of the A.C. solenoid, a hollow copper plunger and an additional mandrel are used in the TLIA. Because the TLIA has one more part, a mandrel, than the AC solenoid it will obviously be more complicated in its construction and slightly more expensive.

1.3.2. Comparison with Linear Motors

The linear induction motor[5] is another well known device which achieves linear motion. The one most analogous to the TLIA may be the tubular linear induction motor. Its main operating principle is the same as its rotating counterpart. A travelling electromagnetic wave must be produced by the windings in the tubular stator. Normally, it has multi-phase windings arranged in its stator lamination. Its construction, compared with the TLIA, is quite complicated.

The TLIA looks like one part of a tubular linear induction motor. For instance, if three phase windings are fixed in the Xi-core model, it will become a tubular linear motor. However, because of its single phase excitation, the operating principle of the TLIA is entirely different from that of the tubular linear induction motor. Of course, the linear induction motor possesses very good characteristics to produce linear motion. It is easy to change the magnitude of the force and the direction of movement as it has multi-phase windings. Its stroke is unlimited. It can be used for both speed and position control with smooth output force in its whole stroke. It has high efficiency and force/power ratio.

The TLIA and solenoids are commonly used for two-position control with short movement. Normally, they use mechanical springs to produce retracting forces. Both of them have a common shortcoming in that there is a double supply frequency component in their output force. If the TLIA is used in circumstances where the force pulsation can be disregarded and the stroke is not long, it has the merit of being simpler and cheaper than the linear induction motor.

1.4 Outline of Thesis

Usually, a small electromagnetic device is designed by an expensive, evolutionary process of trial and error requiring the construction of many prototypes. Most magnets, solenoids and linear motors have been developed for more than one hundred years and designs are still being improved. This method is time consuming and provides no guarantee that the final design is optimal. The overall objective of this study is to create an accurate actuator modelling technique and to apply this tool towards the development and improvement of its design.

Previous sections of this chapter introduced a new TLIA. It has its own topology, operating principle and performance. To save time and cost, the best design approach is to create a numerical model and use numerical methods to find a solution.

With the help of a linear finite element analysis package, Chapter 2 investigates the steady state characteristics of the TLIA with either constant current or constant voltage sources. This includes investigation of the excitation arrangements of the two coils, the material selection of the plunger and the shape of its winding slots. Particular attention is paid to two new phenomena called the shielding effect and the inner end effect. By numerical experiment, it is found that the conducting plunger can shield the flux path so that the second coil will not contribute anything under certain conditions. In addition, induced eddy currents are found to gather at the inner end of the plunger, and approximately obey the penetration depth law in the axial direction. These two effects play important roles in the TLIA and make the analysis difficult.

The TLIA is an inherently transient device. For a fast actuator, the velocity *emf* produced by the moving member must be considered to obtain an accurate solution. Although this is not a new problem[6] and there were several papers[7-9] dealing with similar problems, *i.e.* non-linear, time-dependent electromagnetic field containing eddy currents and moving parts, no details about the procedure of deducing the final stiffness matrix for the computer program are available. Hence, Chapter 3 derives the numerical form of the axisymmetrical time-stepping formulae by the Galerkin method. Particular attention is given to the representation of the moving member which results in an asymmetric global matrix. A 'Fish-bone' storage strategy is created. In order to deal with non-axisymmetric lamination, an equivalent permeability is derived.

Usually, the TLIA is excited by a voltage power supply. Coupling the internal electromagnetic field with its external electric circuit and mechanical load provides a challenge[10] to the researcher and designer. Chapter 4 combines a modified secant method with a parabolic curve fitting technique to ensure that at each time step the solution can be found within 3 to 4 iterations. The moving member results in the requirement of changing mesh shapes and material interface at each time step. This has been tackled in the thesis in a very simple way, by using a special numbering sequence for the elements in the moving area.

All the developed formulae and the computer program must be validated by experimental results. In Chapter 5, an experimental scheme is described. This comprises a program of measurements of the dynamic characteristics of the TLIA using different combinations of power supplies and mechanical loads. The performance of the two-stage model is also simulated and

compared with measured values. All the practical results are in good agreement with the simulations.

Further study by means of the developed computer program is carried out in Chapter 6. Slits machined in the solid steel stator will certainly reduce the eddy currents. However, this turns the problem into a three dimensional one. The function of the slits is firstly discussed and then by consideration of the experimental results, an equivalent conductivity is derived. Consequently, the performance of the TLIA with slits can be simulated by the developed computer program. In order to overcome or weaken the shielding and the inner end effects, a copper clad plunger with iron inside is demonstrated. It is able to produce almost constant force over its whole stroke.

The TLIA can find applications in both bang-bang and position control. In Chapter 7, its control strategies are discussed. First, the velocity influence on its output performance is examined by the computer program. Then bang-bang control is studied, including the time response and the influence of the switch-on angle and lastly position control is investigated when the TLIA is controlled by an A.C. motor speed controller. Finally, an example of using the computer program to simulate the TLIA, controlled by a Triac which provides the simplest way to realize position control, is given. In the rest of the thesis, the computer program is referred to as COUPV.

Chapter 8 reports the conclusions of the whole thesis, and indicates further possible development of the TLIA.

CHAPTER 2 CAD OF THE TLIA BY COMPUTER PROGRAM FEM2D

2.1 Introduction

In the last chapter, a TLIA was introduced. Its fundamental structure, operating principles and characteristics provide a preliminary idea of what the TLIA is. Its advantages and disadvantages compared with AC solenoids and linear induction motors have been listed.

In this chapter, further investigation of its various configurations, performance characteristics and designs is carried out using an existing 2-dimensional linear finite element package[11] called FEM2D. FEM2D which combines the pre-processor, solver and post-processor is very useful for the steady state analysis of linear eddy current problems.

The first step of the investigation concerns the verification of FEM2D. The Xi-core model shown in Fig. 1.5 is analysed. Its stator is made of laminations and there is no closed end between the stator and the mandrel. Therefore, there are two airgaps and its magnetic circuit is almost unsaturated. Then the investigation moves to a two-stage model shown in Fig. 2.1 in which it is assumed that its stator and mandrel are made of ideal laminations with zero conductivity. This not only simplifies the analysis but also makes it easy to understand its characteristics.

With this two-stage model, the study will focus on the following areas. The excitation arrangement is examined first. This includes its steady state performance when it is energised by constant current, constant voltage sources. Its special structure allows the study of several different cases

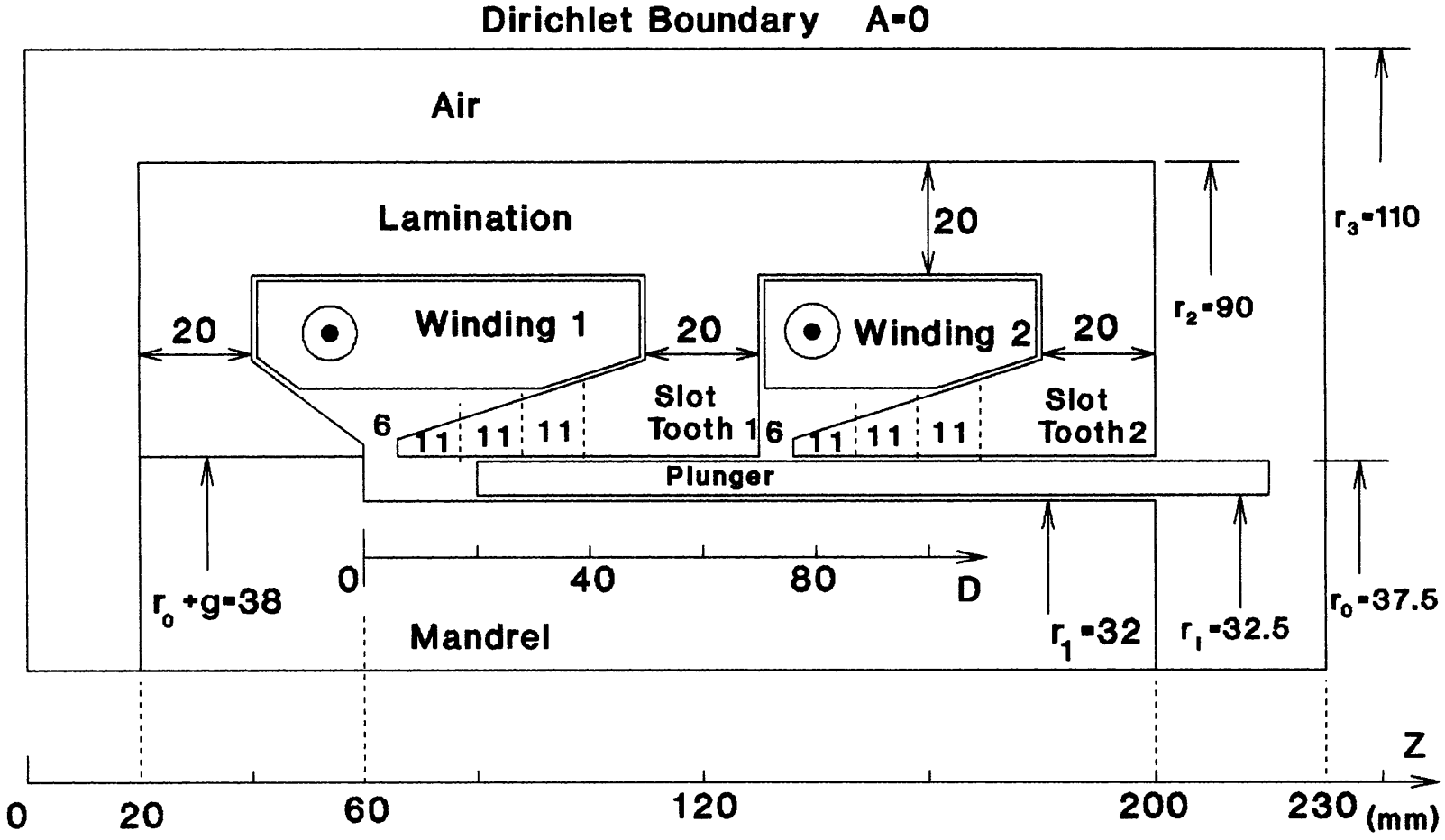

Fig. 2.1 Two-stage Model for FEM2D

such as single stage excitation, two stage excitation or sequenced excitation of each stage. The second investigation is concerned with its slot shape. Four different tooth lengths considered are indicated in Fig. 2.1, *i.e.* with whole tooth present, 1/4 cut, 1/2 cut and 3/4 cut. The third one concerns the material selection for the plunger. Three different conductivities corresponding to copper, aluminum and mild steel are investigated to find out their effects on the TLIA performance. Finally, the relationship between power supply frequency and penetration depth in the TLIA is studied.

The investigations reveal two very important properties of this actuator. One is called the shielding effect, and the other the inner end effect. Both are caused by induced eddy currents in the plunger. They dominate the performance of the TLIA and make its analysis very difficult. In contrast, there is no such shielding effect found in ordinary motors and actuators. The inner end effect is another special feature of the TLIA. It is found that induced eddy currents gather at the end of plunger and attenuate in the axial direction. Both these effects will be described and explained in this chapter ignoring magnetic nonlinearities. They are considered again in Chapter 5 taking nonlinearities into account.

The finite element method is a useful aid in the CAD of novel machines. However, its application must start with a prototype. At the end of this chapter basic consideration and rules for designing a prototype are introduced.

2.2 FEM2D and Xi-core TLIA

2.2.1 FEM2D

FEM2D is a two dimensional finite element analysis package including pre and post processors. It can deal with linear eddy current problems effectively and present results in visual forms aided by computer graphics. For an axisymmetric problem, the electromagnetic field equation can be expressed by a one dimensional magnetic vector potential $\dot{A} = \dot{A}(r, z)$ in θ direction, as,

$$\frac{\partial^2 \dot{A}}{\partial z^2} + \frac{\partial}{\partial r}\left[\frac{1}{r}\cdot\frac{\partial(r\cdot\dot{A})}{\partial r}\right] = -\mu_r\cdot\mu_0\cdot\dot{J} + j\omega\cdot\sigma\cdot\mu_r\cdot\mu_0\cdot\dot{A} \qquad \cdots\cdots(2.1)$$

where $\dot{J}$ is the current density of the stator winding, ω is the angular frequency of power supply, μ_r is relative permeability, μ_0 is permeability in air and σ is conductivity. There is a fixed relationship between $\dot{J}$ and input current $\dot{I}_1$:

$$\dot{J} = \frac{\dot{I}_1\cdot N_1}{A_s}\ (A/m^2) \qquad \cdots\cdots(2.2)$$

where, N_1 is the number of turns of the stator winding and A_s represents the area of the cross section of the stator winding. After the magnetic vector potential $\dot{A}$ has been computed by the FEM2D, the performance predicted by the post-processor is based on the following well known formulae.

1. The Flux Density

$$\dot{B} = \nabla\times\dot{A} = \dot{B}_z\cdot\alpha_z + \dot{B}_r\cdot\alpha_r = \frac{1}{r}\cdot\left[\frac{\partial(r\cdot\dot{A})}{\partial r}\cdot\alpha_z - \frac{\partial(r\cdot\dot{A})}{\partial z}\cdot\alpha_r\right] \qquad \cdots\cdots(2.3)$$

in which α_z and α_r are unit vectors facing z and r direction respectively and consistent with the right-hand rule.

2. Induced Current Density in the Conducting Area

$$\dot{J}_e = -j\omega\cdot\sigma\cdot\mu_r\cdot\mu_0\cdot\dot{A} \qquad \cdots\cdots(2.4)$$

3. Induced Eddy Current in an Element in the Plunger

$$\dot{I}_e^e = \iint_\Delta \dot{J}_e\, drdz = \iint_\Delta (-j\omega\cdot\sigma\cdot\mu_r\cdot\mu_0\cdot\dot{A})drdz \qquad \cdots\cdots(2.5)$$

in which Δ is the area of an element. Therefore, total eddy current in the entire plunger is

$I_e = \sum_{i=1}^{n} I_e^e$, where n is the total number of elements in the plunger.

4. Eddy Loss in an Element & Total Loss

$$P_e^e = \frac{2\cdot\pi}{\sigma}\cdot\iint \mathrm{Re}(\dot{J}_e\cdot\dot{J}_e^*)\cdot r\cdot drdz \qquad \cdots\cdots(2.6)$$

Therefore, total eddy losses in the plunger are $P_e = \sum_{i=1}^{n} P_e^e$.

5. Flux Linkage of Stator Windings

$$\Psi = \frac{N_1}{A_s}\cdot\sum \dot{\psi}^e = \frac{N_1}{A_s}\cdot\sum \iint_\Delta (\nabla\times\dot{A})\cdot drdz = \frac{N_1}{A_s}\cdot\sum \oint \dot{A}\cdot dl \qquad \cdots\cdots(2.7)$$

in which l is a contour and $\dot{\psi}^e$ is the flux linkage of an element. The contour l can be expressed by

$$l = 2\pi\cdot\frac{r_i + r_j + r_k}{3}$$

where, r_i, r_j, and r_k are the coordinate of element vertices.

6. Back Electromotive Force of the Stator Windings

$$\dot{E} = -j\omega \cdot \Psi \qquad \cdots\cdots(2.8)$$

7. Force in both z and r direction

$$\mathbf{F} = \int \mathbf{J} \times \mathbf{B}\, dv = \int \left[\mathrm{Re}(\dot{J}_e \cdot \dot{B}_r^*) \cdot \alpha_z - \mathrm{Re}(\dot{J}_e \cdot \dot{B}_z^*) \cdot \alpha_r \right] \cdot dv$$

$$= F_z \cdot \alpha_z + F_r \cdot \alpha_r \qquad \cdots\cdots(2.9)$$

where v is the volume of the plunger. B_z and B_r are flux density in z and r direction respectively.

In addition to above computation, the post-processor also provides distributions of real and imaginary parts of flux densities. In regions of interest FEM2D will display distributions of flux density, eddy current density and force density along a user defined straight line.

2.2.2 Verification of FEM2D by Experiment

In order to verify the results predicted by FEM2D, experiments were carried out on the Xi-core TLIA. The experiment scheme is shown in Fig. 2.2. The plunger is suspended from a rigid steel bar which imparts the load to two load sensors. These two load sensors are fixed on two frames which can be adjusted up or down manually. Therefore, the plunger can be moved to the desired position relative to the stator. If the power supply is disconnected, each sensor reads $0.5 \cdot m \cdot g$ in which m represents the total mass including the plunger plus steel bar and g is the gravitational constant of 9.81 m/s^2. When energised, each sensor reads W_1 and W_2 due to the lifting force. Therefore, the force produced is equal to

$$F = m \cdot g - W_1 - W_2 \quad (N) \qquad \cdots\cdots(2.10)$$

This simple method proves to be very effective for measuring the force-stroke characteristics. Since this Xi-core TLIA has a large airgap and no closed end between lamination and mandrel, its output force is very low and is not enough to lift the plunger. In cases where the force is large enough to lift the plunger, an additional weight $m_1 \cdot g$ must be added to ensure the position of the plunger remains unchanged as shown in Fig. 2.2. In this case, the expression (2.10) should be changed to

$$F = m \cdot g + m_1 \cdot g - W_1 - W_2 \quad (N) \qquad \cdots\cdots(2.11)$$

Fig. 2.3a shows the force-stroke curves for plunger 1$^{\#}$ with the three windings energised by different constant currents. The bottom and top windings are fed by a constant current of 5 (A) and the middle one by 1.2

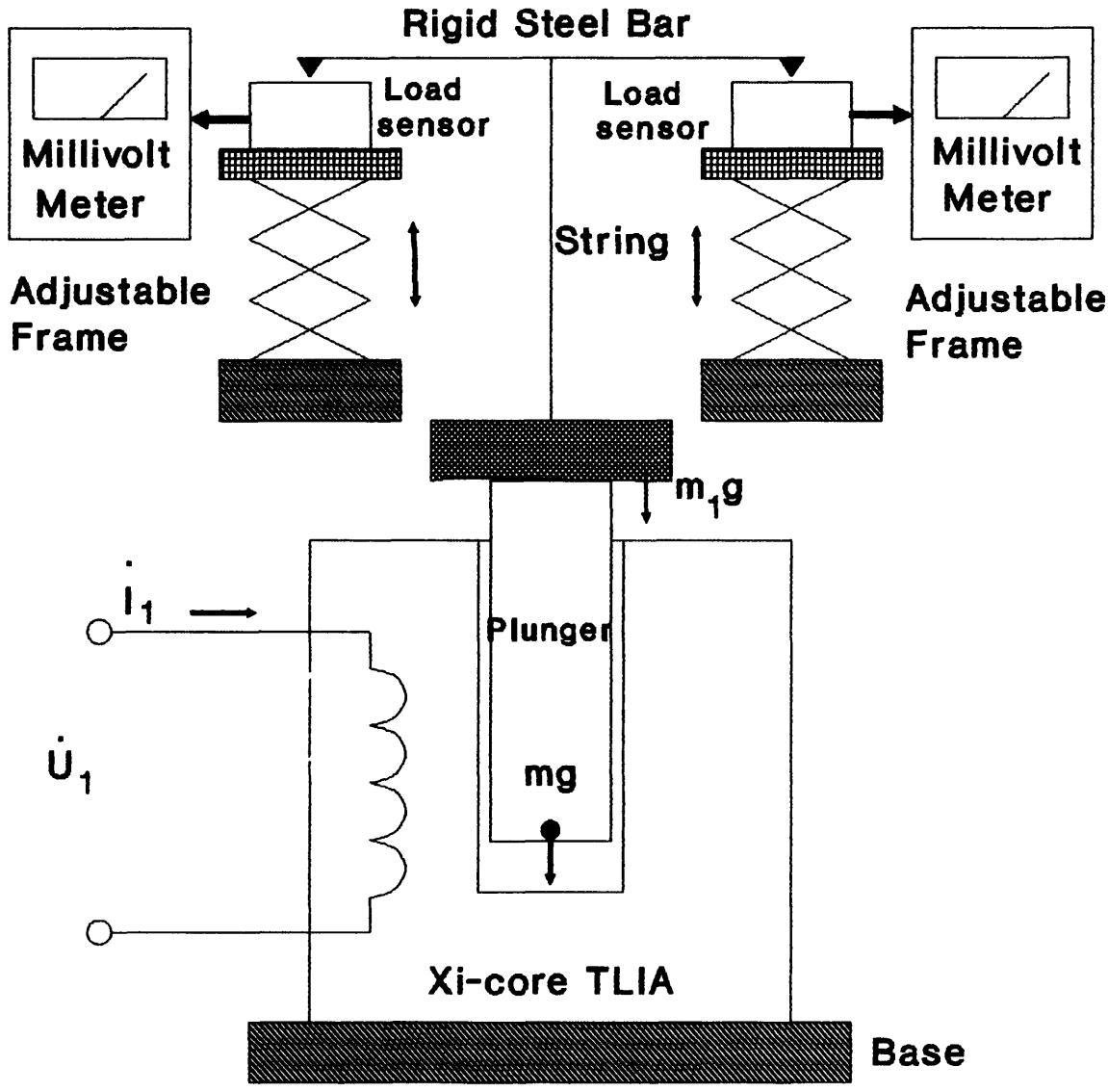

Fig. 2.2 Experiment Scheme for the Xi-core TLIA

(A). It is noticeable that the force-stroke curves calculated by FEM2D are similar to those obtained from the experiment. There is about 10 to 15 percent error between the calculated and measured results. From an engineering point of view the error is within acceptable limits. This error may be attributed to the following.

(1) In the computation by FEM2D, it is assumed that the conductivity σ and the relative permeability μ_r of the mandrel are equal to 0 and 1000 respectively. However the mandrel is made of mild steel. There must be induced eddy currents in it and these will be reflected on the stator side.

(2) In the computation by FEM2D, it is assumed that the TLIA is an axisymmetric device. But in the real machine, its stator laminations are grouped in four separated blocks as shown in Fig. 1.1.

(3) Because the plunger is suspended by a string, it is too difficult to ensure that it is concentric with the stator during the experiment.

Fig. 2.3b shows the flux density distribution, which provides further validation of FEM2D. Thus, the confidence in FEM2D is well placed to undertake the analysis of a two-stage TLIA model later.

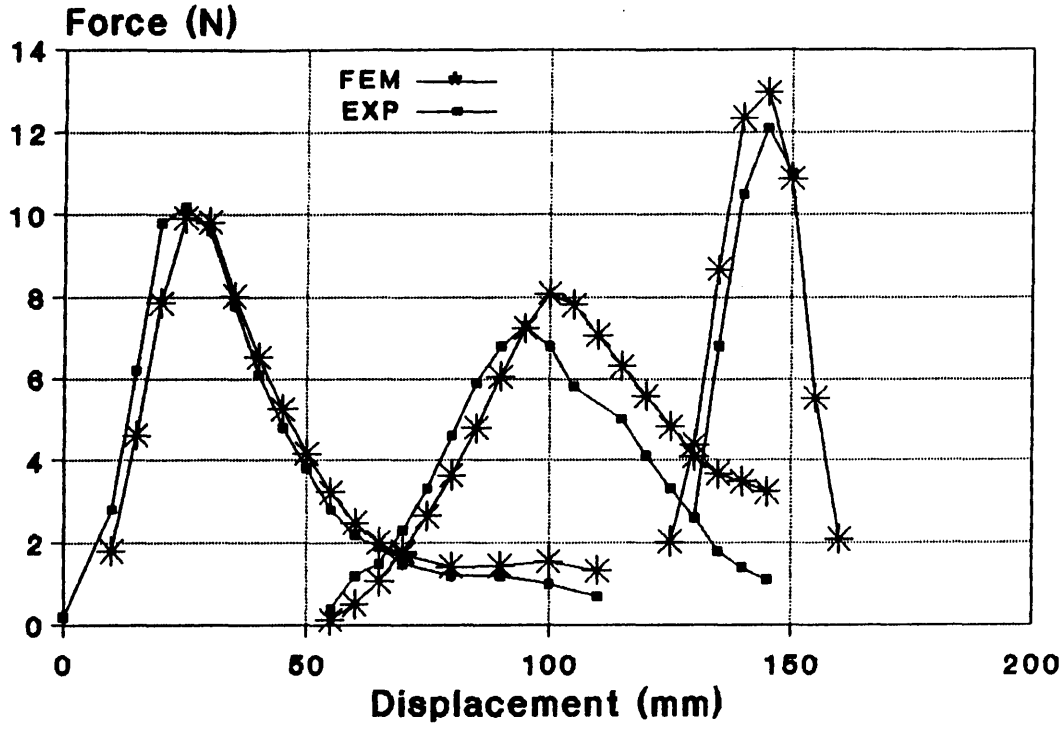

(a) Forces Comparison between Experiment & Simulation Results

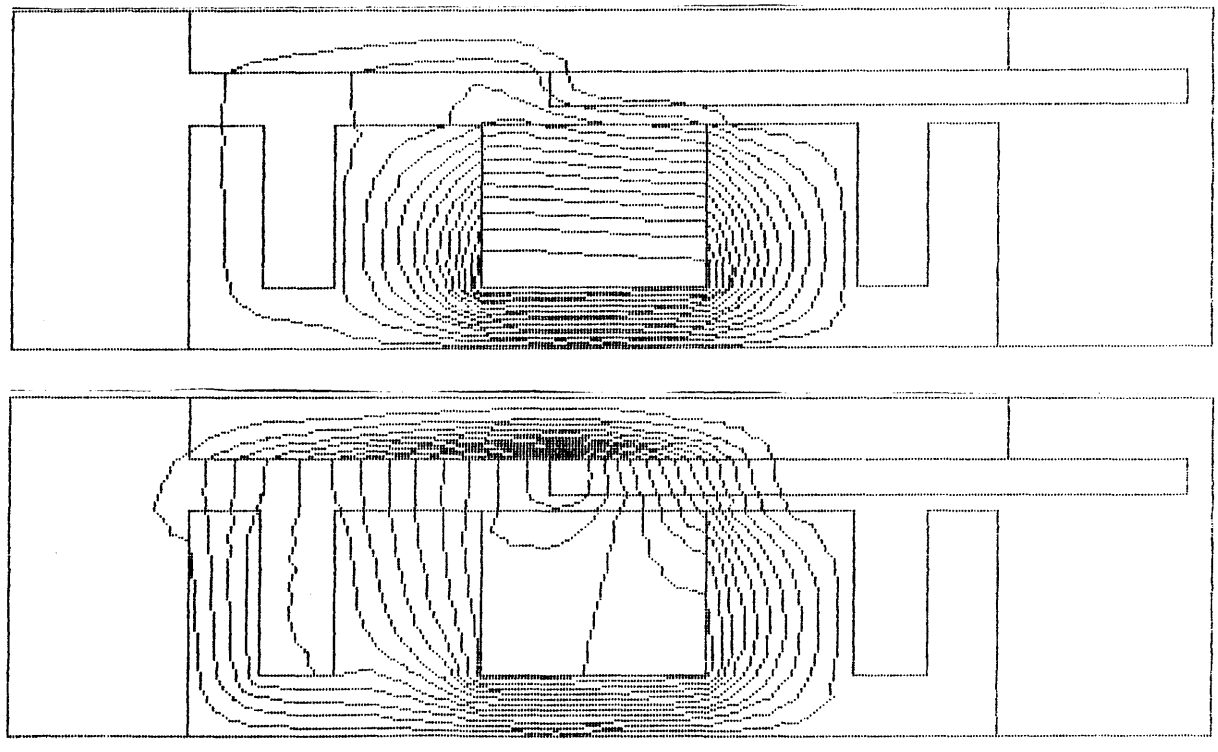

(b) Flux Density Distribution

Fig. 2.3 Investigation of the Xi-core TLIA Performance

2.3 Investigation of TLIA Construction

Like most conventional electric motors and actuators, many design variations apply to TLIAs. For example, the shape of its stator lamination, materials of plungers and mandrels, the excitation arrangement, *etc.* are all worth examining. Because it is a new machine, the study of its steady state characteristics must start at the very beginning. A two-stage model selected for study, using FEM2D, is shown in Fig. 2.1. The electrical parameters of its windings and the properties of materials of its various parts are listed in the table 2.1.

	σ $(\Omega \cdot m)^{-1}$	μ_r	J (A/mm^2)	R (Ω)	N_1 (turn)
stator	0	1500	—	—	—
plunger	5.714×10^{8}	1	—	—	—
mandrel	0	1000	—	—	—
winding 1	—	—	1.67×10^{7}	4.82	500
winding 2	—	—	1.60×10^{7}	3.20	320

Table 2.1 Two-stage Model for FEM2D

The purpose of this investigation is to study the design of an existing TLIA and to understand and master its special features to produce a better design. For example, is it possible or desirable to extend its stroke by using a two-stage configuration? What is the best shape of the winding slot? What are the effects of different materials of the plunger? These are some of the many factors that will influence the output characteristics of the TLIA. Only after determining its basic construction one can undertake further study to optimise the design.

2.3.1. Excitation Arrangement

1. Constant Current Supply in One Stage Only

The first case study is concentrated on the steady state performance of the TLIA, when it is excited by a constant current in winding 1 of Fig. 2.1. This investigation can be directly carried out by FEM2D based on the equation (2.1).

When the two-stage model is energised by a constant amplitude sinusoidally time varying current of 5 (A) in winding 1 of Fig. 2.1, its performance predicted by FEM2D is shown in Fig. 2.4. It shows the output forces, eddy current loss, back *emf* and other parameters as a function of the plunger displacement. The input resistance R_e and reactance X_e have been calculated based on a model shown in Fig. 2.5a. R_e corresponds to the eddy loss in the plunger given by,

$$R_e = \frac{P_e}{I_1^2} \qquad \cdots\cdots(2.12)$$

and X_e corresponds to the reactance introduced by the whole magnetic circuit, at the stator winding side given by,

$$X_e = \sqrt{\left(\frac{E_1}{I_1}\right)^2 - R_e^2} \qquad \cdots\cdots(2.13)$$

A corresponding phasor diagram is drawn in Fig. 2.5b.

Several interesting features can be observed in Fig. 2.4. Firstly, in Fig. 2.4a, there is not much variation of the output axial force and eddy current loss over the effective region of the stroke from 10 (mm) to 120

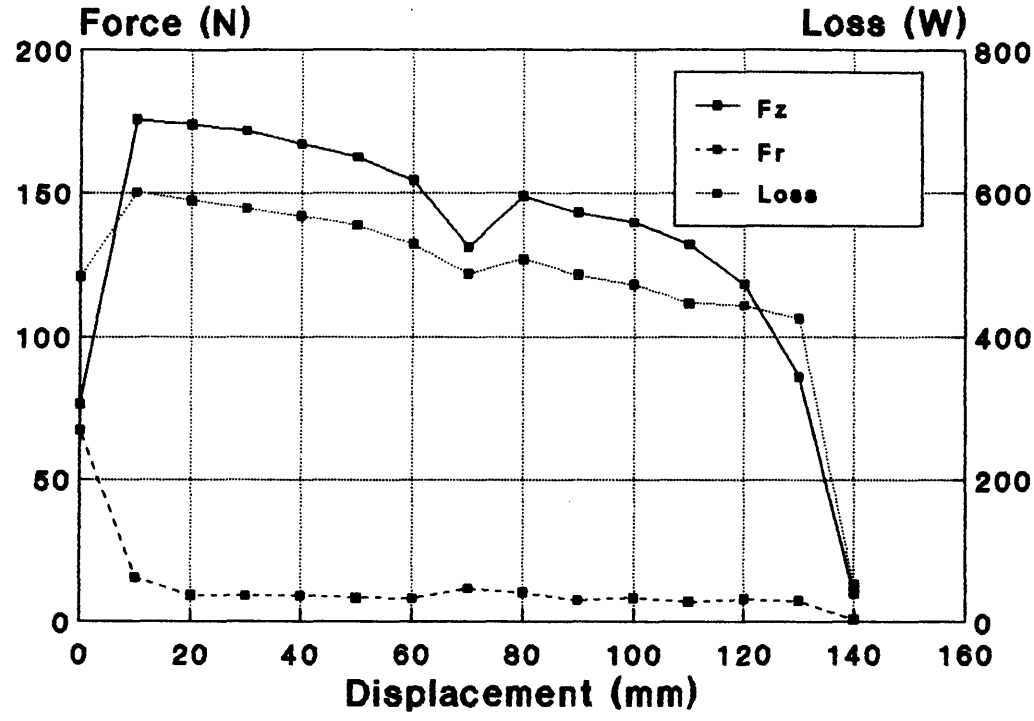

(a) Axial Force and Eddy Current Losses

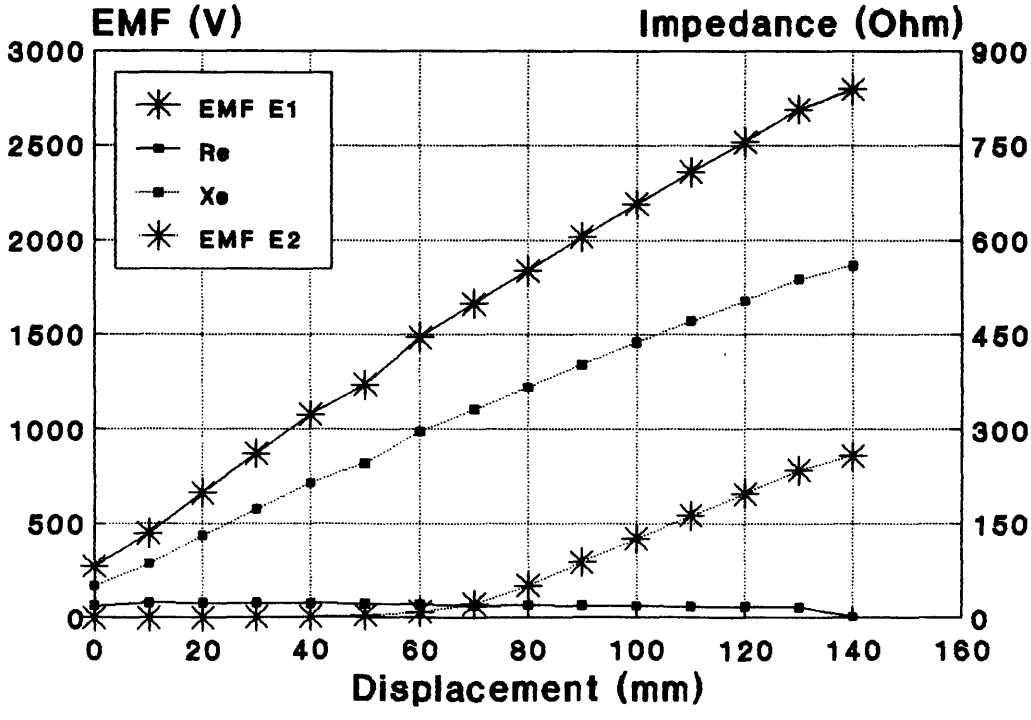

(b) Back *emf* and Equivalent Parameters

Fig. 2.4 Output Performance with Winding 1 Excited

(mm). This is quite a favourable characteristic for applications that require a constant axial thrust with stroke length.

Secondly, the radial force is seen to be quite small. It is easy to deduce that it is influenced by the slot mouth design. When the plunger is located under the slot mouth, the radial force is large. When it moves under the tooth, it becomes very small. The flux density is almost in the radial direction and only a very small axial component exists which interacts with the eddy current to produce radial force. In practice, it is better to have smaller radial force since this force may damage the hollow plunger if its wall is not thick enough.

Thirdly, it is noticeable that in Fig. 2.4b the back *emf* E_1 of the stator winding varies almost linearly from E_1 = 300 (V) at the beginning of the stroke to E_1 = 2800 (V) at the end. This means that the 5 (A) constant current source must be able to provide output voltage up to 2800 (V) assuming the TLIA is magnetically unsaturated. In practice, because of the nonlinearity of ferromagnetic material, the back *emf* will not be so high. However, one should keep in mind that in general the electromagnetic device need not be operated under such seriously saturated conditions.

Fourthly, the induced *emf* E_2 in the second stage winding 2 is almost zero when the plunger is located within the first stage region. This indicates that there is no flux linking the second winding until the plunger leaves the first stage. This is an extremely important phenomenon which suggests that the conventional method of using self-inductance and mutual inductance to estimate the machine performance is not suitable to the TLIA.

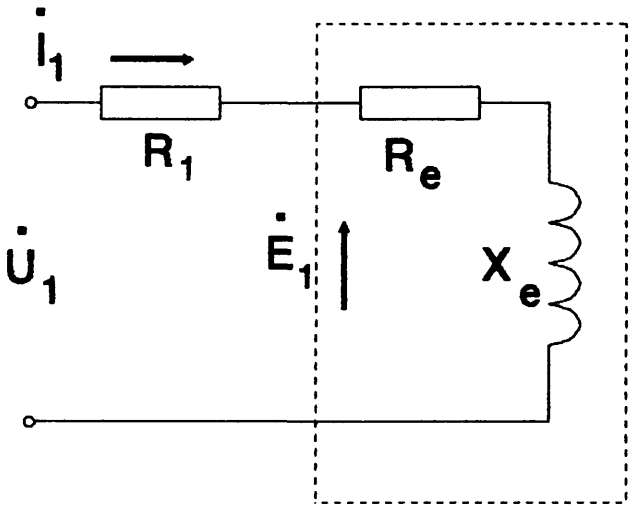

(a) Equivalent Circuit

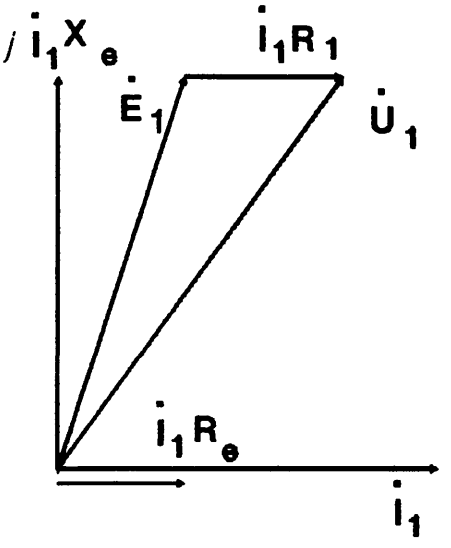

(b) Phasor Diagram

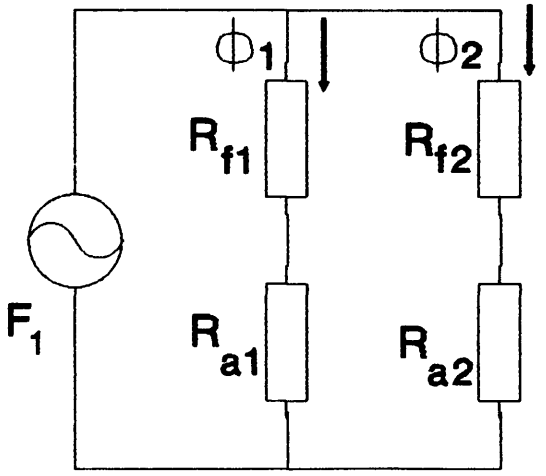

(c) Magnetic Circuit without Plunger

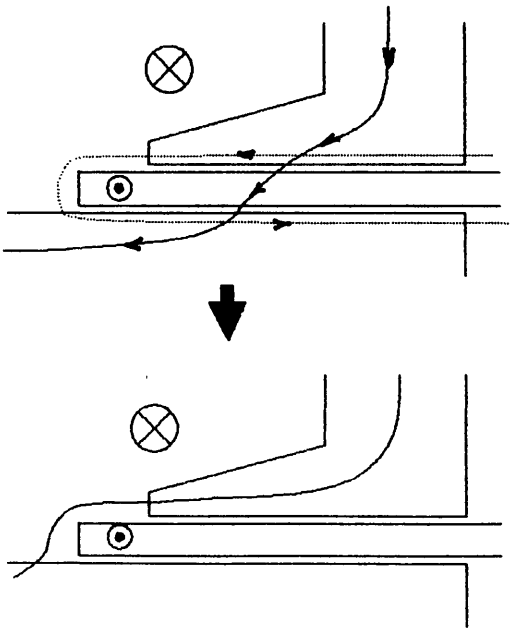

(d) Shielding Effect

Fig. 2.5 Equivalent Models for TLIA

Finally, the input reactance X_e is seen to increase when the plunger moves outward. This too is a very important property of this model. This makes the TLIA different from any other electromagnetic induction device such as linear motors and transformers in which their main reactance and leakage reactance are assumed to remain constant.

The final two phenomena are graphically illustrated in Fig. 2.6 in which the plunger is located at zero displacement. The graph shows that all the flux density and force gather at the inner end of the plunger within a length of 10 to 20 millimeters. There is no flux linkage coupling the second stage winding. This is also shown by Fig. 2.7 in which the flux density, eddy current density and force volume density along a particular line from a point A of coordinate (32, 5) to point B of coordinate (32, 105) are plotted. See Fig. 2.1 for coordinate references. There is very little flux density, eddy current and force beyond z = 0.06 (m). It should be noticed that the coordinate Z is different from the coordinate D as shown in Fig. 2.1. Their relationship in this model is $Z = D + 0.06$ (m).

These phenomena are closely associated with the plunger and its position in the TLIA. It is the presence of the conducting plunger that makes the TLIA different from the ordinary induction devices and makes the analysis difficult. If the plunger is removed, creating the no-load case, there will be no such phenomena. Its equivalent magnetic circuit can be drawn as shown in Fig. 2.5c in which R_{f1} and R_{f2} represent the reluctance of the magnetic flux path for each stage; R_{a1} and R_{a2} represent the reluctance of the airgap for each stage. In the design of the TLIA detailed in Fig. 2.1, R_{a1} and R_{a2} are equal because[12]

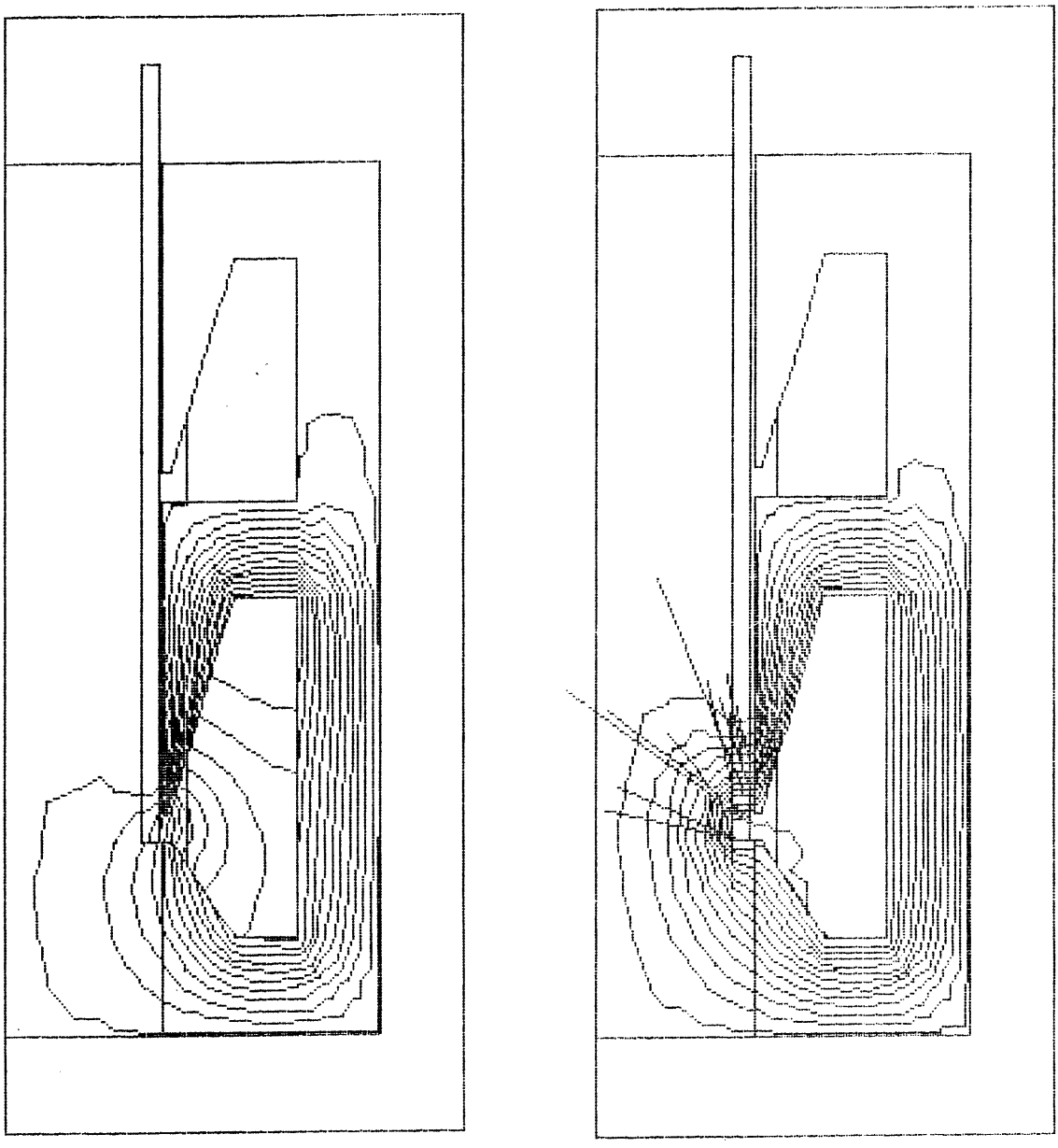

(a) Real Part (b) Imaginary Part

Fig. 2.6 Flux Density Distribution and Force Distribution with First Winding Excitation

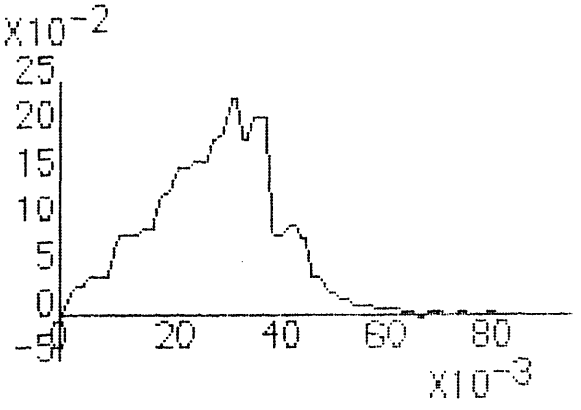

(a) Flux Density B_r (rms)

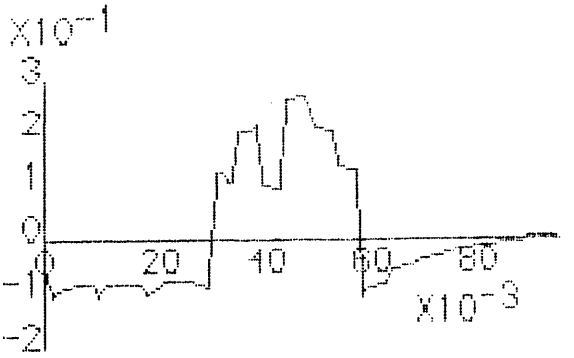

(b) Flux Density B_z (rms)

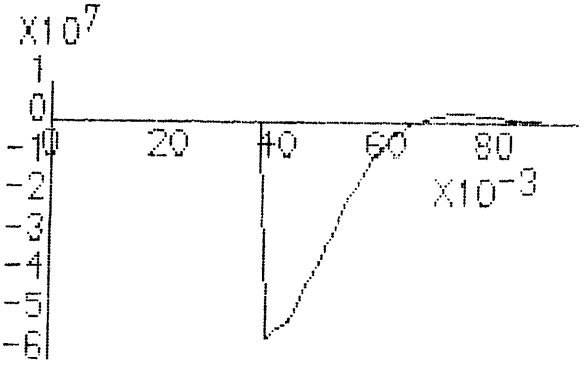

(c) Eddy Current Density (real)

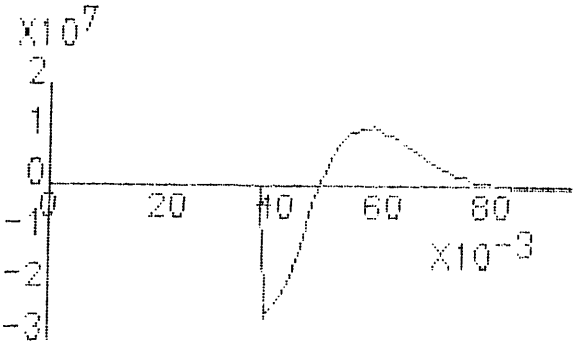

(d) Eddy Current Density (img)

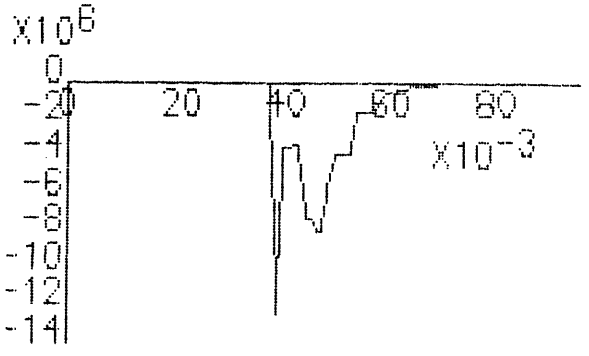

(e) Axial Force Density

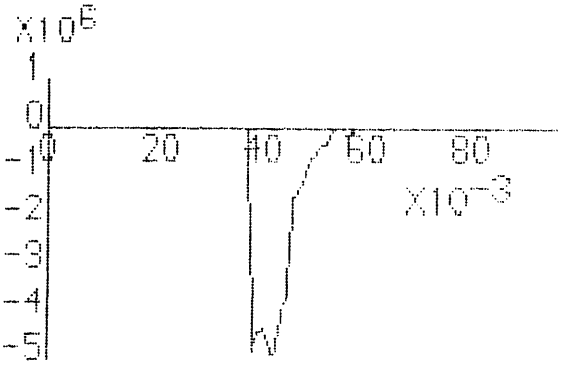

(f) Radial Force Density

Fig. 2.7 Distribution in the Axial Direction

$$R_{a1} = \frac{1}{\mu_0} \cdot \frac{g}{2\pi \cdot (r_1 + \frac{g}{2}) \cdot l_1} = \frac{1}{\mu_0} \cdot \frac{g}{2\pi \cdot (r_1 + \frac{g}{2}) \cdot l_2} = R_{a2}$$

in which l_1 and l_2 are the axial lengths of the airgap between the stator and mandrel of each stage. In this model they are equal.

In view of high permeability of the stator and the assumption that the stator structure is purely axisymmetric, the reluctance of the stator will be much less than that of the airgap. Thus,

$$\Phi_1 = \frac{F_1}{R_{f1} + R_{a1}} \approx \frac{F_1}{R_{a1}} = \frac{F_1}{R_{a2}} \approx \frac{F_1}{R_{f2} + R_{a2}} = \Phi_2 \qquad \cdots\cdots(2.14)$$

Consequently there will be a uniform flux density distribution in the airgap. The plunger in the TLIA acts like a sliding door. When it gradually moves out, flux will go through the opening unimpeded and the total reactance will vary in proportion to this opening. Fig. 2.8 gives the flux density distribution when the plunger is located at a displacement of 130 (mm). In this case, flux is almost evenly distributed under the airgap of both first and second stages. Almost half of the flux links both stages. Referring to Fig. 2.4a, only when the plunger moves beyond a displacement of 60 (mm), there is back *emf* induced in the second stage.

From the above observations, it is very clear that the position of the plunger in the TLIA determines the equivalent input reactance X_e. When the plunger moves in, the field distribution will be pushed backwards. Only a certain part of the flux will penetrate the end region of the plunger. Under unsaturated conditions this can be explained with the aid of Fig. 2.5d in which the combination of the flux produced by both stator current

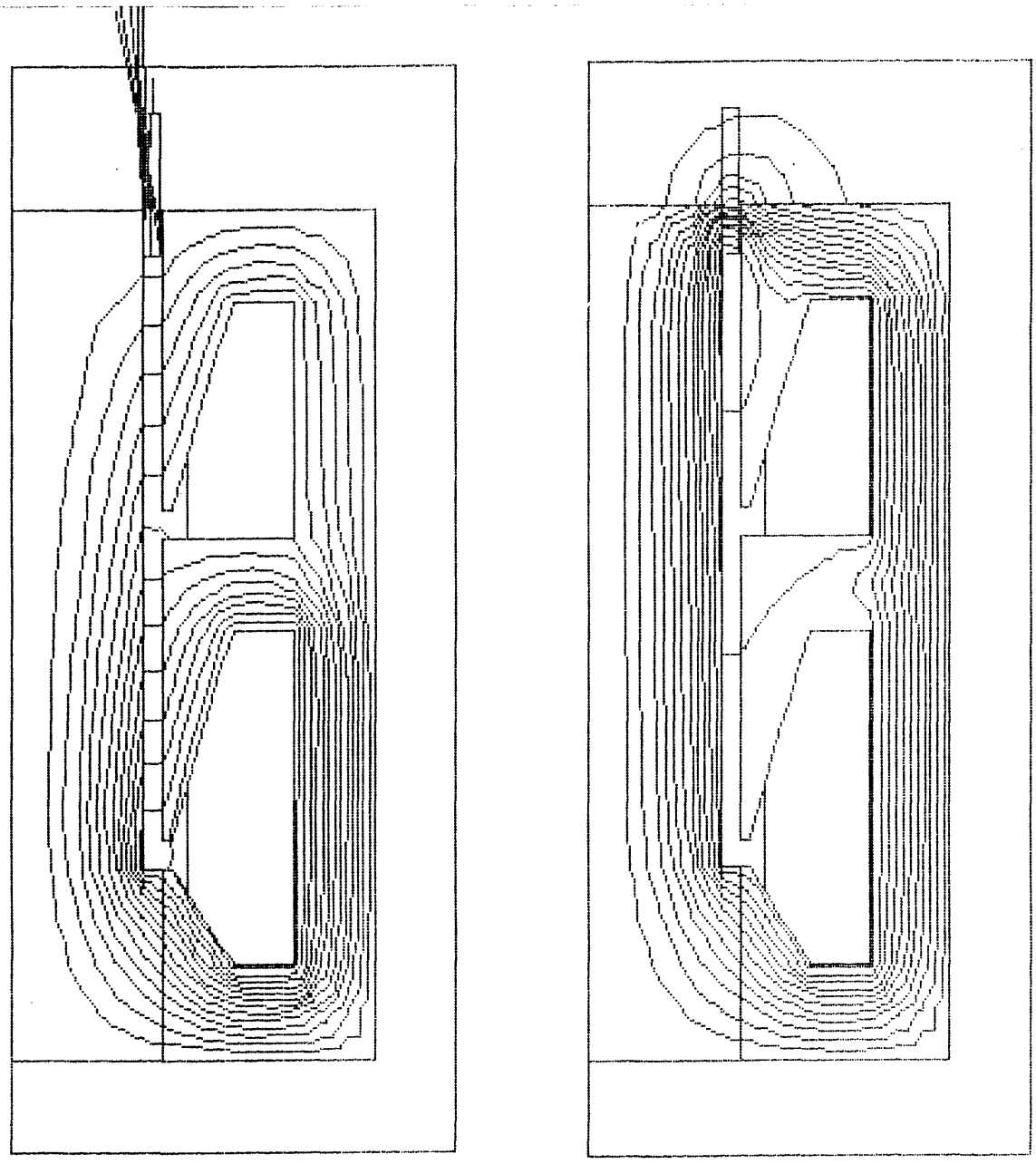

(a) Real Part (b) Imaginary Part

Fig. 2.8 Flux Density Distribution with Displacement of 130 (mm)

and eddy current in the plunger is sketched. The plunger acts as a shield, and for this reason it is called the shielding effect in this thesis.

2. A Constant Voltage Supply in One Stage Only

In general, most of the A.C. motors and actuators are excited from a mains supply which closely approximates to an infinite bus. A voltage forced solution is therefore of great interest to the user and designer alike.

When the TLIA is energised by a constant voltage U_1, the voltage equilibrium equation will be

$$\dot{U}_1 = \dot{I}_1 \cdot R_1 + \dot{E}_1 = \dot{I}_1 \cdot (R_1 + R_e + jX_e) \qquad \cdots\cdots(2.15)$$

where R_e and X_e are the equivalent input resistance and reactance obtained from the field solution and R_1 is the D.C. resistance of the stator winding. Under unsaturated conditions, the superposition principle applies. Therefore the output force with 240 volts excitation can be calculated by

$$F|_{240} = \left(\frac{I_1}{I_c}\right)^2 F_c \qquad \cdots\cdots(2.16)$$

in which I_c and F_c are the input current and output force under constant current excitation.

The resultant input current, output axial force and eddy current loss in the plunger are shown in Fig. 2.9. It is seen that, with the constant voltage excitation, the output axial force can not remain constant over its whole stroke as it does when excited by a constant current source. The

input current decreases quickly when the plunger moves beyond a displacement of 10 (mm). Similarly the output axial force and eddy current loss decrease sharply too. Unlike the case under constant current excitation, the TLIA becomes a constant flux machine when it is fed by a constant voltage. This can be seen from Fig. 2.9b in which the back *emf* is almost constant throughout the whole stroke. If there is no apparent change of X_e, then $I_1 = \frac{E_1}{X_e}$ should be a constant. However, as the plunger moves out, the shielding effect diminishes. Most of the flux will find itself a closed path directly through the airgap and the mandrel. The permeance of this flux leakage path is quite large. Hence, the total equivalent reactance of the magnetic circuit increases and input current decreases.

In the output performance characteristics shown in Fig. 2.9 the axial force remains at about 10% of its starting value, for most of the stroke travel. If it is only used to push an unrestrained object, it will perform well provided that the starting output force is large enough to overcome static friction. In this case, the object must be accelerated fast enough at the beginning and then allowed to reach its destination mainly supported by its inertia. However, if the load produces an opposing force such as the case shown in Fig. 1.8a, then the load may stop in transit due to the drop in axial output force. The performance indicated in Fig. 2.9a must be improved for real applications where considerable opposing forces are involved. The decline of axial force is obviously caused by the large variation of the reactance X_e. In order to balance the voltage equilibrium equation (2.15), the input current has to reduce when reactance X_e increases. Therefore, an important design objective is to find a suitable configuration that would limit the variation of X_e.

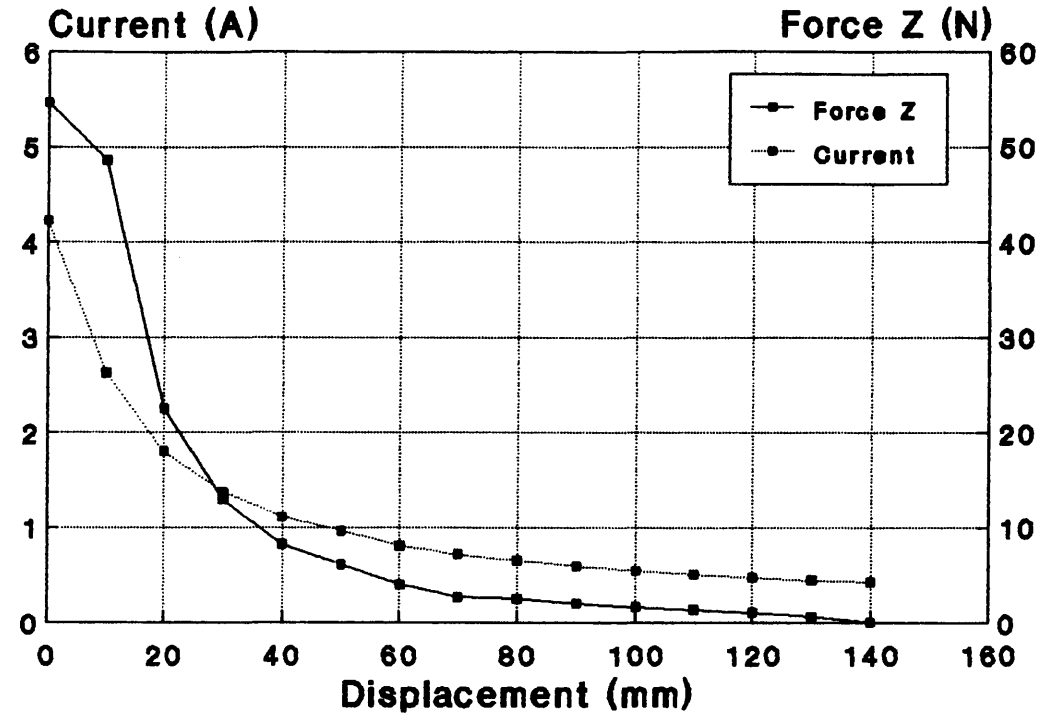

(a) Input Current and Output Axial Force

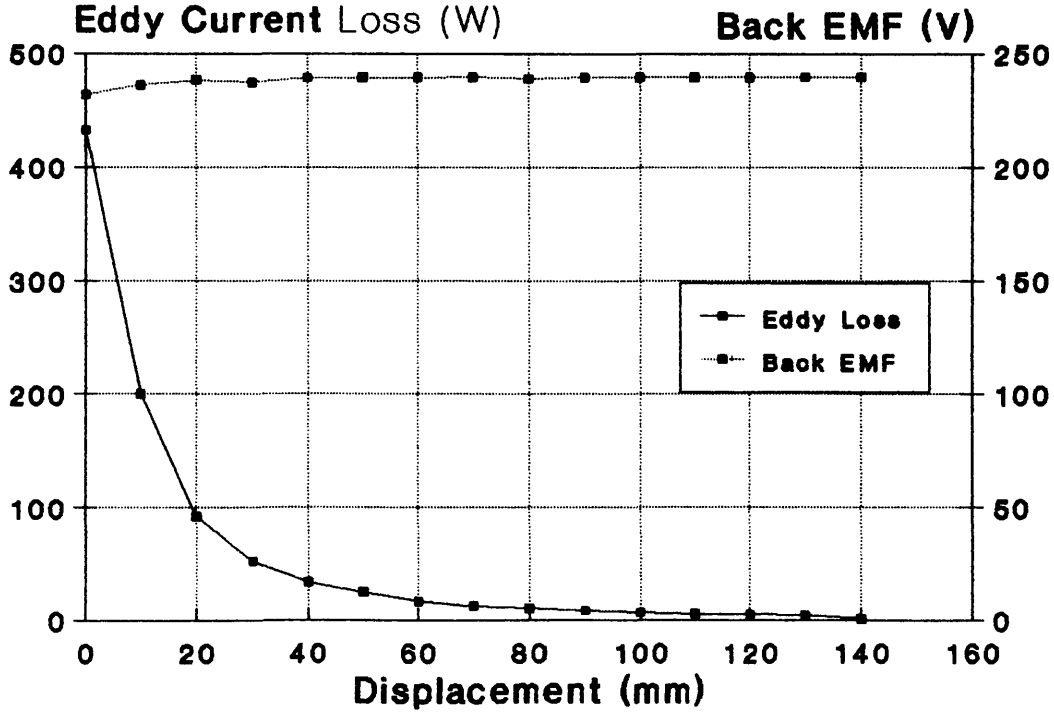

(b) Back *emf* and Eddy Current Losses

Fig. 2.9 Output Performance with Constant Voltage Excitation

3. Energising Strategy of the Two-Stage TLIA

No matter which power supply is selected, the above two cases indicate that the performance of a TLIA with closed slots is heavily dependent on the equivalent reactance X_e. The purpose of this section is to study the two-stage TLIA to determine, if the reduction in the variation of X_e with plunger position can extend its effective stroke. There are two main modes for the excitation of the two-stage TLIA. One is to excite both windings at the same time and connect them in series or in parallel. The other is to energise them at a time in sequence.

Since the analysis by FEM2D has been performed under linear conditions, it is easy to investigate the operation of each stage separately. The results can be superposed to demonstrate its whole performance. From Fig. 2.4b, it is found that X_e versus the displacement is nearly a straight line. This leads to the idea of making use of the second winding to avoid the TLIA operating with high X_e so that maximum X_e for each stage will be only half that in Fig. 2.4b. Under constant voltage excitation, the minimum input current of each stage will be doubled and the minimum output force will increase four times.

When the second stage winding only is fed by a constant current of 5 (A), its calculated output force and eddy current loss curves are shown in Fig. 2.10a. The most important phenomenon here is that when the plunger is located under the first stage region, there is almost no output axial force. Moreover, there is also no back *emf* induced in the first winding as shown in Fig. 2.10b and the field plots of Fig. 2.11. If the plunger is not located at the first stage region, almost half of the flux should pass

around the first stage as shown in Fig. 2.8a and then return through the mandrel because the permeability of the lamination and mandrel is much higher than that of the airgap. Similar phenomenon has already been seen in Fig. 2.4b and Fig. 2.6. When only the first stage winding is excited and the plunger is located at the first stage region, there is no induced *emf* in the second stage. It is the plunger that shields the electromagnetic field so that no flux will be able to link two windings together. Instead, flux penetrates the plunger to the mandrel and returns from it at the middle part of the plunger. Therefore, the axial force is composed of two parts. These two parts are equal to each other in magnitude but opposite in direction. The sum of them is equal to zero. However, its radial force still exists because of the flux density in the axial direction. Further details can be seen from Fig. 2.12 in which the flux density, eddy current density and force density along a straight line (seen in Fig. 2.11) from the point A of coordinate (34, 40) to the point B of coordinate (34, 180) are plotted.

The results presented above lead to a conclusion that the second stage winding will not make any contribution to the axial output force until the plunger moves out of the first stage region. In contrast, it dissipates considerable energy in the form of eddy current loss, especially when the TLIA is fed by a constant voltage supply. Fig. 2.13a illustrates the case in which the second stage winding is excited by a constant voltage of 240 (V). From the displacement of 0 (mm) to 60 (mm), there is no axial output force but very high input current of more than 8 (A) is drawn. Therefore, there is no use in feeding both windings at the beginning irrespective of the kind of power supply and coil inter-connection. A possible choice is to energise the two windings of the TLIA, in sequence, one after the other

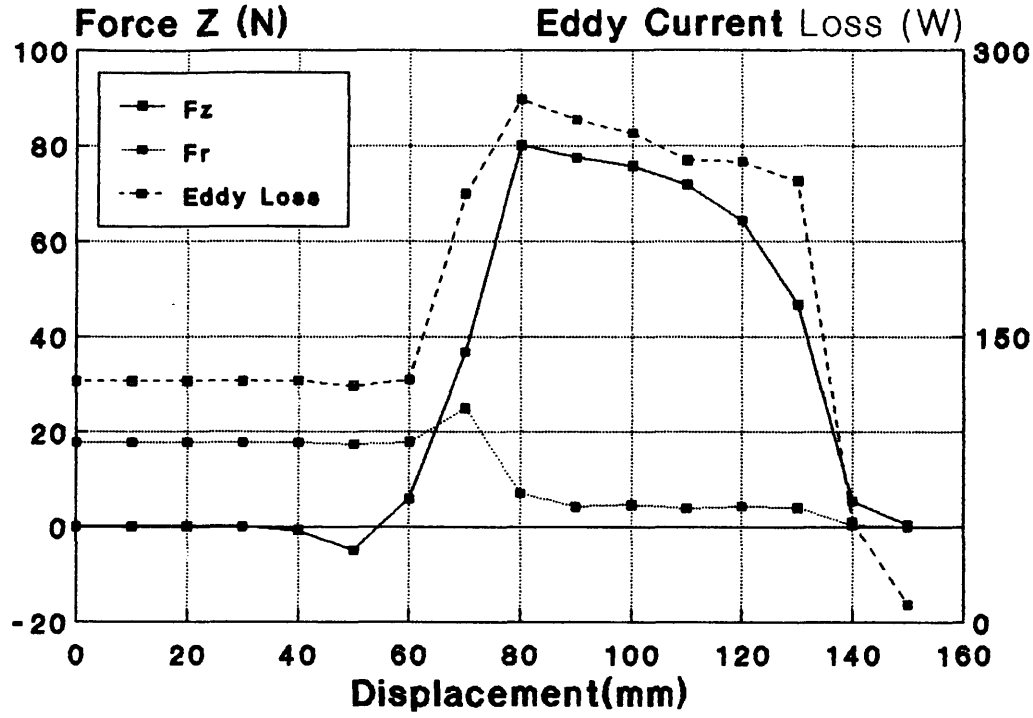

(a) Axial Force and Eddy Current Losses

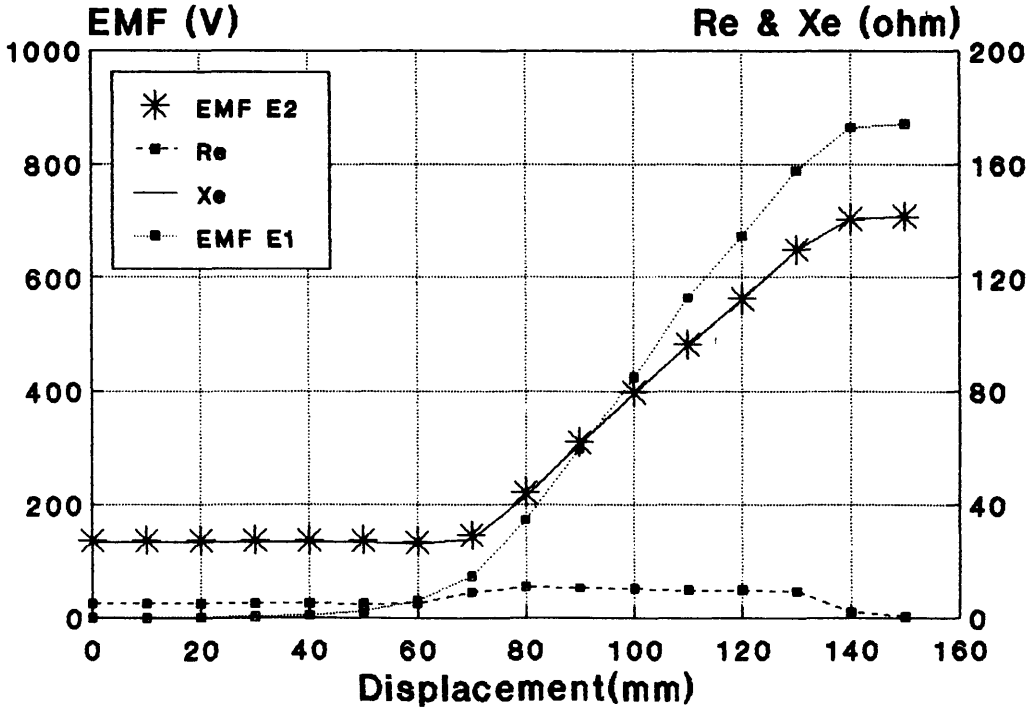

(b) Back *emf* and equivalent Parameters

Fig. 2.10 Output Performance with the Second Winding Excited

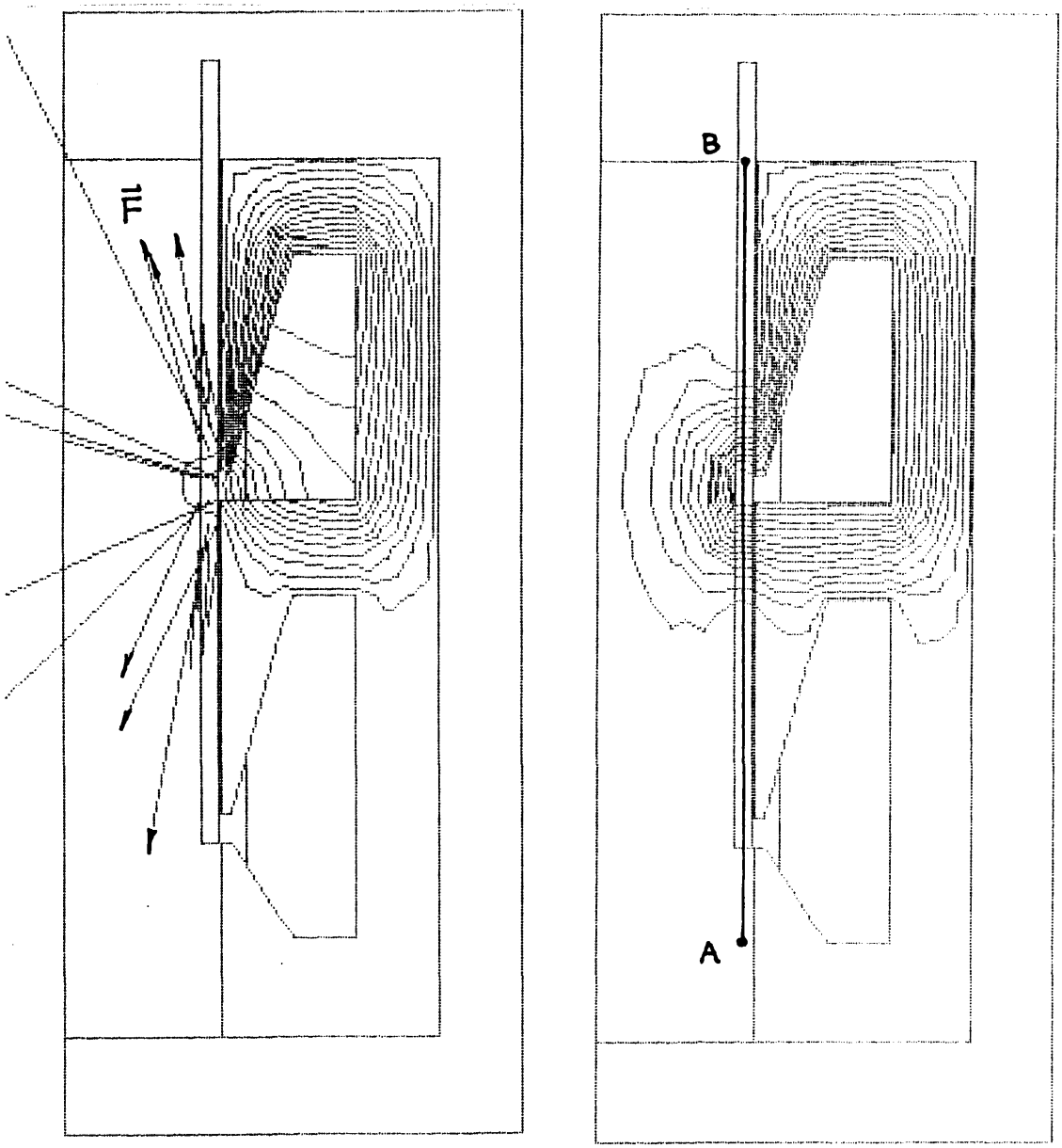

(a) Real Part (b) Imaginary Part

Fig. 2.11 Flux Density Distribution with the Second Winding Excited (Plunger Located at Displacement of 0 mm)

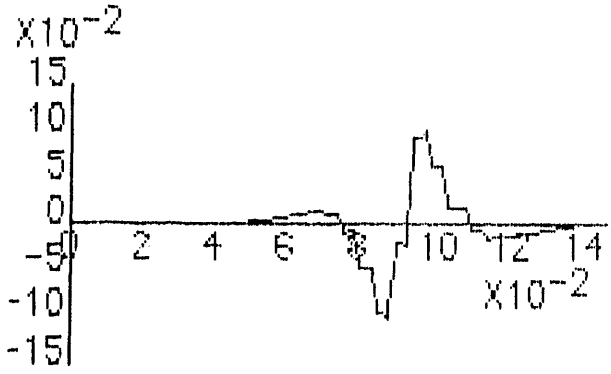

(a) Flux Density B_r (real)

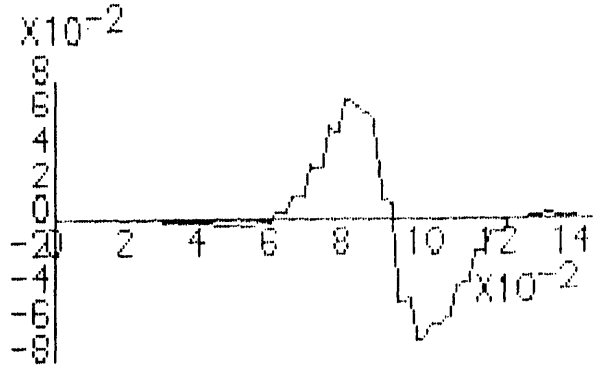

(b) Flux Density B_r (img)

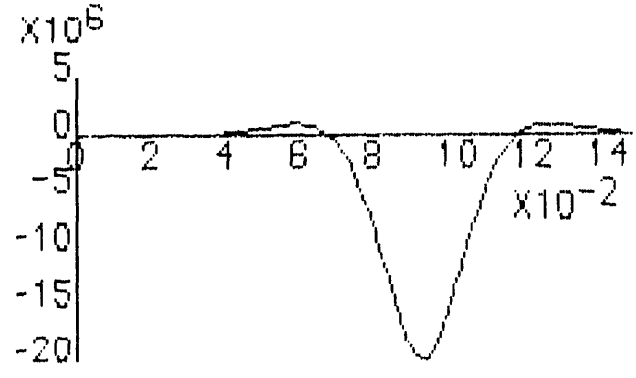

(c) Eddy Current Density (real)

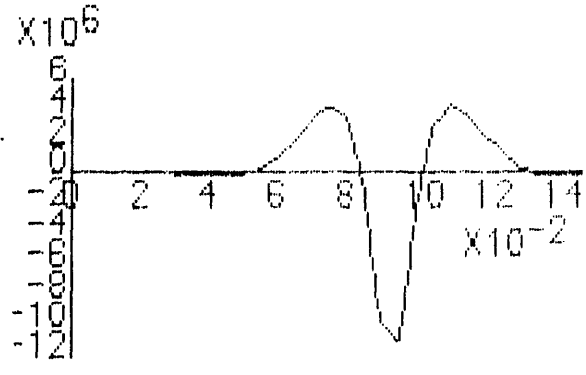

(d) Eddy Current Density (img)

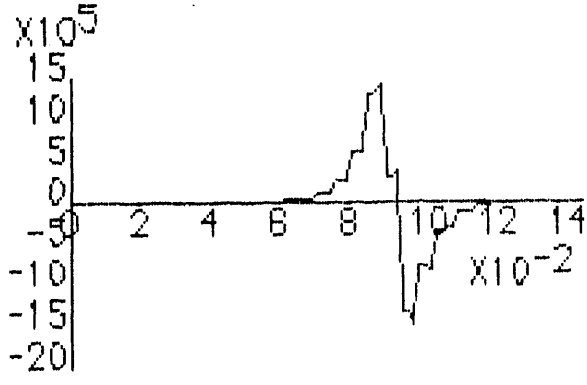

(e) Axial Force Density

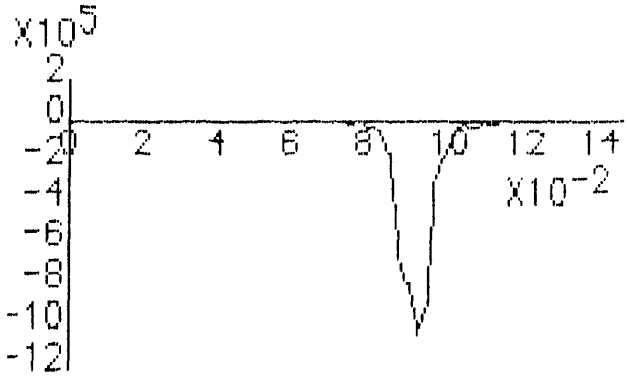

(f) Radial Force Density

Fig. 2.12 Force, Eddy Current & Flux Distribution along Axial Length of Plunger

according to the position of the plunger. This will result in the performance curves shown in Fig. 2.13b.

The strategy of energizing the two-stage TLIA in sequence is easy to realize. We need only turn off the first stage and turn on the second stage when the plunger reaches the interface. Such technology has also been used to control the θ gun[4] when it launches a projectile through several stages. This dynamic problem will be discussed, simulated and experimental work presented in Chapter 5.

The evidence of the reduction in X_e in the two-stage model with sequenced switching strategy can be found by comparing Fig. 2.4b and Fig. 2.10b. If the first stage is switched off at displacement of 70 (mm), its maximum X_e is about 300 (Ω). If the second stage is switched on now, the maximum X_e is about 140 (Ω) as shown in Fig. 2.10b. If only the first stage is used, the maximum X_e will reach 550 (Ω) at its longest stroke of 140 (mm) as shown in Fig. 2.4b.

Although the two-stage TLIA with sequenced excitation will reduce the maximum X_e and increase the input current and hence the output force, it still has a shortcoming in that there is a concavity in its force-stroke curve between the two stage regions as shown in Fig. 2.13b. In fact, this concavity is caused by the variation of X_e in each stage. In order to reduce this variation, the influence of slot shape will be studied in next section.

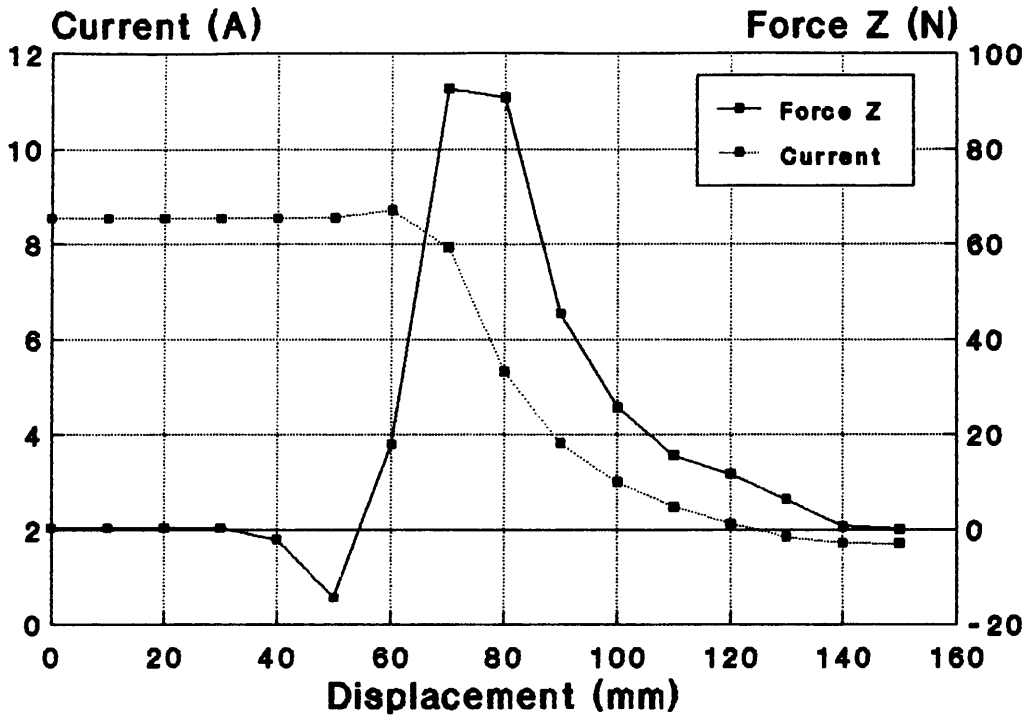

(a) Voltage Source Excitation in the Second Stage Only

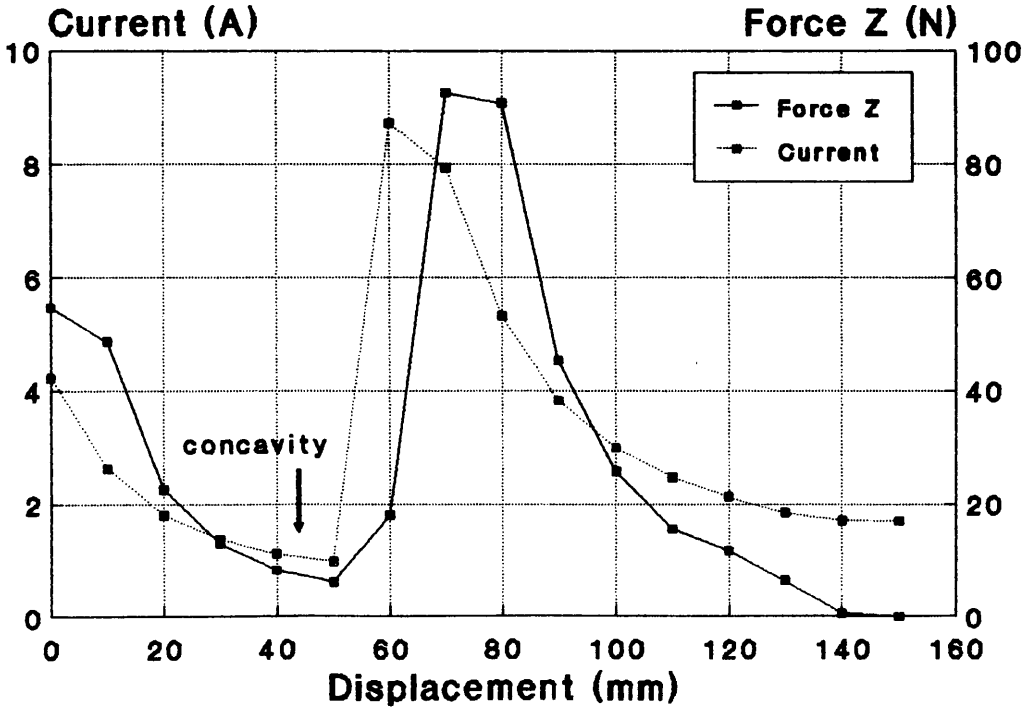

(b) Switching on Two Stages in Sequence

Fig. 2.13 Voltage Source Excitation in Each Winding

2.3.2 Relationship between Slot Shape and Equivalent Reactance

The energisation modes discussed above indicate that the steady state characteristics of the TLIA is mainly dominated by the permeance of its magnetic circuit. In this special actuator, this permeance is controlled by the shielding effect of the plunger. It is this plunger that plays a role of sliding door that controls the flux path. When it is fully inserted into the TLIA, the door is almost closed to the flux. It only leaves a small part to let the flux couple the eddy currents. This part must exist to allow the induced eddy currents to balance the *mmf* produced by the stator winding current. The width of this part can be roughly estimated by the penetration depth Δ of the plunger, which will be discussed in next section. Only in this limited area does the eddy current interact with the radial flux to produce the axial force. Other parts of the flux will try to skirt round the end of the plunger directly into the mandrel. This part becomes the leakage flux and will not produce useful force at all. Obviously the permeance of leakage paths depends entirely on the 'door' location. When the plunger is under the mouth, the flux must make a detour by the corner at the plunger end, thus the reactance X_e becomes small. When the plunger is under the tooth, most of leakage flux can pass directly from the tooth to the mandrel. In this case, because of the high permeability of steel, X_e is mainly dependent on the length of flux path which is the same as the length of the airgap. Therefore, the equivalent reactance will be smaller in the former situation and larger in the latter.

As has been pointed out in the previous section, the main task of the design is to reduce the variation of X_e. Obviously, it is difficult to

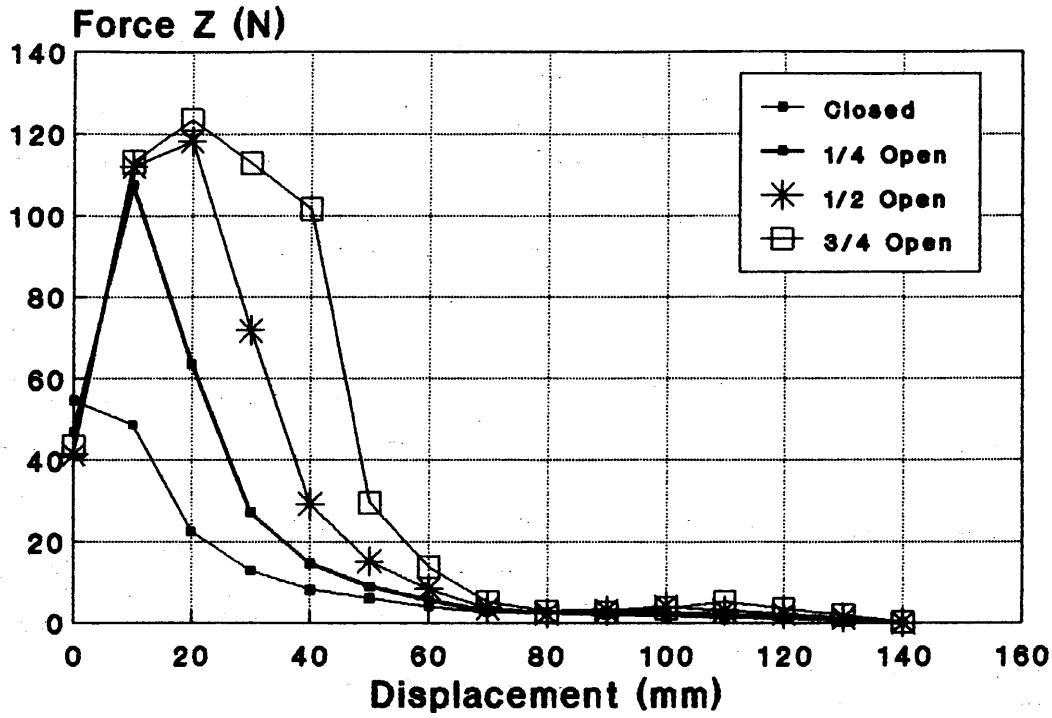

(a) Axial Force versus Displacement

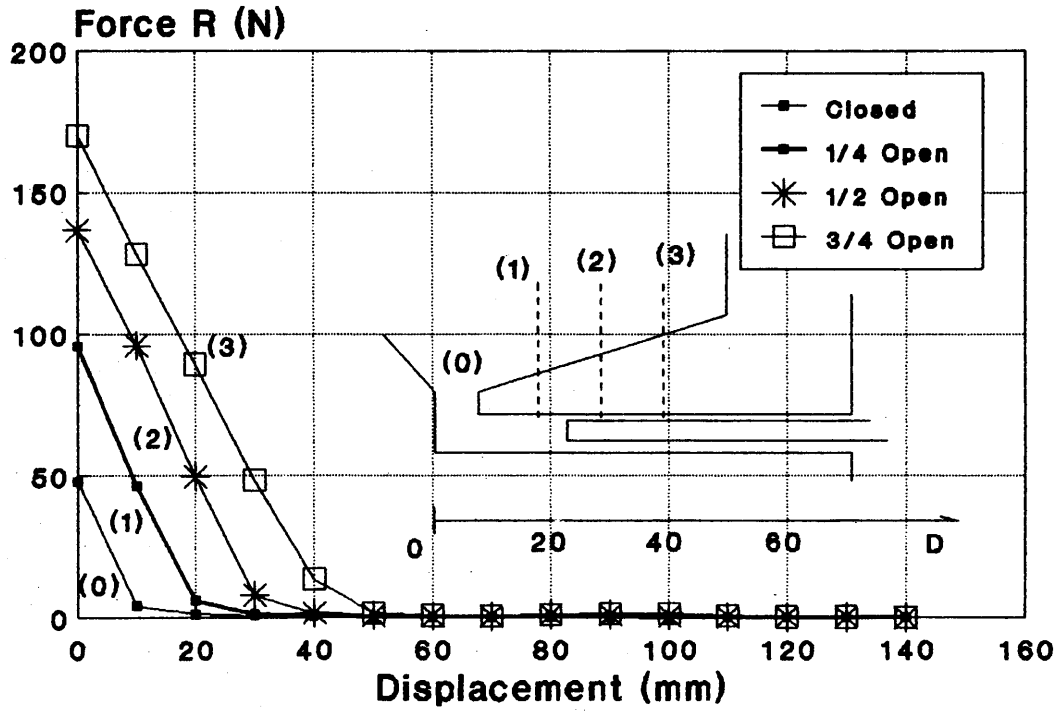

(b) Radial Force versus Displacement

Fig. 2.14 Comparing Results of Different Slot Mouths

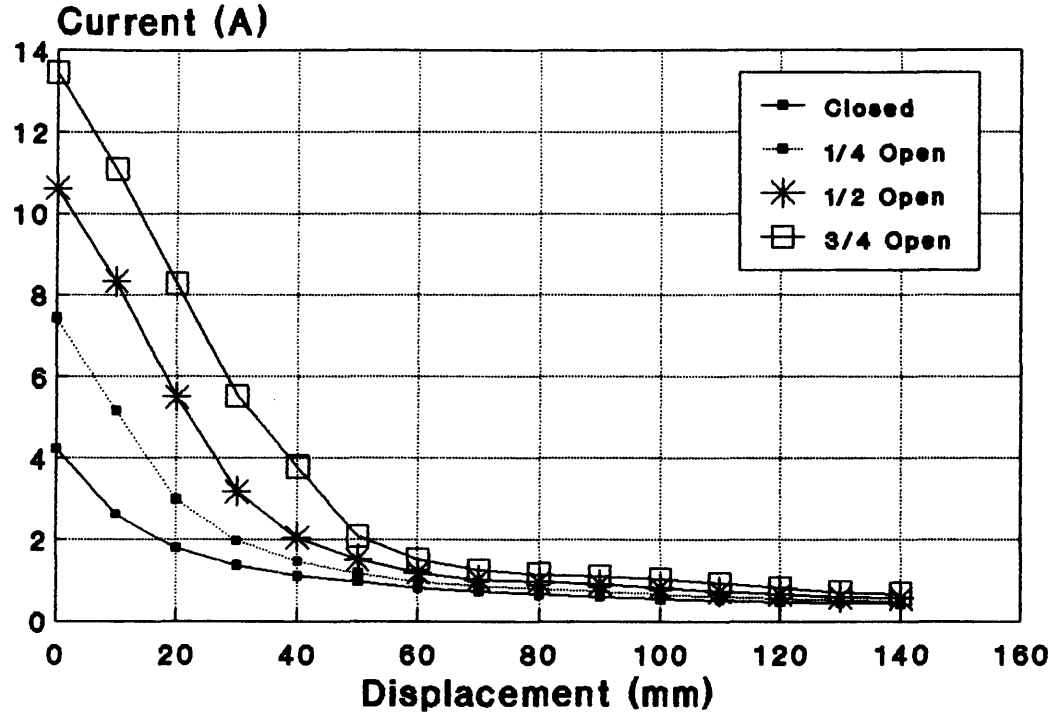

(c) Input Current versus Displacement

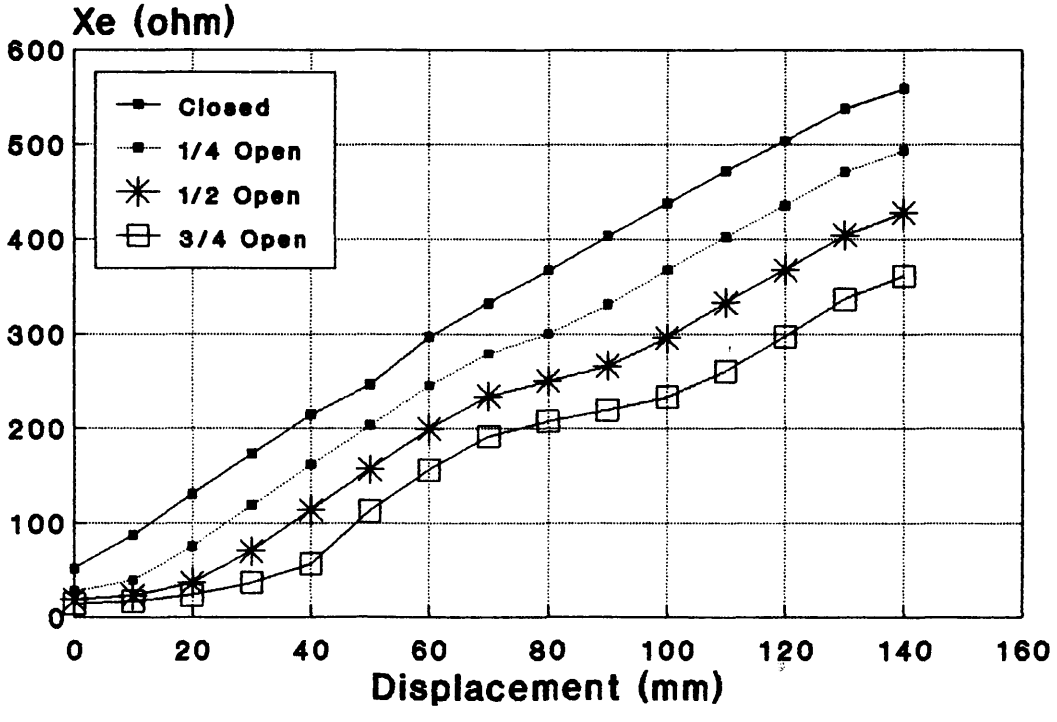

(d) Equivalent Reactance versus Displacement

Fig. 2.14 Comparing Results of Different Slot Mouths

change the inherent shielding effect. Hence, a possible way to limit the variation of X_e is to open the slot mouth as shown in Fig. 2.1. The following comparisons are made with the slot mouth changing from a nearly closed condition into 1/4 opened, 1/2 opened and 3/4 opened conditions under constant voltage excitation. The results are shown in Fig. 2.14.

Fig. 2.14a shows that the output axial force has increased significantly over a wider region with increasing mouth width. If the slot mouth is enlarged from 6 (mm) to 40 (mm) the output axial force region will increase from about 20 (mm) to 50 (mm). In addition, the maximum force is doubled and its location moves toward the center of the mouth. At the same time its input current and radial force increase too, as shown in Fig. 2.14c and b, leading to increased thermal losses. All of these are due to the decrease of X_e when the slot mouth is enlarged. In order to expand the range of axial force without increasing the losses, its input current can be adjusted in the design, for example by changing the number of turns of the winding, *i.e.* increasing X_e because

$$X_e = \omega \cdot \Lambda \cdot N^2 \qquad \cdots\cdots\cdots(2.17)$$

in which, Λ is equivalent permeance of whole magnetic circuit. It should be emphasized here that the most important criterion is the reduction of the variation of X_e, and not the value of X_e itself. Therefore, instead of only having a small axial force over a small displacement range, the open slot TLIA will provide a comparatively large force covering the entire width of the mouth. This advantage allows the TLIA to lift a heavy weight or push a load with an opposing force such as a spring load.

It is quite evident in Fig. 2.14d that the variation of X_e decreases greatly under the open mouth region from 0 (mm) to 40(mm) at the first

stage and from 70 (mm) to 110 (mm) at the second stage when the mouth is of 3/4 opened. But the variational shape of the X_e curve remains the same as in the case of the closed mouth. This is easy to explain by the fact that when the plunger leaves the tooth region, the permeance between the tooth and mandrel is quite large. It can be estimated[12] by

$$\Lambda = \frac{2\pi \cdot \mu_0 \cdot l}{\ln\left(\frac{r_1 + g}{r_1}\right)} \qquad \cdots\cdots\cdots(2.18)$$

in which l is axial distance from the end of the plunger to the tip of the steel tooth. The permeance Λ is proportional to l. Fig. 2.15 shows the axial force and input current variations with stroke, when the slot mouth is 3/4 opened. Compared with the results in Fig. 2.13b, the concavity in its force-stroke curve is greatly reduced. This leads to the conclusion that it is better if the slot mouth is entirely opened and the steel part between two windings is designed as narrow as possible. Obviously, if the load produces an opposing force such as a spring, a better choice is a TLIA with open slot.

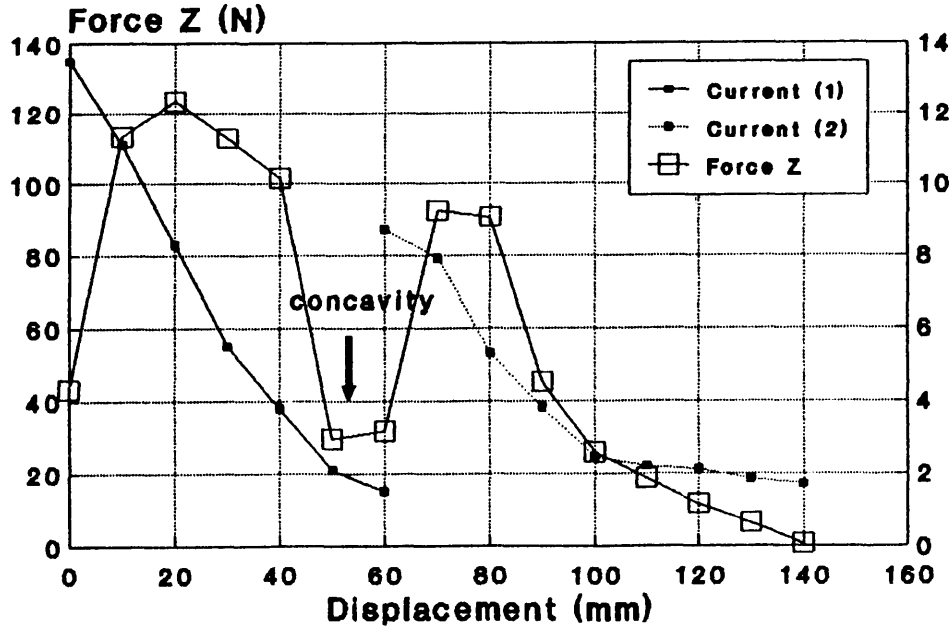

Fig. 2.15 Two-stage with 3/4 Slot Mouth Opened

2.3.3 Material Selection for the Plunger

The plunger is a key component of the TLIA which enables energy conversion from electromagnetic to mechanical to take place. Theoretically, the conversion is based on the Lorentz law $\mathbf{J}\times\mathbf{B}$ to produce the force in the plunger. Therefore, unlike normal A.C. solenoids the plunger must be made of conducting material to enable eddy currents to circulate in its conducting wall. This results in a special feature named the shielding effect which has already been discussed in last two sections. In this section further study concerned with different conductivities is carried out to aid the selection of plunger materials. The combination of different slot shapes and plunger materials leads to several new results.

1. Influence under TLIA with Nearly Closed Slots

When the TLIA is excited by a constant current source, the change of plunger conductivity from 5.7×10^{7} $(\Omega\cdot m)^{-1}$ to 3.0×10^{7} $(\Omega\cdot m)^{-1}$ does not result in significant change in output force. This can be seen in Fig. 2.16a in which the asterisk * represents the output force produced by the plunger with a conductivity of 3.0×10^{7} $(\Omega\cdot m)^{-1}$ which is nearly equal to the conductivity of pure aluminum. Apparently, its axial force is only slightly different from that of the copper plunger with a conductivity of 5.7×10^{7} $(\Omega\cdot m)^{-1}$. The difference occurs at two regions. When the plunger is located under the mouth region, corresponding to a displacement of 0 (mm) in Fig. 2.16a, the plunger with lower conductivity produces higher output force. When the plunger is located near the stator end, in Fig. 2.16a at displacement of 110 (mm), the one with lower conductivity produces lower output force. However, its eddy current loss will increase when the

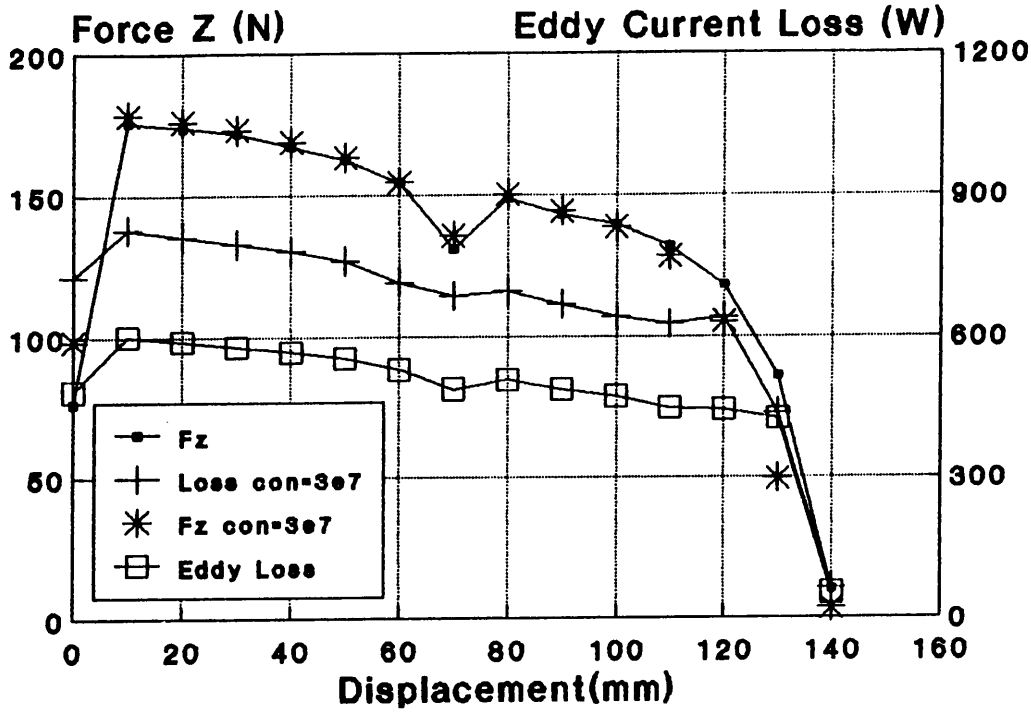

(a) Constant Current Condition

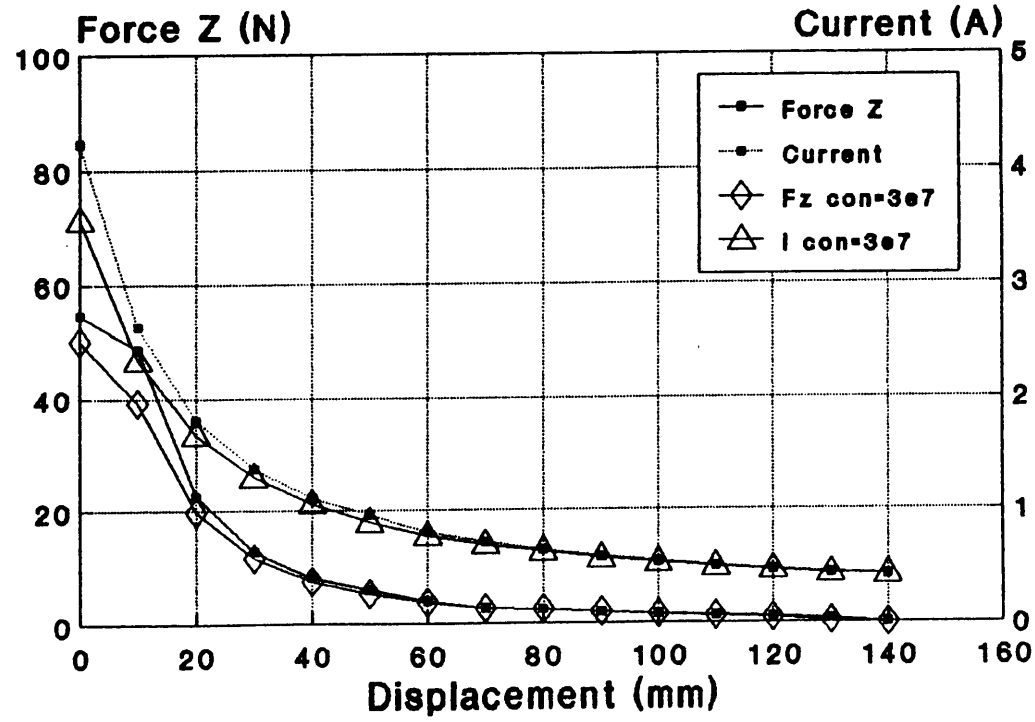

(b) Constant Voltage Condition

Fig. 2.16 Change of the Plunger Conductivity

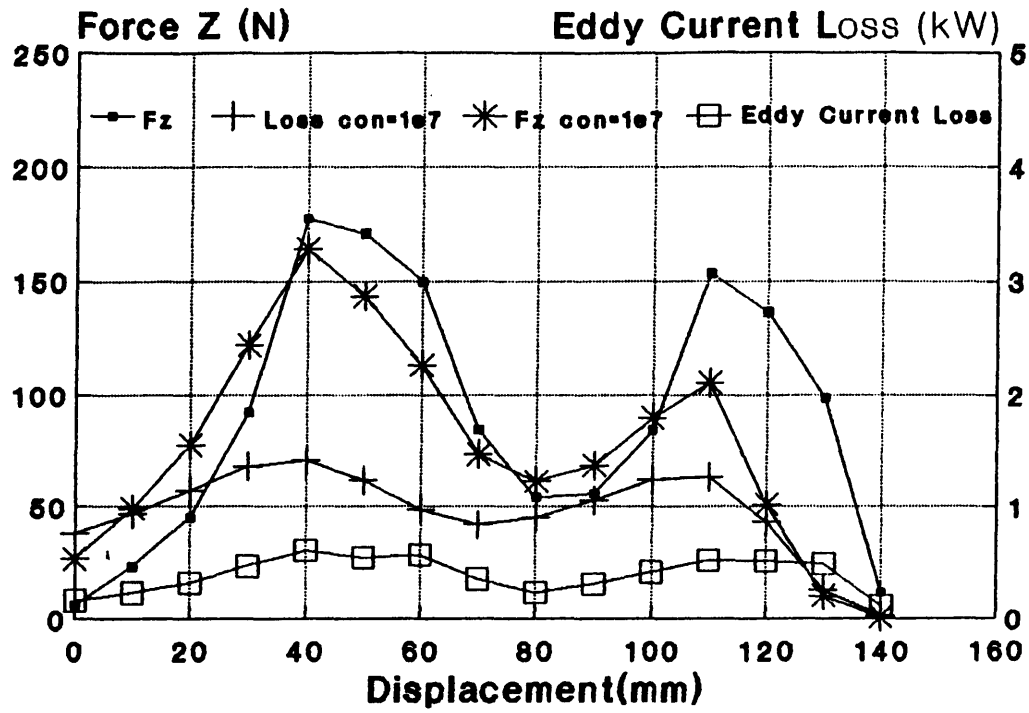

(c) 3/4 Open Slot under Constant Current Condition

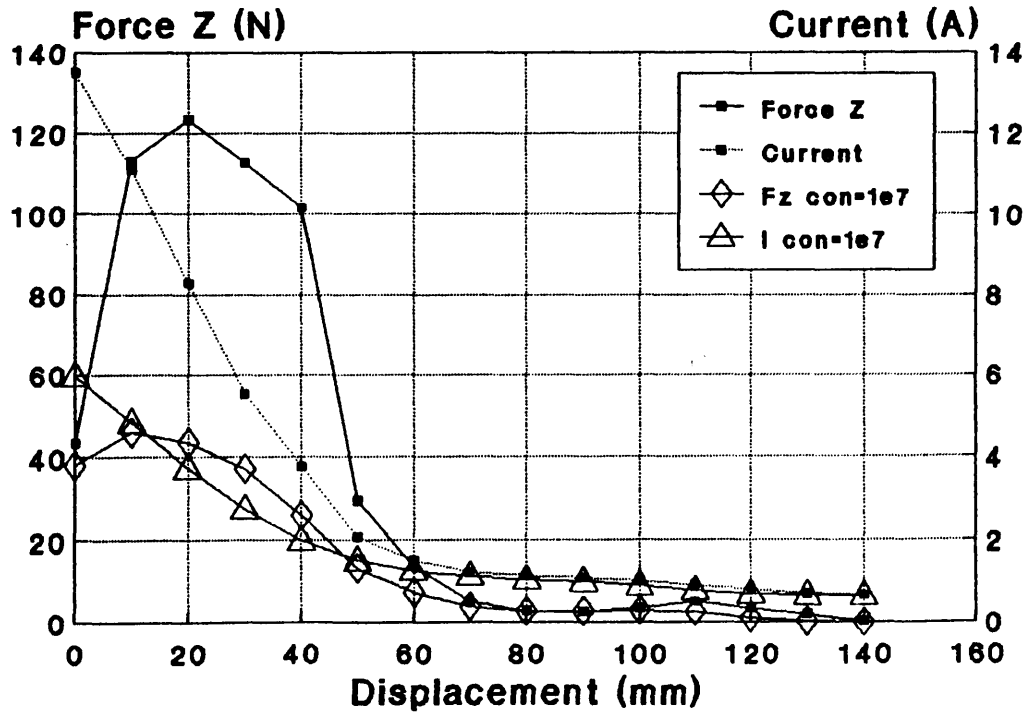

(d) 3/4 Open Slot under Constant Voltage Condition

Fig. 2.16 Change of the Plunger Conductivity

plunger is made of material with lower conductivity . This can be seen in Fig. 2.16a in which the symbol of small square indicates the loss in the plunger with a conductivity of 5.71×10^{7} $(\Omega\cdot m)^{-1}$ and the symbol of plus sign represents that with a conductivity of 3.0×10^{7} $(\Omega\cdot m)^{-1}$. In the numerical investigation by FEM2D it will be shown that the relationship between these losses could be approximately expressed by their a.c. resistance related to the penetration depth Δ.

When the TLIA is energised by a constant voltage source, its input current $\dot{I}_1$ must satisfy the voltage equilibrium equation (2.15). If one uses the normal equivalent circuit of a transformer with its secondary short circuited as shown in Fig. 2.17a, it is obvious that the sum of the leakage reactance of both stator winding and plunger $X_{\sigma 1}+X'_{\sigma 2}$ will determine the input current because $X_{\sigma 1}+X'_{\sigma 2} \gg R'_2$. $X_{\sigma 1}$ changes with the plunger position. It is small when the plunger is fully retracted and increases as the plunger moves out. This feature is totally different from that of normal induction machines or transformers, in which both $X_{\sigma 1}$ and the equivalent reactance $X'_{\sigma 2}$ will not change during their operation. Therefore, the usual way of using an equivalent circuit to predict performance is not suitable for the TLIA. This is why FEM becomes an indispensable tool to study it.

In Fig. 2.16b, when the plunger is located in the region corresponding to displacements of 0 (mm) to 20 (mm), there is a considerable input current and output force drop for the TLIA with a low conductivity plunger. In this case, leakage reactance $X_{\sigma 1}$ is small. Compared with $X_{\sigma 1}$, the equivalent resistance R_e occupies a considerable part of the total impedance. Decrease of conductivity will result in the increase of the equivalent resistance R_e and total impedance. Thus both input current and

output force decrease. After the plunger moves under the steel tooth, *i.e.* under the region beyond 20 (mm), because $X_{\sigma 1}$ becomes much larger than R_e, the change of R_e will not affect the total impedance. Therefore, the input current

$$I_1 = \frac{U_1}{\sqrt{(X_{\sigma 1} + X'_{\sigma 2})^2 + R_e^2}}$$

will not change and so does the output axial force, $F_z \propto I_1^2$.

2. Influence under TLIA with Opened Slot

For the TLIA with opened slot, the effects of changing the conductivity are different. For the purpose of discussion, the TLIA with 3/4 slot opening is chosen as the example. The conductivity of one plunger remains at 5.71×10^7 $(\Omega\cdot m)^{-1}$. The conductivity of a second plunger is chosen as 1.0×10^7 $(\Omega\cdot m)^{-1}$, which is nearly equal to that of mild steel. Fig. 2.16c shows their axial force and eddy current loss variation with stroke, when excited by a constant current of 5 (A). It is seen that the difference between the output force produced by the plungers with different conductivities is greater than that of the closed slot shown in Fig. 2.16a. Before it moves under the tooth, the lower conductivity plunger possesses higher axial force. After it moves under the steel tooth, the lower conductivity plunger develops lower axial force. When the plunger is near the end of its stroke, the axial force of the lower conductivity plunger drops sharply. Under the first stage, the average output forces for both cases are almost the same. However, there is obviously a higher eddy current loss taking place in the low conductivity plunger. Fig. 2.16d

shows the characteristics when the TLIA is energised by a constant voltage source. Comparing Fig. 2.16d with Fig. 2.16b, it is evident that the characteristics are vastly different. With the open slot, input current and output force of the low conductivity plunger drop sharply near the slot mouth region. Unlike the closed slot case, X_e in the equivalent circuit in Fig. 2.17, given by $X_e = X_{\sigma 1} + X'_{\sigma 2}$ is quite small for the open slot TLIA. In the low conductivity plunger it is even smaller than $R_e = R'_2$. Therefore, R'_2 becomes a key factor in determining the input current and the output force. Their variations with the stroke are shown in Fig. 2.17.

3. The Inner End Effect

The name of the inner end effect comes from the fact that when the plunger is located in the TLIA, a large proportion of eddy currents gathers at its inner end. Moreover, it has been found that the width of this eddy current area will vary with plunger conductivity. This variation is found to approximately obey the law of penetration depth.

Although it has been mentioned that all the flux density and eddy current density concentrations in the plunger always accumulate at its end, it has not been explained and analysed it quantitatively. This is because it is difficult to find an exact mathematical model. From the investigations carried out using FEM2D, it is found that the penetration depth theory applies here. This is illustrated in several flux distribution graphs shown in Fig. 2.6, 2.8 and 2.11 and also in the graphs of flux and current density distribution in the axial direction, *e.g.* Fig. 2.7 and Fig. 2.12. In these graphs, the penetration depth is

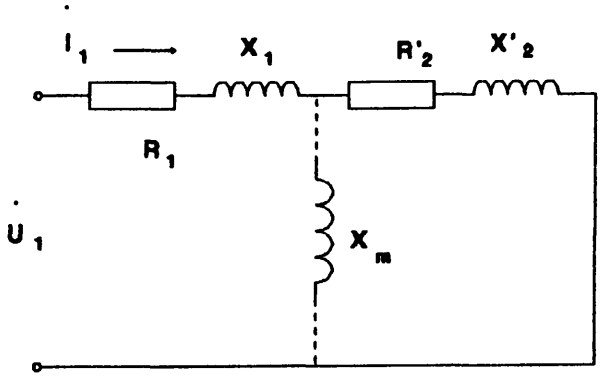

(a) Equivalent Circuit for Transformer

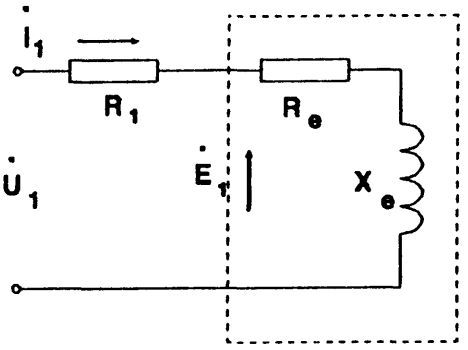

(b) Equivalent Circuit for TLIA

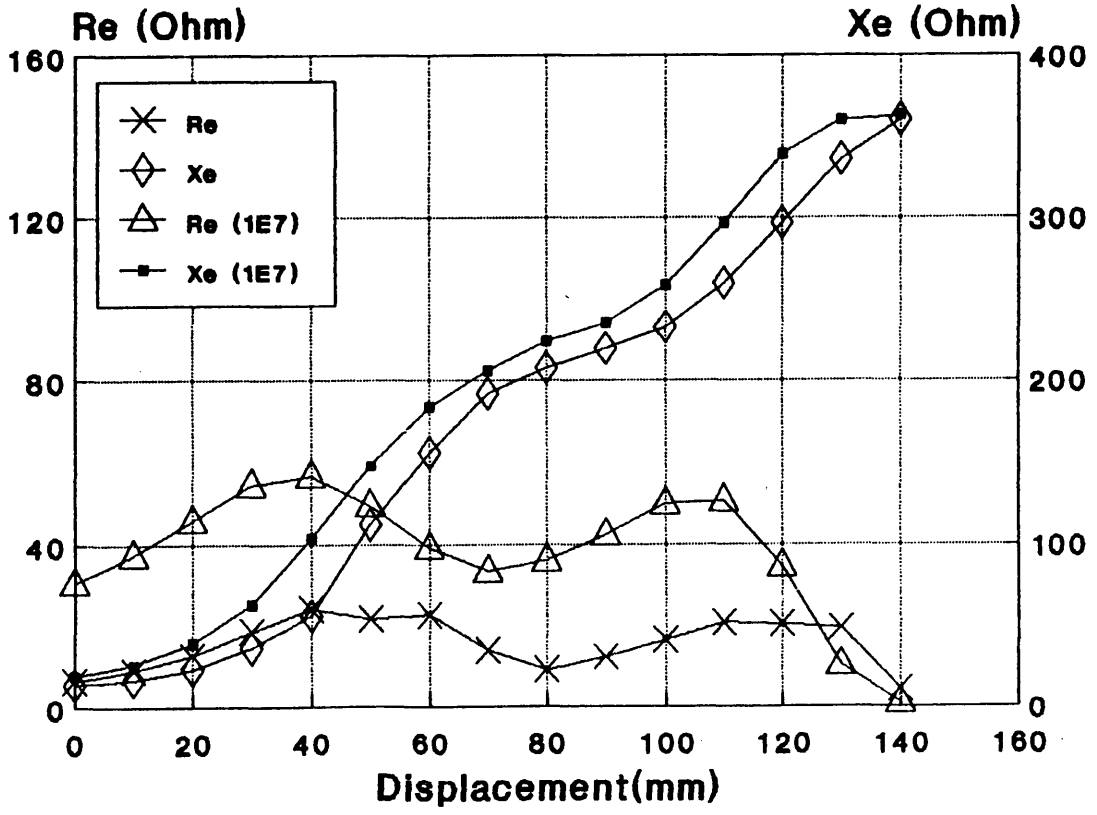

Fig. 2.17 Equivalent Circuit & Its Parameters

$$\Delta_1 = \sqrt{\frac{2}{\omega \cdot \sigma_1 \cdot \mu_0}} = \sqrt{\frac{2}{2\pi \times 50 \times 5.71 \times 10^7 \times 4\pi \times 10^{-7}}} = 9.4 \text{ (mm)}$$

In the case of a conductivity of 3.0×10^7 $(\Omega \cdot m)^{-1}$, the penetration depth will be

$$\Delta_2 = \sqrt{\frac{2}{\omega \cdot \sigma_2 \cdot \mu_0}} = \sqrt{\frac{2}{2\pi \times 50 \times 3.0 \times 10^7 \times 4\pi \times 10^{-7}}} = 13.0 \text{ (mm)}$$

Fig. 2.18 shows the comparison for different conductivities when the plungers are located at a displacement of 80 (mm). Eddy current density distribution can be seen at the top of the graph. The coordinate of the starting point is at D = 0.06 (m). The length of $4 \cdot \Delta$ of the low conductivity plunger is about 40 (mm) and that of the high conductivity plunger is more than 50 (mm).

4. A.C. Resistance and Eddy Current Losses

The results of the above numerical experiment suggest that the relationship of A.C. resistance to the plunger conductivity is approximately given by,

$$\frac{R_{\sim 2}}{R_{\sim 1}} = \frac{\Delta_2}{\Delta_1} = \sqrt{\frac{\sigma_1}{\sigma_2}} \qquad \cdots\cdots(2.19)$$

The equilibrium principle of magnetomotive force leads to the following magnetizing equation,

$$\dot{I}_1 \cdot N_1 + \dot{I}_e \cdot N_e = \dot{I}_m \cdot N_1 \qquad \cdots\cdots(2.20a)$$

in which $N_e = 1$ represents the turns of the plunger and $\dot{I}_m$ is magnetizing component. Similar to the case of a transformer with its secondary short

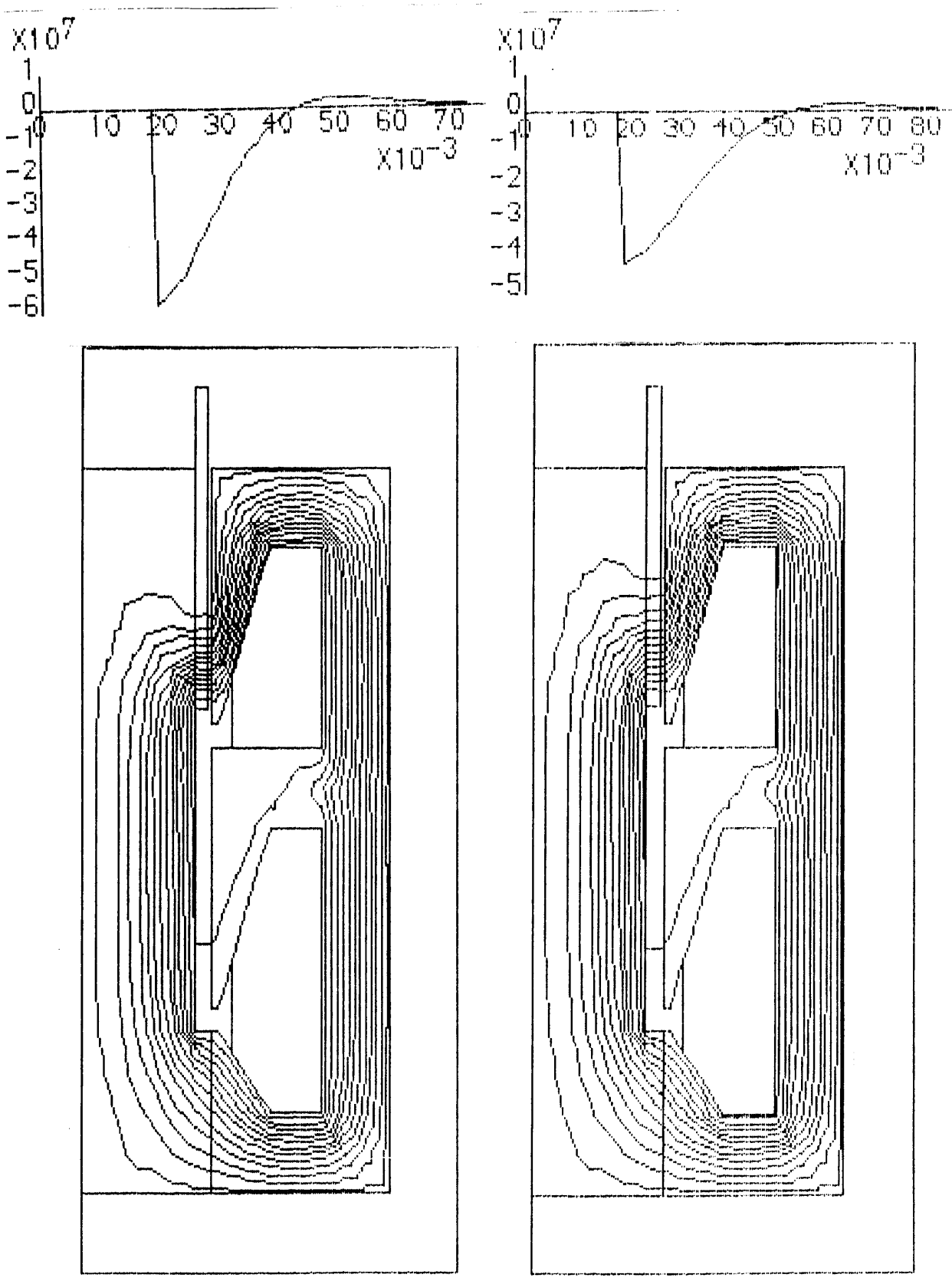

(a) $\sigma = 5.71 \times 10^7$ (b) $\sigma = 3.0 \times 10^7$

Fig. 2.18 Change of the Plunger Conductivity

circuited, I_m in the TLIA is quite small compared with I_1. Therefore,

$$\dot{I}_e \cdot N_e = \dot{I}_e \approx -\dot{I}_1 \cdot N_1 \qquad \cdots\cdots(2.20b)$$

Because the TLIA is fed by a constant current source, it becomes a constant *mmf* machine and I_e too remains constant. Hence, the relationship between the eddy current losses due to different conductivities can be expressed by

$$\frac{P_{e2}}{P_{e1}} = \frac{I_{e2}^2 \cdot R_{\sim 2}}{I_{e1}^2 \cdot R_{\sim 1}} \approx \frac{R_{\sim 2}}{R_{\sim 1}} = \frac{\Delta_2}{\Delta_1} = \sqrt{\frac{\sigma_1}{\sigma_2}} \qquad \cdots\cdots(2.21)$$

Therefore the eddy current loss in the plunger with lower conductivity will be 1.38 times the loss for the plunger with higher conductivity. This result calculated by FEM2D is compared in Fig. 2.16a.

From the above investigation, one can conclude that changes in the plunger conductivity will not result in significant changes in average output force over the whole stroke, if the input current is kept constant. However there will be a considerable increase in eddy current loss if a conductivity is reduced. Therefore, it is better to chose a higher conductivity material for the plunger.

2.3.4 Penetration Depth and Frequency

In section 2.3.3, it was shown that the distribution of the eddy current in the plunger obeys the law of penetration depth. This inner end effect occurs in the axial direction and has been verified by changing the conductivity σ in the following formula,

$$\Delta = \sqrt{\frac{2}{\omega \cdot \sigma \cdot \mu}} \qquad \cdots\cdots(2.22)$$

In order to confirm this, its variation due to frequency is examined. Fig. 2.19 shows the eddy current density distribution in the plunger for three different frequencies, exciting only the first stage. It is clear that the lower the frequency, the longer the penetration depth. The lengths of $4 \cdot \Delta$ measured from Fig. 2.19 for each frequency are listed in the following table.

Frequency (Hz)	10	25	50	100
Penetration Depth $\times 4$ $4 \cdot \Delta$ (mm)	85	65	38	27
Penetration Depth Δ (mm)	21.0	13.3	9.4	6.6

Table 2.3 Penetration Depth

They are seen to agree well with the penetration depth calculated by (2.22) and the relationship of

$$\frac{\Delta_1}{\Delta_2} = \sqrt{\frac{\omega_2}{\omega_1}} \qquad \cdots\cdots(2.23)$$

This confirms that the eddy currents gather at the end of the plunger obeying the law of penetration depth. Its influence on the TLIA's

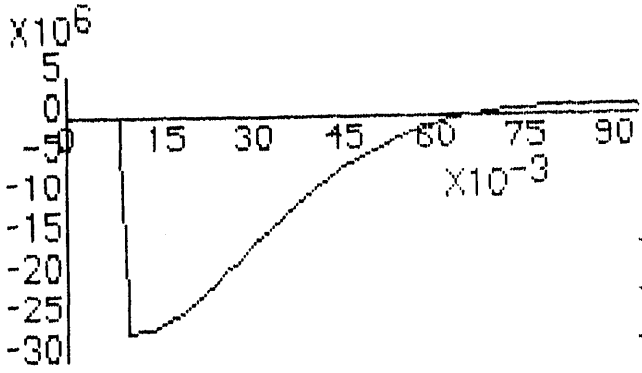

10 Hz

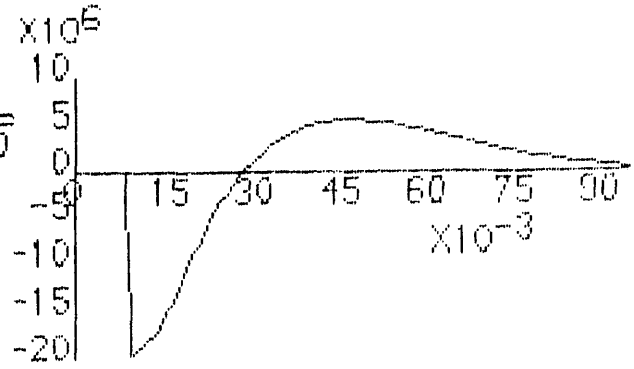

10 Hz

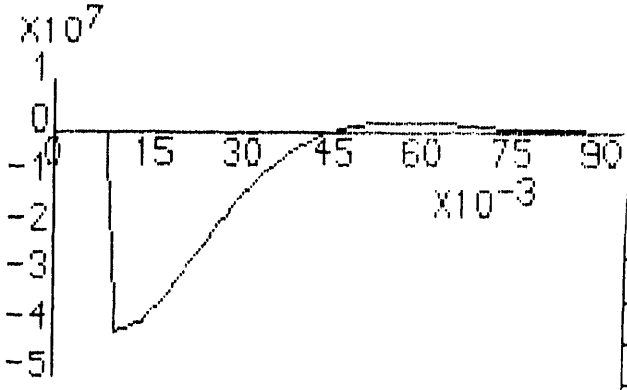

25 Hz

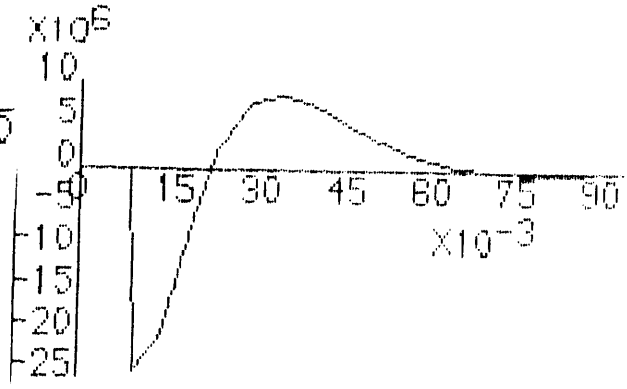

25 Hz

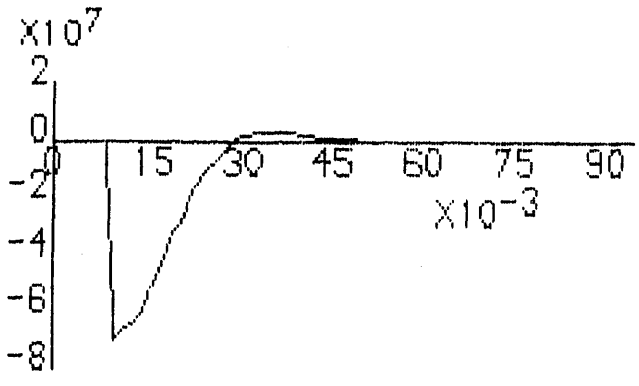

100 Hz

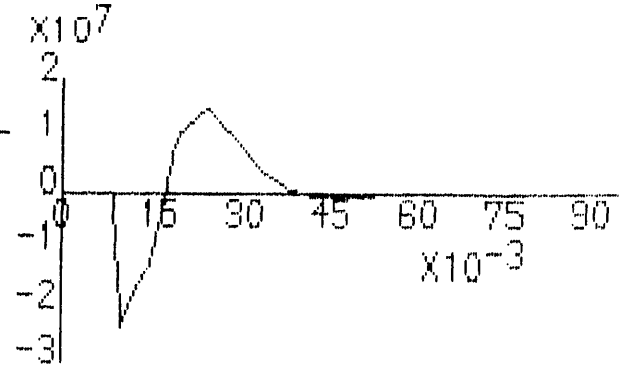

100 Hz

(a) Eddy Current (real)

(b) Eddy Current (img)

Fig. 2.19 Penetration Depth Variation with Frequency

performance will be reflected in the equivalent parameters X_e and R_e. If the total permeance of the flux path associated with the stator winding in (2.17) is divided into two parts, the equation (2.17) can be rewritten as

$$X_e = \Lambda \cdot \omega \cdot N_1^2 = (\Lambda_p + \Lambda_1) \cdot \omega \cdot N_1^2 \qquad \cdots\cdots(2.24)$$

in which Λ_p represents the permeance of flux path going through the plunger and Λ_1 represents the permeance of path bypassing the plunger. The variations in angular frequency ω will only affect Λ_p due to the change of penetration depth but not Λ_1. Consequently, the variation of X_e will be dependent on two factors. When the plunger is blocked under the slot mouth, Λ_p cannot be neglected because Λ_1 is not very large. However, if the plunger moves under the tooth, Λ_1 will greatly increase and Λ_p becomes a negligible part of the total. Although it is impossible to separate it by normal magnetic circuit analysis, one can estimate it by setting up its upper and lower limits. If the angular frequency ω is changed to ω_1, a corresponding equivalent reactance X_{e1} can be estimated by the following formulae. If $\omega_1 > \omega$,

$$X_e \cdot \sqrt{\frac{\omega_1}{\omega}} < X_{e1} < X_e \cdot \frac{\omega_1}{\omega} \qquad \cdots\cdots(2.25)$$

If $\omega_1 < \omega$,

$$X_e \cdot \sqrt{\frac{\omega_1}{\omega}} > X_{e1} > X_e \cdot \frac{\omega_1}{\omega} \qquad \cdots\cdots(2.26)$$

Its variation with frequency is shown in Fig. 2.20a.

When the TLIA is energised by a constant current source, its output axial force for different frequencies are plotted in Fig. 2.20a. Within the stroke range of 0 (mm) to 10 (mm), frequency variations affect the output force while beyond 10 (mm) the output force is almost unchanged. Unlike

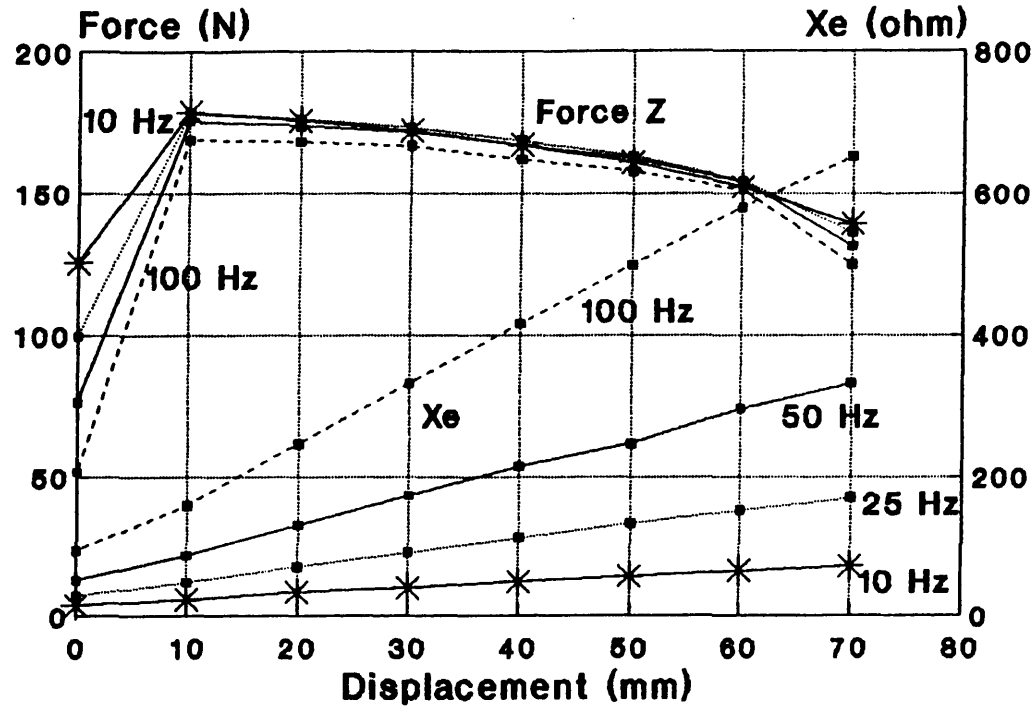

(a) Axial Force & Equivalent Reactance X_e

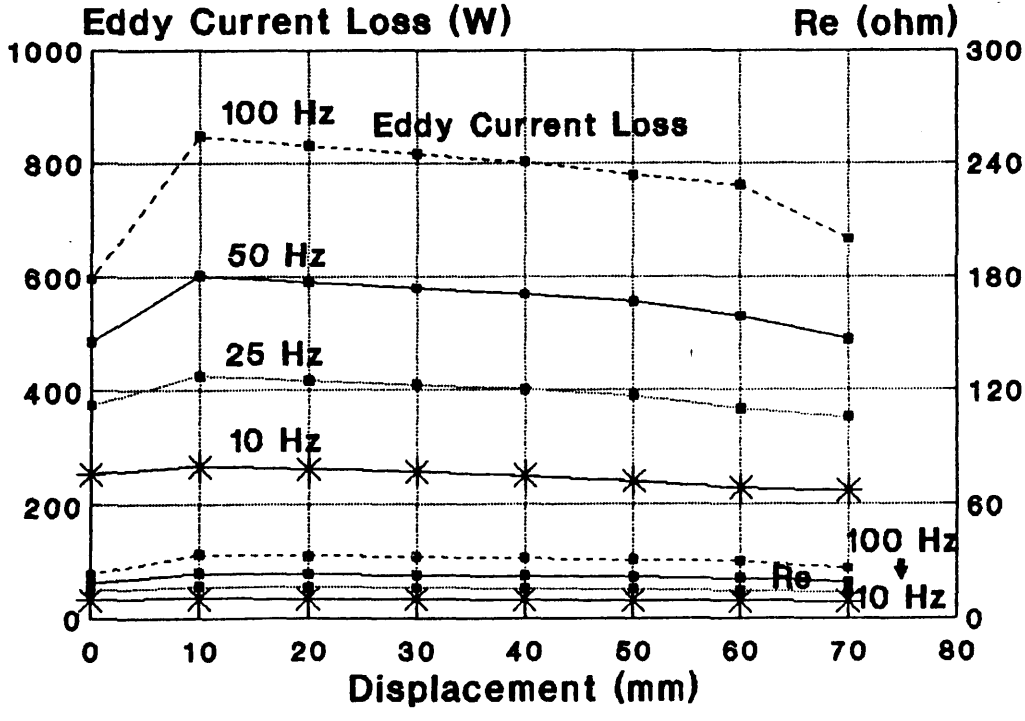

(b) Eddy Current Losses Related to R_e

Fig. 2.20 Constant Current Operation with Different Frequency

the equivalent reactance X_e, the equivalent resistance R_e corresponds to the eddy current loss in the plunger referred to the stator side. It is related to the AC resistance $R_\sim$ of the plunger by,

$$R_e = R_\sim \cdot N_1^2$$

When frequency varies from ω to ω_1,

$$\frac{R_{e1}}{R_e} = \frac{R_{\sim 1}}{R_\sim} = \frac{\Delta_1}{\Delta} = \sqrt{\frac{\omega}{\omega_1}} \qquad \cdots\cdots\cdots(2.27)$$

Its variation with the frequency is shown in Fig. 2.20b. If the excitation current remains constant, increase of frequency will result in increased eddy current loss given by,

$$\frac{P_{e1}}{P_e} = \frac{R_{e1}}{R_e} = \frac{\Delta_1}{\Delta} = \sqrt{\frac{\omega}{\omega_1}}$$

If the TLIA is fed by a constant voltage, increase of frequency will result in decrease of input current and output force. Obviously, this is because both X_e and R_e will increase following the increase of frequency. In practice, in order to ensure certain degree of saturation, the ratio of frequency to turns of the stator winding is maintained constant. If not, since $X_e \gg R_e$ the input current will be inversely proportional to frequency. The force and eddy current loss will be inversely proportional to ω^2. This is seen in Fig. 2.21.

As described in the section 2.3.2, it is preferable to use an open slot to increase the stroke range. Low frequency will produce higher output force and lower eddy current loss for the same current. Moreover, low frequency will also reduce iron loss in both the stator and the mandrel. However, there are two main disadvantages caused by a low frequency power supply. One is that it will produce low frequency ripples in its output force. This

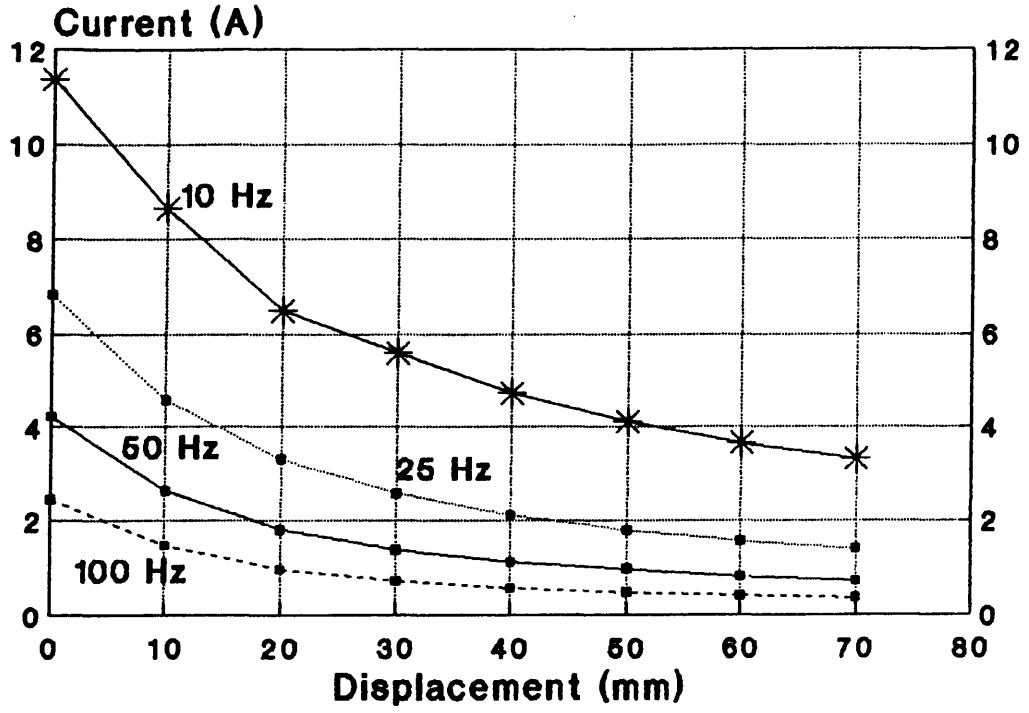

(a) Input Current versus Stroke

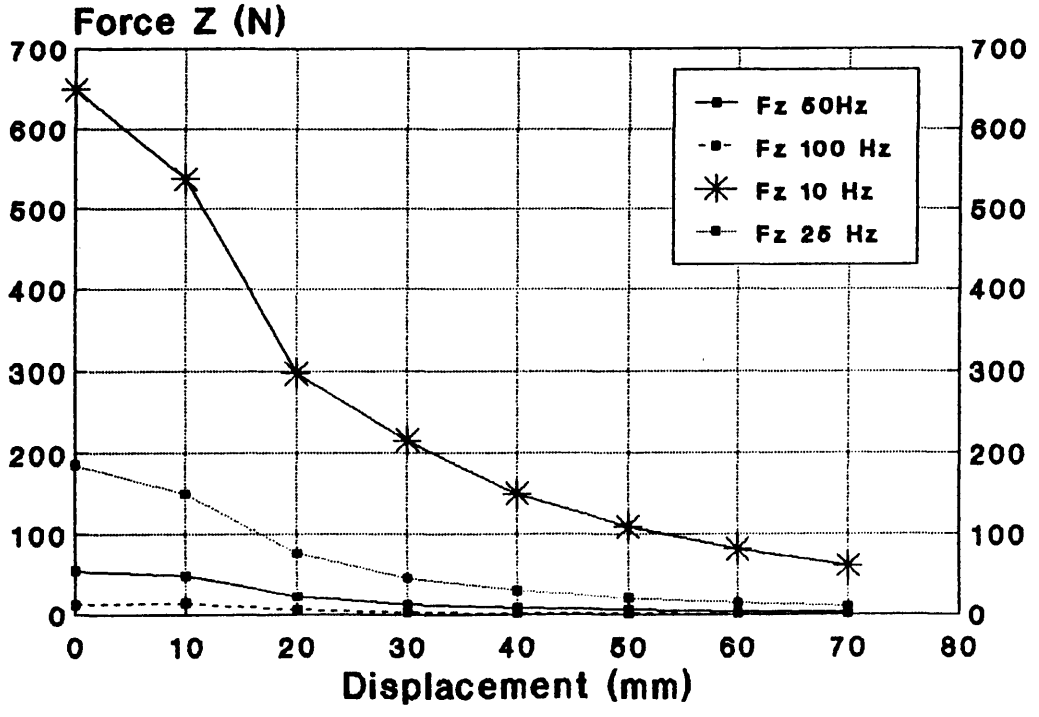

(b) Axial Force versus Stroke

Fig. 2.21 Constant Voltage Operation with Different Frequency

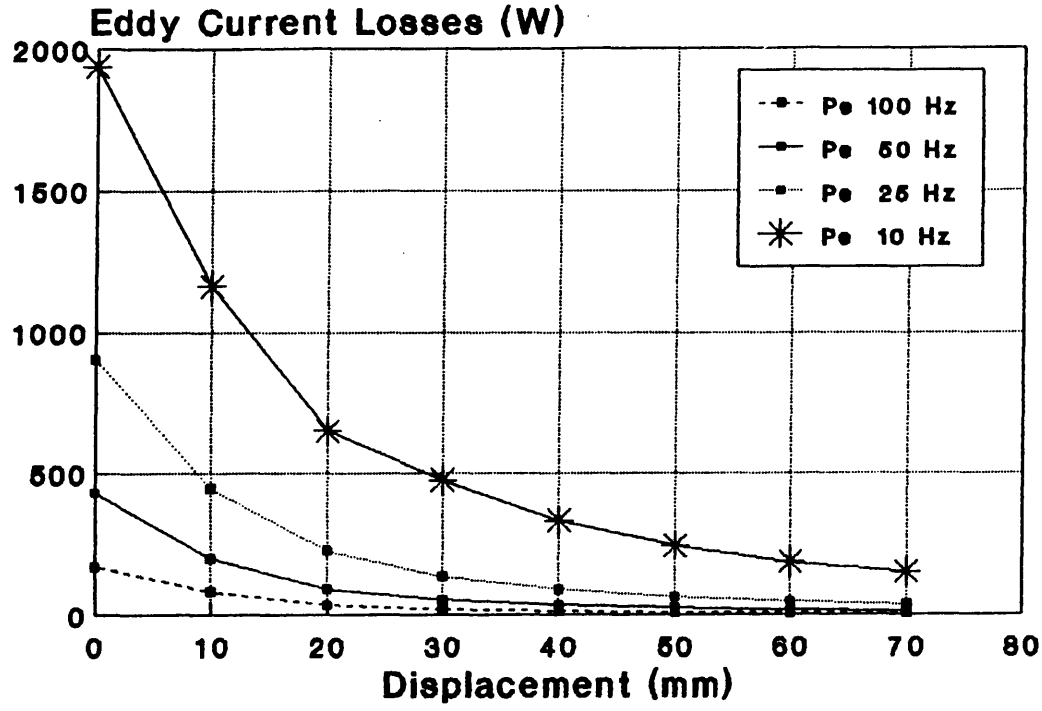

(c) Eddy Current Losses versus Stroke

Fig. 2.21 Constant Voltage Operation with Different Frequency

could be dangerous if there is large opposing force. This force ripple can also produce acoustic noise. It cannot be predicted by FEM2D because it can only handle steady state problems. In Chapter 5, it will be simulated and discussed. Moreover, in order to maintain same flux level, the low frequency machine needs more winding turns. This will not only increase the volume and cost but also the copper loss in the stator winding. Therefore, a compromise must be made by the designer.

2.4 Preliminary Consideration for Design

An electrical machine design procedure routinely includes two phases. Firstly the designer follows physical laws which govern the operation of the particular machine. Secondly, since the total number of variables is always more than the equations expressing the physical laws, he makes use of empirical rules to judge his design. These empirical rules or data are usually derived from his previous experience in designing similar machines.

The TLIA is a new machine and there is no previous experience available. The best and effective way to arrive at empirical rules is by FEM numerical experiments. Based on the results presented so far a preliminary procedure for design can be set up.

The procedure of designing a TLIA to meet given specifications is an essentially heuristic procedure. Starting from a set of specifications such as voltage U_1, angular frequency ω, output axial force F_z and stroke L, the task of the designer is to arrive at a reasonable size, cost and efficiency to match the specification. It is the purpose of this section to set forth several fundamental physical relationships governing the design of the TLIA. Some of them are derived from physical laws but some are directly obtained as a result of the FEM investigations. With this information, before using FEM to calculate an exact performance or to improve the design, one will be able to produce a prototype before undertaking optimization.

2.4.1 Goodness Factor for TLIA

The TLIA is normally used as a force machine. When it is operating in a standstill condition, it is impossible to define or estimate its efficiency. Following the practice in linear induction motors[5], a goodness factor is introduced given by,

$$G = \frac{F_z}{P_e} \qquad \cdots\cdots(2.28)$$

As described in preceding section, the inner end effect occurs at the end of the plunger. All the flux and eddy current gather with a penetration depth of Δ. Hence, an effective volume of the plunger is given by,

$$V_e = \Delta\cdot(r_o^2 - r_i^2)\cdot\pi = \Delta\cdot(r_o - r_i)\cdot(r_o + r_i)\cdot\pi$$

$$= \Delta\cdot\delta\cdot(\delta + 2\cdot r_i)\cdot\pi \qquad \cdots\cdots(2.29)$$

where, r_o and r_i are outer and inner radii of the plunger and δ is its wall thickness. If we use average flux density $\bar{B}_r$ and average eddy current density $\bar{J}_e$ to describe the equation (2.9), the axial force can be written as

$$F_z = \int \mathrm{Re}(\dot{J}_e\cdot\dot{B}_r^*)\cdot dv = \int |\dot{J}_e|\cdot|\dot{B}_r|\cdot\cos\varphi\cdot dv \approx \bar{J}_e\cdot\bar{B}_r\cdot\cos\bar{\varphi}\cdot V_e \qquad \cdots\cdots(2.30)$$

where, $\bar{\varphi}$ represents an average phase angle between $\bar{J}_e$ and $\bar{B}_r$. On the other hand, the eddy current losses in the effective volume can be expressed as

$$P_e = \frac{1}{\sigma}\cdot|\dot{J}_e|^2\cdot V_e = \frac{1}{\sigma}\cdot\bar{J}_e^2\cdot V_e \qquad \cdots\cdots(2.31)$$

Since the goodness factor is

$$G = \frac{F_z}{P_e} = \sigma\cdot\frac{\bar{B}_r}{\bar{J}_e}\cdot\cos\bar{\varphi} \qquad \cdots\cdots(2.28)$$

it is better to design for high flux density and low eddy current density.

2.4.2 Determination of the Outer Diameter of the Mandrel

In the TLIA, its mandrel has two main functions. One is to support and guide the plunger to move in the axial direction. The other is to provide a magnetic return path for flux. In order to reduce the eddy current loss, it is necessary to use laminations. Physical size is determined by the outer diameter D_o and axial length L_m. The latter is dependent on the total stroke L. Its only requirement is to satisfy the inequality $L_m > L$.

One can choose the outer diameter D_o in terms of the law of electromagnetic induction. This results in the formula

$$D_o = 2.0 \cdot \sqrt{\frac{0.9 \cdot U_1}{\omega \cdot N_1 \cdot B \cdot \pi}} \qquad \cdots\cdots(2.32)$$

When the TLIA is fed by 240 volts, 50 Hz power supply, the relationship between D_o and N_1 for different flux density levels in mandrel can be expressed by a cluster of curves as shown in Fig. 2.22.

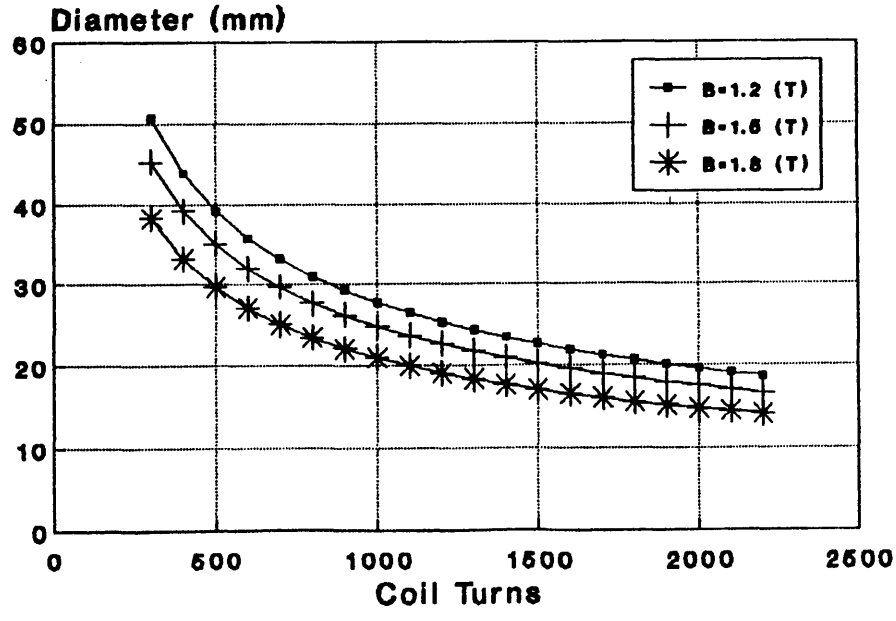

Fig. 2.22 Choosing Outer Diameter of the Mandrel

2.4.3 Thickness of the Plunger Wall

According to the expression (2.29), the effective volume of the plunger will be mainly determined by its inner radius r_i and the wall thickness δ, and the depth of penetration Δ. The effective axial length is no longer the length of the plunger itself. It is limited by the penetration depth Δ.

Fig. 2.23a illustrates the equivalent parameters of two models with different wall thicknesses of 5 (mm) and 2.5 (mm) respectively. The slot mouths of both models are 3/4 opened. Both equivalent reactance and resistance of the TLIA with the thin wall plunger are found to increase considerably with displacement. The comparison of their flux and eddy current density variations along a straight line from the coordinate of (36, 50) to (36, 150) is shown in Fig. 2.24. The plunger is located at a position given by D = 0.04 (m). The eddy current density in the thin wall is almost twice that in the thick wall. This suggests that the reduction of wall thickness by half will double its eddy current density because the total eddy current must remain unchanged to balance the *mmf* produced by the stator winding. The increase in flux density is not comparable to the increase in eddy current density. Although the reduction in wall thickness will increase the whole permeance Λ, this increase will not be proportional to the wall thickness as it only occupies a part of whole flux path.

For the same amount of axial force produced, $\bar{J}_e$ will be inversely proportional to the thickness δ but not $\bar{B}_r$ as shown in Fig. 2.24. By this reasoning, one prefers to use a thick wall plunger. However, in practice, this choice is limited by many other factors such as weight, volume, mechanical time constant and cost. Therefore a compromise must be made in

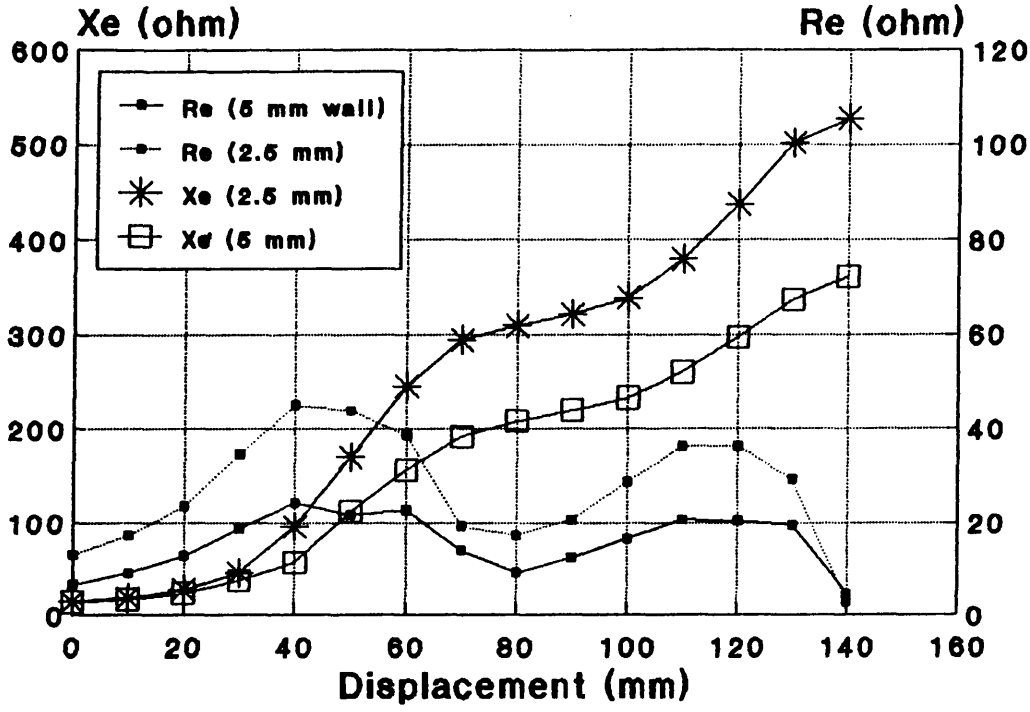

(a) Parameters versus Stroke

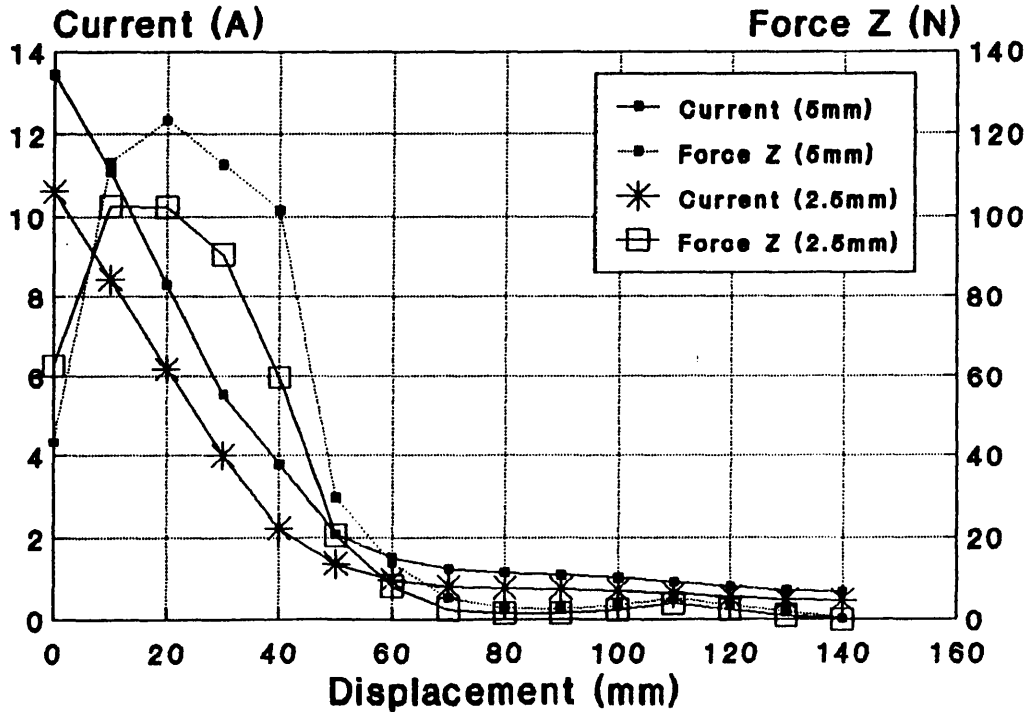

(b) Input Current & Axial Force versus Stroke

Fig. 2.23 Parameters & Performance with Different Wall Thickness

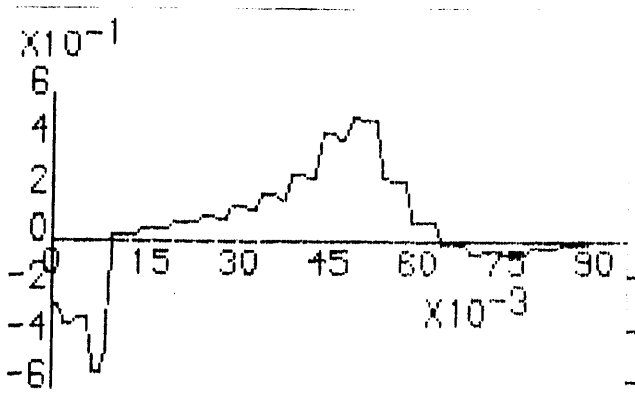

Flux Density B_r (rms)

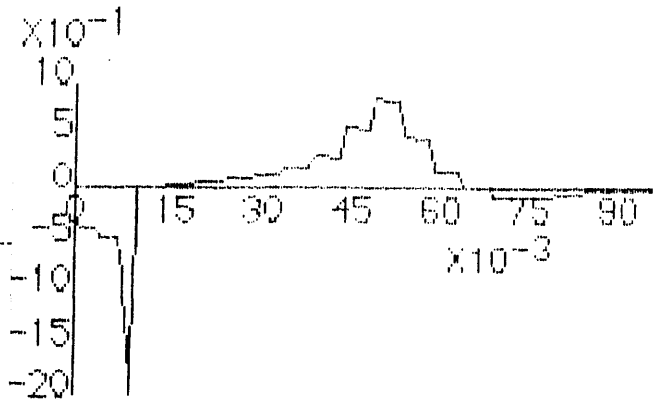

Flux Density B_r (rms)

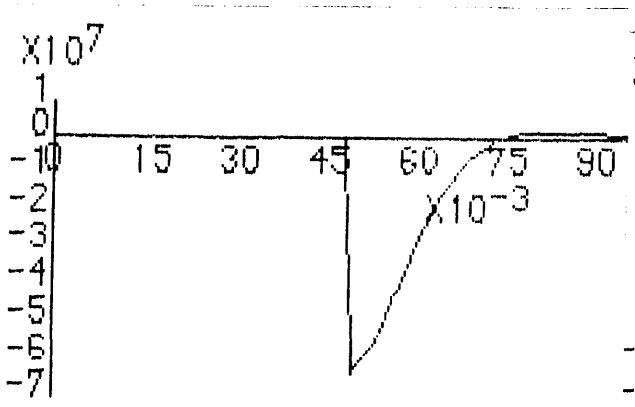

Eddy Current Density (real)

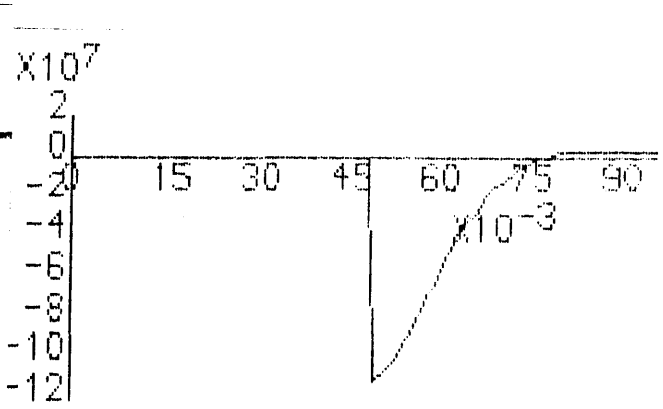

Eddy Current Density (real)

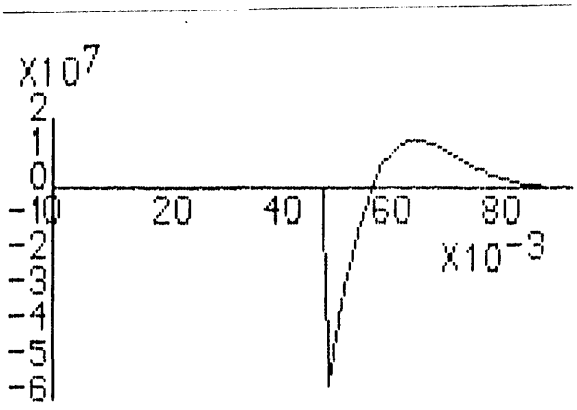

Eddy Current Density (img)

(a) Thick Wall

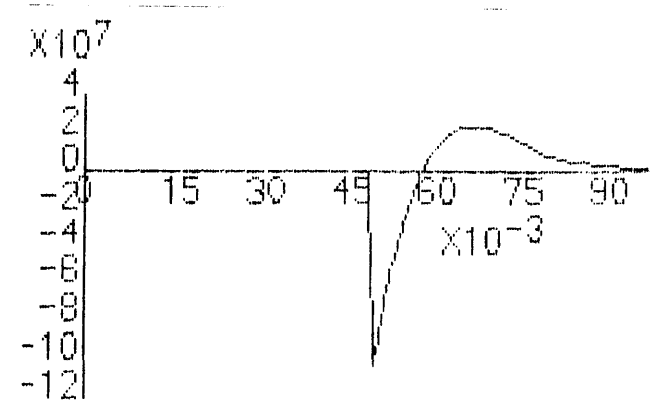

Eddy Current Density (img)

(b) Thin Wall

Fig. 2.24 Eddy Current & Flux Density with Different Wall Thickness

the design.

In the design of a conventional induction machine, one always prefers to have a small airgap in order to increase efficiency. This is because to produce the same quantity of flux, small airgap will lead to considerable reduction in the required *mmf*. However, in the TLIA, the meanings of the airgap is not quite the same. Firstly, its airgap must include the plunger thickness. Secondly, if we consider the flux path from the steel tooth to mandrel via the effective part of the plunger as an airgap, the length of this airgap will change significantly when the plunger moves under the open mouth region. Unlike the case of the normal induction machine where one pays close attention to the airgap, in the case of the TLIA the whole magnetic circuit must be considered.

When two TLIA with different plungers are energized by 240 volts power supply, their current and axial force variations with stroke are shown in Fig. 2.23b. The thick wall plunger will draw a higher current and produce a larger force with almost the same eddy current losses as the thin wall plunger.

In addition to the wall thickness δ, the inner radius r_i of the plunger can be determined by its effective volume V_e. One can choose large r_i with small δ. Alternatively, one can choose small r_i with large δ depending on the requirement.

2.4.4. Stator Winding & Lamination

After having selected an initial size for the plunger, one can estimate the number of turns of the stator winding, for different slot shapes by,

$$N_1 = \frac{\sqrt{2}\cdot U_1}{\omega \cdot B_a \cdot A_a} \qquad \text{.....(2.33)}$$

in which B_a is the required peak flux density in the airgap and A_a is the area of the airgap under steel tooth. A_a can be calculated by

$$A_a = 2\pi\cdot(r_o + \delta)\cdot L_t$$

where, L_t is the length of the tooth. Whether this N_1 is a reasonable one or not is then checked against the desired no-load current I_0 in,

$$I_0\cdot N_1 = \frac{B_a}{\mu_0}\cdot(\delta + 2g) + \sum H_i\cdot L_i \qquad \text{.....(2.34)}$$

in which H_i and L_i are the magnetic field strength and corresponding length of the magnetic path. If I_0 is acceptable, the equivalent reactance at this no-load condition is

$$X_e \approx \frac{U_1}{I_0}$$

The size of the stator winding depends on wire diameter. Of course, the larger the diameter of the winding wire, the less its copper loss. However, this must be limited by the permitted stator volume, weight and cost. Finally, the winding must be placed inside the laminated structure. The area of cross section can be estimated by

$$A_1 = \frac{\sqrt{2}\cdot U_1}{\omega \cdot B_1 \cdot N_1} \qquad \text{.....(2.35)}$$

in which, B_1 can be 1.0 to 1.5 Tesla. This simple estimation produces a prototype machine for further investigation by the FEM.

5.0 Conclusions

Two special effects, the shielding effect and the inner end effect have been described and analysed by numerical investigations, for a two-stage TLIA. Both effects are caused by induced eddy current in the plunger. The shielding effect has two aspects to it. Firstly, only a part of the flux can pass through the plunger. Most of flux is forced to make a detour round the inner end of the plunger. Secondly, when whole plunger is located under the first stage, the shielding effect will isolate the two stages of the TLIA. If the first stage is excited, no back *emf* is found in the second one. On the other hand, if the second stage is excited, there is no back *emf* in the first stage. Therefore the concept of mutual inductance between two windings becomes meaningless. This leads to the conclusion that the exciting strategy for the two-stage model should be sequenced switching of one coil at a time.

The inner end effect arises from the fact that induced eddy currents always accumulate at the inner end of the plunger. It has been shown in the eddy current density distribution graphs, that its distribution along the axial direction obeys the law of the penetration depth. This is further confirmed by the numerical experiments of changing the conductivity of the plunger and the frequency of power supply. The concept of the effective volume of the plunger is then proposed.

Both effects dominate the performance of the TLIA and make its analysis and design very complicated. The classical methods of analyzing solenoids and induction motors are of no use. This is why FEM is selected as the analytical tool in the thesis. A set of basic rules for the design have been developed and presented to produce a primary prototype for numerical analysis.

CHAPTER 3 TIME-STEPPING FINITE ELEMENT THEORY AND MODEL

3.1 Introduction

In last chapter, the steady state characteristics of the TLIA was examined by FEM2D. However, the TLIA is an inherently transient device which seldom operates in the steady state. Therefore, the simulation of its dynamic characteristics in actuating applications is important. Its specifications such as time response, velocity and displacement variations with time need to be carefully investigated. Although the time harmonic steady state finite element analysis provides useful design information explained in Chapter 2, it is not suitable to simulate the dynamic behaviour of the TLIA with saturated magnetic regions. Furthermore, if the TLIA is fed by a non-sinusoidal power supply, the analysis will be even more complicated.

In order to achieve dynamic simulation properly, a time-stepping finite element method is adopted. A 2-Dimensional axisymmetric finite element computer program will be developed in this chapter, which takes into account the speed variation of the moving plunger, eddy currents and material non-linearities. The velocity term in the partial differential equation results in two main problems. One is that it is not easy to find a functional for the partial differential equation. Hence, a weighted residual Galerkin method[13] is employed. The other is that the inclusion of the velocity term yields an asymmetric global matrix so that a new strategy for storage needs to be introduced. The time variation is treated by finite difference[14] in time. This allows any kind of input source

waveform to be considered.

Starting from the original Maxwell equations, this chapter makes use of the Galerkin method and Green's theorem to formulate the problem in finite element terms using the magnetic vector potential as the field variable. With the help of a time difference approach, the time-stepping 2-D axisymmetric spatial problem is transformed into a large sparse algebraic matrix equation involving the unknown magnetic vector potential at each node at each time instant. Then a 'Fish-bone' 1-D compact storage technique combined with the Newton-Raphson method is described. This is very effective in saving the storage capacity and computing time. The Jacobian matrix containing the velocity term is derived by the Newton-Raphson method which linearises the stiffness matrix equation. Finally, the Gaussian elimination method is used in every iteration to solve the matrix equations.

In practice, the laminated stator has a non-axisymmetric structure. Therefore, an equivalent reluctance is created to approximate the 3-D problem to a 2-D axisymmetric one. At the end of this chapter, a post-processor for estimating the flux linkage, back *emf*, electromagnetic forces, eddy currents and power losses is described with emphasis on axisymmetric geometry.

3.2 Electromagnetic Field Model

3.2.1 Maxwell Equations

When a conductor moves in a time-varying electromagnetic field, there will be two kinds of *emf*s induced in the moving conductor. One is due to the magnetic field varying in time called transformer *emf* and the other is due to its movement relative to the magnetic field. The time-stepping finite element approach described in this chapter is based on Maxwell equations[15] supplemented by a velocity term.

$$\begin{cases} \text{curl}\ \mathbf{H} = \mathbf{J} = \mathbf{J}_c + \sigma\cdot(\mathbf{E} + \mathbf{V} \times \mathbf{B}) \\ \text{curl}\ \mathbf{E} = -\dfrac{\partial \mathbf{B}}{\partial t} \\ \text{div}\,\mathbf{B} = 0 \\ \text{div}\,\mathbf{D} = 0 \end{cases} \qquad \cdots\cdots(3.1)$$

where $\mathbf{J}_c$ is the applied current density, $\sigma\cdot\mathbf{E}$ is the induced current density due to the transformer *emf* and $\sigma\cdot\mathbf{V} \times \mathbf{B}$ is the current density due to the movement of the conductor.

Two simplifications have been made in equations (3.1). One is the omission of the displacement current $\frac{\partial \mathbf{D}}{\partial t}$ in the first equation of (3.1), because the time variation of the electric displacement vector **D** is very low compared with the current density vector **J**. The other is that there is no electric charge density q in the actuator. Therefore, the last equation of (3.1), *i.e.* Guass's law, becomes div **D** = 0.

3.2.2 2-D Axisymmetric Magnetic Vector Potential

The magnetic vector potential **A** is chosen as a field variable instead of the magnetic flux density vector **B** or magnetic field intensity vector **H**. This is because the 2-D axisymmetric field can be expressed with only one component A_θ.

Let $\mathbf{B} = \nabla\times\mathbf{A}$ and choose the Coulomb gauge $\nabla\cdot\mathbf{A} = 0$ to ensure the uniqueness of the solution. The second equation of (3.1) can be rewritten as

$$\nabla\times\mathbf{E} = -\frac{\partial}{\partial t}\nabla\times\mathbf{A} \quad \text{and} \quad \mathbf{E} = -\frac{\partial \mathbf{A}}{\partial t} .$$

Substituting the latter into the right side of the first partial differential equation of (3.1), the total source current density becomes

$$\mathbf{J} = \mathbf{J}_c + \sigma\cdot(\mathbf{E} + \mathbf{V}\times\mathbf{B}) = \mathbf{J}_c + \sigma\cdot(-\frac{\partial \mathbf{A}}{\partial t} + \mathbf{V} \times \text{curl } \mathbf{A}) \qquad \cdots\cdots(3.2)$$

Because curl **H** = curl $\nu\cdot\mathbf{B}$ = curl ($\nu\cdot$curl **A**), the first equation of (3.1) can be expressed by the magnetic vector potential **A** as,

$$\text{curl } (\nu\cdot\text{curl } \mathbf{A}) = \mathbf{J}_c + \sigma\cdot(-\frac{\partial \mathbf{A}}{\partial t} + \mathbf{V} \times \text{curl } \mathbf{A}) \qquad \cdots\cdots(3.3)$$

where, $\nu = \nu(|\mathbf{B}|)$ represents the reluctivity of ferromagnetic material, and varies with the flux density in a nonlinear manner. In a cylindrical coordinate system, for an axisymmetric model, the magnetic vector potential only has the θ component $\mathbf{A} = A\cdot\alpha_\theta$. Thus

$$\text{curl } \mathbf{A} = \begin{vmatrix} \frac{\alpha_r}{r} & \alpha_\theta & \frac{\alpha_z}{r} \\ \frac{\partial}{\partial r} & \frac{\partial}{\partial \theta} & \frac{\partial}{\partial z} \\ 0 & r\cdot A & 0 \end{vmatrix} = \frac{-\alpha_r}{r}\cdot\left(\frac{\partial(r\cdot A)}{\partial z}\right) + \frac{\alpha_z}{r}\cdot\left(\frac{\partial(r\cdot A)}{\partial r}\right)$$

$$= -\frac{\partial A}{\partial z}\cdot\alpha_r + \frac{1}{r}\cdot\frac{\partial A}{\partial r}\cdot\alpha_z$$

and,

$$\text{curl}\ (\nu\cdot\text{curl}\ \mathbf{A}) = \begin{vmatrix} \frac{\alpha_r}{r} & \alpha_\theta & \frac{\alpha_z}{r} \\ \frac{\partial}{\partial r} & \frac{\partial}{\partial \theta} & \frac{\partial}{\partial z} \\ -\nu\frac{\partial A}{\partial z} & 0 & \frac{\nu}{r}\cdot\frac{\partial (r\cdot A)}{\partial r} \end{vmatrix}$$

$$= -\left[\frac{\partial}{\partial r}\left(\frac{\nu}{r}\cdot\frac{\partial(r\cdot A)}{\partial r}\right) + \frac{\partial}{\partial z}\left(\nu\cdot\frac{\partial A}{\partial z}\right)\right]\cdot\alpha_\theta$$

where, α_r, α_θ and α_z are three unit vectors as shown in the Fig. 3.1.

Considering that **V** only has a Z-direction component, *i.e.* $\mathbf{V} = V_z\cdot\alpha_z$, and **J**, $\mathbf{J}_c$ only have θ-direction components, (3.2) can be changed to

$$J = J_c - \sigma\cdot\left(\frac{\partial A}{\partial t} + V_z\cdot\frac{\partial A}{\partial z}\right)$$

so that an axisymmetric electromagnetic field with its associated boundary conditions becomes a scalar differential equation,

$$\begin{cases} \Omega: & \frac{\partial}{\partial z}\left(\nu\cdot\frac{\partial A}{\partial z}\right) + \frac{\partial}{\partial r}\left(\frac{\nu}{r}\cdot\frac{\partial(r\cdot A)}{\partial r}\right) = -J_c + \sigma\cdot\frac{\partial A}{\partial t} + \sigma\cdot V_z\cdot\frac{\partial A}{\partial z} \\ s1: & A = A_0 \\ s2: & \frac{\nu}{r}\cdot\frac{\partial(r\cdot A)}{\partial n} = -H_t \end{cases} \quad \cdots\cdots(3.4)$$

in which Ω represents the area modelled by 3.4, s1 represents the Dirichlet boundary and s2 represents the Neumann boundary as shown in Fig. 3.2. Let $\nu = r\cdot\nu_r$, $\sigma = r\cdot\sigma_r$ and A, A_0 be multiplied by *r*. Then equation (3.4) can changes to

$$\begin{cases} \Omega: & \frac{\partial}{\partial z}\left(\nu_r\cdot\frac{\partial(r\cdot A)}{\partial z}\right) + \frac{\partial}{\partial r}\left(\nu_r\cdot\frac{\partial(r\cdot A)}{\partial r}\right) = -J + \sigma_r\cdot\frac{\partial(r\cdot A)}{\partial t} + \sigma_r\cdot V_z\cdot\frac{\partial(r\cdot A)}{\partial z} \\ s1: & r\cdot A = r\cdot A_0 \\ s2: & \nu_r\cdot\frac{\partial(r\cdot A)}{\partial n} = -H_t \end{cases} \quad \cdots\cdots(3.5)$$

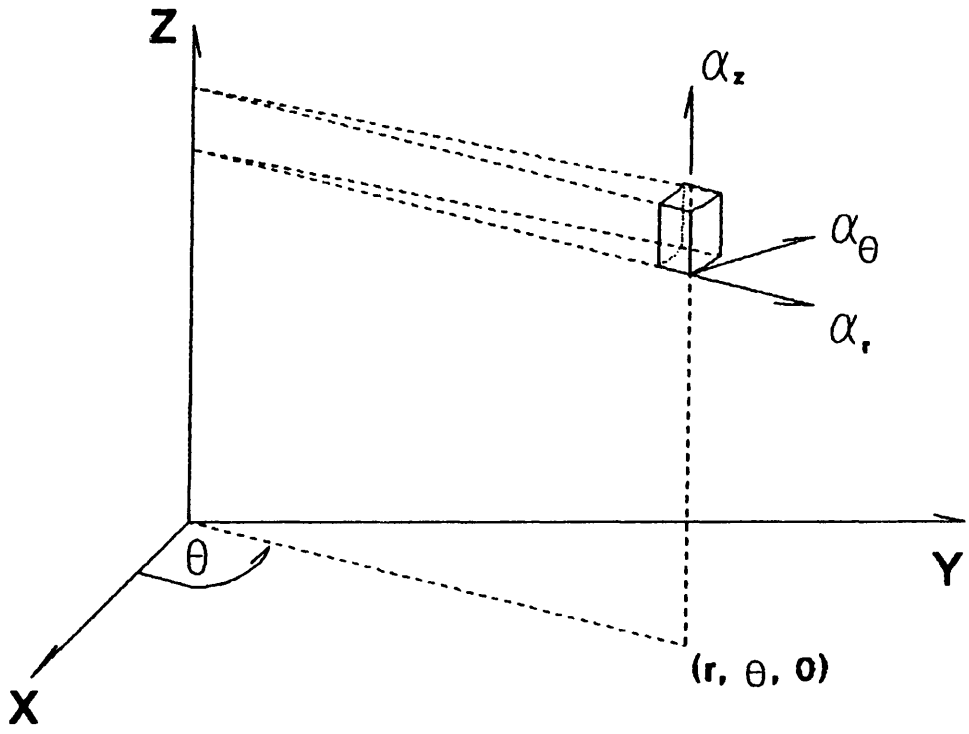

Fig. 3.1 Cylindrical Coordinate System

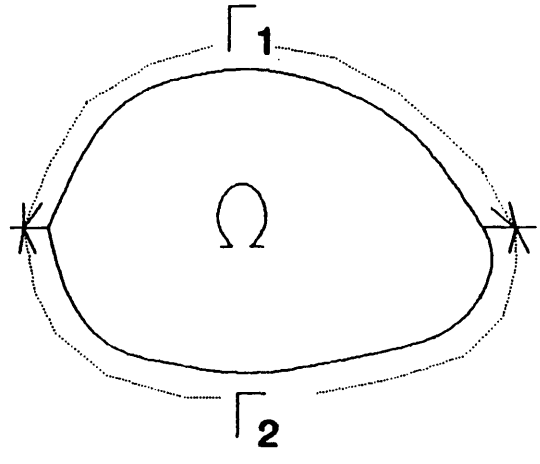

Fig. 3.2 Area Being Modelled

Let $\acute{A} = r \cdot A$ and $\acute{A}_0 = r \cdot A_0$. Equation (3.5) becomes,

$$\begin{cases} \Omega: & \frac{\partial}{\partial z}\left(\nu_r \cdot \frac{\partial \acute{A}}{\partial z}\right) + \frac{\partial}{\partial r}\left(\nu_r \cdot \frac{\partial \acute{A}}{\partial r}\right) = -J_c + \sigma_r \cdot \frac{\partial \acute{A}}{\partial t} + \sigma_r \cdot v_z \cdot \frac{\partial \acute{A}}{\partial z} \\ s1: & \acute{A} = \acute{A}_0 \\ s2: & \nu_r \cdot \frac{\partial \acute{A}}{\partial n} = -H_t \end{cases} \quad \cdots\cdots (3.6)$$

This equation with the initial conditions J(0) and Á(0) forms the mathematical model of the TLIA. It represents a time dependent axisymmetric electromagnetic field including moving parts, eddy currents and nonlinear materials.

3.2.3 Time Discretisation

In time domain, a time difference algorithm is used, which discretises time into intervals of δt, small enough to get an accurate solution,

$$\beta \cdot \frac{\partial \acute{A}}{\partial t}\bigg|_{t+\delta t} + (1 - \beta) \cdot \frac{\partial \acute{A}}{\partial t}\bigg|_{t} = \frac{\acute{A}(t+\delta t) - \acute{A}(t)}{\delta t}$$

where, $0 \leq \beta \leq 1$. If $\beta = 1$, the algorithm corresponds to the particular case of forward difference; $\beta = 0.5$, to the Crank-Nichoslon algorithm;[16] and $\beta = 0$, to backward difference. In order to simplify the derivation, $\beta = 1$ is selected in this chapter. However, β can be chosen between 0 and 1 arbitrarily in the computer program similar to the method presented by Bouillault.[17]

Using δt instead of ∂t, a formula for the *(n+1)th* time step can be obtained from (3.6) as,

$$\begin{cases} \dfrac{\partial}{\partial z}\left(\nu_r \cdot \dfrac{\partial \acute{A}^{(n+1)}}{\partial z}\right) + \dfrac{\partial}{\partial r}\left(\nu_r \cdot \dfrac{\partial \acute{A}^{(n+1)}}{\partial r}\right) + f - \dfrac{\sigma_r}{\delta t} \cdot \acute{A}^{(n+1)} - \sigma_r \cdot V_z^{(n)} \cdot \dfrac{\partial \acute{A}^{(n+1)}}{\partial z} = 0 \\ \acute{A}^{(0)}(r,\ z,\ 0) = 0,\ V_z^{(0)} = 0, \quad (n = 0,\ 1,\ 2 \cdots\cdots) \end{cases} \qquad \cdots\cdots (3.7)$$

where, $f = J^{(n+1)} + \sigma_r \cdot \dfrac{\acute{A}^{(n)}}{\delta t}$, represents the present input $J^{(n+1)}$ plus the previous effect of the magnetic vector potential $A^{(n)}$ in the *nth* time step. In (3.7) the velocity in the Z direction V_z is the only variable associated with the load movement. In every *(n+1)th* time step V_z is assumed to remain constant at $V_z^{(n)}$ corresponding to the *nth* time step.

The finite element approximation in terms of the above equation is derived in the next section.

3.3 Finite Element Theory

3.3.1 The Weighted Residual Method

The finite element method is a numerical technique for solving boundary value problems. In one of the methods of its development, the partial differential equations modelling the field are transformed into an energy expression called functionals. Approximate solutions to the field problem are the solutions which minimise these functionals. However, if the partial different equation is not elliptic but instead parabolic or hyperbolic, it will be difficult to find their energy functionals. Therefore, an alternative method called the weighted residual method is used in this thesis. The Residual method has a major advantage over the variational method. It may be applied to many problems for which no functional can be found, even though the differential equation may be simple.

Starting with a governing boundary value problem, the differential equation is written so that one side of the equation is zero in (3.7). Expressing equation (3.7) in an operator form, in every time step, we have

$$G(r,z,\acute{A}^{(n+1)}) = 0$$

Substitution of an approximate solution $\acute{A}^{*} \cong \acute{A}^{(n+1)}$, into the differential equation results in an erroneous value ε, *i.e.*

$$G(r,z,\acute{A}^{*}) = \varepsilon, \qquad \text{where } \varepsilon = \varepsilon(r,z) \text{ is called the error function.}$$

The error ε is then multiplied by a weighting function W(r,z) and the product is integrated over the solution region Ω. The result is called residual $\Re$ and is set equal to zero, *i.e.*

$$\Re = \iint_{\Omega} \varepsilon \cdot W \cdot drdz = 0 \qquad \cdots\cdots\cdots(3.8)$$

There exists a weighting function W and a residual $\Re$ for each unknown nodal variable, so the result is a global set of algebraic equations.

In this thesis, the residual has following form,

$$\Re = -\iint_{\Omega} W \cdot \left\{ \frac{\partial}{\partial z}\left(\nu_r \cdot \frac{\partial \acute{A}^*}{\partial z} \right) + \frac{\partial}{\partial r}\left(\nu_r \cdot \frac{\partial \acute{A}^*}{\partial r} \right) + f - \frac{\sigma_r}{\delta t} \cdot \acute{A}^* - \sigma_r \cdot V_z \cdot \frac{\partial \acute{A}^*}{\partial z} \right\} \cdot drdz = 0 \qquad \cdots\cdots(3.9)$$

Separating $\Re$ into two parts $\Im_1$ and $\Im_2$,

$$\Im_1 = -\iint_{\Omega} W \cdot \left\{ \frac{\partial}{\partial z}\left(\nu_r \cdot \frac{\partial \acute{A}^*}{\partial z} \right) + \frac{\partial}{\partial r}\left(\nu_r \cdot \frac{\partial \acute{A}^*}{\partial r} \right) \right\} \cdot drdz \qquad \text{and}$$

$$\Im_2 = -\iint_{\Omega} W \cdot \left\{ f - \frac{\sigma_r}{\delta t} \cdot \acute{A}^* - \sigma_r \cdot V_z \cdot \frac{\partial \acute{A}^*}{\partial z} \right\} \cdot drdz$$

Since

$$\frac{\partial}{\partial z}(W \cdot \nu_r \cdot \frac{\partial \acute{A}^*}{\partial z}) + \frac{\partial}{\partial r}(W \cdot \nu_r \cdot \frac{\partial \acute{A}^*}{\partial r}) = W \cdot \frac{\partial}{\partial z}(\nu_r \cdot \frac{\partial \acute{A}^*}{\partial z}) + W \cdot \frac{\partial}{\partial r}(\nu_r \cdot \frac{\partial \acute{A}^*}{\partial r}) + \frac{\partial W}{\partial z} \cdot (\nu_r \cdot \frac{\partial \acute{A}^*}{\partial z}) + \frac{\partial W}{\partial r} \cdot (\nu_r \cdot \frac{\partial \acute{A}^*}{\partial r})$$

and according to the Green's theorem:

$$\iint_s (\frac{\partial P}{\partial x} + \frac{\partial Q}{\partial y})\, ds = \oint_l \left(P \cdot \cos(n,x) + Q \cdot \cos(n,y) \right) dl$$

the surface integral of the two items on the left side of the equal sign becomes

$$\iint \left(\frac{\partial}{\partial z}(W \cdot \nu_r \cdot \frac{\partial \acute{A}^*}{\partial z}) + \frac{\partial}{\partial r}(W \cdot \nu_r \cdot \frac{\partial \acute{A}^*}{\partial r}) \right) drdz$$

$$= \oint W \cdot \nu_r \cdot \left(\frac{\partial \acute{A}^*}{\partial z} \cdot \cos(n,z) + \frac{\partial \acute{A}^*}{\partial r} \cdot \cos(n,r) \right) dl = \oint_{\Gamma} W \cdot \nu_r \cdot (\frac{\partial \acute{A}^*}{\partial n})\, dl$$

in which Γ represents the length along the boundary of the solution region

Ω and $\frac{\partial \acute{A}^*}{\partial n}$ is the normal gradient of the vector potential on the Γ. Therefore, $\Im_1$ could be modified as,

$$\Im_1 = \iint_{\Omega}\left\{\frac{\partial W}{\partial z}\cdot\left(\nu_r\cdot\frac{\partial \acute{A}^*}{\partial z}\right) + \frac{\partial W}{\partial r}\cdot\left(\nu_r\cdot\frac{\partial \acute{A}^*}{\partial r}\right)\right\} dzdr - \oint_{\Gamma_2} W\cdot\nu_r\cdot\frac{\partial \acute{A}^*}{\partial n}\,dl \qquad \cdots\cdots(3.10)$$

in which Γ is replaced by Γ_2 because $\frac{\partial \acute{A}^*}{\partial n}$ is non-zero only on Γ_2.

3.3.2 The Galerkin Method

The weighted residual methods may take one of several forms such as subdomain, Galerkin, least squares or point collocation depending on the weighting function selected. The Galerkin method employs weighting functions of the same type as the interpolation functions which approximate the solution Á(r, z). In the finite element method, the whole area Ω is divided into small meshes composed of triangles. In a typical finite element triangle *e*, its contribution to the *i*th residual associated with node *i* is

$$\Re_i^e = -\iint_{\Omega^e}\left\{\frac{\partial}{\partial z}\left(\nu_r\cdot\frac{\partial \acute{A}^*}{\partial z}\right) + \frac{\partial}{\partial r}\left(\nu_r\cdot\frac{\partial \acute{A}^*}{\partial r}\right) + f - \frac{\sigma_r}{\delta t}\cdot\acute{A}^* - \sigma_r\cdot V_z\cdot\frac{\partial \acute{A}^*}{\partial z}\right\}\cdot N_i^e\cdot drdz \qquad \cdots\cdots\cdots(3.11)$$

where Ω^e is the area of the triangle element *e* and N_i^e is the shape function associated with it. Accordingly,

$$\Im_{1i} = \iint_{\Omega}\left\{\frac{\partial N_i^e}{\partial z}\cdot\left(\nu_r\cdot\frac{\partial \acute{A}^*}{\partial z}\right) + \frac{\partial N_i^e}{\partial r}\cdot\left(\nu_r\cdot\frac{\partial \acute{A}^*}{\partial r}\right)\right\} dzdr - \oint_{\Gamma} N_i^e\cdot\nu_r\cdot\frac{\partial \acute{A}^*}{\partial n}\,dl \qquad \cdots\cdots(3.12a)$$

and $$\vartheta_{2i} = -\iint_{\Omega} N_i^e \cdot \left\{ f - \frac{\sigma_r}{\delta t} \cdot \acute{A}^* - \sigma_r \cdot V_z \cdot \frac{\partial \acute{A}^*}{\partial z} \right\} \cdot dr dz \qquad \cdots\cdots(3.12b)$$

$\acute{A}^*$ could be expressed by the interpolation method in terms of the vector potential $\acute{A}_i$, $\acute{A}_j$ and $\acute{A}_k$ at three nodes *i, j* and *k* respectively as,

$$\acute{A}^* = N_i^e \cdot \acute{A}_i + N_j^e \cdot \acute{A}_j + N_k^e \cdot \acute{A}_k \qquad \cdots\cdots\cdots(3.13)$$

For simplicity, '*' is omitted from $\acute{A}^*$ and *e* from N_i^e, N_j^e and N_k^e in the following discussion. Here, N_i, N_j and N_k are called the shape function or pyramid functions. As aforementioned in the Galerkin method the shape function is chosen as the weighting function. N_i, N_j and N_k can be expressed as follows,

$$\begin{cases} N_i = \frac{1}{2\Delta}(a_i + b_i \cdot z + c_i \cdot r) \\ N_j = \frac{1}{2\Delta}(a_j + b_j \cdot z + c_j \cdot r) \\ N_k = \frac{1}{2\Delta}(a_k + b_k \cdot z + c_k \cdot r) \end{cases} \qquad \cdots\cdots\cdots(3.14)$$

where Δ denotes the area of the element,

$$\Delta = \frac{1}{2} \cdot \begin{vmatrix} 1 & z_i & r_j \\ 1 & z_j & r_j \\ 1 & z_k & r_k \end{vmatrix}$$

and the coefficients in (3.14) are

$$\begin{cases} a_i = z_j \cdot r_k - z_k \cdot r_j \\ b_i = r_j - r_k \\ c_i = z_k - z_j \end{cases} \quad \begin{cases} a_j = z_k \cdot r_i - z_i \cdot r_k \\ b_j = r_k - r_i \\ c_j = z_i - z_k \end{cases} \quad \begin{cases} a_k = z_i \cdot r_j - z_j \cdot r_i \\ b_k = r_i - r_j \\ c_k = z_j - z_i \end{cases}$$

From the expressions (3.14), we have

$$\frac{\partial}{\partial z}\cdot\begin{Bmatrix} N_i \\ N_j \\ N_k \end{Bmatrix} = \frac{1}{2\Delta}\cdot\begin{Bmatrix} b_i \\ b_j \\ b_k \end{Bmatrix} \qquad \frac{\partial}{\partial r}\cdot\begin{Bmatrix} N_i \\ N_j \\ N_k \end{Bmatrix} = \frac{1}{2\Delta}\cdot\begin{Bmatrix} c_i \\ c_j \\ c_k \end{Bmatrix} \qquad \cdots\cdots(3.15)$$

From (3.13) and (3.14),

$$\frac{\partial \acute{A}}{\partial z} = \frac{\partial}{\partial z}\left(\{ N_i\ N_j\ N_k\}\cdot\{ \acute{A}_i\ \acute{A}_j\ \acute{A}_k\}^t\right) = \frac{1}{2\Delta}\cdot(b_i\cdot\acute{A}_i + b_j\cdot\acute{A}_j + b_k\cdot\acute{A}_k) \quad \text{and}$$

$$\frac{\partial \acute{A}}{\partial r} = \frac{\partial}{\partial r}\left(\{ N_i\ N_j\ N_k\}\cdot\{ \acute{A}_i\ \acute{A}_j\ \acute{A}_k\}^t\right) = \frac{1}{2\Delta}\cdot(c_i\cdot\acute{A}_i + c_j\cdot\acute{A}_j + c_k\cdot\acute{A}_k) \qquad \cdots\cdots(3.16)$$

If we define the surface integral and the contour integral in (3.12a) as $\Im'_{1i}$ and $\Im''_{1i}$ respectively, then the surface integral becomes

$$\Im'_{1i} = \frac{\nu}{4\Delta}\Big(b_i\cdot(b_i\cdot\acute{A}_i + b_j\cdot\acute{A}_j + b_k\cdot\acute{A}_k) + c_i\cdot(c_i\cdot\acute{A}_i + c_j\cdot\acute{A}_j + c_k\cdot\acute{A}_k)\Big)\cdot\iint\frac{1}{r}\cdot d\Omega \qquad \cdots\cdots(3.17)$$

The second term of 3.12a is a contour integral $\Im''_{1i}$, which has non-zero values only on the boundary Γ_2. If the element containing the node *i* is not on the boundary, this term is equal to zero. However, if the element has one or two edges on Γ_2, the normal gradient along the edges must be evaluated. This will be discussed in section 3.3.3.

Substituting (3.13), (3.14) and (3.16) into the equation (3.12b),

$$\Im_{2i} = -\iint\left(-\sigma_r\cdot V_z\cdot\frac{\partial \acute{A}}{\partial z} - \frac{\sigma_r}{\delta t}\cdot\acute{A} + f\right)\cdot N_i\cdot dzdr$$

$$= \frac{V_z}{2\Delta}\cdot(b_i\cdot\acute{A}_i + b_j\cdot\acute{A}_j + b_k\cdot\acute{A}_k)\cdot\iint N_i\cdot\sigma_r\cdot d\Omega + \left\{\frac{\acute{A}_i}{\delta t}\cdot\iint N_i^2\cdot\sigma_r\cdot d\Omega + \frac{\acute{A}_j}{\delta t}\cdot\iint N_i\cdot N_j\cdot\sigma_r\cdot d\Omega + \frac{\acute{A}_k}{\delta t}\cdot\iint N_i\cdot N_k\cdot\sigma_r\cdot d\Omega\right\} - \iint f\cdot N_i\, d\Omega \qquad \cdots\cdots(3.18)$$

where,

$$\iint f\cdot N_i\cdot d\Omega = \iint(J^{(n+1)} + \sigma_r\cdot\frac{\acute{A}^{(n)}}{\delta t})\cdot N_i d\Omega$$

$$= \iint J^{(n+1)} \cdot N_i \, d\Omega + \frac{\sigma_r}{\delta t} \cdot \iint (N_i \cdot \acute{A}_i^{(n)} + N_j \cdot \acute{A}_j^{(n)} + N_k \cdot \acute{A}_k^{(n)}) \cdot \frac{N_i}{r} \, d\Omega$$

$$= J^{(n+1)} \iint N_i \cdot d\Omega + \frac{\sigma_r}{\delta t} \left[\acute{A}_i^{(n)} \cdot \iint \frac{N_i^2}{r} \cdot d\Omega \right.$$

$$\left. + \acute{A}_j^{(n)} \cdot \iint \frac{1}{r} \cdot N_i \cdot N_j \cdot d\Omega + \acute{A}_k^{(n)} \cdot \iint \frac{1}{r} \cdot N_i \cdot N_k \cdot d\Omega \right]$$

Except the current density $J^{(n+1)}$, the last term of (3.18) all the other variables are known from the previous time step. Thus both are known quantities in the *(n+1)th* time step.

3.3.3 Boundary Conditions

As shown in Fig. 2.1 in the last chapter, the boundary condition of the TLIA is very simple. It only has the Dirichlet boundary and all the node potentials $\acute{A}|_{\Gamma_1}$ are equal to zero. The treatment of the Dirichlet boundary is well known[18] in finite element analysis. After the global linear equations are formed, the magnetic vector potential $\acute{A}|_{\Gamma_1}$ of every Dirichlet boundary node is set to its boundary value. Therefore, the total number of equations is the number of total nodes minus the number of Dirichlet boundary nodes. Because the computer program in the thesis is written for a general application for axisymmetric models, it also deals with the Neumann boundary condition appearing in the equations (3.12a).

If one or two edges of an element e are located on the Neumann boundary Γ_2 and if they are not homogeneous ones, *i.e.* $-\nu_r \cdot \frac{\partial \acute{A}}{\partial n} = H_t$, then their contribution to the global equation can be calculated by a line integral in the equation (3.12a):

$$\vartheta''_{1i} = H_t \cdot \int_{\Gamma_2} N_i \cdot dl = \frac{1}{2} \cdot H_t \cdot L_2 \qquad \text{.....(3.19)}$$

For simplicity, all these contributions will be added to a matrix called $\{c'\}^e$. If the element e has only one edge on the boundary as illustrated in Fig. 3.3b, $\{c'\}^e$ will be

$$\{c'\}^e = -\begin{Bmatrix} \frac{1}{2} \cdot H_t \cdot L_{ij} \\ \frac{1}{2} \cdot H_t \cdot L_{ij} \\ 0 \end{Bmatrix} \qquad \text{.....(3.20a)}$$

If there are two edges overlapping on the boundary like as in Fig. 3.3c, $\{c'\}^e$ will be

$$\{c'\}^e = -\begin{Bmatrix} \frac{1}{2} \cdot H_t \cdot L_{ij} + \frac{1}{2} \cdot H_t \cdot L_{ik} \\ \frac{1}{2} \cdot H_t \cdot L_{ij} \\ \frac{1}{2} \cdot H_t \cdot L_{ik} \end{Bmatrix} \qquad \text{.....(3.20b)}$$

In (3.19) and (3.20), L_2, L_{ij}, L_{ik}, and L_{jk} represent the lengths of the element sides, connecting the Neumann boundary nodes as shown in Fig. 3.3. It is quite evident that

$$L_{ij} = \sqrt{(r_i - r_j)^2 + (z_i - z_j)^2}, \quad L_{jk} = \sqrt{(r_j - r_k)^2 + (z_j - z_k)^2} \quad \text{and}$$

$$L_{ki} = \sqrt{(r_k - r_i)^2 + (z_k - z_i)^2}.$$

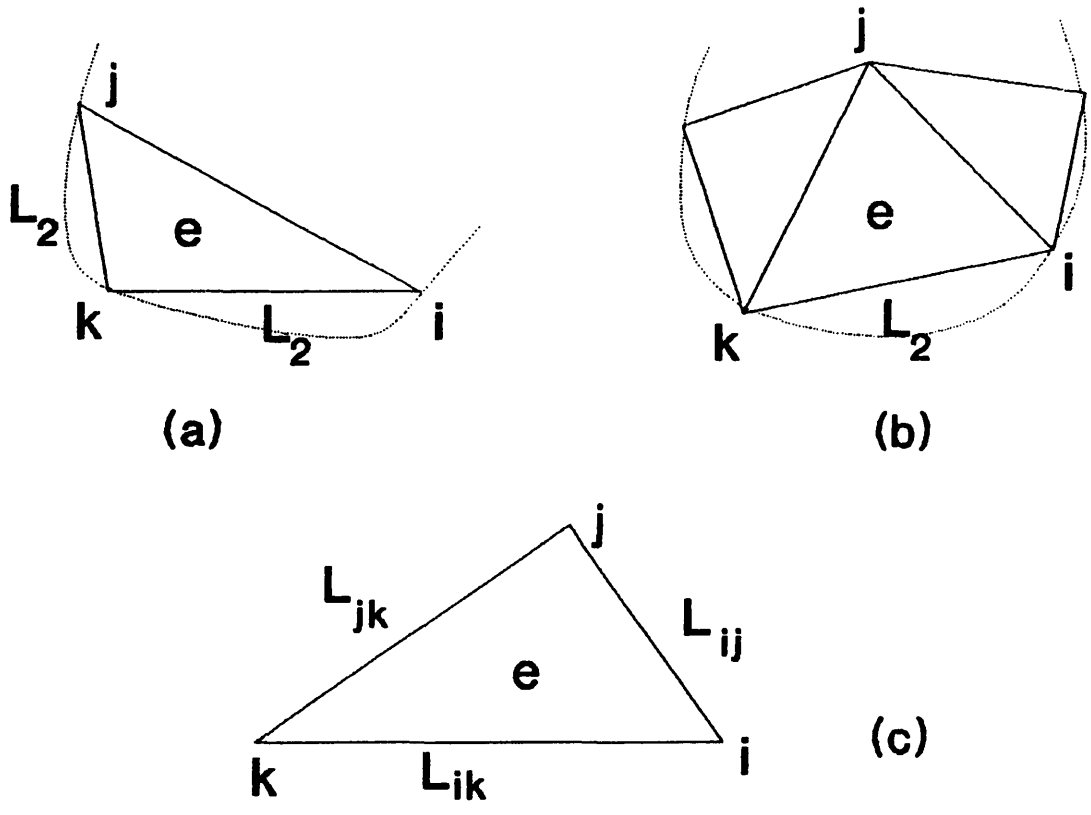

Fig. 3.3 Boundary Conditions of the Sides in e

3.3.4 Stiffness Matrix

The element residual $\mathcal{R}_i^e$ can be described in terms of potentials $\acute{A}_i$, $\acute{A}_j$ and $\acute{A}_k$ from equations (3.17), (3.18) and (3.20). However, there are several integral expressions left which need expansion. They are

$$1.\ \iint \frac{1}{r}\cdot d\Omega \qquad 2.\ \iint N_i^2\cdot\frac{1}{r}\cdot d\Omega \qquad 3.\ \iint N_i\cdot N_j\cdot\frac{1}{r}\cdot d\Omega$$

$$4.\ \iint N_i\cdot N_k\cdot\frac{1}{r}\cdot d\Omega \qquad 5.\ \iint N_i\cdot\frac{1}{r}\cdot d\Omega \qquad 6.\ \iint N_i\cdot d\Omega$$

Making use of the numerical integral[19] (see in Appendix I),

$$\iint_{\Delta} F(N_i,\ N_j,\ N_k)\cdot dzdr = \Delta\cdot\Sigma\ \rho^{(n)}\cdot F(N_i^{(n)},\ N_j^{(n)},\ N_k^{(n)})$$

and choosing a second order approximate formula, the above six integrals can be expressed as,

$$1.\ \iint \frac{1}{r}\cdot dzdr = \frac{2\Delta}{3}\cdot\left(\frac{1}{r_i+r_j}+\frac{1}{r_j+r_k}+\frac{1}{r_k+r_i}\right) = \Delta\cdot\gamma^{-1}$$

in which, $\gamma = \frac{2}{3}\cdot\left(\frac{1}{r_i+r_j}+\frac{1}{r_j+r_k}+\frac{1}{r_k+r_i}\right)^{-1}$

$$2.\ \iint N_i^2\cdot\frac{1}{r}\cdot dzdr = \frac{\Delta}{6}\cdot\left(\frac{1}{r_k+r_i}+\frac{1}{r_i+r_j}\right)$$

$$3.\ \iint N_i\cdot N_j\cdot\frac{1}{r}\cdot dzdr = \frac{\Delta}{6}\cdot\left(\frac{1}{r_i+r_j}\right)$$

$$4.\ \iint N_i\cdot N_k\cdot\frac{1}{r}\cdot dzdr = \frac{\Delta}{6}\cdot\left(\frac{1}{r_i+r_k}\right)$$

$$5.\ \iint N_i\cdot\frac{1}{r}\cdot dzdr = \frac{\Delta}{3}\cdot\left(\frac{1}{r_k+r_i}+\frac{1}{r_i+r_j}\right)$$

$$6.\ \iint N_i\cdot dzdr = \iint N_j\cdot dzdr = \iint N_k\cdot dzdr = \frac{\Delta}{3}$$

The details of the derivation are given in Appendix I. If one edge of an element is on the axis of symmetry, *i.e.* any two of r_i, r_j or r_k are zero, then the above integrations have to be expressed using first order approximation, in which

γ is changed into $\frac{1}{3}\cdot(r_i+ r_j+ r_k)$;

$\frac{\Delta}{6}\cdot[(r_i+ r_j)^{-1}+ (r_j+ r_k)^{-1}]$, $\frac{\Delta}{6}\cdot[(r_i+ r_k)^{-1}+ (r_j+ r_k)^{-1}]$,

$\frac{\Delta}{6}\cdot[(r_i+ r_j)^{-1}+ (r_i+ r_k)^{-1}]$, $\frac{\Delta}{6}\cdot(r_i+ r_j)^{-1}$, $\frac{\Delta}{6}\cdot(r_j+ r_k)$ or

$\frac{\Delta}{6}\cdot(r_i+ r_k)^{-1}$ into $\frac{\Delta}{3}\cdot(r_i+ r_j+ r_k)^{-1}$ and

$\frac{\Delta}{3}\cdot\left(\frac{1}{r_i+ r_j}+\frac{1}{r_i+ r_k}\right)$ into $\frac{\Delta}{r_i+ r_j+ r_k}$.

Substituting the above expressions into (3.17) and (3.18), $\mathcal{R}_i^e$ can be described as a residual vector for an element *e* with node *i*, *j* and *k* as,

$$\begin{Bmatrix} R_i \\ R_j \\ R_k \end{Bmatrix} = [s]^e\cdot\begin{Bmatrix} \acute{A}_i \\ \acute{A}_j \\ \acute{A}_k \end{Bmatrix}^{(n+1)} - \{c\}^e - [m]^e\cdot\begin{Bmatrix} \acute{A}_i \\ \acute{A}_j \\ \acute{A}_k \end{Bmatrix}^{(n)} \qquad \text{.....(3.21)}$$

where,

$$[s]^e = \begin{bmatrix} s_{ii} & s_{ij} & s_{ik} \\ s_{ji} & s_{jj} & s_{jk} \\ s_{ki} & s_{kj} & s_{kk} \end{bmatrix} \qquad \text{and}$$

$$s_{ii}= \frac{\nu}{4\Delta}\cdot(b_i^2 + c_i^2)\cdot\frac{1}{\gamma} + \frac{\sigma\cdot\Delta}{6\cdot\delta t}\cdot\left(\frac{1}{r_k+ r_i}+\frac{1}{r_i+ r_j}\right) + \frac{\sigma\cdot V_z\cdot b_i}{6}\cdot\left(\frac{1}{r_k+ r_i}+\frac{1}{r_i+ r_j}\right)$$

$$s_{ij}= \frac{\nu}{4\Delta}\cdot(b_i\cdot b_j + c_i\cdot c_j)\cdot\frac{1}{\gamma} + \frac{\sigma\cdot\Delta}{6\cdot\delta t}\cdot\left(\frac{1}{r_i+ r_j}\right) + \frac{\sigma\cdot V_z\cdot b_j}{6}\cdot\left(\frac{1}{r_k+ r_i}+\frac{1}{r_i+ r_j}\right)$$

$$s_{ik}=\frac{\nu}{4\Delta}\cdot(b_i\cdot b_k+c_i\cdot c_k)\cdot\frac{1}{\gamma}+\frac{\sigma\cdot\Delta}{6\cdot\delta t}\cdot\left(\frac{1}{r_i+r_k}\right)+\frac{\sigma\cdot V_z\cdot b_k}{6}\cdot\left(\frac{1}{r_k+r_i}+\frac{1}{r_i+r_j}\right)$$

$$s_{ji}=\frac{\nu}{4\Delta}\cdot(b_i\cdot b_j+c_i\cdot c_j)\cdot\frac{1}{\gamma}+\frac{\sigma\cdot\Delta}{6\cdot\delta t}\cdot\left(\frac{1}{r_i+r_j}\right)+\frac{\sigma\cdot V_z\cdot b_i}{6}\cdot\left(\frac{1}{r_k+r_j}+\frac{1}{r_i+r_j}\right)$$

$$s_{jj}=\frac{\nu}{4\Delta}\cdot(b_j^2+c_j^2)\cdot\frac{1}{\gamma}+\frac{\sigma\cdot\Delta}{6\cdot\delta t}\cdot\left(\frac{1}{r_k+r_j}+\frac{1}{r_i+r_j}\right)+\frac{\sigma\cdot V_z\cdot b_j}{6}\cdot\left(\frac{1}{r_k+r_j}+\frac{1}{r_i+r_j}\right)$$

$$s_{jk}=\frac{\nu}{4\Delta}\cdot(b_k\cdot b_j+c_k\cdot c_j)\cdot\frac{1}{\gamma}+\frac{\sigma\cdot\Delta}{6\cdot\delta t}\cdot\left(\frac{1}{r_k+r_j}\right)+\frac{\sigma\cdot V_z\cdot b_k}{6}\cdot\left(\frac{1}{r_k+r_j}+\frac{1}{r_i+r_j}\right)$$

$$s_{ki}=\frac{\nu}{4\Delta}\cdot(b_i\cdot b_k+c_i\cdot c_k)\cdot\frac{1}{\gamma}+\frac{\sigma\cdot\Delta}{6\cdot\delta t}\cdot\left(\frac{1}{r_i+r_k}\right)+\frac{\sigma\cdot V_z\cdot b_i}{6}\cdot\left(\frac{1}{r_k+r_i}+\frac{1}{r_k+r_j}\right)$$

$$s_{kj}=\frac{\nu}{4\Delta}\cdot(b_k\cdot b_j+c_k\cdot c_j)\cdot\frac{1}{\gamma}+\frac{\sigma\cdot\Delta}{6\cdot\delta t}\cdot\left(\frac{1}{r_k+r_j}\right)+\frac{\sigma\cdot V_z\cdot b_j}{6}\cdot\left(\frac{1}{r_k+r_i}+\frac{1}{r_k+r_j}\right)$$

$$s_{kk}=\frac{\nu}{4\Delta}\cdot(b_k^2+c_k^2)\cdot\frac{1}{\gamma}+\frac{\sigma\cdot\Delta}{6\cdot\delta t}\cdot\left(\frac{1}{r_k+r_i}+\frac{1}{r_k+r_j}\right)+\frac{\sigma\cdot V_z\cdot b_k}{6}\cdot\left(\frac{1}{r_k+r_i}+\frac{1}{r_k+r_j}\right)$$

.....(3.22)

In the equation (3.21), the matrix $[m]^e$ is equal to

$$[m]^e=\frac{\sigma\cdot\Delta}{6\delta t}\cdot\begin{bmatrix}\frac{1}{r_k+r_i}+\frac{1}{r_i+r_j} & \frac{1}{r_i+r_j} & \frac{1}{r_k+r_i}\\ \frac{1}{r_i+r_j} & \frac{1}{r_j+r_i}+\frac{1}{r_k+r_j} & \frac{1}{r_k+r_j}\\ \frac{1}{r_k+r_i} & \frac{1}{r_k+r_j} & \frac{1}{r_k+r_i}+\frac{1}{r_k+r_j}\end{bmatrix}$$

and $\{c\}^e$ is composed of the input current density term in (3.18) and the Neumann boundary contribution of (3.20),

$$\{c\}^e = \begin{bmatrix} \frac{J^{(n+1)}\cdot\Delta}{3} + \frac{1}{2}\cdot H_t \cdot L_{ij} + \frac{1}{2}\cdot H_t \cdot L_{ik} \\ \frac{J^{(n+1)}\cdot\Delta}{3} + \frac{1}{2}\cdot H_t \cdot L_{ij} + \frac{1}{2}\cdot H_t \cdot L_{jk} \\ \frac{J^{(n+1)}\cdot\Delta}{3} + \frac{1}{2}\cdot H_t \cdot L_{ki} + \frac{1}{2}\cdot H_t \cdot L_{kj} \end{bmatrix} \qquad \cdots\cdots(3.23)$$

After the residual vectors expressed by equation (3.21) have been found for all the elements, the global stiffness matrix can be established. The contribution of every element is added to the global matrix [S], [M] and array {C}, yielding the equation,

$$\{R\} = [S]\cdot\{\acute{A}\}^{(n+1)} - \{C\} - [M]\cdot\{\acute{A}\}^{(n)} = 0 \qquad \cdots\cdots(3.24)$$

The matrix equation (3.24) is an algebraic one. {C} refers to the input current density at the *(n+1)th* time step and the Neumann boundary contribution. $[M]\cdot\{\acute{A}\}^{(n)}$ denotes the effects of the previous state, *i.e.* that of the *nth* time step. If the reluctivity ν of the material is a constant, then (3.24) is a linear algebraic matrix equation. If the model contains materials with non-linear physical properties, *i.e.* the reluctivity ν is not a constant, then (3.24) becomes a non-linear matrix equation.

3.3.5 Non-linear Consideration

In general, a set of non-linear equations can be expressed in matrix form

$$[S]\cdot\{A\} = \{P\} \qquad \cdots\cdots\cdots(3.25)$$

where the coefficient matrix [S] is the function of the unknown array {A}. The array {P} is composed of known constants. $\{P\} = \{C\} + [M]\cdot\{\acute{A}\}^{(n)}$ is already known from the previous *nth* time step. Let the left side of (3.25) be an array $\{f\}$. Its *lth* term can be written as

$$f_l = \sum_{h=1}^{m} s_{lh}\cdot A_h \qquad (l = 1, 2, \cdots, m). \qquad \cdots\cdots\cdots(3.26)$$

Assuming that the first approximate solution is $\{A\}^{(0)}$, *i.e.*

$$f_l^{(0)} = \sum_{h=1}^{m} s_{lh}\cdot A_h^{(0)}, \quad (l = 1, 2, \cdots, m).$$

we can expand every component of $\{f\}$ into a first order Taylor series,

$$f_1 \cong f_1^{(0)} + \frac{\partial f_1^{(0)}}{\partial A_1}\cdot(A_1 - A_1^{(0)}) + \frac{\partial f_1^{(0)}}{\partial A_2}\cdot(A_2 - A_2^{(0)}) + \cdots + \frac{\partial f_1^{(0)}}{\partial A_m}\cdot(A_m - A_m^{(0)})$$

$$f_2 \cong f_2^{(0)} + \frac{\partial f_2^{(0)}}{\partial A_1}\cdot(A_1 - A_1^{(0)}) + \frac{\partial f_2^{(0)}}{\partial A_2}\cdot(A_2 - A_2^{(0)}) + \cdots + \frac{\partial f_2^{(0)}}{\partial A_m}\cdot(A_m - A_m^{(0)})$$

.....

$$f_m \cong f_m^{(0)} + \frac{\partial f_m^{(0)}}{\partial A_1}\cdot(A_1 - A_1^{(0)}) + \frac{\partial f_m^{(0)}}{\partial A_2}\cdot(A_2 - A_2^{(0)}) + \cdots + \frac{\partial f_m^{(0)}}{\partial A_m}\cdot(A_m - A_m^{(0)})$$

In matrix form, the above expressions become

$$\begin{Bmatrix} f_1 \\ f_2 \\ \cdots \\ f_m \end{Bmatrix} \cong \begin{Bmatrix} f_1^{(0)} \\ f_2^{(0)} \\ \cdots \\ f_m^{(0)} \end{Bmatrix} + \begin{bmatrix} \frac{\partial f_1^{(0)}}{\partial A_1} & \frac{\partial f_1^{(0)}}{\partial A_2} & \cdots & \frac{\partial f_1^{(0)}}{\partial A_m} \\ \frac{\partial f_2^{(0)}}{\partial A_1} & \frac{\partial f_2^{(0)}}{\partial A_2} & \cdots & \frac{\partial f_2^{(0)}}{\partial A_m} \\ \cdots & \cdots & \cdots & \cdots \\ \frac{\partial f_m^{(0)}}{\partial A_1} & \frac{\partial f_m^{(0)}}{\partial A_2} & \cdots & \frac{\partial f_m^{(0)}}{\partial A_m} \end{bmatrix} \cdot \begin{Bmatrix} A_1 - A_1^{(0)} \\ A_2 - A_2^{(0)} \\ \cdots \\ A_m - A_m^{(0)} \end{Bmatrix}$$

or $$\{f\} \cong \{f\}^{(0)} + \frac{\partial\{f\}^{(0)}}{\partial\{A\}}\cdot(\{A\} - \{A\}^{(0)}) \ . \qquad \cdots\cdots(3.27)$$

As is well known, the square, m by m, matrix $[J] = \frac{\partial\{f\}}{\partial\{A\}}$ is called the Jacobian matrix. Similar to the one dimensional Newton-Raphson method, if the approximate equality symbol is replaced by the equal symbol, (3.27) becomes a linear algebraic matrix equation.

$$[J]^{(0)}(\{A\}^{(1)} - \{A\}^{(0)}) = \{P\}^{(0)} - \{f\}^{(0)}$$

$\{A\}^{(1)}$ can be solved from the above equation but it is still an approximate solution of (3.25). However, this process can be iterated according to

$$[J]^{(k)}(\{A\}^{(k+1)} - \{A\}^{(k)}) = \{P\}^{(k)} - \{f\}^{(k)} \qquad \cdots\cdots(3.28)$$

until at the *kth* iteration, the following condition is satisfied,

$$\sum_{l=1}^{m} (p_l^{(k)} - f_l^{(k)})^2 \le \varepsilon \quad \text{or} \quad \frac{\|\{A\}^{(k+1)} - \{A\}^{(k)}\|}{\|\{A\}^{(k+1)}\|} \le \varepsilon \ .$$

In the finite element method, the Jacobian matrix elements need to be found for every element.

Let $$\{\delta A\}^{(k)} = \{A\}^{(k+1)} - \{A\}^{(k)}, \quad \{\delta P\}^{(k)} = \{P\}^{(k)} - \{f\}^{(k)}$$

then $$[J]^{(k)}\{\delta A\}^{(k)} = \{\delta P\}^{(k)} \qquad \cdots\cdots(3.29)$$

In a single element,

$$[J]^e = \begin{bmatrix} \frac{\partial f_i}{\partial Á_i} & \frac{\partial f_i}{\partial Á_j} & \frac{\partial f_i}{\partial Á_k} \\ \frac{\partial f_j}{\partial Á_i} & \frac{\partial f_j}{\partial Á_j} & \frac{\partial f_j}{\partial Á_k} \\ \frac{\partial f_k}{\partial Á_i} & \frac{\partial f_k}{\partial Á_j} & \frac{\partial f_k}{\partial Á_k} \end{bmatrix} \qquad \{\delta P\}^e = \begin{Bmatrix} p_i - f_i \\ p_j - f_j \\ p_k - f_k \end{Bmatrix}$$

$$\begin{cases} f_i = s_{ii}\cdot Á_i + s_{ij}\cdot Á_j + s_{ik}\cdot Á_k \\ f_j = s_{ji}\cdot Á_i + s_{jj}\cdot Á_j + s_{jk}\cdot Á_k \\ f_k = s_{ki}\cdot Á_i + s_{kj}\cdot Á_j + s_{kk}\cdot Á_k \end{cases}$$

If materials are of linear, $[s]^e$ is independent of $\{Á\}^e$ so that,

$$\frac{\partial f_i}{\partial Á_i} = s_{ii} \qquad \frac{\partial f_i}{\partial Á_j} = s_{ij} \qquad \frac{\partial f_i}{\partial Á_k} = s_{ik}$$

$$\frac{\partial f_j}{\partial Á_i} = s_{ji} \qquad \frac{\partial f_j}{\partial Á_j} = s_{jj} \qquad \frac{\partial f_j}{\partial Á_k} = s_{jk}$$

$$\frac{\partial f_k}{\partial Á_i} = s_{ki} \qquad \frac{\partial f_k}{\partial Á_j} = s_{kj} \qquad \frac{\partial f_k}{\partial Á_k} = s_{kk}$$

Therefore, the Jacobian matrix $[J]^e$ is the same as $[s]^e$ and (3.29) is the same as (3.24) because both $\{Á\}^{(0)}$ and $\{f\}^{(0)}$ are equal to zero. This means that the Newton-Raphson method can be used to solve a system of linear equations, for which it converges on the first iteration. In this thesis, ν is assumed to be a constant in the initial calculation. This can avoid a possible divergence when the first guess is too far away from the solution. If the material is non-linear the first component in $[J]^e$ is

$$\frac{\partial f_i}{\partial Á_i} = s_{ii} + \frac{\partial s_{ii}}{\partial Á_i}\cdot Á_i + \frac{\partial s_{ij}}{\partial Á_i}\cdot Á_j + \frac{\partial s_{ik}}{\partial Á_i}\cdot Á_k$$

$$= s_{ii} + \frac{\partial s_{ii}}{\partial \nu}\cdot\frac{\partial \nu}{\partial \acute{A}_i}\cdot\acute{A}_i + \frac{\partial s_{ij}}{\partial \nu}\cdot\frac{\partial \nu}{\partial \acute{A}_i}\cdot\acute{A}_j + \frac{\partial s_{ik}}{\partial \nu}\cdot\frac{\partial \nu}{\partial \acute{A}_i}\cdot\acute{A}_k$$

$$= s_{ii} + \left(\frac{\partial s_{ii}}{\partial \nu}\cdot\acute{A}_i + \frac{\partial s_{ij}}{\partial \nu}\cdot\acute{A}_j + \frac{\partial s_{ik}}{\partial \nu}\cdot\acute{A}_k \right)\cdot\frac{\partial \nu}{\partial \acute{A}_i}$$

Consider $\frac{\partial s_{ii}}{\partial \nu}$ first.

$$\frac{\partial s_{ii}}{\partial \nu} = \frac{\partial}{\partial \nu}\left\{ \frac{\nu}{4\Delta}\cdot(b_i^2 + c_i^2)\cdot\frac{1}{\gamma} + \frac{\sigma\cdot\Delta}{6\cdot\delta t}\cdot\left(\frac{1}{r_k + r_i} + \frac{1}{r_i + r_j}\right) \right.$$

$$\left. + \frac{\sigma\cdot V_z\cdot b_i}{6}\cdot\left(\frac{1}{r_k + r_i} + \frac{1}{r_i + r_j}\right)\right\} = \frac{1}{4\Delta}\cdot(b_i^2 + c_i^2)\cdot\frac{1}{\gamma}$$

Let $\frac{\nu}{4\Delta}\cdot(b_i^2 + c_i^2)\cdot\frac{1}{\gamma} = T_{ii}$ so that $\frac{\partial s_{ii}}{\partial \nu} = \frac{1}{\nu}\cdot T_{ii}$

Using the same method, one can get $\frac{\partial s_{ij}}{\partial \nu} = \frac{1}{\nu}\cdot T_{ij}$ and

$\frac{\partial s_{ik}}{\partial \nu} = \frac{1}{\nu}\cdot T_{ik}$, where

$$T_{ij} = \frac{\nu}{4\Delta}\cdot(b_i\cdot b_j + c_i\cdot c_j)\cdot\frac{1}{\gamma}\,, \qquad T_{ik} = \frac{\nu}{4\Delta}\cdot(b_i\cdot b_k + c_i\cdot c_k)\cdot\frac{1}{\gamma}$$

An intermediate variable $\mathfrak{C}$ is introduced so that

$$\frac{\partial \nu}{\partial \acute{A}} = \frac{\partial \nu}{\partial \mathfrak{C}}\cdot\frac{\partial \mathfrak{C}}{\partial \acute{A}} \qquad \cdots\cdots(3.30)$$

where, $\mathfrak{C} = \sqrt{\left(\frac{\partial \acute{A}}{\partial r}\right)^2 + \left(\frac{\partial \acute{A}}{\partial z}\right)^2} = r\cdot|B|$.

The first multiplier of the right side in (3.30) represents the magnetization characteristics of the ferromagnetic materials, *i.e.*

$$\therefore \frac{\partial \nu}{\partial \mathfrak{C}} = \frac{\partial \nu}{\partial |B|}\cdot\frac{1}{r} \approx \frac{\partial \nu}{\partial |B|}\cdot\frac{1}{\gamma}$$

The second one can be deduced as follows,

$$\frac{\partial \mathbb{C}}{\partial \acute{A}_i} = \frac{\partial}{\partial \acute{A}_i}\left[\left(\frac{\partial \acute{A}}{\partial r}\right)^2 + \left(\frac{\partial \acute{A}}{\partial z}\right)^2\right]^{\frac{1}{2}} = \frac{1}{\mathbb{C}}\cdot\left[\left(\frac{\partial \acute{A}}{\partial r}\right)\cdot\frac{\partial}{\partial \acute{A}_i}\left(\frac{\partial \acute{A}}{\partial r}\right) + \left(\frac{\partial \acute{A}}{\partial z}\right)\cdot\frac{\partial}{\partial \acute{A}_i}\left(\frac{\partial \acute{A}}{\partial z}\right)\right]$$

$$= \frac{1}{\mathbb{C}}\cdot\left[\frac{1}{2\cdot\Delta}\cdot(c_i\cdot\acute{A}_i + c_j\cdot\acute{A}_j + c_k\cdot\acute{A}_k)\cdot\frac{c_i}{2\cdot\Delta} + \frac{1}{2\cdot\Delta}\cdot(b_i\cdot\acute{A}_i + b_j\cdot\acute{A}_j + b_k\cdot\acute{A}_k)\cdot\frac{b_i}{2\cdot\Delta}\right.$$

$$= \frac{1}{\mathbb{C}}\cdot\frac{1}{4\cdot\Delta^2}\cdot\left[(b_i^2 + c_i^2)\cdot\acute{A}_i + (b_i\cdot b_j + c_i\cdot c_j)\cdot\acute{A}_j + (b_i\cdot b_k + c_i\cdot c_k)\cdot\acute{A}_k\right]$$

$$= \frac{\gamma}{\mathbb{C}\cdot\nu\cdot\Delta}\cdot\left(T_{ii}\cdot\acute{A}_i + T_{ij}\cdot\acute{A}_j + T_{ik}\cdot\acute{A}_k\right) = \frac{\gamma}{\mathbb{C}\cdot\nu\cdot\Delta}\cdot g_i$$

where, $g_i = T_{ii}\cdot\acute{A}_i + T_{ij}\cdot\acute{A}_j + T_{ik}\cdot\acute{A}_k$.

Therefore,

$$\frac{\partial f_i}{\partial \acute{A}_i} = s_{ii} + \frac{1}{\nu}\cdot\left(T_{ii}\cdot\acute{A}_i + T_{ij}\cdot\acute{A}_j + T_{ik}\cdot\acute{A}_k\right)\cdot\frac{\partial \nu}{\partial \acute{A}_i}$$

$$= s_{ii} + \frac{1}{\nu}\cdot g_i\cdot\frac{\partial \nu}{\partial |B|}\cdot\frac{1}{\gamma}\cdot\frac{\gamma}{\mathbb{C}\cdot\nu\cdot\Delta}\cdot g_i$$

$$= s_{ii} + \frac{1}{|B|\cdot\Delta\cdot\gamma\cdot\nu^2}\cdot g_i^2\cdot\frac{\partial \nu}{\partial |B|}$$

With the aid of a similar procedure, all the elements in the Jacobian Matrix can be found and are listed below,

$$\frac{\partial f_i}{\partial \acute{A}_i} = s_{ii} + \frac{1}{|B|\cdot\Delta\cdot\gamma\cdot\nu^2}\cdot g_i^2\cdot\frac{\partial \nu}{\partial |B|}$$

$$\frac{\partial f_j}{\partial \acute{A}_j} = s_{jj} + \frac{1}{|B|\cdot\Delta\cdot\gamma\cdot\nu^2}\cdot g_j^2\cdot\frac{\partial \nu}{\partial |B|}$$

$$\frac{\partial f_k}{\partial \acute{A}_k} = s_{kk} + \frac{1}{|B|\cdot\Delta\cdot\gamma\cdot\nu^2}\cdot g_k^2\cdot\frac{\partial \nu}{\partial |B|}$$

$$\frac{\partial f_i}{\partial \acute{A}_j} = s_{ij} + \frac{1}{|B|\cdot\Delta\cdot\gamma\cdot\nu^2}\cdot g_i\cdot g_j\cdot\frac{\partial \nu}{\partial |B|}$$

$$\frac{\partial f_i}{\partial \acute{A}_k} = s_{ik} + \frac{1}{|B|\cdot\Delta\cdot\gamma\cdot\nu^2}\cdot g_i\cdot g_k\cdot\frac{\partial \nu}{\partial |B|}$$

$$\frac{\partial f_j}{\partial \acute{A}_i} = s_{ji} + \frac{1}{|B|\cdot\Delta\cdot\gamma\cdot\nu^2}\cdot g_j\cdot g_i\cdot\frac{\partial \nu}{\partial |B|}$$

$$\frac{\partial f_j}{\partial \acute{A}_k} = s_{jk} + \frac{1}{|B|\cdot\Delta\cdot\gamma\cdot\nu^2}\cdot g_j\cdot g_k\cdot\frac{\partial \nu}{\partial |B|}$$

$$\frac{\partial f_k}{\partial \acute{A}_i} = s_{ki} + \frac{1}{|B|\cdot\Delta\cdot\gamma\cdot\nu^2}\cdot g_k\cdot g_i\cdot\frac{\partial \nu}{\partial |B|}$$

$$\frac{\partial f_k}{\partial \acute{A}_j} = s_{kj} + \frac{1}{|B|\cdot\Delta\cdot\gamma\cdot\nu^2}\cdot g_k\cdot g_j\cdot\frac{\partial \nu}{\partial |B|} \qquad \text{.....(3.31)}$$

Similar to the preceding section, the residual form of an element *e* with nodes *i, j* and *k*, is

$$\begin{Bmatrix} R_i \\ R_j \\ R_k \end{Bmatrix} = [J]^e\cdot\begin{Bmatrix} \acute{A}_i \\ \acute{A}_j \\ \acute{A}_k \end{Bmatrix}^{(n+1)} - \{c\}^e - [m]^e\cdot\begin{Bmatrix} \acute{A}_i \\ \acute{A}_j \\ \acute{A}_k \end{Bmatrix}^{(n)} \qquad \text{.....(3.32)}$$

Adding the contribution of every element to a global matrix, we have

$$\{R\} = [J]^{(n+1)}\cdot\{\acute{A}\}^{(n+1)} - \{C\} - [M]\cdot\{\acute{A}\}^{(n)} = 0 \qquad \text{.....(3.33)}$$

for each time step. It has the same form as the equation (3.24). The only difference is that in (3.33) the Jacobian matrix $[J]^{(n+1)}$ is present in place of the stiffness matrix [S] in (3.24).

3.4 Computing Strategy

3.4.1 Fish-bone Storage Technique

Because of the presence of the velocity term, the global matrix formed by finite element theory becomes asymmetric. Therefore the conventional storage method is not suitable here. Fortunately, although the matrix is not symmetric in its value it is symmetric in the sparsity structure. This leads to the possibility of using a 1-Dimensional bandwidth condensation storage approach.[20] To implement it a 'fish-bone' storage technique is created.

If all the materials in the problem are linear, then (3.24) becomes a set of linear equations. If it contains non-linear materials, then the Newton-Raphson method can be used in every iteration and [S] is replaced by the Jacobian matrix [J] as in (3.32). The latter has the same topology as the former so the storage method can be the same. For this reason, only [S] is discussed here. If the node sequence is arranged appropriately, [S] will become a very sparse one, in which all non-zero items gather along the two sides of the diagonal of the matrix. This is likened to a 'fish-bone' in the thesis because of its shape. A well known numbering scheme for reducing the bandwidth is the Cuthill-McKee algorithm.[21] As the TLIA has a simple topology, a simple numbering scheme is developed to produce the same effect as the Cuthill-McKee algorithm. For example, Fig. 3.4a shows the numbering scheme in reference [21] which has the bandwidth of 4. Fig. 3.4b demonstrates the numbering strategy adopted in this thesis which leads to the same bandwidth of 4. In this strategy, the numbering sequence simply starts from the corner of the mesh and progresses from top to

bottom, and column by column. The key point is that we must choose a column or a row which has less nodes as a starting column or row. For example, in Fig. 3.4, every row has six nodes but every column has only 4 nodes. Therefore, we choose a numbering sequence of column by column. If the numbering sequence is chosen as row by row, the bandwidth will be 6 rather than 4. This method is quite easy for renumbering an existing model.

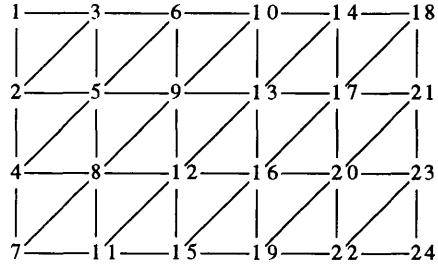

(a) Cuthill-McKee Numbering Scheme (Bandwidth 4)

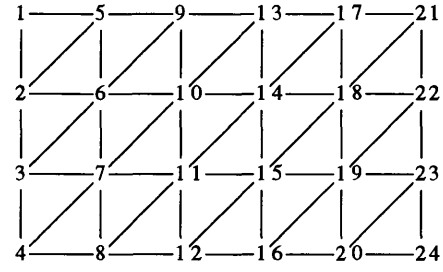

(b) Numbering Scheme in COUPV (Bandwidth 4)

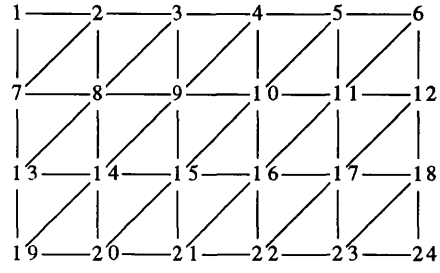

(c) Numbering Scheme of Bandwidth 6

Fig. 3.4 Comparison with the Cuthill-McKee Algorithm

In order to explain clearly, an example of 8 elements with 9 nodes is shown in Fig. 3.5a. Obviously, $[s]^e$ is not a symmetric matrix because of the moving part so that [S] is not symmetric as well. The matrix [S] is asymmetric, because $S_{ij} \neq S_{ji}$, (i, j = 1, 2, ..., m and i≠j), where m is the sum of the nodes connected to node *i*, but its structure is symmetric with respect to the diagonal as shown in the Fig. 3.5b.

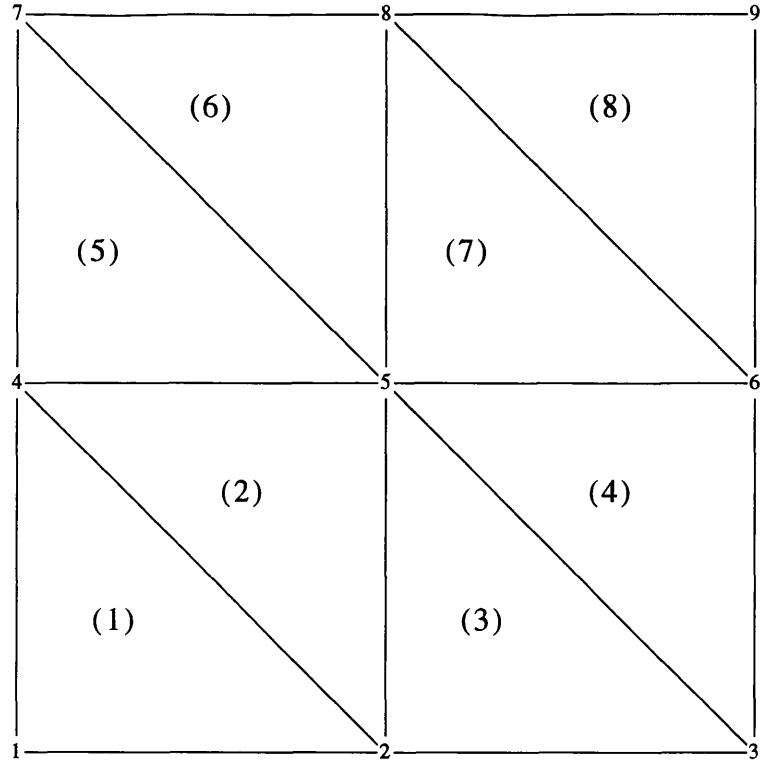

(a) Mesh Distribution of 8 Elements

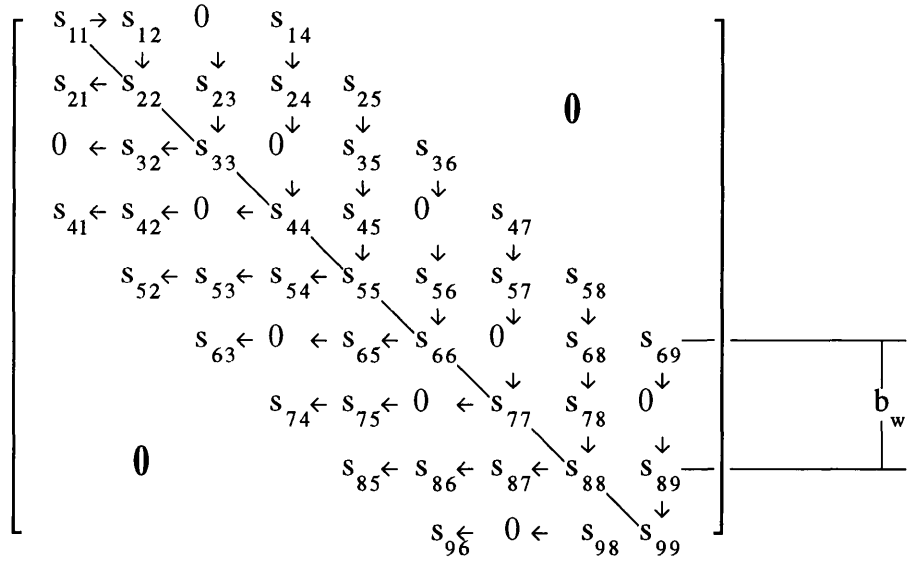

(b) Global Matrix [S] Corresponding to (a)

Fig. 3.5 A Example of 9 Nodes Matrix [S]

In principle, the *'fishbone'* storage strategy adopted in this work requires only two 1-D arrays to keep all the information about the global matrix [S]. One is {S} which records all the elements in [S]. The elements in {S} are arranged in the sequence indicated by the arrows shown in Fig. 3.5b, which is illustrated in Table 3.1.

$$
\begin{array}{rl}
 & \underline{1}\ \ 2\ \underline{3}\ \ 4\ \ \ 5\ \underline{6}\ \ 7\ \ \ 8\ \ 9\ \ 10\ \underline{11}\ \ 12\ \ 13 \\
\{S\} = \{ & s_{11} \mid s_{12}\ s_{22}\ s_{21} \mid s_{23}\ s_{33}\ s_{32} \mid s_{14}\ s_{24}\ \ 0\ \ s_{44}\ \ 0\ \ s_{42} \\
 & 14\ \ 15\ \ 16\ \ 17\ \underline{18}\ \ 19\ \ 20\ \ 21\ \ \ 22\ \ 23\ \ 24\ \underline{25}\ \ 26\ \ 27 \\
 & s_{41} \mid s_{25}\ s_{35}\ s_{45}\ s_{55}\ s_{54}\ s_{53}\ s_{52} \mid s_{36}\ 0\ \ s_{56}\ \ s_{66}\ \ s_{65}\ 0 \\
 & 28\ \ 29\ \ 30\ \ 31\ \underline{32}\ \ 33\ \ 34\ \ 35\ \ \ 36\ \ 37\ \ 38\ \ \underline{39}\ \ 40 \\
 & s_{63} \mid s_{47}\ s_{57}\ 0\ \ s_{77}\ 0\ \ s_{75}\ s_{74} \mid s_{58}\ \ s_{68}\ \ s_{78}\ \ s_{88}\ s_{87} \\
 & 41\ 42\ \ \ 43\ \ 44\ \ 45\ \underline{46}\ \ 47\ \ 48\ \ 49 \\
 & s_{86}\ s_{85} \mid s_{69}\ 0\ \ s_{89}\ \ s_{99}\ \ s_{98}\ \ 0\ \ s_{96}\ \}
\end{array}
$$

Table 3.1 {S} and Its Sequence

Since {S} only records from the first non-zero element, column by column in the upper triangle and row by row in the lower triangle, the total memory is less than $m\cdot(1 + 2\cdot b_w)$, where b_w is the bandwidth shown in Fig. 3.4b. Therefore, the total memory required will be $m\cdot(1 + 2\cdot b_w) \ll m^2$. If b_w is chosen as short as possible, this method will reduce the total memory requirement significantly.

The other array is called $\{\alpha\}$, which records the address of every term s_{ii} on the main diagonal in {S}, *i.e.*,

$\{\alpha\}$ = { 1, 3, 6, 11, 18, 25, 32, 39, 46}, corresponding to {S} in Table3.1. For convenience, an auxiliary array $\{\beta\}$ is introduced to record all the

bandwidths, $\{\beta\} = \{1, 1, 3, 3, 3, 3, 3, 3\}$. This is because although $\{\alpha\}$ and $\{S\}$ contain all the information needed, it is tedious to obtain the bandwidth from them.

The algebraic equations are solved by Gaussian Elimination. The 'Fishbone' storage method is very convenient to retrieve the elements needed during the operation, as arrays $\{\alpha\}$, $\{\beta\}$ and $\{S\}$ contain the address and element information of the global matrix in [S]

For example, if S_{ij} is needed and $i<j$, first, we look for the jth element n_j in $\{\alpha\}$ to find the address of s_{jj} in $\{S\}$, then s_{ij} can be found in the location $j-i$ ahead of s_{jj}. If $i>j$, we can first find the ith element of α_i in $\{\alpha\}$ and then s_{ij} will be located $i-j$ positions before s_{ii}.

The address of S_{32} in $\{S\}$ could be obtained in the following manner,

1. pick up the address of S_{33} in $\{S\}$, which is 6, in $\{\alpha\}$
2. $6 + (i-j) = 6 + (3-2) = 7$, so that
3. S_{32} can be found in $\{S\}$ of the address 7 as shown in Fig. 3.5.

3.4.2 Treatment of Non-axisymmetric Stator

As illustrated in Fig. 1.1 the stator of the TLIA is not an axisymmetric but is actually composed of four laminated blocks. In order to get more accurate results by 2D axisymmetric modelling, an algorithm based on the equivalent reluctance principle is created. Its purpose is to find an equivalent reluctivity $\nu'(r)$ in place of the real reluctivity ν so that under certain excitation conditions the flux density distribution in the 2-D axisymmetric model will be the same as in the real TLIA.

Fig. 3.6 illustrates a quarter of the stator section, in which the magnetic flux is assumed to flow along the path ABCD as shown in Fig. 3.6b. As is well known, the reluctance of a magnetic circuit is given by $R_m = \nu \cdot \frac{l_m}{A_m}$, in which A_m represents the average area of cross section and l_m represents the average length of the magnetic circuit. The magnetic circuit in Fig. 3.6b can be roughly divided into two parts. One is represented by a horizontal line CB with an average length of l_{ha} in which all the flux is assumed to flow in the horizontal direction. Another is represented by a vertical line AB or CD with an average length of l_{va} in which all the flux is assumed to flow in the vertical direction.

1. The Equivalent Reluctivity of the Horizontal Part

If the horizontal part of the lamination is divided into small sectors in the radial direction in the 2D axisymmetric model. Each 1/8 of the sector with a length of l_{ha} and section area of $A_{RR'QQ'}$ at the radial position r has a reluctance of $R'_m = \nu' \cdot \frac{l_{ha}}{A_{RR'QQ'}}$. However, the real reluctance of the

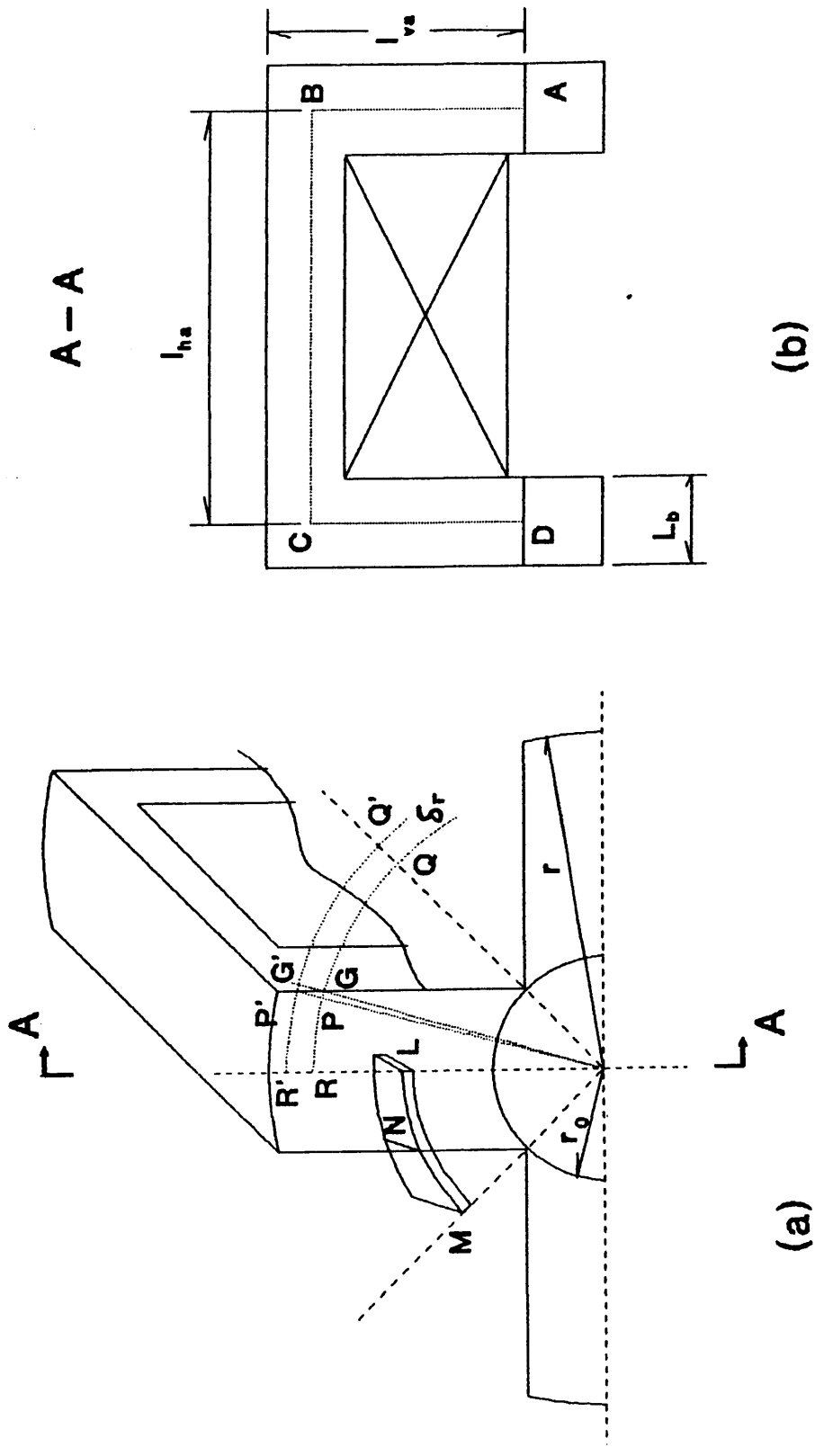

Fig. 3.6. Non-axisymmetric Stator Lamination

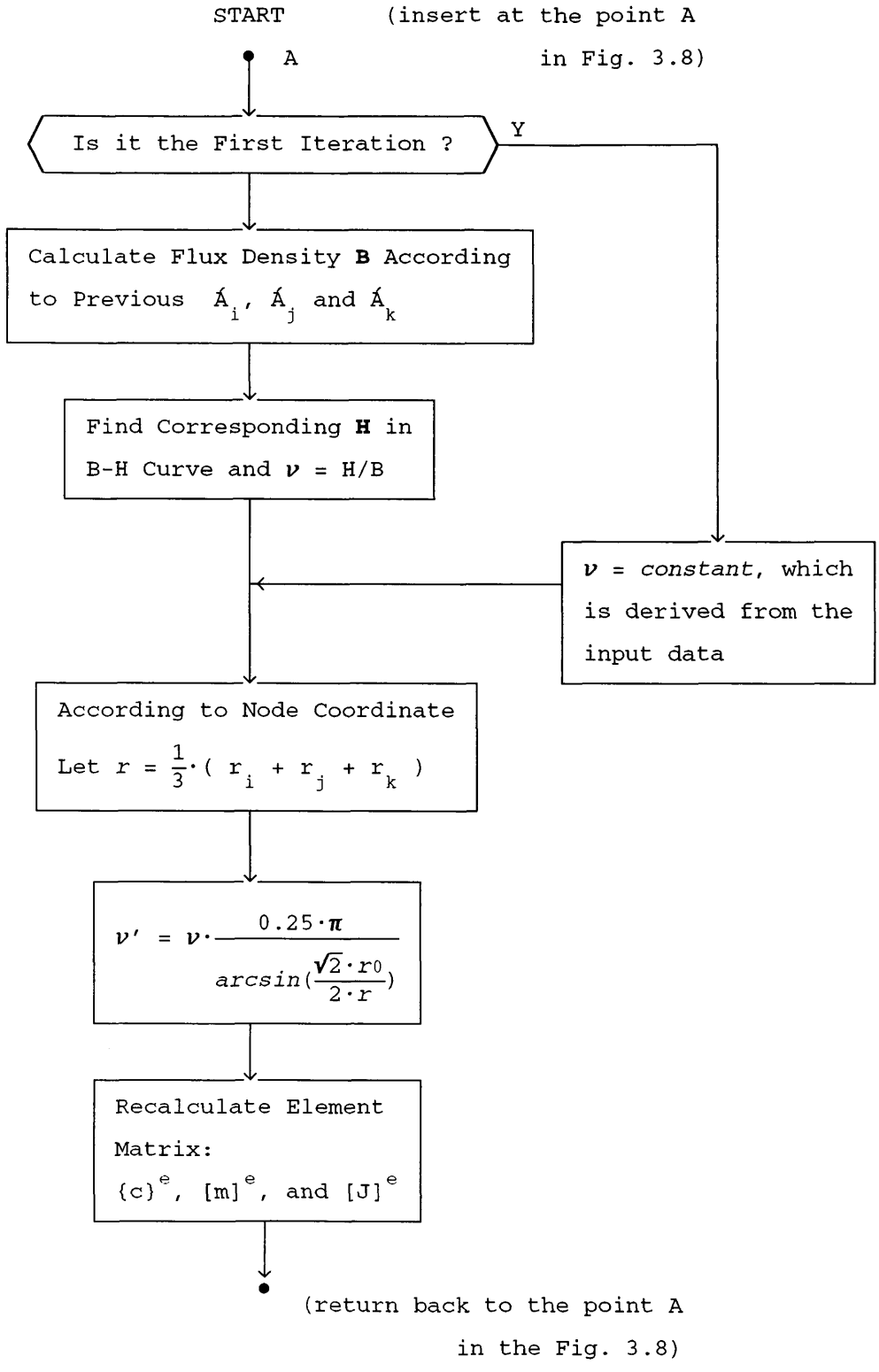

Fig. 3.7 Procedure to Find Equivalent Reluctivity

lamination should be $R_{mr} = \nu \cdot \frac{l_{ha}}{A_{RR'P'G}}$, in which $A_{RR'P'G}$ represents the lamination area with thickness δr at the radial position r. In order to obtain an equivalent electromagnetic effect, R_{mr} must equal to R'_m. Therefore, $R_{mr} = \nu \cdot \frac{l_{ha}}{A_{RR'P'G}} = R'_m = \nu' \cdot \frac{l_{ha}}{A_{RR'QQ'}}$ *i.e.*

$$\nu' = \nu \cdot \frac{A_{RR'QQ'}}{A_{RR'P'G}} \qquad \text{.....(3.34).}$$

Assuming that the triangle area $A_{PP'G} = A_{GG'P'}$ and calculating the area $A_{RR'QQ'}$ and $A_{RR'P'G}$, we can use the r coordinate to re-write (3.34) in the form,

$$\nu'(r) = \nu \cdot \frac{0.5 \cdot \pi}{\arcsin\frac{\sqrt{2} \cdot r_0}{2 \cdot r} + \arcsin\frac{\sqrt{2} \cdot r_0}{2 \cdot (r + \delta r)}} \qquad \text{.....(3.35)}$$

in which r_0 is the inner radius of the lamination, r is the radius at which the equivalent reluctivity $\nu'(r)$ needs to be calculated and δr is the radial width.

2. The Equivalent Reluctivity of the Vertical Part

Similarly, the equivalent reluctivity in the vertical part with path AB or CD can be approximated as

$$\nu'(r) = \nu \cdot \frac{0.25 \cdot \pi}{\arcsin\frac{\sqrt{2} \cdot r_0}{2 \cdot r}} \qquad \text{.....(3.36)}$$

In Fig. 3.6a, we define a small volume with thickness δr and width L_b within the lamination as V_A. We expand V_A to M to form a larger volume V_B, which represents the volume corresponding to V_A in 2-D axisymmetric model. The reluctance of these two volumes at the radial position r are

$$R_A = \frac{\nu \cdot \delta r}{L_b \cdot \text{arc}(LN)} \quad \text{and} \quad R_B = \frac{\nu' \cdot \delta r}{L_b \cdot \text{arc}(LN)} \quad \text{respectively.}$$

Therefore, $\nu'(r) = \nu \cdot \frac{\text{arc}(LM)}{\text{arc}(LN)} = \nu \cdot \frac{0.25 \cdot \pi}{\arcsin \frac{\sqrt{2} \cdot r_0}{2 \cdot r}}$.

In the computer program, this modification is carried out after the reluctivity is chosen from the B-H curve. For an individual element with node *i*, *j* and *k*, *r* and δr are given by

$$\begin{cases} r = (r_i + r_j + r_k)/3 \\ \delta r = 0.5 \cdot (|r_i - r_j| + |r_j - r_k| + |r_k - r_i|). \end{cases}$$

In the horizontal part, δr is very small comparing with *r*, especially when the mesh is quite small, *i.e.* $\delta r \ll r$ so that the formula (3.35) can be simplified and it become the same as the formula (3.36)

$$\nu'(r) = \nu \cdot \frac{0.5 \cdot \pi}{\arcsin \frac{\sqrt{2} \cdot r_0}{2 \cdot r} + \arcsin \frac{\sqrt{2} \cdot r_0}{2 \cdot (r + \delta r)}} = \frac{0.5 \cdot \pi}{\arcsin \frac{\sqrt{2} \cdot r_0}{2 \cdot r} + \arcsin \frac{\sqrt{2} \cdot r_0}{2 \cdot r}}$$

$$= \nu \cdot \frac{0.25 \cdot \pi}{\arcsin \frac{\sqrt{2} \cdot r_0}{2 \cdot r}}.$$

As a result, in this case, we just use (3.36) to find the equivalent reluctivity $\nu'(r)$ for both cases. The whole procedure is shown in the flow chart of Fig. 3.7.

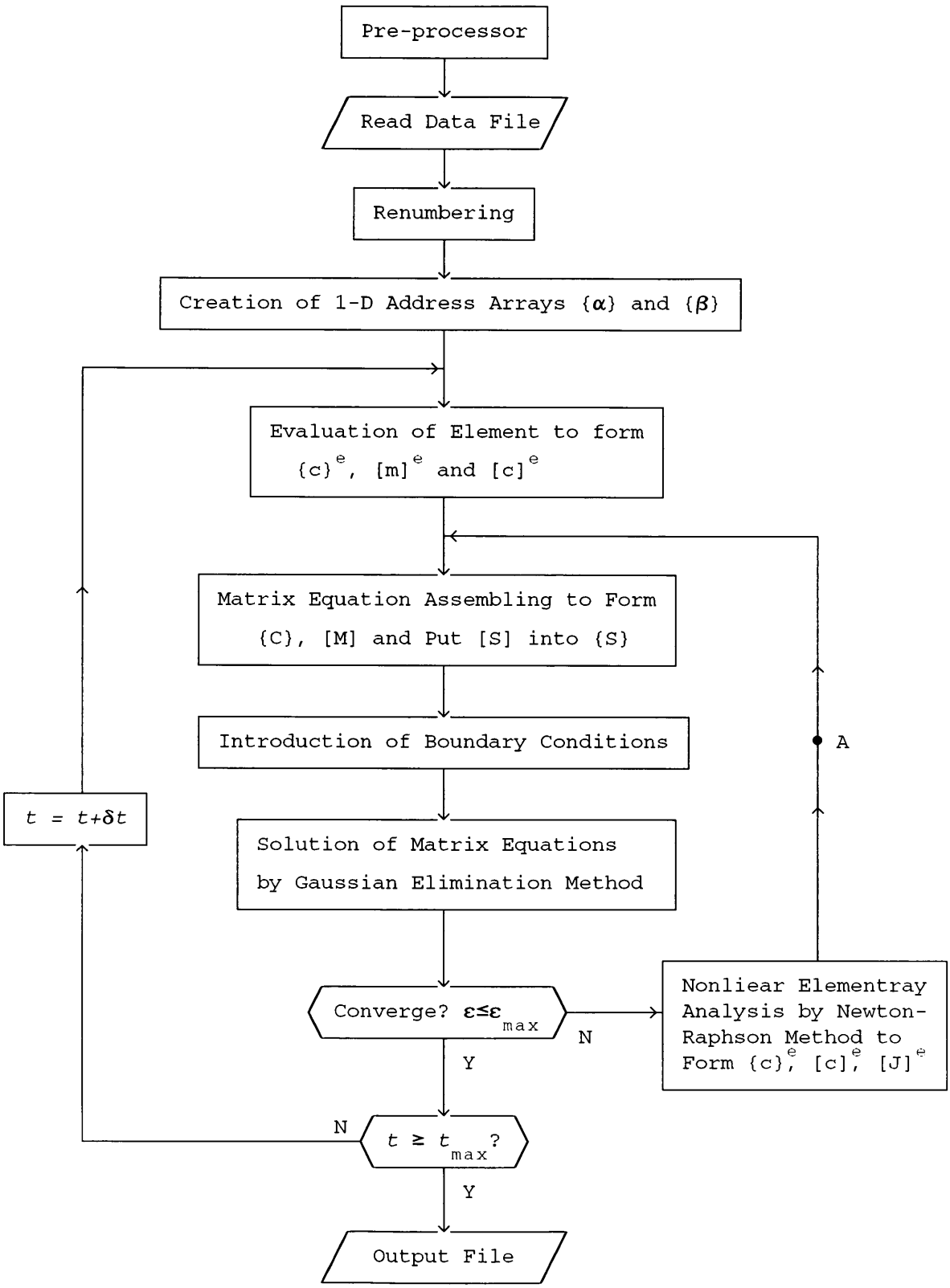

Fig. 3.8 The Solver CENV

3.4.3 The Block Chart of the FEM Solver CENV

The algorithms developed in the preceding sections form the basis of the finite element solver CENV. The pre-processor for preparing the input data is indispensable for implementing the CENV. Reading the output file from an existing pre-processor[22], a data transfer renumbers by means of the scheme introduced in section 3.4.1 to reduce the bandwidth.

As is well known, the pre-processor accomplishes four main functions: (1) description of the geometry of the object; (2) mesh generation; (3) introduction of material properties and physical characteristics; (4) description of boundary conditions. All these are carried out and written to an output file by a renumbering program and then fed to the solver CENV.

The computing procedure of CENV is shown in the flow chart of Fig. 3.8. After reading the geometry, material and boundary condition details, firstly, the CENV creates two 1-D arrays $\{\alpha\}$ and $\{\beta\}$ to record the exact position of each element in the 1-D condensed array $\{S\}$. Then at every time step, the reluctivity ν of the ferromagnetic material is selected as a constant in the first iteration. This constant is derived from the linear part of the B-H curve. And then, following the matrix assembly and boundary condition considerations, the program solves the large matrix equation by the Gaussian elimination method. If the solution converges, the calculation goes to the next step. Otherwise, the code starts the non-linear iterations by the Newton-Raphson method until the error is smaller than a predetermined tolerance. The stop command is set by the user. Normally, it is a maximum time or a maximum number of the time steps. After all the calculation are completed, the simulation results are

written into several output files.

The computer program CENV solves problems with currents sources. It is fed by a current density J_c which corresponds the input current. The input current can have any kind of waveforms such as sine waves, square waves or just pure d.c. At each time step, the input current density J_c is calculated from the input current according to

$$J_c = \frac{i \cdot N_c}{A_s}$$

in which N_c is the number of turns of the winding and A_s is the area occupied by the winding.

There are two main differences between the solver CENV and a normal 2-D time dependent finite element solver. One is that the CENV deals with the velocity problem so that its stiffness matrix is no longer a symmetric one. This leads to the increase of the storage and computing time required. The fish-bone storage strategy solves the problems associated with the storage capacity. The other is that if the stator of the TLIA is not axisymmetric, an equivalent reluctivity will be used in each time step according to the radial location of the element. This changes a real 3-D problem into a 2-D model significantly expanding the range of application of the CENV. Moreover, it can either be used as an independent main program as introduced in this chapter or as a subroutine for the coupled problem to be described in the next chapter.

3.5 Calculation of the Flux Linkage and Back EMF

The TLIA is fed by a time varying power supply. The back *emf* induced in its stator coil plays a very important role in coupling the external electric circuit to the internal electromagnetic field. After the magnetic vector potential distribution is calculated by the FEM, the flux density **B** is determined and the magnetic flux ϕ is evaluated by the surface integral of the normal component of the magnetic field over an area. In terms of the Stokes's theorem, it can also be written as a contour integral.

$$\phi = \int_a \mathbf{B}\cdot d\mathbf{a} = \int_a \text{rot}\ \mathbf{A}\cdot d\mathbf{a} = \oint_l \mathbf{A}\cdot d\mathbf{l}$$

For a single element with a single turn coil per unit area, it will link an amount of flux

$$\phi^{(e)} = \oint_l \mathbf{A}\cdot d\mathbf{l} = \oint_l A_\theta \cdot r \cdot d\theta = \int_0^{2\pi} \acute{A}\cdot d\theta = 2\pi\cdot\acute{A}$$

Therefore, if the section area of the exciting coil is A_s and the coil has N_c turns, *i.e.* $\frac{N_c}{A_s}$ turns in a unit area, the flux linkage in an element can be described as follows,

$$\psi^{(e)} = \iint \phi^{(e)}\cdot\frac{N_c}{A_s}\cdot drdz = 2\pi\cdot\frac{N_c}{A_s}\iint \acute{A}\cdot drdz = 2\pi\cdot\frac{\Delta\cdot N_c}{3\cdot A_s}\cdot(\acute{A}_i + \acute{A}_j + \acute{A}_k)$$

Finally, the back *emf* can be determined by Faraday's law as,

$$emf = -\frac{d\psi}{dt} = -\sum\frac{d\psi^{(e)}}{dt}$$

$$= -2\pi\cdot\frac{N_c}{3\cdot A_s}\cdot\sum\Delta\cdot\left[(\acute{A}_i^{(n+1)} + \acute{A}_j^{(n+1)} + \acute{A}_k^{(n+1)}) - (\acute{A}_i^{(n)} + \acute{A}_j^{(n)} + \acute{A}_k^{(n)})\right]$$

.....(3.37)

In next chapter, the input current of the TLIA will be calculated depending on this back *emf*.

3.6 Calculation of Electromagnetic Force

The most important specification of a linear actuator could be its output force. In the TLIA, due to eddy currents the conductor tube experiences a body force given by $\mathbf{f} = \mathbf{J} \times \mathbf{B}$. In an individual element,

$$\mathbf{B}^e = B_z \cdot \alpha_z + B_r \cdot \alpha_r = \text{rot } \mathbf{A} = \frac{1}{r} \cdot \left(\frac{\partial (r \cdot A)}{\partial r} \cdot \alpha_z - \frac{\partial (r \cdot A)}{\partial z} \cdot \alpha_r \right) = \frac{1}{r} \cdot \left(\frac{\partial \acute{A}}{\partial r} \cdot \alpha_z - \frac{\partial \acute{A}}{\partial z} \cdot \alpha_r \right)$$

$$= \frac{1}{2 \cdot \Delta \cdot r} \cdot \left((c_i \cdot \acute{A}_i + c_j \cdot \acute{A}_j + c_k \cdot \acute{A}_k) \cdot \alpha_z + (b_i \cdot \acute{A}_i + b_j \cdot \acute{A}_j + b_k \cdot \acute{A}_k) \cdot \alpha_r \right), \qquad \cdots\cdots (3.38)$$

and

$$J^e = -\sigma \cdot \left(\frac{\partial A}{\partial t} + V_z \cdot \frac{\partial A}{\partial z} \right) = -\frac{\sigma}{r} \cdot \left(\frac{\partial (r \cdot A)}{\partial t} + \frac{\partial (r \cdot A)}{\partial z} \right) = -\frac{\sigma}{r} \cdot \left(\frac{\partial \acute{A}}{\partial t} + V_z \cdot \frac{\partial \acute{A}}{\partial z} \right)$$

$$= -\frac{\sigma}{r} \cdot \left\{ \frac{1}{\delta t} \cdot \left[N_i \cdot (\acute{A}_i^{(n+1)} - \acute{A}_i^{(n)}) + N_j \cdot (\acute{A}_j^{(n+1)} - \acute{A}_j^{(n)}) + N_k \cdot (\acute{A}_k^{(n+1)} - \acute{A}_k^{(n)}) \right] \right.$$

$$\left. + \frac{V_z}{2\Delta} \cdot (b_i \cdot \acute{A}_i^{(n+1)} + b_j \cdot \acute{A}_j^{(n+1)} + b_k \cdot \acute{A}_k^{(n+1)}) \right\}$$

Therefore, the force produced in one element is

$$\mathbf{F}^e = F_r^e \cdot \alpha_r + F_z^e \cdot \alpha_z = \int_{V^e} \mathbf{J} \times \mathbf{B} \cdot dv = \alpha_r \cdot \int_{V^e} J \cdot B_z \cdot dv - \alpha_z \cdot \int_{V^e} J \cdot B_r \cdot dv$$

in which F_r^e and F_z^e represent the radial and axial forces respectively.

$$F_r^e = \int_{V^e} J \cdot B_z \cdot dv = \int_0^{2\pi} \iint J \cdot B_z \cdot r \cdot dr dz d\theta = 2\pi \cdot \iint J \cdot B_z \cdot r \cdot dr dz$$

Let $B_a = b_i \cdot \acute{A}_i^{(n+1)} + b_j \cdot \acute{A}_j^{(n+1)} + b_k \cdot \acute{A}_k^{(n+1)}$, $C_a = c_i \cdot \acute{A}_i + c_j \cdot \acute{A}_j + c_k \cdot \acute{A}_k$,

$\ddot{A}_i = \acute{A}_i^{(n+1)} - \acute{A}_i^{(n)}$, $\ddot{A}_j = \acute{A}_j^{(n+1)} - \acute{A}_j^{(n)}$ and $\ddot{A}_k = \acute{A}_k^{(n+1)} - \acute{A}_k^{(n)}$.

Therefore,

$$F_r^e = 2\pi\cdot\iint -\frac{\sigma}{r}\cdot\left[\frac{1}{\delta t}\cdot\left(N_i\cdot\ddot{A}_i + N_j\cdot\ddot{A}_j + N_k\ddot{A}_k\right) + V_z\cdot\frac{B_a}{2\Delta}\right]\cdot\left(\frac{C_a}{2\Delta\cdot r}\right)\cdot r\cdot drdz$$

$$= -2\pi\cdot\sigma\cdot\left[\frac{1}{\delta t}\cdot\left(\ddot{A}_i\cdot\iint\frac{N_i}{r}\cdot drdz + \ddot{A}_j\cdot\iint\frac{N_j}{r}\cdot drdz + \ddot{A}_k\cdot\iint\frac{N_k}{r}\cdot drdz\right)\right.$$

$$\left. + V_z\cdot\frac{B_a}{2\Delta}\cdot\iint\frac{1}{r}\cdot drdz\right]\cdot\frac{C_a}{2\Delta} \qquad \cdots\cdots(3.40)$$

$$F_z^e = -\int_{V^e} J\cdot B_r\cdot dv = -\int_0^{2\pi}\iint J\cdot B_r\cdot r\cdot drdzd\theta = -2\pi\cdot\iint J\cdot B_r\cdot r\cdot drdz$$

$$= -2\pi\cdot\iint -\frac{\sigma}{r}\cdot\left[\frac{1}{\delta t}\cdot\left(N_i\cdot\ddot{A}_i + N_j\cdot\ddot{A}_j + N_k\ddot{A}_k\right) + V_z\cdot\frac{B_a}{2\Delta}\right]\cdot\left(\frac{-B_a}{2\Delta\cdot r}\right)\cdot r\cdot drdz$$

$$= -2\pi\cdot\sigma\cdot\left[\frac{1}{\delta t}\cdot\left(\ddot{A}_i\cdot\iint\frac{N_i}{r}\cdot drdz + \ddot{A}_j\cdot\iint\frac{N_j}{r}\cdot drdz + \ddot{A}_k\cdot\iint\frac{N_k}{r}\cdot drdz\right)\right.$$

$$\left. + V_z\cdot\frac{B_a}{2\Delta}\cdot\iint\frac{1}{r}\cdot drdz\right]\cdot\frac{B_a}{2\Delta} \qquad \cdots\cdots(3.41)$$

Finally, the total electromagnetic forces of the plunger in both axial and radial directions are:

$$F_z = \sum F_z^e \text{ and } F_r = \sum F_{r.}^e$$

If there is an iron member involved in the plunger, the output force should be estimated by the Maxwell stress method since the Lorentz formula can lead to errors by neglecting the forces which act directly on the iron. The Maxwell stress is a well known method by which the force on a volume can be calculated by integrating the electromagnetic stress over its surface:

$$F = \iint_S \left[\mu \cdot H_t \cdot H_n \cdot \vec{t} + \frac{\mu}{2} \cdot (H_n^2 - H_t^2) \cdot \vec{n} \right] \cdot ds$$

$$= \iint_S (f_t \cdot \vec{t} + f_n \cdot \vec{n}) \cdot ds \qquad \cdots\cdots(3.42)$$

In the TLIA, the cross section of this surface is shown as in Fig. 3.9 in which the surface can be divided into four parts s_1, s_2, s_3 and s_4. Therefore, in each part

$$s_1: \quad F_{s1} = \int_0^{2\pi} \int_{z_0}^{z_1} (f_t \cdot \vec{t} + f_n \cdot \vec{n}) \cdot r_0 \cdot dz d\theta = 2\pi \cdot r_0 \cdot \sum_{i=1}^{m} (f_{ti} \cdot \vec{t} + f_{ni} \cdot \vec{n}) \cdot \delta z \qquad \cdots\cdots(3.43)$$

$$s_2: \quad F_{s2} = \int_0^{2\pi} \int_{r_i}^{r_o} (f_t \cdot \vec{t} + f_n \cdot \vec{n}) \cdot r \cdot dr d\theta \approx 2\pi \cdot \sum_{i=1}^{m} (f_{ti} \cdot \vec{t} + f_{ni} \cdot \vec{n}) \cdot r_i \cdot \delta r \qquad \cdots\cdots(3.44)$$

$$s_3: \quad F_{s3} = 2\pi \cdot r_i \cdot \sum_{i=1}^{m} (f_{ti} \cdot \vec{t} + f_{ni} \cdot \vec{n}) \cdot \delta z \qquad \cdots\cdots(3.45)$$

$$s_4: \quad F_{s4} \approx 2\pi \cdot \sum_{i=1}^{m} (f_{ti} \cdot \vec{t} + f_{ni} \cdot \vec{n}) \cdot r_i \cdot \delta r \qquad \cdots\cdots(3.46)$$

in which m is the number of the segments along z or r direction, δz or δr is the length of each segment and f_{ti} or f_{ni} is the force acting on the segment.

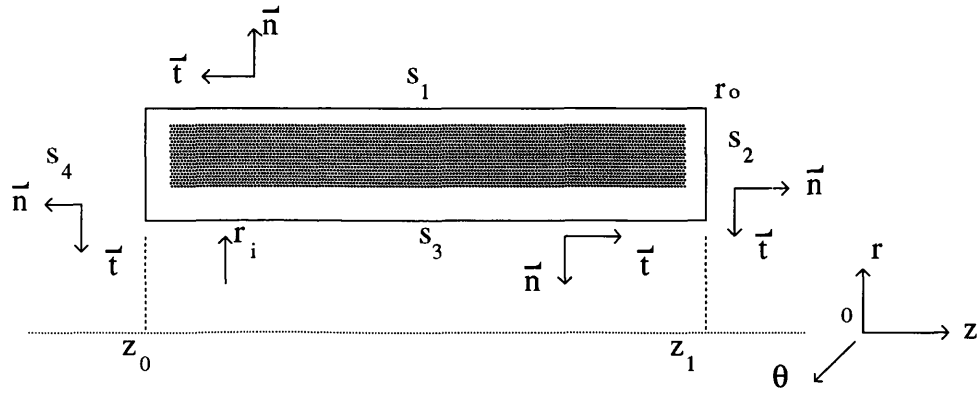

Fig. 3.9 Surface for Integration

3.7 Calculation of Eddy Current and Its Losses

The TLIA is a good example of utilising eddy currents to do useful work but the associated losses should be carefully estimated. The eddy current in an element can be calculated by integrating the eddy current density over the element area.

$$I_e^e = \iint J \cdot drdz = \iint -\frac{\sigma}{r} \cdot \left[\frac{1}{\delta t} \cdot \left(N_i \cdot \ddot{A}_i + N_j \cdot \ddot{A}_j + N_k \cdot \ddot{A}_k \right) + V_z \cdot \frac{B_a}{2\Delta} \right] \cdot drdz$$

$$= - \sigma \cdot \left[\frac{1}{\delta t} \cdot \left(\ddot{A}_i \cdot \iint \frac{N_i}{r} \cdot drdz + \ddot{A}_j \cdot \iint \frac{N_j}{r} \cdot drdz + \ddot{A}_k \cdot \iint \frac{N_k}{r} \cdot drdz \right) \right.$$

$$\left. + V_z \cdot \frac{B_a}{2\Delta} \cdot \iint \frac{1}{r} \cdot drdz \right] \qquad \cdots\cdots(3.42)$$

The total eddy current, therefore, is $I_e = \sum I_{e.}^e$

The eddy current losses can be calculated in two ways. One is deduced directly from the eddy current density. In a single element,

$$P_e^e = \int J_e^e \cdot E^e \cdot dv = 2\pi \cdot \int (J_e^e)^2 \cdot \frac{r}{\sigma} \cdot drdz$$

$$= 2\pi\sigma \cdot \iint \frac{1}{r} \cdot \left[\frac{1}{\delta t} \cdot \left(N_i \cdot \ddot{A}_i + N_j \cdot \ddot{A}_j + N_k \cdot \ddot{A}_k \right) + V_z \cdot \frac{B_a}{2\Delta} \right]^2 \cdot drdz$$

$\cdots\cdots(3.43)$

Another method makes use of the eddy current I_e^e and the equivalent resistance of a copper ring with a cross section of an element. The equivalent resistance can be defined as

$$R_{eq} = \frac{l_e}{\sigma \cdot \Delta}$$

in which l_e is an equivalent perimeter $l_e = 2\pi \cdot (r_i + r_j + r_k)/3$.

Consequently, $P_e^e = (I_e^e) \cdot R_{eq}$ and the total eddy current losses is $P_e = \sum P_e^e$.

3.8 Conclusions

A 2-D axisymmetric time-stepping finite element method has been developed in this chapter which takes eddy currents, non-linearity and the moving part into account. Because there is a velocity term in the partial differential equation, it is difficult to find its functionals. Therefore, the Galerkin method is adopted to change the Maxwell equations into a large sparse linear matrix equation. The procedures have been described in detail in this chapter.

The velocity term also results in an asymmetric stiffness matrix, for which a 'fish-bone' storage technique has been introduced. The total amount of computer storage required is twice that used for the symmetric stiffness matrix without the velocity term.

In order to make use of a 2-D model to simulate the 3-D laminated stator with four limbs, a modified reluctivity has been introduced in the elemental analysis based on the equivalent reluctance principle. At the end of this chapter, a set of formulae for calculating flux linkage, back *emf*, eddy current and eddy current losses are introduced, specially for the axisymmetric model. The computer program for current forced problems described in this chapter makes it possible to develop a computing strategy for coupled problems in the next chapter.

CHAPTER 4 COUPLING THE FIELD PROBLEM WITH ELECTRIC CIRCUITS AND MECHANICAL SYSTEMS

4.1 Introduction

Since 80's, the coupling problem has become a popular topic in electromagnetic field computations and dynamic simulations of electromechanical devices. The rapid technical progress in super computers makes it possible to solve the whole electromechanical system quickly and efficiently. In fact, most electromechanical systems are physically composed of three main parts, an electrical or electronic circuit, an electromagnetic device and a mechanical load. Its physical model can be seen in Fig. 4.1. Physical variables such as i, Ψ or V in these parts are affected by each other. In some circumstances, decoupling these three parts are impossible or very difficult without paying the price of low accuracy solution or long computing time costs.

Normally, an ideal CAD procedure would be a solution of the differential field equation coupled to an applied voltage source rather than a current source because most of the electromechanical devices are driven by the former and not the latter. Furthermore, the power supply as depicted in Fig. 4.1a may not be a simple pure D.C. or sinusoidal A.C. supply because of the use of power electronics[23]. Nowadays, many electromagnetic devices are driven by power semiconductor converters such as d.c. choppers, Triac voltage controllers, PWM inverters, *etc.* They are neither pure DC nor sinusoidally varying voltage power supplies. In addition, since most electromagnetic devices are always designed with some degree of magnetic saturation, to predict the current waveform under a non-sinusoidal or

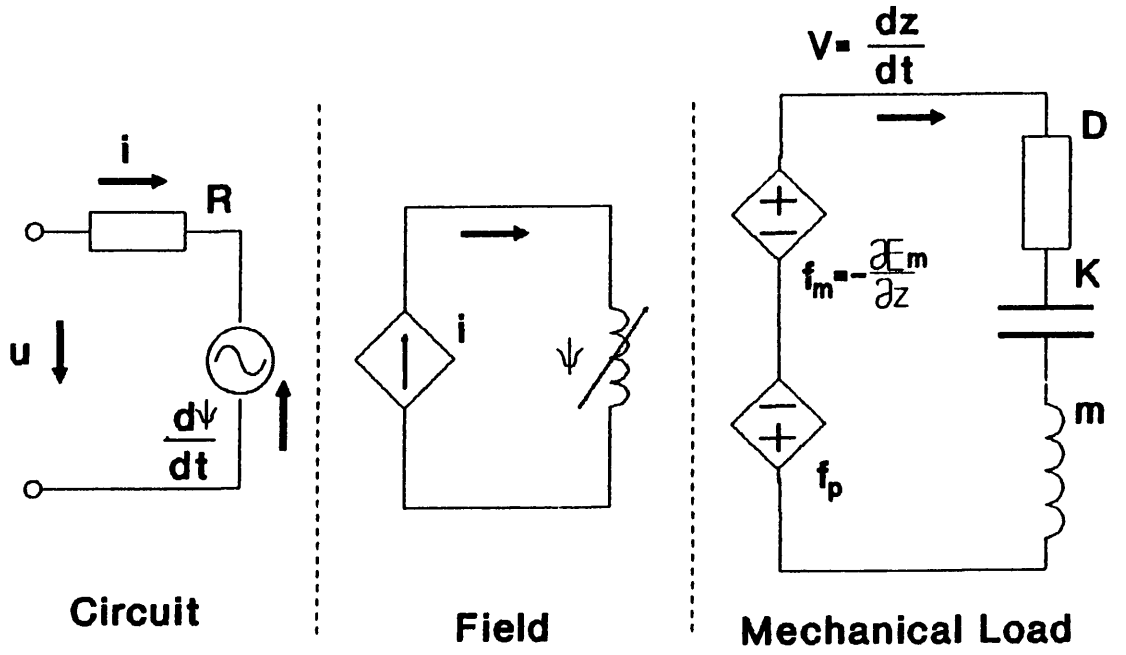

(a) General Conception of EM System

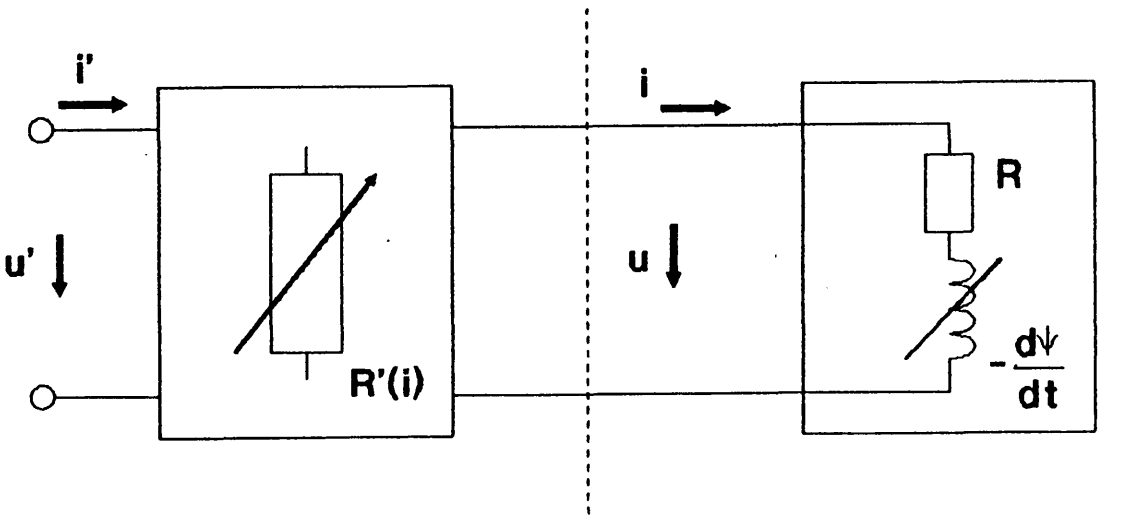

(b) Non-linear Circuit Connection

Fig. 4.1 Physical Models

non-D.C. voltage excitation,[24] becomes very difficult. For the actuating application, many devices such as magnets, solenoids and actuators are inherently transient devices with fast-acting moving parts. Therefore, the reaction caused by the moving parts can not be neglected.

In short, an ideal computer simulation program should be able to deal with the whole electromechanical system together and also take non-linearity of materials, eddy current and velocity effects into account.

The main contribution of this chapter is to develop a dynamic computer program called COUPV which fulfills the above functions. There are two main difficulties in solving the coupling problem[10]. One is the determination of the current that will satisfy both the circuit equations and the field equations. The other is to modify the mesh distortion caused by the displacement of the moving part at every time step.

In order to deal with these two problems, two strategies are adopted in this chapter. The first one is concerned with finding the current which satisfies both the electric circuit and the electromagnetic field by means of a one dimensional search strategy.[25] This strategy combines a modified secant method with a parabolic curve fitting technique to achieve a fast convergence in the one dimensional search. Unlike the secant method in which the end of each secant is always fixed at a point chosen at start, in the modified secant method, this point is variable and depends on the previous results. The parabolic curve fitting technique enables each first guess for the modified secant method to be as near the solution as possible. Their combination ensures the convergence of the algorithm within 3 to 4 iteration at each time step.

The second strategy is a mesh changing technique which must be able to deal with two tasks. One is to move the interface between the plunger and the airgap. The other is to change the material properties if the element moves from the plunger side to the airgap side. The particular geometry of the TLIA enables the numbering of the elements in the plunger in a special sequence. In addition, in the data file prepared for the COUPV, all the elements in the air region are numbered just before the elements in the plunger area. This method proves very simple and effective for the mesh changes that occur when the plunger moves.

4.2 Coupled Mathematical Model

From the physical model in Fig. 4.1, a coupled mathematical model for TLIA can be formulated as follows. The three equations governing the three parts to be coupled are,

in the electric circuit:

$$u = R \cdot i + \frac{d\psi}{dt} \qquad \cdots\cdots(4.1)$$

where, u --- applied voltage,

ψ --- coil flux linkage,

R --- coil resistance;

in the axisymmetric field:

$$\frac{\partial}{\partial z}\left(\nu \cdot \frac{\partial A}{\partial z}\right) + \frac{\partial}{\partial r}\left(\frac{\nu}{r} \cdot \frac{\partial (r \cdot A)}{\partial r}\right) = -J_c + \sigma \cdot \frac{\partial A}{\partial t} + \sigma \cdot V_z \cdot \frac{\partial A}{\partial z} \qquad \cdots\cdots(4.2)$$

where, $\mathbf{J}_c$ --- current density in coil region,

σ --- material conductivity,

ν --- material reluctivity,

V_z --- plunger velocity in Z direction;

and the motion of the plunger:

$$m \cdot \frac{d^2 z}{dt^2} + D \cdot \frac{dz}{dt} + K \cdot z + f_p = f_m \qquad \cdots\cdots(4.3)$$

where, m --- moving mass,

D --- viscous damping coefficient,

K --- spring constant,

f_p --- preload,

f_m --- total electromagnetic force on moving plunger.

The three variables i, Ψ and V_z play key roles in these equations. All of them are connected by the electromagnetic field.

4.3 Computing Strategy

The finite element computer program CENV developed in Chapter 3, is further developed into a program called COUPV according to the flow chart in Fig. 4.2. As introduced in Chapter 3, the CENV corresponds to the electromagnetic field model described by (4.2). Its input variable is the current density J_c, whose relationship to the input current i is given by,

$$J_c = \frac{i \cdot N_c}{A_s} \qquad \cdots\cdots(4.4)$$

in which N_c is the number of turns of the stator winding and A_s is the cross sectional area of the winding. This value of J_c will yield the electromagnetic field in the TLIA and the corresponding magnetic linkage Ψ (see 3.37). In this chapter, the key problem addressed is the determination of both i and Ψ to satisfy (4.1). In order to develop a computer program, (4.1) and (4.3) should be expressed in their discrete forms. At the *nth* time step instant t_n, (4.1) becomes,

$$U_n = R \cdot I_n + \left(\frac{\Psi_n}{\delta t} - \frac{\Psi^*_{n-1}}{\delta t} \right) \qquad \cdots\cdots\cdots(4.5)$$

in which, I_n --- input current, $J_c \propto I_n$ to energise the magnetic field,

Ψ_n --- flux linkage produced by I_n,

Ψ^*_{n-1} ---- flux linkage calculated at the previous instant t_{n-1}, which is a constant in the equation (4.5)

U_n --- $U_n = u(t_n)$, the instantaneous applied voltage at the instant of t_n.

The equation (4.3) can be changed into state space equations in the first instance as,

$$\begin{cases} \dfrac{dz}{dt} = V \\ \dfrac{dV}{dt} = -\dfrac{K}{m} \cdot z - \dfrac{D}{m} \cdot V - \dfrac{f_p}{m} + f_m \end{cases} \qquad \cdots\cdots\cdots(4.6)$$

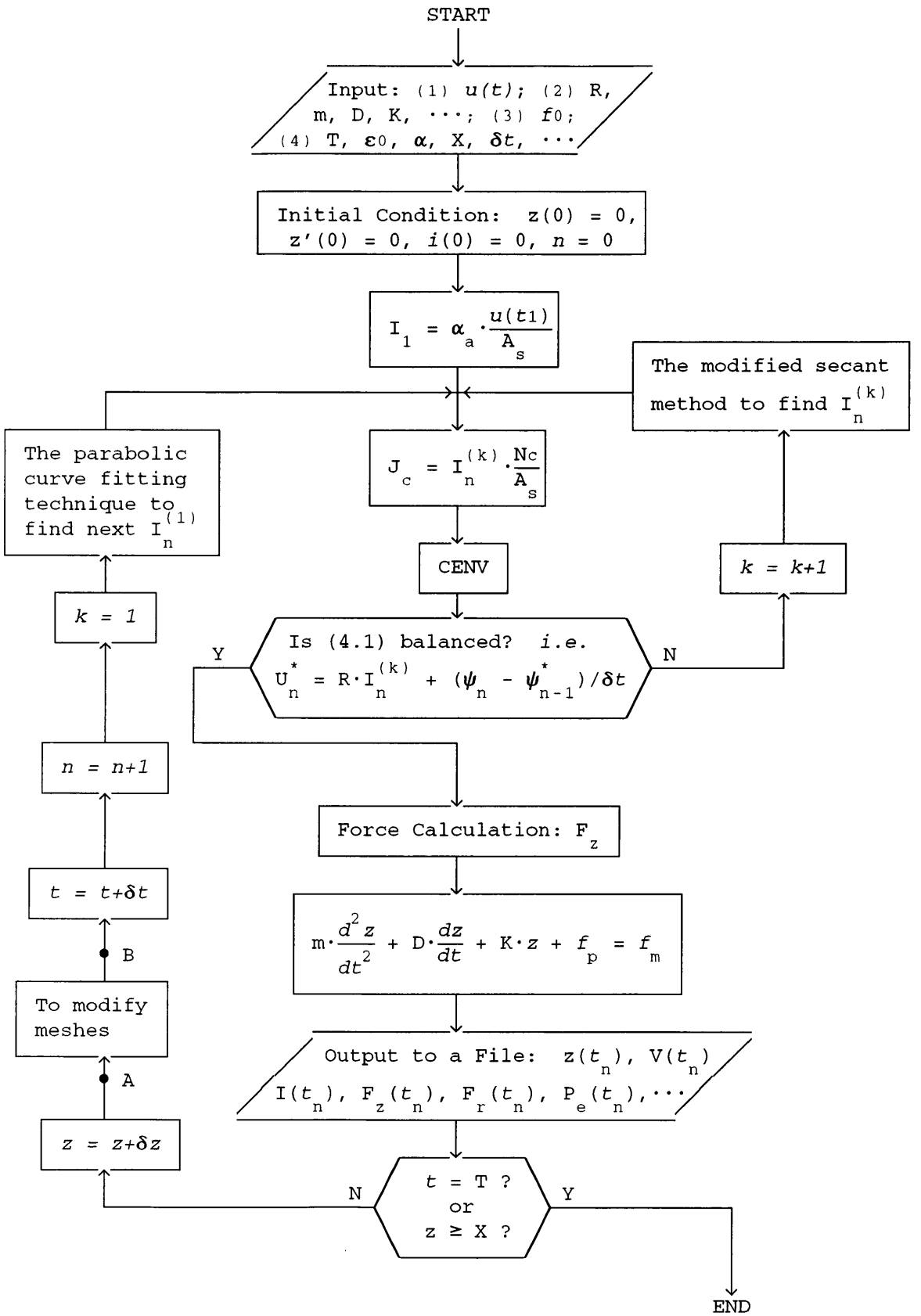

Fig. 4.2 The Coupling Code COUPV

in which, V is the time-dependent velocity in the Z direction omitting the subscript 'z' for simplicity. The discrete form of (4.6) is,

$$\begin{cases} \dfrac{z_n - z_{n-1}}{\delta t} = V_n \\ \dfrac{V_n - V_{n-1}}{\delta t} = -\dfrac{K}{m} z_n - \dfrac{D}{m} V_n - \dfrac{f_p}{m} + f_m \end{cases} \qquad \cdots\cdots(4.7)$$

In the COUPV, the inputs can be classified into six groups. The first one is the power source. For the TLIA there is only a single voltage source *u(t)*. It should include information about its frequency and waveform. The waveform can be sinusoidal, square, PWM or phase controlled triac wave. The second input concerns system parameters, for instance, R in the circuit; m, D and K in the mechanical system. The third group has named constraints. The analysis in this chapter considers f_p only. The fourth consists of several control variables such as T, the total simulating time duration expected; ε_0, the error tolerance; α_a, the accelerating convergence factor; X, the total displacement of the plunger, *etc.* The fifth group is made up of several state variables. Some of these are independent such as *i(t)*, $\Psi(t)$ and *z(t)* while some are dependent variables such as $F_z(t)$, $P_e(t)$, *etc.* Finally the sixth group contains some initial conditions. In general, the actuator is started from standstill with its energising circuit disconnected. Therefore, its initial conditions are $i(0)=0$, $z(0)=0$ and $\frac{d}{dt}z(0)=0$.

The main part of the COUPV is the CENV which deals with the electromagnetic field described by (4.2) and has already been described in the last chapter. After obtaining all the input data, the first guess $I_1^{(1)}$ is determined by

$$I_1^{(1)} = \alpha_a \cdot \frac{u(t_1)}{R}, \qquad \cdots\cdots(4.8)$$

where $0 < \alpha_a \leq 1$ is called the accelerating convergence factor which depends on whether $u(t_1)$ is relatively smooth or experiences a large transient. Due to the continuous nature of the input current, $I_1^{(1)}$ will not jump to a high level from $i(0)=0$. If $u(t)$ is a sine wave, α_a is chosen from 0.2 to 0.4. If $u(t)$ is of square wave, α_a is chosen from 0.3 to 0.5. These are empirical constants. The function of α_a is to prevent the first guess of $I_1^{(1)}$ from being far removed from the solution. This enables fast convergence to be reached. $I_1^{(1)}$ is a circuit variable. In order to couple the field it should be changed to a current density J_c by (4.4). If the input current $I_1^{(1)}$ and the computed $\Psi_1^{(1)}$ are able to balance the equation (4.5), all the results such as electromagnetic force F_{1z} in Z direction, F_{1r} in the radial direction, eddy current I_{1e}, eddy current losses P_{1e}, displacement z_1 and velocity V_1 will be calculated and written in an output file. Then the program continues on its next time step, of changing meshes to simulate movement, predicting the next source current by the parabolic curve fitting technique, and so on. If (4.5) is not satisfied, the program finds another input current $I_1^{(2)}$ by the modified secant method to repeat another iteration until the error ε is smaller than the tolerance ε_0. The program will stop either when $t \geq T$ or $z \geq X$ according to user's choice. T and X are the total simulating time and the total axial displacement, respectively.

In addition to creating the output file that contains the transient results such as $F_z(t)$, $F_r(t)$, $i(t)$, *etc.*, the program can also supply information about the distribution of the flux density, the force and eddy current losses alone the plunger length. These graphs enable engineers or researchers to understand the design and judge its quality.

4.4 Coupling with an External Circuit

The coupling problem arises by the need to use voltage sources to analyse the electromagnetic field instead of current sources. Up to date, two basic[26] strategies are used by authors who have presented their research concerning this topic. One is called the direct technique which solves the field and the circuit equations simultaneously by treating to the vector potential and the current as unknowns. Shen[27] used this method to analyse an electromagnetic relay and a shaded-pole motor in the frequency domain. Piriou[28] presented a time-dependent simulation of a saturated magnetic core coil. Although the direct method needs only one calculation at each time step, its global stiffness matrix will be asymmetric and the bandwidth will be much larger. This results in increased CPU time at each time step. The other is called the indirect technique which uses an iterative procedure to match both circuit and field models. MacBain[29] developed a program called the ANTIC to simulate a D.C. solenoid. Pawlak[30] described a fast-acting D.C. solenoid controlled by a diode. Yuan[31] proposed an algorithm which employed an electric field strength **E** as an iterative variable and a fuel injector was used as an example. The latter two consider the velocity in the mathematical model but no details are given in their papers.

The main advantage of the indirect methods is that they can be easily connected to an external circuit with non-linear components involved[32] as shown in Fig. 4.1b. Its stiffness matrix is symmetric in sparsity structure. Its disadvantage is that at every time step, the algorithm must take several iterations. All the authors interested in the indirect method prefer to use the secant method to conduct the one dimensional search.

Adopting a different approach, this chapter attempts to improve the convergence speed and reduce the iteration time by means of a modified secant method.

4.4.1 One Dimensional Search for the Exciting Current by the Modified Secant Method

Before introducing the modified secant method, let's examine two conventional one dimensional search methods. If we hope to find the root of an equation f(x) = 0 and if f(x) has an explicit expression for the derivation f'(x), then the Newton-Raphson method is the best one, provided that the first guess x_0 is sufficiently close to the solution $\bar{x}$. This is illustrated in Fig. 4.3a. It has a quadratically converging characteristics. Its *kth* iterative formula is

$$x_{k+1} = x_k - \frac{f(x_k)}{f'(x_k)} \qquad (k = 1, 2, 3, \cdots)$$

If we change the equation (4.1) into a discrete form at the *nth* time step, it will become

$$f(I_n, \Psi_n) = U_n^* - R \cdot I_n - \frac{\Psi_n}{\delta t} + \frac{\Psi_{n-1}^*}{\delta t} = 0$$

Obviously, there is no explicit derivative expression for it. Therefore, the Newton-Raphson method is not useful here.

The secant method used by the aforementioned authors is illustrated in Fig. 4.3b. The *kth* iterative formula is

$$x_{k+1} = x_0 - \frac{x_k - x_0}{f(x_k) - f(x_0)} \cdot f(x_k) \qquad (k = 1, 2, 3, \cdots)$$

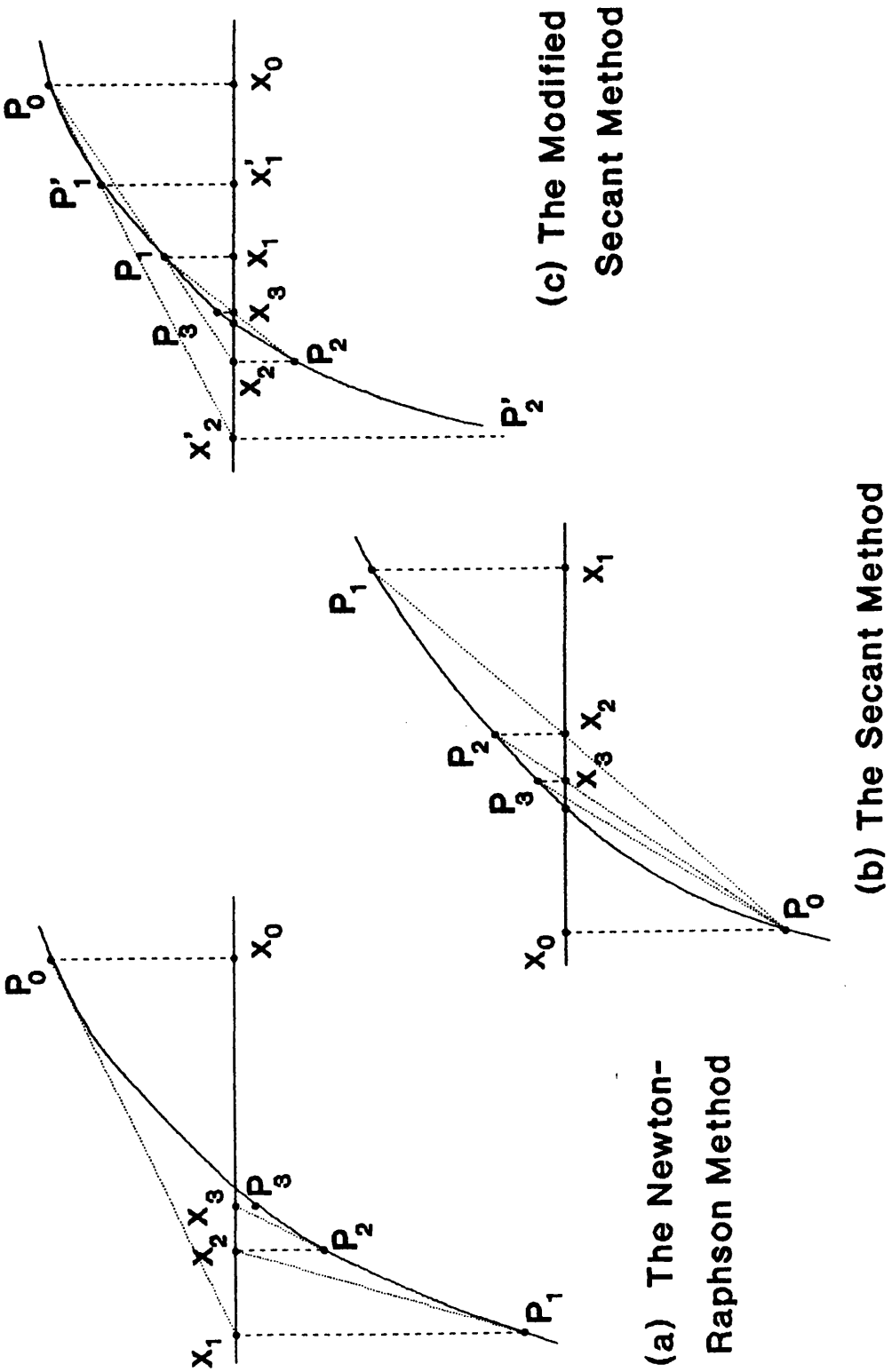

Fig. 4.3 One Dimensional Searching Methods

This method ensures convergency for a monotonously increasing function, no matter how far the first guess is and no expression for the derivative of the function is needed. The drawback is that, compared with the Newton-Raphson method, its convergence rate[33] is slower, especially when the solution is near convergence. This shortcoming can not be ignored, as in the coupled problem every iteration includes a finite element computation which involves significant computation time.

The modified secant method created in this chapter lies between the above two methods. As shown in Fig. 4.3c, it makes use of a secant in place of a tangent used by the Newton-Raphson method. Changing the derivative,

$$f'(x) \text{ into } \frac{f(x_k) - f(x_{k-1})}{x_k - x_{k-1}}.$$

Its *kth* iterative formula is

$$x_{k+1} = x_k - \frac{x_k - x_{k-1}}{f(x_k) - f(x_{k-1})} f(x_k) \qquad (k = 1, 2, 3, \cdots)$$

It overcomes the secant method's shortcoming of slow convergence rate, but like the Newton-Raphson method, it can easily diverge if the first two guesses are not properly chosen. For instance, in Fig. 4.3c, if the second guess is chosen at the point P_1', the extension of line P_0P_1' will cross the *X* axis at the point P_2'. This results in the vertical line form P_2' never intersecting the curve f(x) again. Fortunately, because of two fundamental physical facts, this will never happen in our particular case so long as we design an appropriate algorithm and procedure with care. The first fact is that, at every time step, the calculation of both circuit equation (4.1) and field equation (4.2) can be regarded as that of a D.C. circuit and nonlinear steady state finite element analysis with a D.C. input current. All the variables in the equations (4.5) and (3.7) become time independent.

Both equation (4.5) and (3.7) only vary with the current and not time. Therefore, the 1-Dimensional search problem is focused on finding a suitable current I_n^* as solution, to satisfy the external impressed instantaneous voltage U_n^*. If we know the relationship between $U_n(I_n)$ and I_n in analysis form or if there is a U_n-I_n curve available, it will be easy to find the solution. The second fact is that the U_n-I_n curve is fixed at the *nth* time step. If a coil is wound on a ferromagnetic core and fed by a direct current and if I_n is increased gradually, a curve $\Psi = \Psi(I)$ in Ψ-I plane will have a shape similar to that of the B-H curve describing its ferromagnetic characteristics. This is the second physical fact which helps to understand why the modified secant method will not fail to converge in the program code COUPV.

For the same reason, we can conclude that if we change I_n, the equation (3.7) and (3.37) in conjunction with the program CENV will produce a *curve (1)*:

$$U_L(I_n) = (\Psi_n - \Psi^*_{n-1})/\delta t$$

versus I_n in a U-I plan as shown in Fig. 4.4a. Likewise, we can have a *curve (2)*:

$$U_R = R \cdot I_n.$$

Thus, at the *nth* time step, the equation (4.1) in its discrete form is,

$$U(I_n) = U_R + U_L = R \cdot I_n + (\Psi_n - \Psi^*_{n-1})/\delta t \qquad \cdots\cdots(4.9)$$

drawn as a *curve (3)* in the U-I plane. Without doubt, the *curve (3)* is a monotonous function with the shape of a B-H curve. The objective is to find the current solution I_n^* to satisfy $U_n^* = U(I_n^*)$. It should be noted

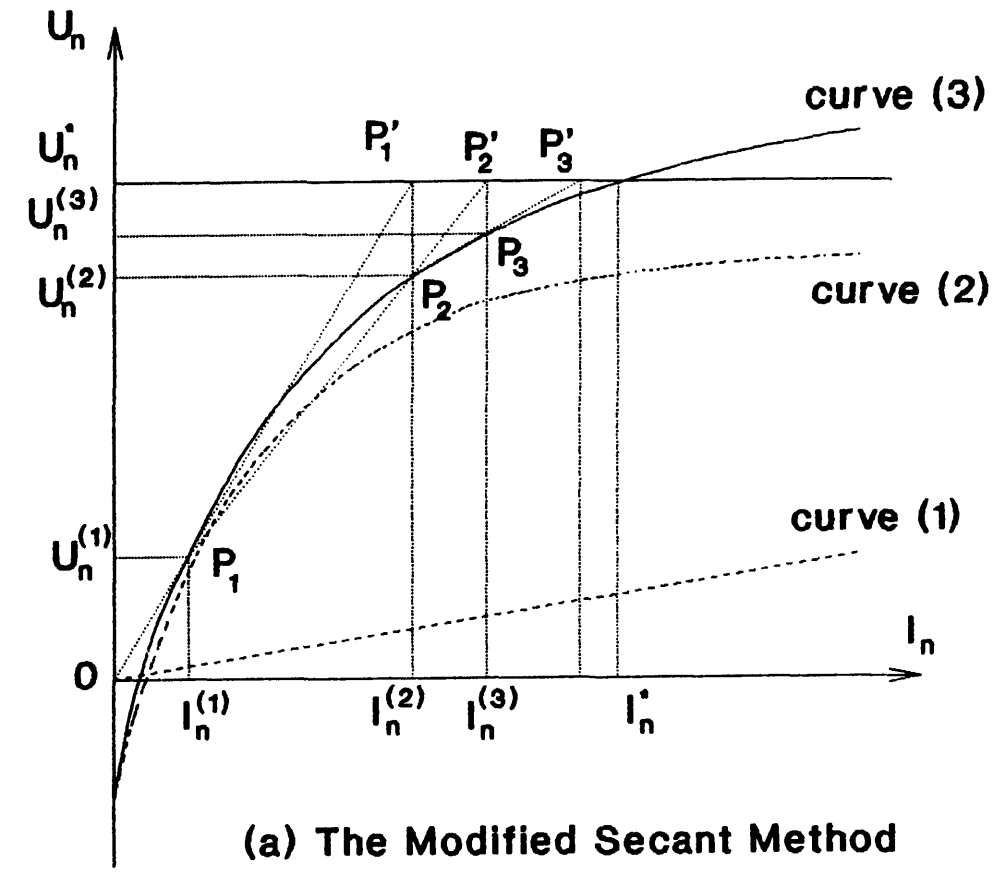

(a) The Modified Secant Method

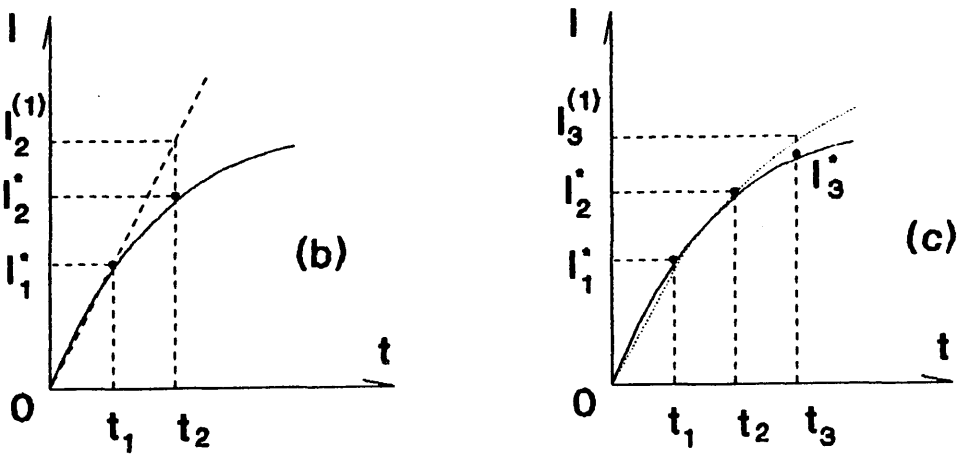

(b) & (c) The Parabolic Curve Fitting Technique

Fig. 4.4 Hybrid Method to Find Current Solution

that only half the curve is shown in Fig. 4.4a. There is another half in the third quadrant for negative values of I_n. Hence, theoretically, I_n can vary from $-\infty$ to $+\infty$.

Now, let's consider the one dimensional search in more detail. Actually, the first guess $I_n^{(1)}$ is not picked at random. This method of choice will be introduced in the next section. Starting from $I_n^{(1)}$ and calculating (4.4), (3.7), (3.37) and (4.9), we can get $U_n^{(1)}$ at the point P_1 with its coordinate $(I_n^{(1)}, U_n^{(1)})$, *(step 1)*. Then the second value $I_n^{(2)}$ is determined in terms of $I_n^{(1)}$ as,

$$I_n^{(2)} = I_n^{(1)} \cdot \frac{U_n^*}{U_n^{(1)}} \qquad \textit{(step 2)}$$

In geometrical terms, we extend the line OP_1 to intersect the line $U(I_n) = U_n^*$ at P_1'. Then a vertical line from P_1' to the I_n axis will give $I_n^{(2)}$. And then, we use $I_n^{(2)}$ to calculate (4.4), (3.7), (3.37) and (4.9) again to find $U_n^{(2)}$, *(step 3)*. This produces a new point P_2 with its coordinate $(I_n^{(2)}, U_n^{(2)})$. In Fig. 4.4a, it the point of intersection of the *curve (3)* and a vertical line from P_1'. However, because the *curve (3)* is non-existent curve, we must follow *step 3*.

Based on $I_n^{(1)}$, $U_n^{(1)}$ and $I_n^{(2)}$, $U_n^{(2)}$, $I_n^{(3)}$ can be determined by following expression,

$$I_n^{(3)} = I_n^{(1)} + (I_n^{(2)} - I_n^{(1)}) \cdot \frac{U_n^* - U_n^{(1)}}{U_n^{(2)} - U_n^{(1)}}, \qquad \textit{(step 4)}.$$

Its geometric significance can be explained as follows. Connecting the points P_1 to P_2 and extending the line P_1P_2 to intersect the line $U(I_n) = U_n^*$, P_2' will be fixed. Drawing a vertical line from P_2', we can

locate the point of intersection which becomes the next input current $I_n^{(3)}$. Following this process the expression to find $I_n^{(k)}$ at the *kth* guessing step can be written as,

$$I_n^{(k)} = I_n^{(k-2)} + [I_n^{(k-1)} - I_n^{(k-2)}] \cdot \frac{U_n^* - U_n^{(k-2)}}{U_n^{(k-1)} - U_n^{(k-2)}} \qquad \cdots\cdots\cdots(4.10)$$

In the computer program, we stop the computation when the error ε satisfies,

$$\varepsilon \leq \left| \frac{U_n^* - U_n^k}{U_n^*} \right| = 0.3\%$$

If $U_n^* = 0$, the criteria will be $\varepsilon \leq |U_n^* - U_n^k| = 0.1$ (v).

Evidently, this procedure ensures that every secant and line $U_n(I_n) = U_n^*$ will cross at points P_1', P_2', P_3', *etc* and every vertical line these points will intersect the *curve (3).* Therefore, divergence will not be experienced in this algorithm and its convergence rate is nearly equal to that of the Newton-Raphson method.

4.4.2 Prediction of an Initial Current at Each Time Step by the Parabolic Curve Fitting Technique

The curve fitting technique introduced here stems from the polynomial interpolation method, which approximates a real valued function $f(x)$ from values that are only known at some discrete points. If we choose Lagrange-polynomials $L_i(x)$ to express $f(x)$, then $f_n(x)$ with n known points can be written as

$$f_n(x) = \sum_{i=1}^{n} y_i \cdot \prod_{\substack{j=1 \\ j \neq i}}^{n} \frac{x - x_j}{x_i - x_j}$$

in which, $y_i = f_n(x_i)$ is the *ith* known function value. If we assume that $f(x)$ is a second order polynomial and has three known points x_1, x_2 and x_3, then this special case to determine the curve is called the parabolic curve fitting technique given by,

$$f(x) = y_1 \cdot \frac{(x - x_2)(x - x_3)}{(x_1 - x_2)(x_1 - x_3)} + y_2 \cdot \frac{(x - x_1)(x - x_3)}{(x_2 - x_1)(x_2 - x_3)} + y_3 \cdot \frac{(x - x_2)(x - x_1)}{(x_3 - x_2)(x_3 - x_1)} \qquad \cdots\cdots(4.11)$$

Therefore, if one is interested in the function value $y_4 = f(x_4)$ at the point x_4, it is easy to obtain it from (4.11). Within the program COUPV, during the first time step, an initial guess $I_1^{(1)}$ should be carefully chosen according to the formula (4.8) before using the modified secant method.

During second time step, the initial current $I_2^{(1)}$ predicted is as shown in Fig. 4.4b and is given by,

$$I_2^{(1)} = I_1^* \cdot \frac{t2}{t_1} \qquad \cdots\cdots(4.12)$$

During the third time step, we already have 3 previous known time instants 0, t_1, t_2 and the corresponding current values 0, I_1^* and I_2^* so that the initial current $I_3^{(1)}$ for the third time step is

$$I_3^{(1)} = \frac{t_3 \cdot (t_3 - t_2)}{t_1 \cdot (t_1 - t_2)} \cdot I_1^* + \frac{t_3 \cdot (t_3 - t_1)}{t_2 \cdot (t_2 - t_1)} \cdot I_2^* \qquad \cdots\cdots(4.13a)$$

which is shown in Fig. 4.4c. For all subsequent time instants every initial guess $I_n^{(1)}$ for the *nth* time step is determined by the parabolic curve fitting technique. Three previous solutions of $I_{(n-3)}^*$, $I_{(n-2)}^*$ and $I_{(n-1)}^*$ are employed by the parabolic curve fitting to predict the starting value $I_n^{(1)}$ for the *nth* step as

$$I_{(n)}^{(1)} = \frac{(t_n - t_{n-2}) \cdot (t_n - t_{n-1})}{(t_{n-3} - t_{n-2}) \cdot (t_{n-3} - t_{n-1})} \cdot I_{(n-3)}^*$$

$$+ \frac{(t_n - t_{n-3}) \cdot (t_n - t_{n-1})}{(t_{n-2} - t_{n-3}) \cdot (t_{n-2} - t_{n-1})} \cdot I_{(n-2)}^*$$

$$+ \frac{(t_n - t_{n-2}) \cdot (t_n - t_{n-3})}{(t_{n-1} - t_{n-2}) \cdot (t_{n-1} - t_{n-3})} \cdot I_{(n-1)}^* \qquad \cdots\cdots(4.13b)$$

If δt is a constant, the formula (4.13b) becomes very simple:

$$I_{(n)}^{(1)} = I_{(n-3)}^* - 3 \cdot I_{(n-2)}^* + 3 \cdot I_{(n-1)}^* \quad .$$

In the computer program COUPV, this hybrid method ensures that the search for I_n^* will end within 3 to 4 iterations.

4.5 Coupling with Mechanical Load

4.5.1 Velocity Considerations

The effects of velocity on moving parts are well known and are encountered in many practical eddy current applications. Most of earlier studies ignored these effects either because the motional *emf* is relatively low or the models are simple. However, there are a number of important applications, in which full account of velocity must be taken such as electromagnetic launchers[34], electromagnetic brakes[35] or the starting of electric machines[36]. To treat such problems, we can introduce the term $\mathbf{J}_v = \sigma \cdot (\mathbf{V} \times \mathbf{B})$ in the electromagnetic field equations as in equation (3.1) to represent the motional *emf* due to movement. The resulting asymmetric stiffness matrix and the associated storage technique are discussed in the previous chapter. Recent developments in this aspect are significant. Davat[37] gave a theoretical description of the problems of tackling the moving interface. Rodger[38] presented a new formulation for 3D problems in which the moving part moves at a constant speed.

Unlike conventional electric machines, TLIA has a special structure with three airgaps around the plunger's wall shown in Fig. 4.5. When the plunger moves, the airgap beside the end of the plunger changes length. This makes it necessary to change the material properties of the elements at both sides of the interface at the same time. In view of this special structure, a quite simple method can be introduced which treats the mesh distortion at every time step.

4.5.2 Mesh Distortion and Modification

During the dynamic simulation of the TLIA the finite element meshes have to be modified at every time step. When the solution pair $\{\acute{A}_n\}$, I_n satisfying both (4.1) and (4.2) is available, the total electromagnetic force F_z is computed and the equation (4.3) is solved to determine the new plunger position. This movement gives a new mesh topology in the local area. A simpler method is used which imposes certain restrictions in the pre-processing of the model. The meshes in the plunger area are made of right angled triangles which are numbered in a certain sequence as shown in Fig. 4.5. The lengths of each element along the Z and *r* directions are α and γ respectively. The shaded area of Fig. 4.5 represents the plunger and the line OO' is the air/conductor interface which needs to be moved by the displacement predicted by the equation (4.3) or (4.7) at each time step. The mesh re-organisation is achieved by one of the following two steps.

If the displacement is such that

$$(k\text{-}1)\cdot\alpha \leq Z < 0.5\cdot k\cdot\alpha$$

where (k = 1, 2, 3, ···) then the new interface OO' is created by moving PP'. This is achieved by enlarging the elements *1* to *4* and compressing the elements *5* to *8* as in Fig. 4.5b. If the displacement is such that $0.5\cdot k\cdot\alpha \leq Z < k\cdot\alpha$, where k = 1, 2, 3, etc, the new interface is created by,

(*a*) restoring the elements *1* to *4* to their original shape,

(*b*) compressing the elements *5* to *8* and enlarging the elements *9* to *12*, and

(*c*) changing the material properties of the elements *5* to *8* to those of air.

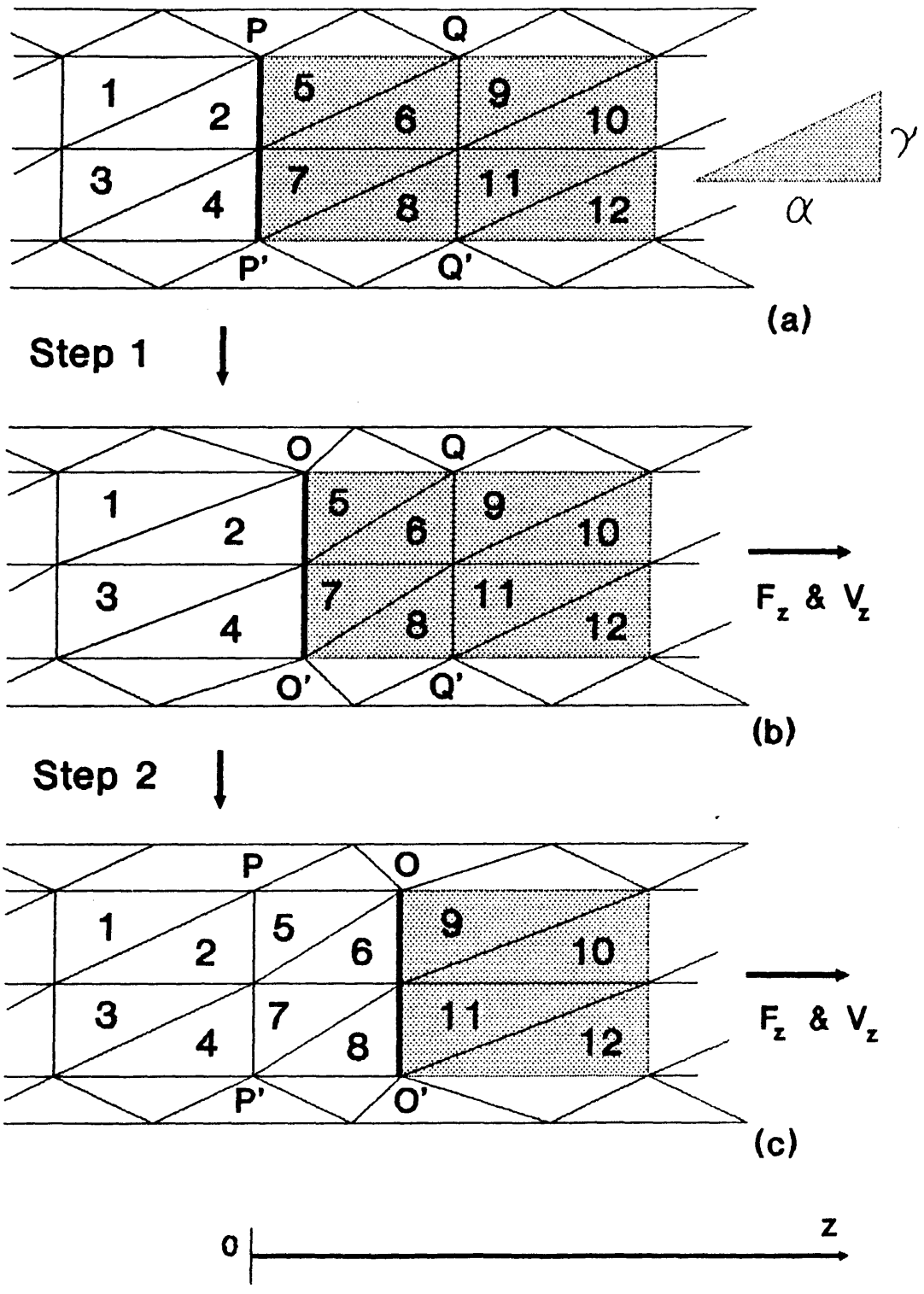

Fig. 4.5 Mesh Changing Technique

In fast-acting actuators or electromagnetic launchers, if the time interval is not chosen properly, the accuracy of results may be poor. The Peclet number[39] is usually adopted as a criterion to prevent numerical oscillations during the computation involving moving parts. In general, the Peclet number should be less than 1.0, *i.e.*

$$p = \frac{\sigma \cdot \mu \cdot \alpha \cdot V}{0.2} \leq 1.0 \qquad \cdots\cdots(4.14)$$

The properties of the copper plunger in TLIA are

$$\sigma = 0.57 \times 10^{8}\ (\Omega \cdot m)^{-1}, \qquad \mu = 4\pi \times 10^{-7}(H/m) \qquad \text{and } \alpha = 0.004\ (m)$$

Therefore, the limitation can be determined by (4.14) with the following result,

$$V \leq \frac{2.0}{\sigma \cdot \mu \cdot \alpha} = 6.78\ (m/s)$$

Instead of considering to the transient speed, the displacement increment in a time interval is selected as the criterion. If δt is equal to 0.001(s), the displacement increment must obey $\delta z = \delta t \cdot V = 0.001 \times 6.78 \approx 0.0068$ (m). In order to ensure the accuracy, we choose $\delta z \leq 0.5 \cdot \alpha$. If the displacement increment δz_n at the *nth* time step is larger than $0.5 \cdot \alpha$, the computer program will change the time interval automatically by the formula,

$$\delta t_{new} = \alpha_t \cdot \frac{0.5 \cdot \alpha}{\delta z_n} \cdot \delta t_{old} \qquad \cdots\cdots(4.15)$$

in which α_t is chosen from 0.4 to 0.6. The flow chart concerning this aspect is shown in Fig. 4.6.

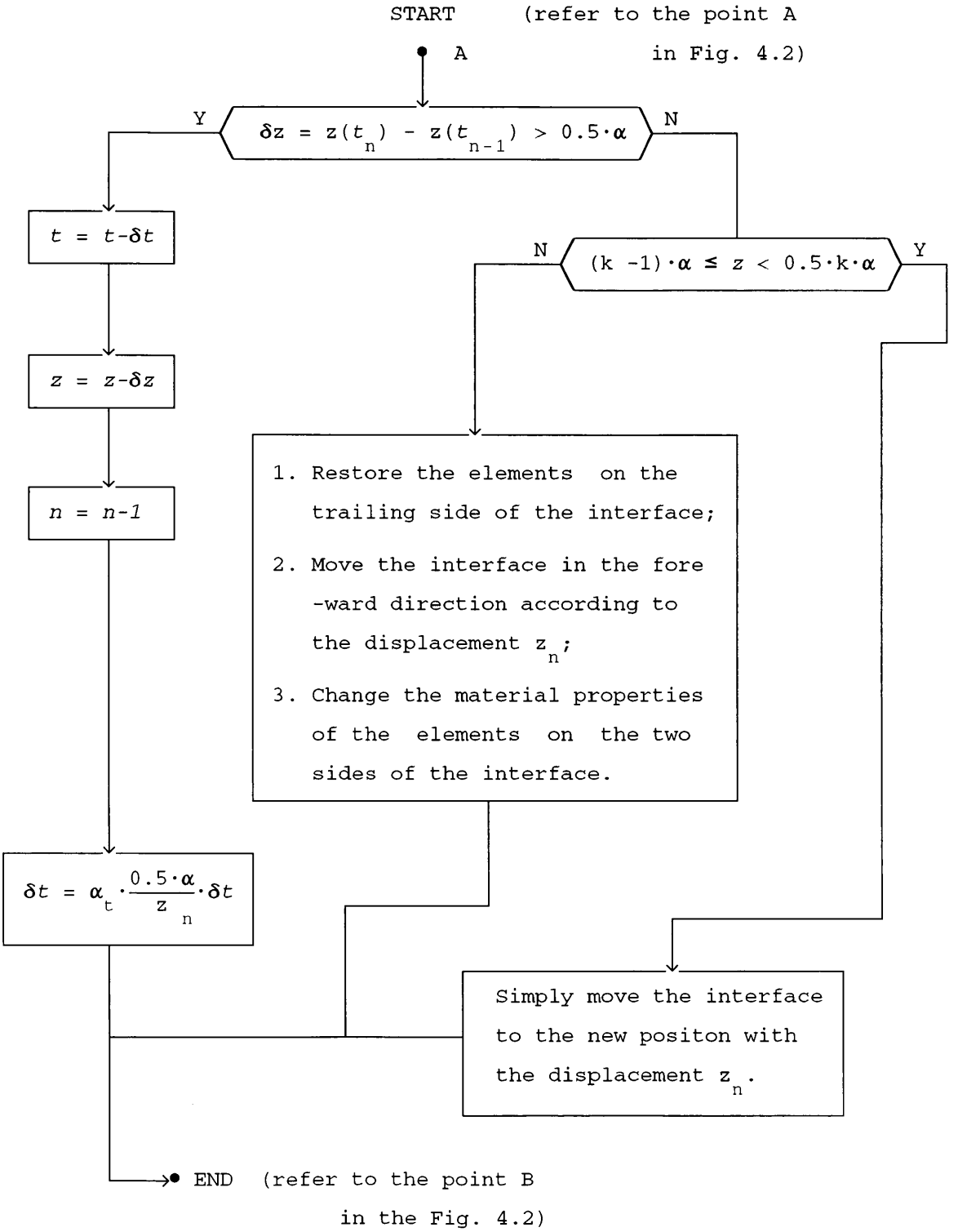

Fig. 4.6 The Method of Changing the Meshes

4.6 Conclusion

This chapter has addressed two difficult aspects of solving the coupled problem by numerical methods. One is that, at every time step, a suitable current I_n^* must be found to satisfy both the external electric circuit equation and the partial differential field equation. The modified secant method created ensures its convergence in this special application. Combined with the parabolic curve fitting technique it only needs 3 to 4 iterations to reach the solution and reduces computation time significantly. The other is the movement of the movable member requiring modification of the distorted meshes. A simple method ensuring a minimum mesh distortion has been developed for this special TLIA which has three airgaps. This method is based on a special numbering sequence of the elements within the moving area. When the finite element model contains a moving part, its velocity and mesh size will affect the convergence of the algorithm. Therefore, the Peclet number is estimated during the computation to prevent the oscillation.

The computer program developed provides much useful insight on the transient behaviour of the actuator. Predicted results indicated in the next chapter are in good agreement with experimental results.

CHAPTER 5 DYNAMIC SIMULATION AND EXPERIMENTATION OF A SOLID STEEL STATOR MODEL

5.1 Introduction

The only way of establishing confidence in the methods described in the last two chapters and the developed computer program COUPV is to check their validity by experimentation. Additionally, the experimental study in parallel with computer simulation gives deeper understanding of the actuator's dynamic behaviour. The initial verifications are made on a simple configuration of a TLIA with a solid steel stator which requires no special assumptions. In the experiment, this actuator is energized by sinusoidal and square wave voltages. Excited by these two power supplies, the TLIA is experimented with different loads in the dynamic and locked states. These experiments provide insight into the dynamic characteristics including the input current, output force, transient speed, displacement, *etc.* All the simulated results are in good agreement with the experiment.

Besides all the external dynamic characteristics of the TLIA, the program COUPV also provides details about internal flux, eddy current and power loss distributions. As previously explained in Chapter 2, although the TLIA is quite simple in structure, its electromagnetic field distribution is quite complex. The reason for this is that its main magnetic flux path is distorted by the conducting plunger. It acts like a magnetic shield to obstruct flux from passing through the airgap into the mandrel directly. It has been explained Chapter 2 that according to the Faraday's law of electromagnetic induction,the induced eddy currents in the plunger will push the flux backwards to the stator winding. It is this phenomenon that

makes it extremely difficult to determine the parameters required for dynamic simulation as in the dynamic analysis of conventional electric machines. In addition to some fundamental dynamic specifications such as time response, acceleration and transient velocity, the time-stepping finite element analysis can reveal some very important properties of the TLIA, such as ripple force, magnetic saturation due to non-sinusoidal current waveforms, *etc.* It can also deal with the two-stage model with sequenced switching strategy. In the following sections, the results predicted by COUPV are presented.

In addition to this brief introduction there are six sections in this chapter. First, the machine and the experimental setup are introduced in sections 5.2 and 5.3. Then in section 5.4 the simulated and experimental results for the locked state TLIA are presented and discussed. The simulation and experiment are focused on the dynamic state with different mechanical loads in section 5.5. A two-stage model is simulated in section 5.6 and the conclusions are given in section 5.7. Finally, it should be mentioned and explained here that this solid steel stator actuator was used only for verifying the computer program.

5.2 Experimental Models

In order to limit the uncertainty factors, a TLIA with solid steel stator was manufactured as shown in Fig. 5.1 and Fig. 5.2a. Certainly, there will be considerable eddy currents induced in the stator but it has the merit of being a real axisymmetric device. The reasons of using this structure can be listed as follows,

1. There is no need to modify the algorithm for estimating the non-axisymmetric effects of the stator such as the modification introduced in section 3.4.2.
2. There exists another solid steel stator with the same dimensions but having radial narrow slits to reduce the eddy currents. This model will not only supply information on the eddy current effects in an axisymmetric electromagnetic device but also provides a means to test the effectiveness of the slits.

As shown in Fig. 5.1, this model consists of four main parts: a steel stator, a copper plunger, a hollow steel mandrel and two stator windings. Its material characteristics are listed in table 5.1.

	σ (20°C)	ν
stator	0.33×10^{7}	B-H curve (Appendix II)
plunger	5.714×10^{8}	0.8×10^{-8}
mandrel	0.33×10^{7}	B-H curve (Appendix II)

Table 5.1 The Properties of the Materials

The stator consists of two stages, the original purpose being to extend its stroke. In this chapter, it is primarily used to find out if the computer

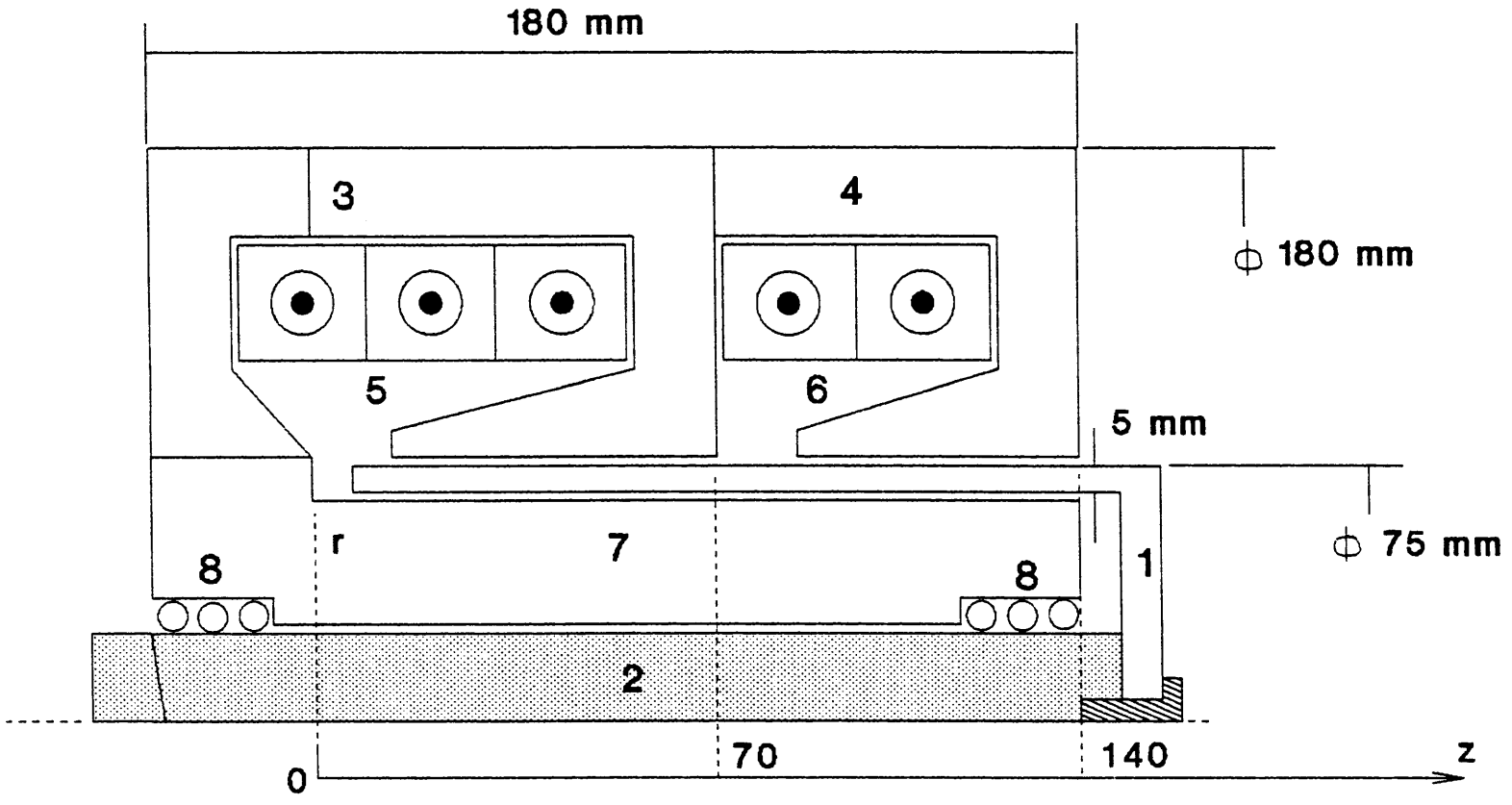

1. Copper Plunger
2. Steel Spindle
3. Steel Stator (1st stage)
4. Steel Stator (2nd stage)
5. Slot 1 with 3 Coils
6. Slot 2 with 2 Coils
7. Steel Mandrel
8. Linear Bearings

Fig. 5.1 A TLIA Model for Validation

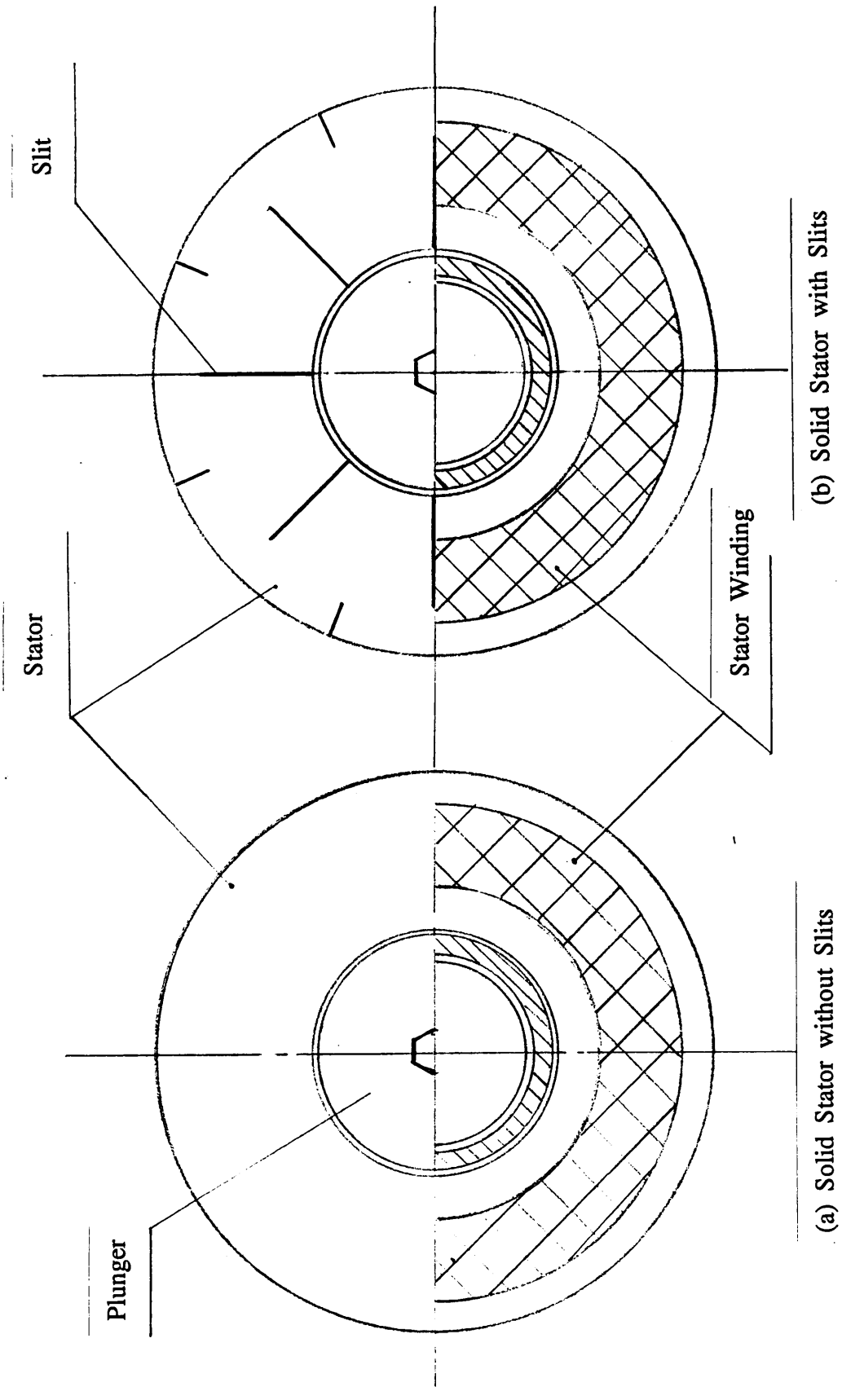

Fig. 5.2 Cross Section of the TLIA Model

program is suitable for simulating the performance of the multi-stage actuator or the θ gun. There are two samples for the first stage. One is made of solid steel which was constructed particularly for the verification of the computer program COUPV. The other was constructed but with narrow slits as shown in Fig. 5.2b. In the next chapter, the comparison between these two samples will indicate the effectiveness of the slits for suppressing eddy currents. There is only one sample for the second stage, which has slits as in the first stage.

In the first stage, the stator winding is composed of three pancake coils. One has 180 turns and other two have 160 turns each. In the second stage, there are two pancake coils with 140 and 180 turns each. Their electrical parameters are listed in Table 5.2. Their slot mouths are nearly closed, whose function has already been studied in Chapter 2 with reference to a laminated stator. However, it will be shown in the later sections that because of the skin effect, in the solid stator flux always gathers along the interior surface of the slot. It will not evenly distribute itself in the airgap between the slot tooth and mandrel even though the plunger has moved out.

Stator Coil	Turns	Wire Diameter	Resistance (20°C)
A	180	1.0 (mm)	1.62 (Ω)
B	160	1.0 (mm)	1.6 (Ω)
C	160	1.0 (mm)	1.6 (Ω)
D	180	1.0 (mm)	1.7 (Ω)
E	140	1.0 (mm)	1.3 (Ω)

Table 5.2 Specification of Stator Coils

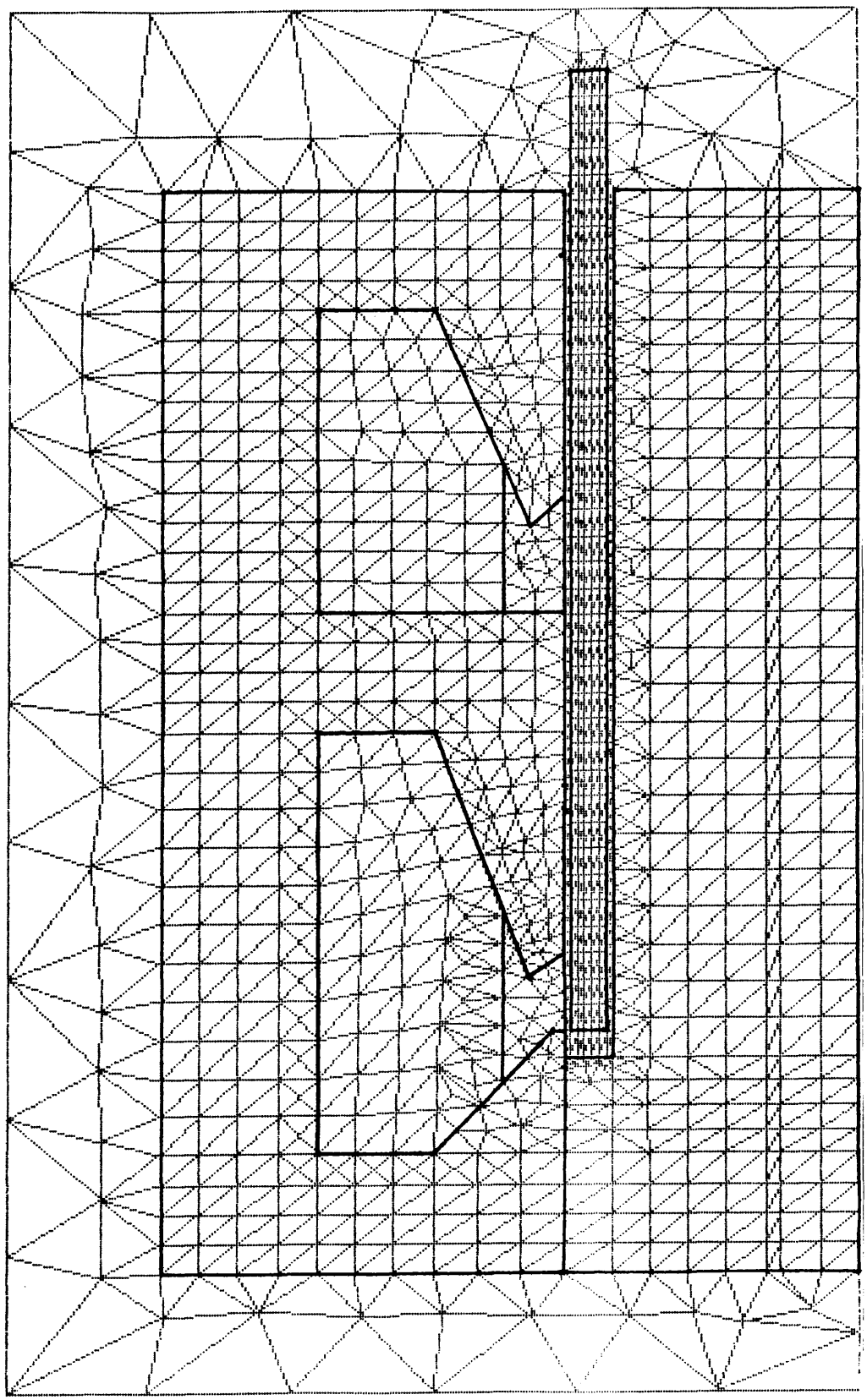

Fig. 5.3 Mesh Arrangement

Mesh generation is the first step in the finite element analysis. One elementary rule for mesh generation is that more nodes or elements should be arranged where the field variation is high. In the solid steel stator and mandrel magnetic flux and eddy currents will gather at the inner surface of the stator and the outer surface of the mandrel due to the skin effects. In order to ensure the accuracy, the skin depth of these two parts are firstly estimated by

$$\Delta = \left(\frac{2}{\mu_r \cdot \mu_0 \cdot \sigma \cdot \omega} \right)^{1/2}$$

If μ_r = 100 is chosen, there is $\Delta|_{100}$= 4 (mm). If μ_r = 1000 is chosen, there is $\Delta|_{1000}$= 1.26 (mm). Hence, in this chapter, the mesh size within the conducting areas has been chosen according to these two values. Fig. 5.3 shows the full finite element mesh. In total, there are 1171 nodes and 2278 elements in this model.

All the simulation carried out by the COUPV in this chapter are based on this solid steel stator TLIA. The various simulations and experiments described are for different combinations of coils, stages, power supplies and mechanical loads.

5.3 Experimental Investigations

In order to compare numerical results with experiment an experimental scheme shown in Fig. 5.4. was designed. The major components are:

(1) different types of electric power supplies,

(2) mechanical loads and the associated attachments,

(3) measuring instruments.

The first group can be further subdivided into 3 parts according to their functions: (*a*) the D.C. power supplies with output voltages of 12, 15, -15, 10 and -10 volts respectively; Their function is to supply stable voltages to sensors, amplifiers, relays, *etc.* (*b*) a switching point controller; When sine wave voltage is impressed, different switching-on instants will produce different transient current waves. By means of this controller, we can adjust the switch-on angle φ of the sinusoidal supply voltages. (*c*) an A.C. motor speed controller for producing adjustable square wave voltages. Its output frequency can be changed proportionally to the output voltage so as to keep the flux constant.

The second group consists of two main parts. One is a plunger stop which is necessary for the locked state experiment. A load sensor is fixed against it to measure the standstill force. The other is a pulley frame which allows the attachment of a spring or weights, so that the dynamic study can be carried out under different load conditions.

The third group includes one current sensor, two load sensors and two photo-transistor sensors. The current sensor transforms large currents at high voltage into a low voltage small signal for a digital oscilloscope.

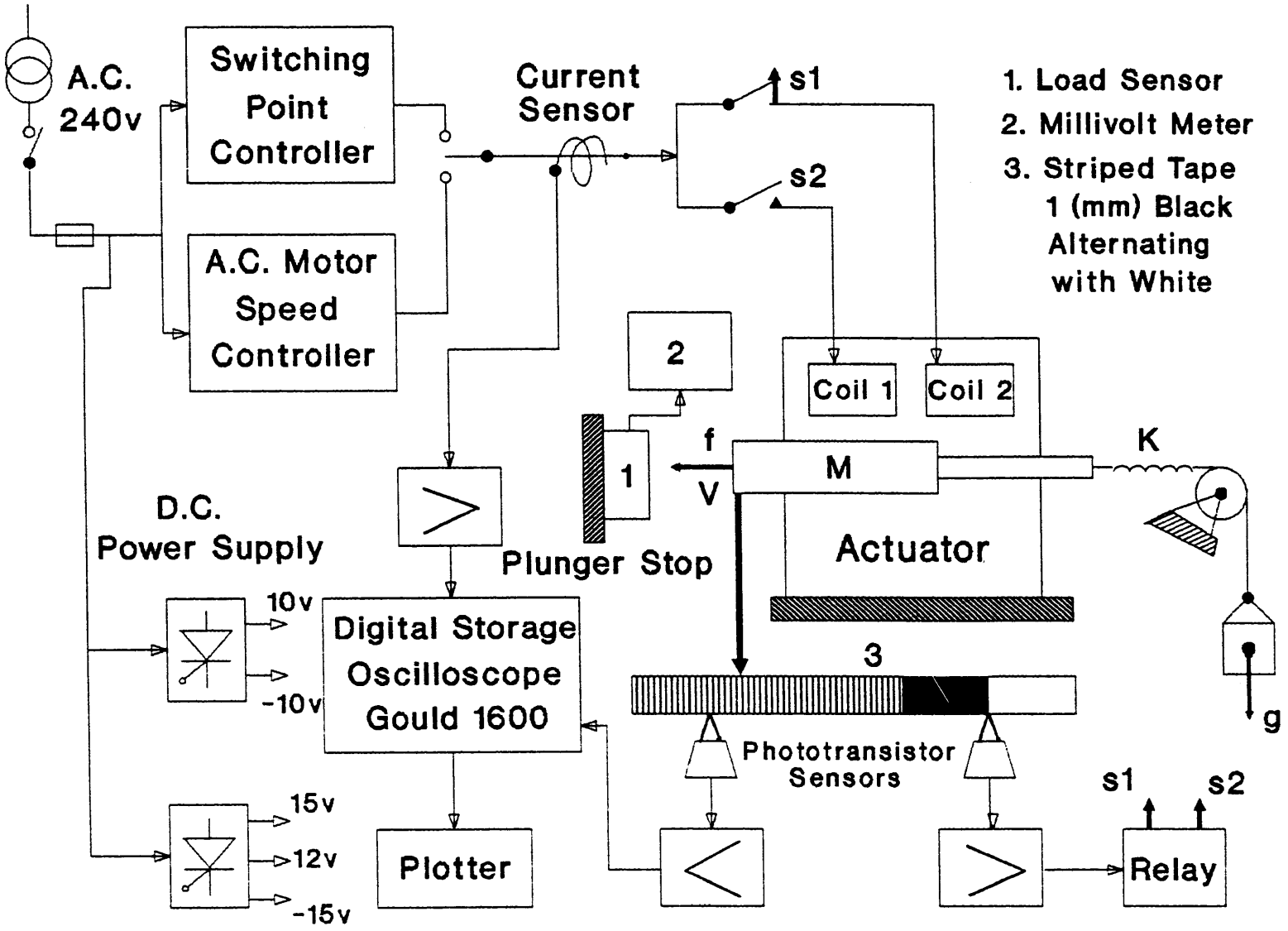

Fig. 5.4 The Experimental Scheme

This sensor has a high sensitivity and linear characteristics. Its main specifications are listed in Table 5.3.

supply voltage	±15V ±10%	frequency range	DC to 100kHz
voltage output	100mV/A	voltage withstand (1 min)	3kV at 50Hz
current range	50 A (rms)		

Table 5.3 Specifications of Current Sensor

The load sensor is fixed against the plunger stop to measure the standstill force. The position of the stop can be adjusted in order that the force, current and input power versus the plunger displacement characteristics may be obtained. The ratings of the load sensor are listed in Table 5.4.

Load Cell	A	B
rated load	2 kg	20 kg
maximum excitation	15 Vdc	15 Vdc
recommended excitation	10 Vdc	10 Vdc
output at rated load	2 mV	2 mV

Table 5.4 The Specification of the Load Sensors

The two photo-transistor sensors play different roles in the experimental setup. One is used to detect and measure the displacement of the plunger. It is composed of a Gallium Arsenide infra-red emitting diode and a silicon photo-transistor. The latter responds to the emitted radiation from the former when a reflective object is within the field of view of the photo-transistor. A striped tape of one millimeter width in black and

white is used as a reflecting object on the plunger. When the plunger moves, the photo-transistor will output a series of pulses due to the different reflective properties of the black and white striped tape. These square pulses are fed into an high speed voltage comparator and then sent to a digital storage oscilloscope. The time duration of one pulse corresponds to the time of displacement of two millimeters. With the aid of this oscilloscope the displacement versus the time characteristics is found easily. The approximate instantaneous velocity of the plunger can be obtained by dividing the two millimeters by the time duration of the corresponding pulse.

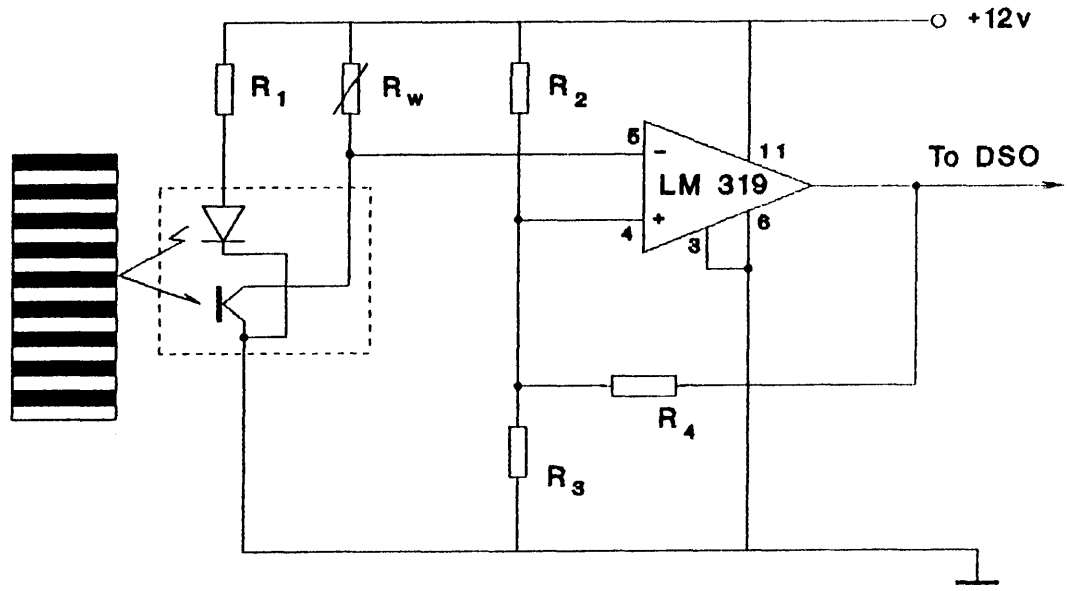

Fig. 5.5 The Photo-transistor Switch Circuit

Another photo-transistor switch with the same working principle is used to control the two-stage actuator. When the plunger has passed the effective length of the first stage, a relay will switch off the power supply to the first stage and at the same time switch on the power for the second stage. The circuit is shown in Fig. 5.5.

5.4 Locked State Simulation & Experimental Verification

The 'locked state' introduced in this section means that the plunger of the TLIA is always stopped by an obstacle and can not move. The experiment in the locked state can be carried out in two phases for two aspects of the verification. When the power supply is suddenly switched on, the TLIA experiences a transient. A digital storage oscilloscope will record this through the signal form the current sensor. In this case, we can compare the transient current waveform recorded by the digital storage oscilloscope with that obtained from the simulation. After the transient has died, the TLIA is in steady state. Its current, power losses and forces can be measured by a traditional method with meters and the load sensors.

If it is assumed that the stator and mandrel are made of laminations, the resulting current waveform due to the sudden switching-on can be expected to be similar to the well known in-rush current of a transformer. When the plunger is blocked, the actuator can be likened to a transformer with its secondary winding short circuited. The only difference between them is that the copper plunger of the TLIA takes on the role of the secondary winding in the transformer. Therefore, the transient response for both can be obtained from a first order differential equation with the initial condition $i(0) = 0$. This prediction will be shown to be true in simulation and experiment.

5.4.1 Excited by Sine Wave Voltage

The following experimental and simulation results were obtained with the plunger blocked at the displacement D = 0 and with supply voltage of 213 volts, with switching point angle $\varphi = 0^{\circ}$. This voltage is impressed on the winding with three coils in series with a total of 500 turns in the first solid steel stage. The winding of the second stage is left on open circuit. The purpose of this experiment is to verify the COUPV dealing with the dynamic coupled problem.

Fig. 5.6 shows the two current waves obtained from the computer simulation and experiment. The amplitude of the measured curve is denoted by a series of small square dots '■'. The corresponding experimental current waveform recorded by the digital storage oscilloscope is shown in Fig. 5.7. The shape of the current wave is similar to the well known result of the transformer suddenly short circuited. The measured result is about 5% large than the simulated one. This can be due to two main reasons. The first is that the hysteresis loss is ignored in the computer program. If the stator is made of laminations, the total iron losses including the eddy current losses will also be neglected. The second is that the copper and steel conductivities are chosen from standard data sheets,but in practice these values may differ by ±10%.

Fig. 5.8 shows the force in Z direction varying with time. In addition to the average component, the double supply frequency component dominates the output force. This is as would be expected. If all the higher order harmonics are neglected, the eddy current density J_e and the flux density B_r within the plunger can be expressed as follows,

$$J_e = J_m \cdot sin(\omega t+\varphi_1) \quad \text{and} \quad B_r = B_{rm} \cdot sin(\omega t+\varphi_2)$$

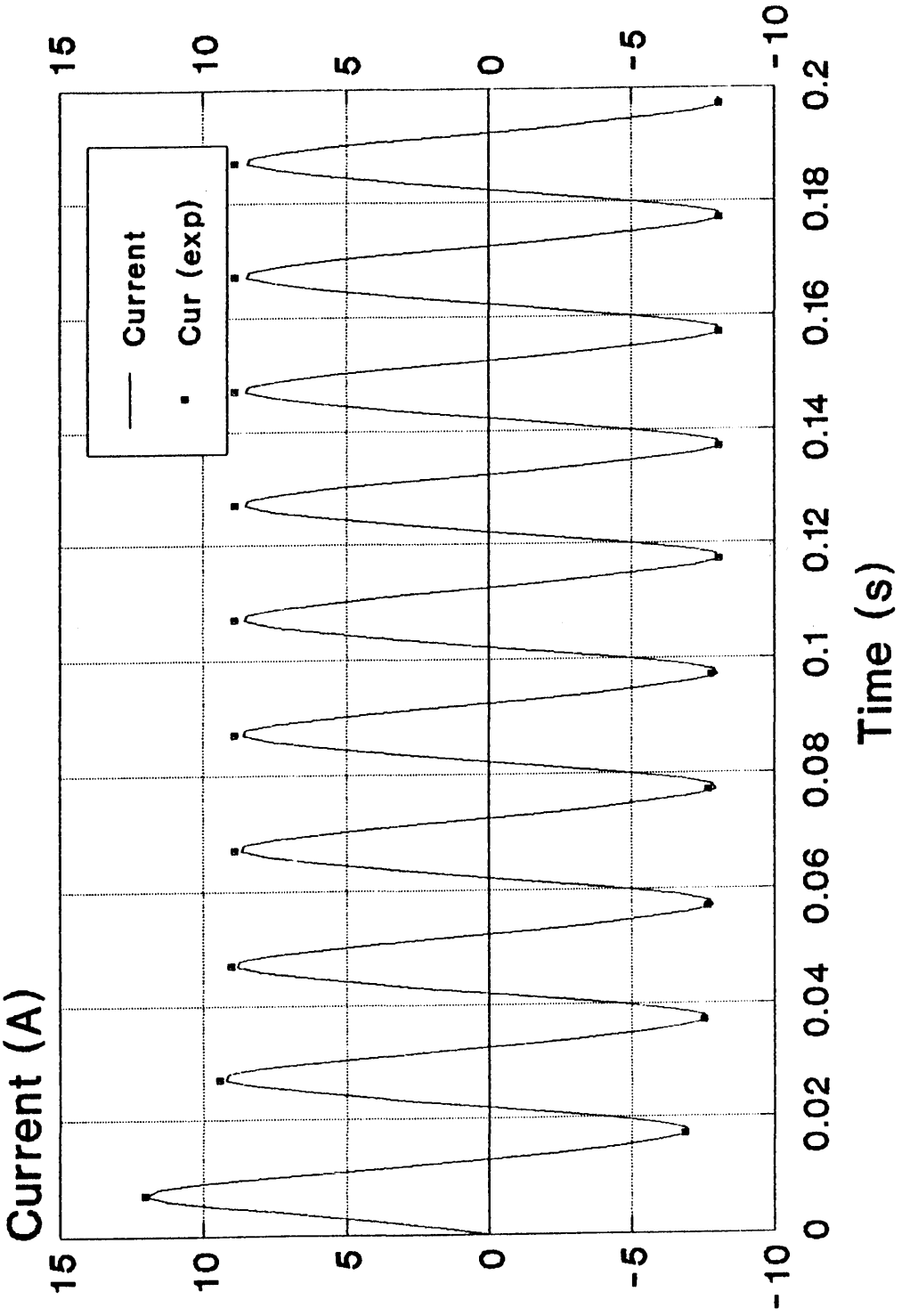

Fig. 5.6 The Locked State with a Sine Wave Supply

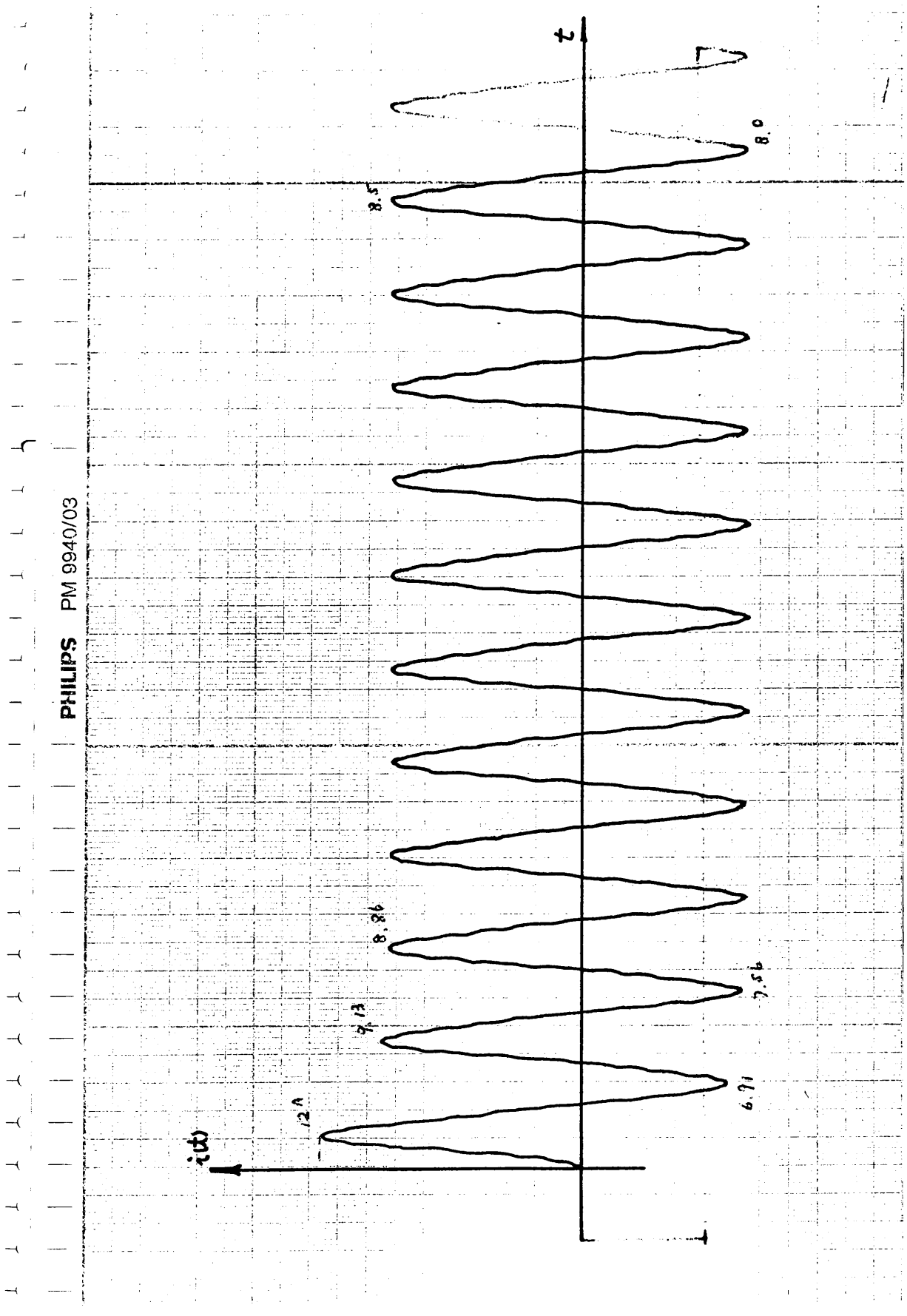

Fig. 5.7 Recorded Stator Current Waveform

Evidently, the force density in the Z direction will be

$$f_z = J \cdot B_r = J_m \cdot sin(\omega t+\varphi_1) \cdot B_{rm} \cdot sin(\omega t+\varphi_2)$$

$$= \frac{J_m \cdot B_{rm}}{2} \cdot \left[cos(\varphi_1-\varphi_2) - cos(2\omega t+\varphi_1+\varphi_2) \right]$$

where, φ_1 and φ_2 are phase angles related to the supply voltage; J_m and B_{rm} are the peak eddy current and radial flux density respectively. This expression is composed of a mean component and a double supply frequency component. The latter leads to oscillation and noise. If the load is heavy it might operate like an electromagnetic shaker.[40]

From Fig. 5.8 we can see that the output force still possesses a considerable transient component after 0.2 second. This is because the direct current component does not decay completely. In Fig. 5.6 and Fig. 5.7 both experimental and simulated results show that the magnitude of the positive current peak is slightly larger than that of the negative current peak even though the stator current appears to have reached steady state. This small unbalance leads to a considerable unstable force because the force is almost proportional to the square of the current, *i.e.* $F_z \propto I^2$.

The electromotive force always plays a very important role in the design of induction motors and transformers, since the analysis of induction devices is based on an assumption that they have a constant flux linkage. In Fig. 5.9 the *emf* variation of the stator winding shows that its magnitude is almost equal to 90% of the supply voltage. This is a significant empirical data for the design, and is well known in the design of transformers. The eddy current induced in the plunger is also shown in Fig. 5.9.

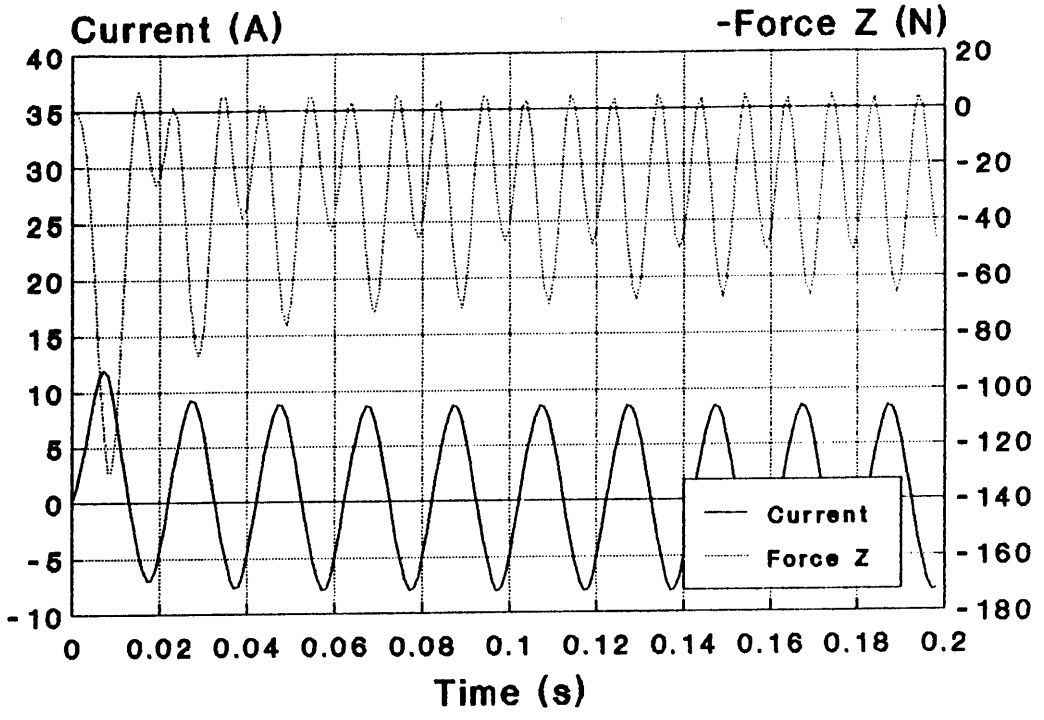

Fig. 5.8 Transient Stator Current and Axial Force

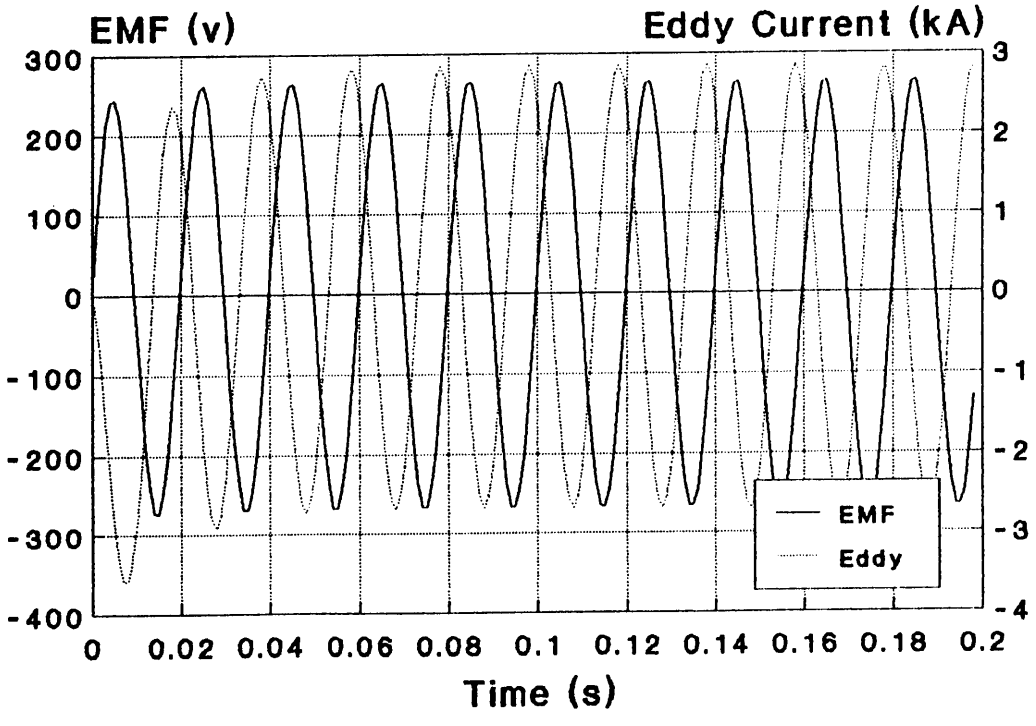

Fig. 5.9 EMF and Eddy Current Waveform

The COUPV can also provide information about the radial force as shown in Fig. 5.10. In the TLIA, this force will have no significant effect on the plunger. However, in other applications, such as the θ gun, this force may be large enough to deform the projectile. Therefore, the calculation of this force is also useful for determining the upper limits of the input current or to estimate the stresses on the projectile.

In each time step, the COUPV locates the highest flux density and writes it into an output file. It has been plotted as shown in Fig. 5.10. This helps the design engineers to check and modify their designs. The eddy current losses in every conducting area are shown in Fig. 5.11. The eddy current loss in the solid steel stator is quite large and is almost as much as that in the plunger. Of course, this loss will be reduced significantly if a laminated stator is used. A very interesting phenomenon is that compared with those in the stator and the plunger, the eddy current loss in the mandrel is quite small. This can be explained by the shielding effect of the hollow copper plunger. A detail discussion of this will be conducted in the next section.

During dynamic simulation, the COUPV can demonstrate the field distribution at each time step. Fig. 5.12 shows 18 graphs in one time cycle from the instant 182 (ms) to 199 (ms), at 1 or 2 (ms) interval each, while the TLIA is operating near the steady state and its plunger is blocked at the displacement of D = 0.008 (m). These field plots show some interesting phenomena which appear only when eddy currents are involved.

Firstly, most of the flux lines accumulate along the interior surface of the solid steel stator due to the skin effect. This can be explained

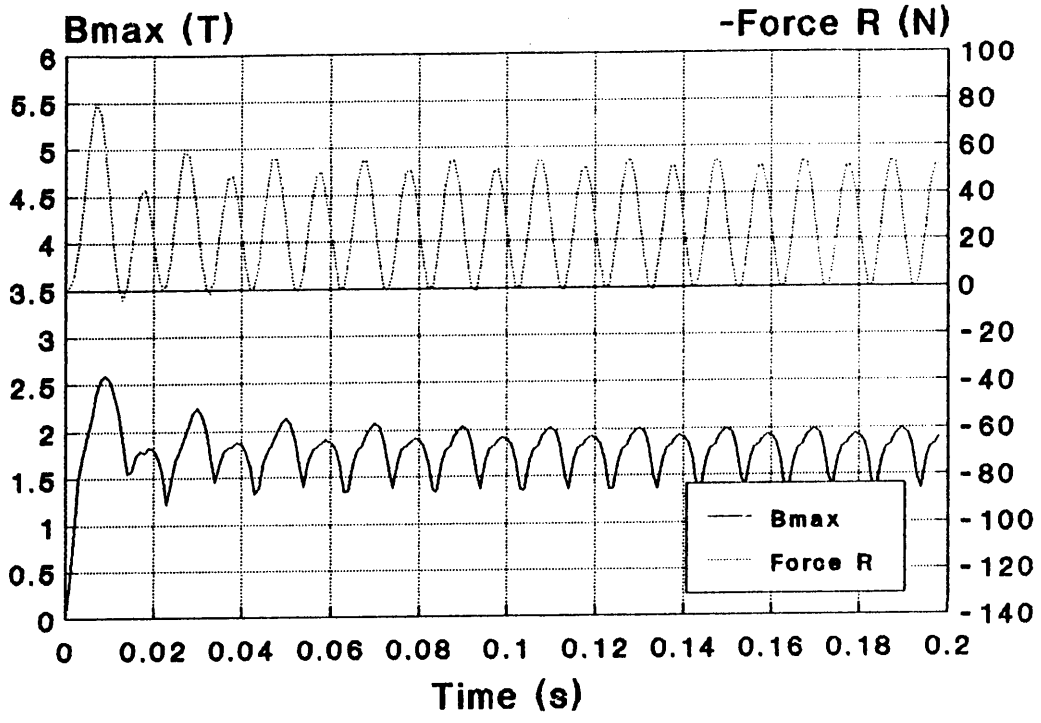

Fig. 5.10 Maximum Flux Density and Radial Force

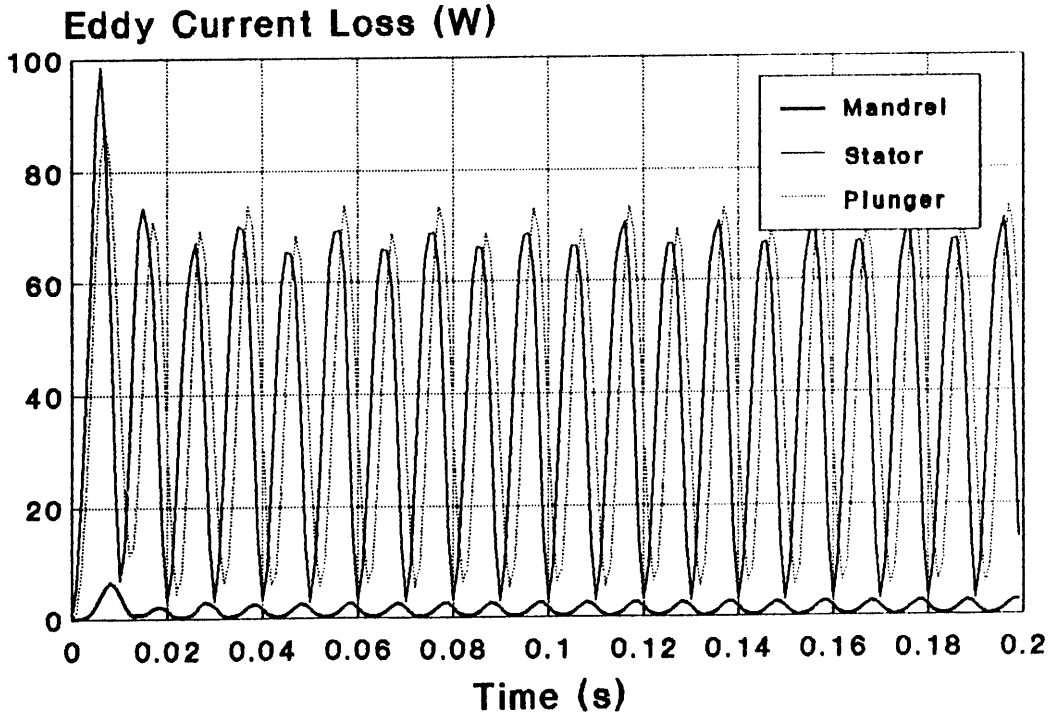

Fig. 5.11 Eddy Current Losses in Each Conducting Area

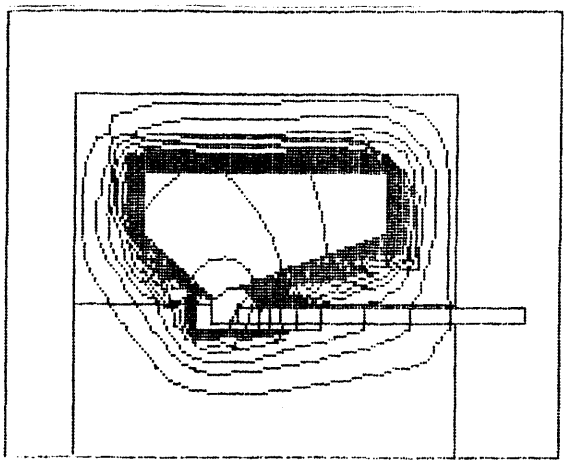

t = 182 (ms)

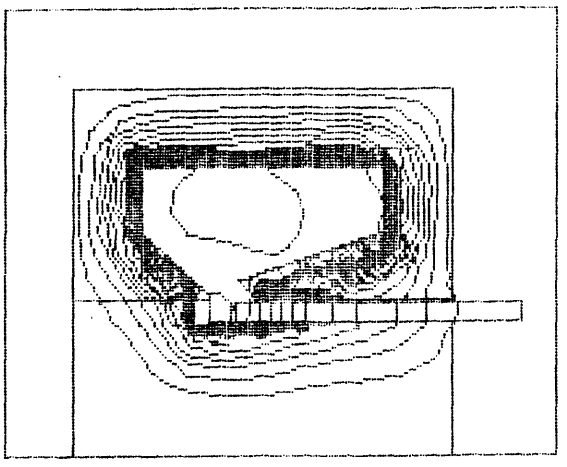

t = 183 (ms)

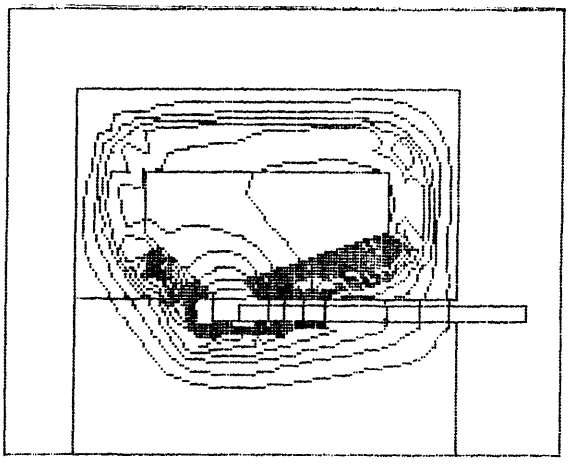

t = 184 (ms)

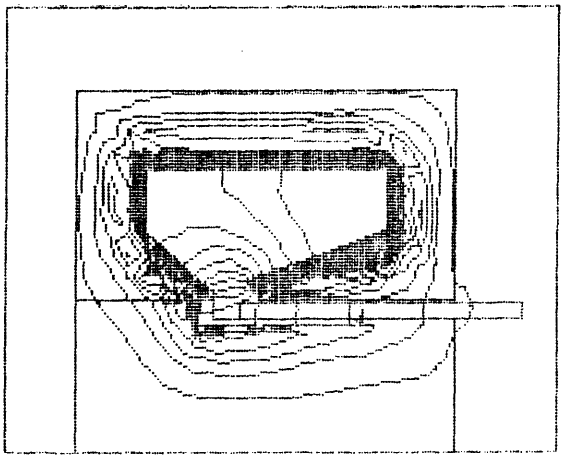

t = 185 (ms)

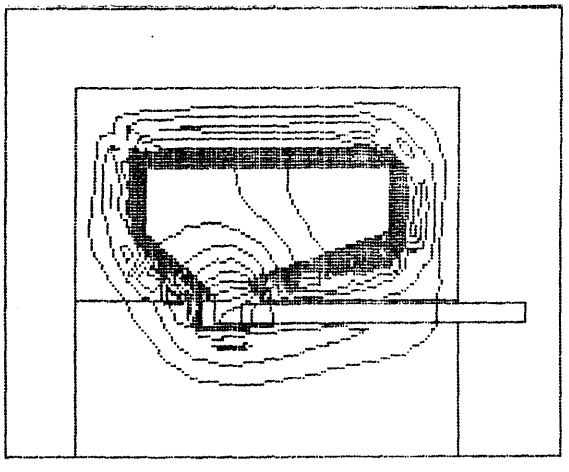

t = 186 (ms)

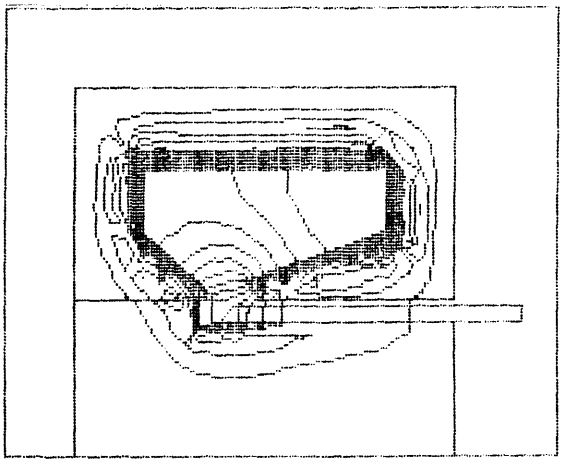

t = 187 (ms)

Fig. 5.12-1 Flux Density Distribution of a Solid Steel Stator TLIA

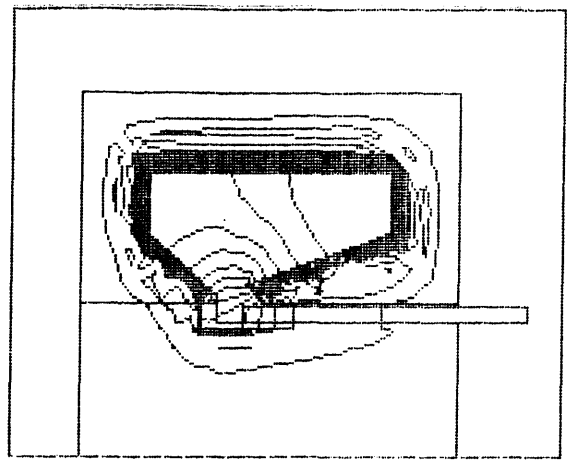

t = 188 (ms)

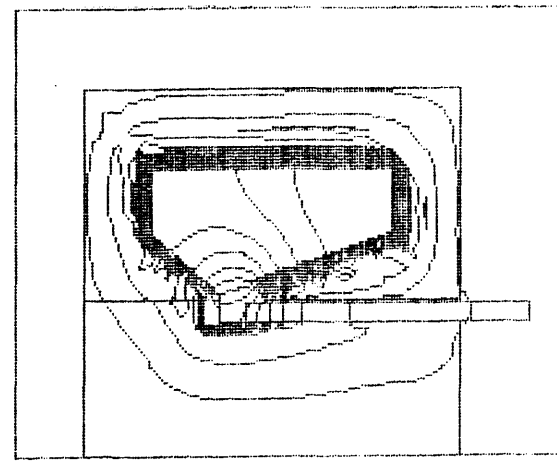

t = 189 (ms)

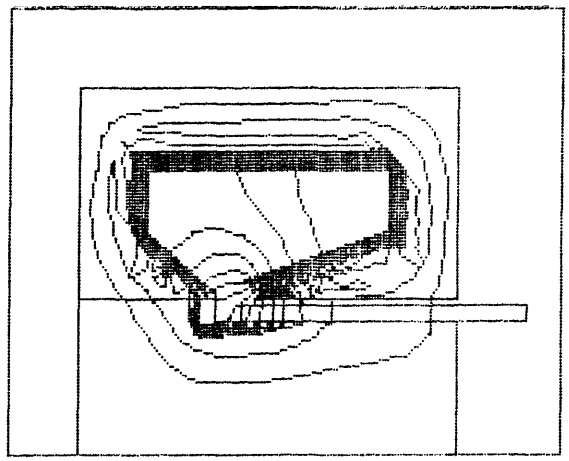

t = 190 (ms)

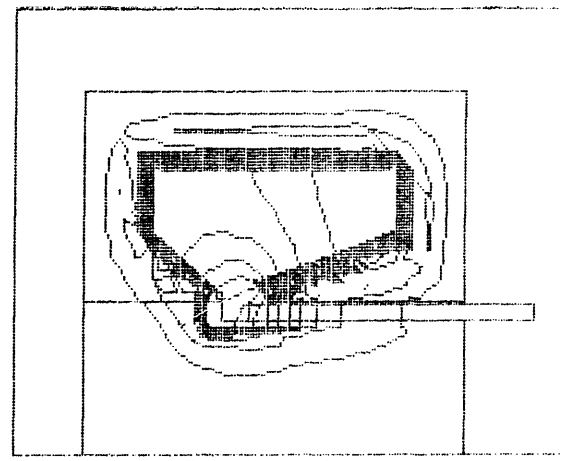

t = 191 (ms)

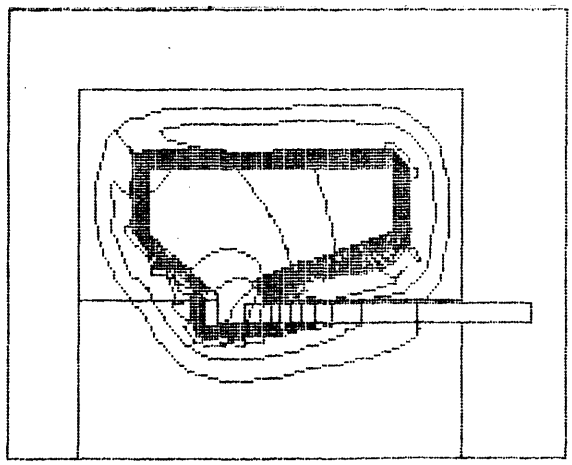

t = 192 (ms)

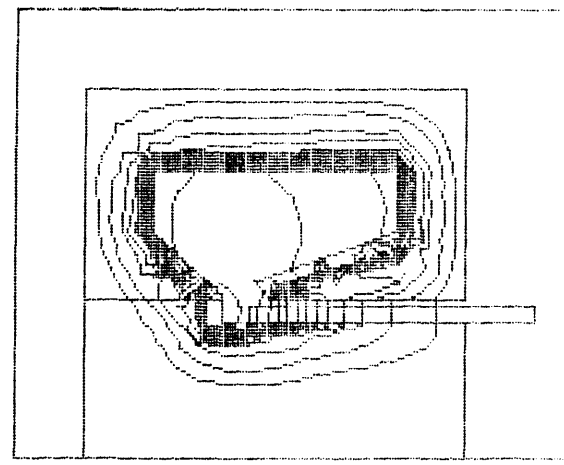

t = 193 (ms)

Fig. 5.12-2 Flux Density Distribution of a Solid Steel Stator TLIA

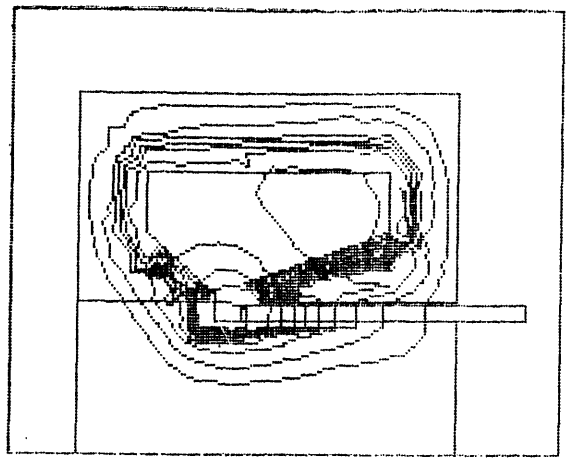

t = 194 (ms)

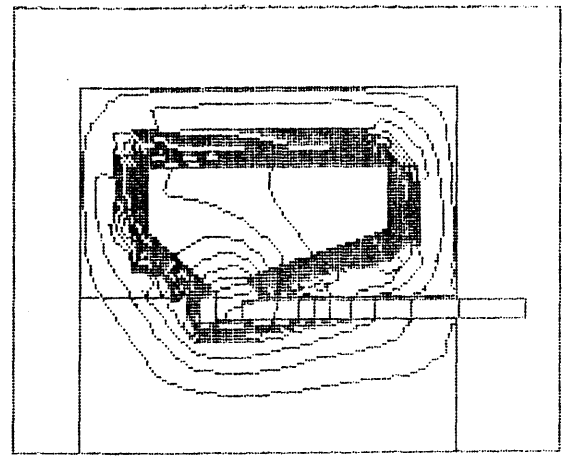

t = 195 (ms)

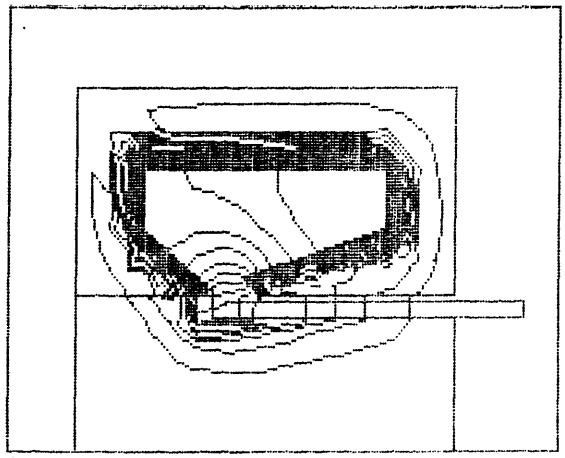

t = 196 (ms)

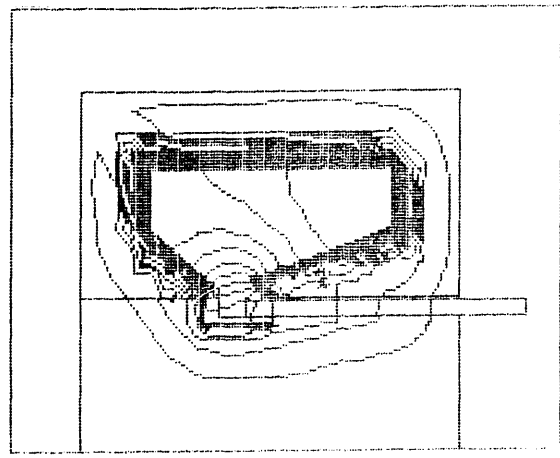

t = 197 (ms)

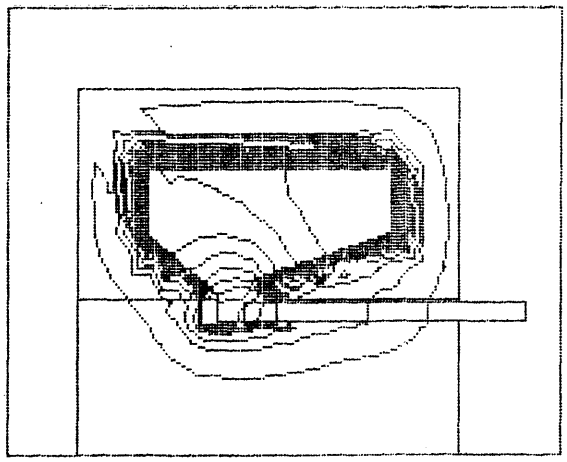

t = 198 (ms)

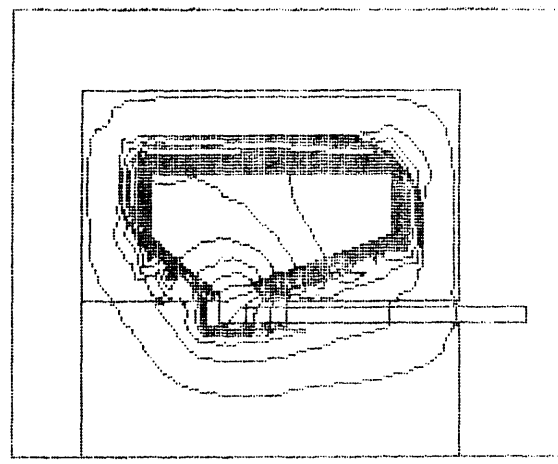

t = 199 (ms)

Fig. 5.12-3 Flux Density Distribution of a Solid Steel Stator TLIA

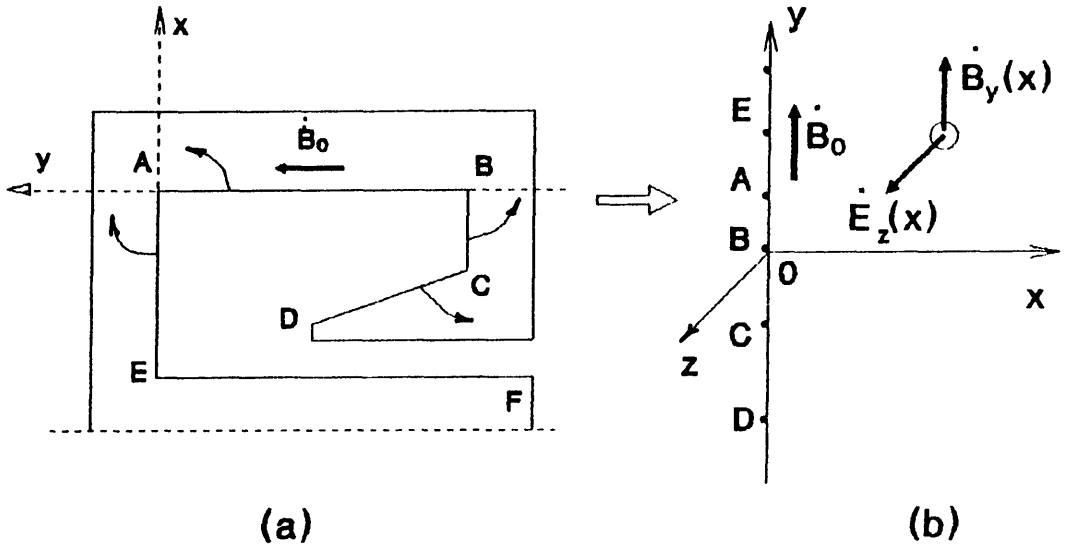

Fig. 5.13 A Semi-infinite Model

qualitatively by a very simple model, consisting of a semi-infinite conductor. As shown in Fig. 5.13a, if the stator has been unfolded in a way that makes the broken line EABCD become a straight line and then cut by a radial plane and unrolled, the solid steel stator can be modeled as a semi-infinite conductor as shown in Fig. 5.13b. This approximation is not new. It has been used to analyse eddy currents in conductors for many decades. Based on this simple model, a 3-D eddy current problem is simplified to a 1-D model, in which the flux density has a component in y direction only, $\mathbf{B} = B_y \cdot \alpha_y$ and the electric field strength has a component in Z direction only, $\mathbf{E} = E_z \cdot \alpha_z$. B_y and E_z only vary in the x direction and are independent of y and z, *i.e.* $\frac{\partial}{\partial y} = \frac{\partial}{\partial z} = 0$. Therefore, we have

$$\begin{cases} \dfrac{\partial^2 B_y}{\partial x^2} = \mu \cdot \sigma \cdot \dfrac{\partial B_y}{\partial t} \\ \dfrac{\partial^2 E_z}{\partial x^2} = \mu \cdot \sigma \cdot \dfrac{\partial E_z}{\partial t}. \end{cases} \qquad \cdots\cdots(5.1)$$

The solutions of these diffusion equations are well known. If the flux density at the boundary x=0 is assumed to be $B_y|_{x=0} = B_0 \cdot \cos(\omega t)$, the solution will be

$$B_y = B_0 \cdot exp(-\frac{x}{\Delta}) \cdot \cos(\omega t - \frac{x}{\Delta}) \qquad \cdots\cdots(5.2)$$

where, Δ is the skin depth. The expression (5.2) indicates that the flux density is a travelling wave attenuating along the coordinate axis *x*. In Fig. 5.12 we find that flux density at the exterior surface of the stator is very low. If the thickness of the solid steel stator wall is more than 4 times the skin depth, the flux density at the exterior surface of the stator will be only about e^{-4} = 1.8% of the interior flux density.

Secondly, the distribution of the field is 'unusual'. The word 'unusual' is used here to compare the flux lines in Fig. 5.12 with the flux distribution in a 2-D magnetostatic problem. Usually the experienced engineers may use the method of curvilinear squares[41] to draw equipotentials and flux lines at right angles to each other. However this method is restricted to problems described by Poission's and Laplace's partial differential equations. When the problem is described by a diffusion equation, things become different. In this TLIA with a solid steel stator and mandrel, there are three conducting areas. The eddy currents induced in those areas will have different peak values and different phase angles. This means that there will be more than one 'current source centre' in the model. Each current source will produce flux lines around it. The nonlinearity of the material makes things even much complicated. It is extremely difficult to predict when, where and how the eddy current appears so that the flux distribution becomes unusual. There will be several curls in those conducting areas. Up to date, to author's knowledge only a few authors have presented similar diagrams and

not many papers deal with the problem containing multiple eddy current regions. Aldefeld[42] includes a field plot describing a high-speed actuator with moving iron parts operating under pulsed excitation. His results are obtained by the finite difference method. MacBain[43] introduces his study of a D.C. solenoid with a steel frame and a steel plunger. When the D.C. excitation 'dies', an 'unusual' flux distribution appears in the solid steel frame. This kind of flux distribution will also happen when the diffusion equation is solved by the Fourier harmonic analysis, which can be found in Rodger's paper[9] concerning a linear induction tachometer.

Finally, it is easily seen that the structure of the nearly closed or half closed slot is not appropriate to the solid steel stator. Flux is confined to a path along the inner surface of the solid stator. The shielding effect pushes the flux to the tip of the slot tooth. This leads to two results. One is the considerable increase in leakage flux. The other is that when the plunger moves beyond the tip of the tooth, the flux will pass through the airgap and mandrel then return to the stator. Not much flux will go through the plunger to interact with the induced eddy current. The output force therefore decreases drastically.

In addition to the field plots, the COUPV can also provide the details about the eddy current density, flux density and force distribution along an specific line. This will be shown in the next section when the shielding effect is discussed.

From Fig. 5.7 it can be concluded that the transient current lasts only 2 or 3 cycles, *i.e.* 40 to 60 milliseconds. Afterwards, the TLIA can be

considered as operating in a steady state. At the last simulation cycle, the COUPV will calculate r.m.s. current, mean force and mean power losses. In general, the time step length of the simulation is chosen as δt = 1 (ms). At the last simulation cycle, the steady state values are calculated by

$$I = \left(\frac{1}{T} \cdot \int_0^T i^2 \cdot dt \right)^{\frac{1}{2}} = \left(\frac{1}{T} \cdot \sum_{n=1}^{20} I_n^2 \right)^{\frac{1}{2}}, \quad \text{(r.m.s. current);} \qquad \cdots\cdots(5.3)$$

$$F = \frac{1}{T} \cdot \int_0^T f \cdot dt = \frac{1}{T} \cdot \sum_{n=1}^{20} f_n, \quad \text{(mean force); and} \qquad \cdots\cdots(5.4)$$

$$P = \frac{1}{T} \cdot \int_0^T p \cdot dt = \frac{1}{T} \cdot \sum_{n=1}^{20} p_n, \quad \text{(mean power losses)} \qquad \cdots\cdots(5.5)$$

where, T = 20·δt = 20 ms corresponding to the period of 50 Hz power supply.

With each different plunger position, the COUPV provides corresponding stable characteristics of the TLIA. Fig. 5.14 shows the stator winding current and the axial force versus the plunger displacement. After the plunger moves beyond 10 millimeter, the axial force drops more than 50% because the flux can find a way to bypass the plunger and pass through the mandrel as elucidated before. This results in noticeable decrease of the flux density in the plunger and thus reduces the output force.

The back *emf* always plays an important role in the induction machine because it couples the electric circuit and the electromagnetic field. Like most induction motors, this back *emf* in the TLIA is almost constant whatever the load. In Fig. 5.15, we can see that there is only a slight difference between its values at the displacement of less than 10 (mm) and

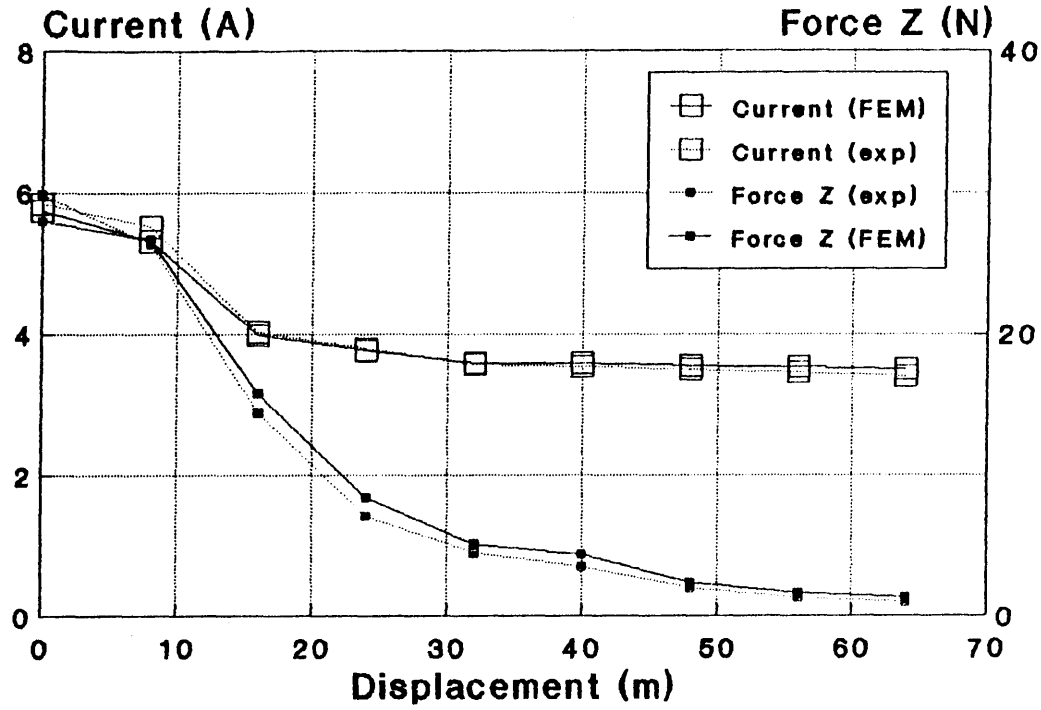

Fig. 5.14 Steady State Current and Force versus the Stroke

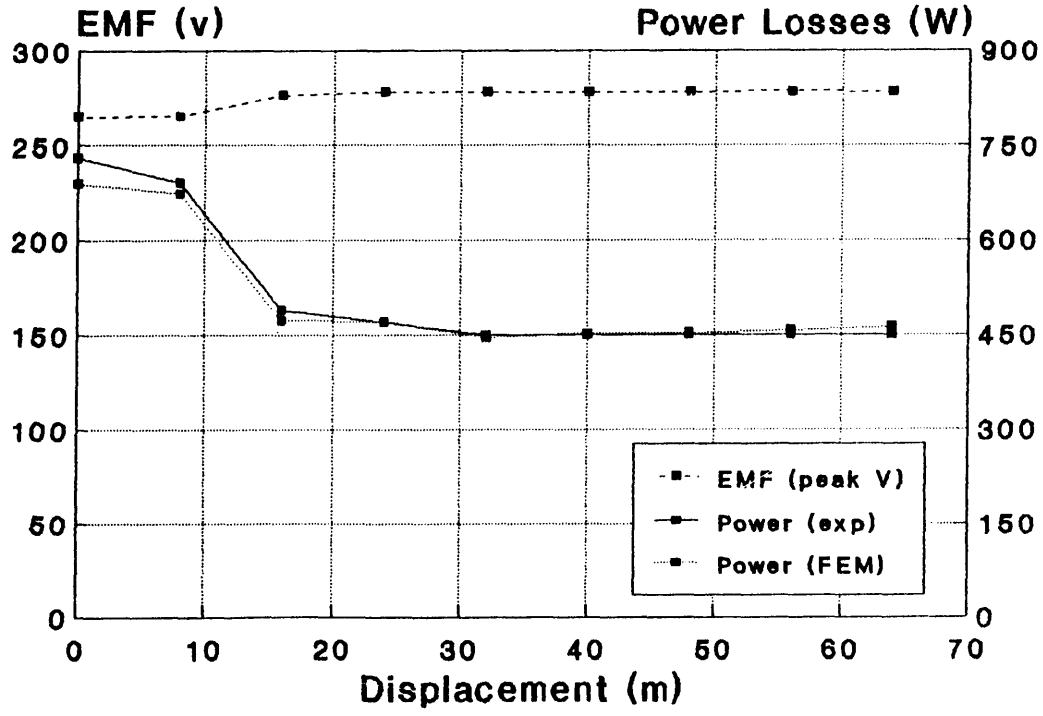

Fig. 5.15 Steady State EMF and Power Losses versus the Stroke

beyond 20 (mm). This can also be considered as the difference between the no-load *emf* and the full-load *emf*, as we can see in Fig. 5.14 that after the plunger has moved out about 30 (mm), the current is almost constant and only a very low output force exists.

The total power loss is also shown in Fig. 5.15. Together with the results in Fig. 5.14, the simulated results are in very good agreement with those from experiments. As aforementioned, this actuator is built only for the verification of the COUPV. Hence the ratio of the output force to the input power is very low. Within the displacement of 20 (mm), the average ratio is around

$$G|_{z<20mm} \approx \frac{24}{600} = 0.04 \text{ (N/W)}$$

When the displacement is more than 20 (mm), the average ratio is only about

$$G|_{z>20mm} \approx \frac{6}{450} \approx 0.013 \text{ (N/W)}.$$

Compared with the $^{Force}/_{power}$ ratio of about 0.1 (N/W) of conventional linear motors and solenoids[5], this figure is very low.

It is easy for the COUPV to isolate the Ohmic losses occurring in different conducting areas. Fig. 5.16 shows the power losses in each part versus the displacement. The loss in the solid stator forms a large proportion of the total loss even much higher than that in the plunger. This loss almost keeps constant no matter what position the plunger is at. It occupies one third of the total loss within the displacement of 15 (mm) and two third at rest of the displacements.

The eddy current losses in the plunger have a different characteristics. They drop dramatically after the plunger moves beyond the slot mouth. A great amount of flux goes directly through the airgap into the mandrel and becomes leakage flux. The farther the plunger moves out, the more the leakage flux produced. Therefore, the total flux and losses will increase slightly in the mandrel.

The increased losses in the mandrel can also be ascribed to the shielding effects of the plunger. This will be studied in the next section. When the TLIA has an open slot, this effect becomes much more pronounced.

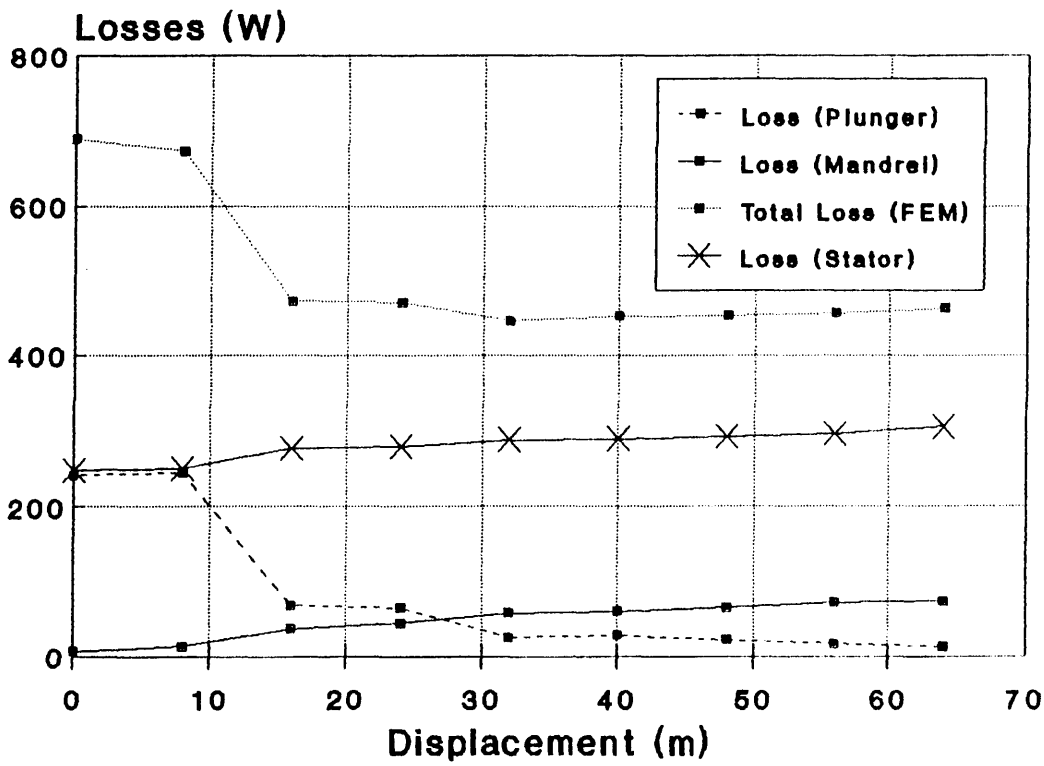

Fig. 5.16 Eddy Current Losses in Each Parts

5.4.2 Shielding & Inner End Effects of the Plunger

In Chapter 2, the shielding effect and the inner end effect of the conducting plunger were discussed by means of the FEM2D. In this section these two effects are investigated and reviewed with the aid of the COUPV which considers non-linearity, velocity and the external voltage source. The final conclusions reached are similar to those obtained by FEM2D. The main consequence of the shielding effect is that flux can not totally go through the plunger. A considerable part of the flux will be pushed back and become leakage flux. The rest which passes through the plunger appears mainly at the inner end of the plunger. All the induced eddy currents will gather at this end. For a model with a nearly closed slot mouth, the eddy current induced in the plunger will attenuate in the axial direction and obey the penetration depth law.

Fig. 5.12 in the last section highlights this phenomenon again in which a major part of the flux penetrates through the end of the plunger in each plot. However, there may be an argument about this model because of its solid steel stator. It leads to the possibility that flux goes through the end of the plunger and eddy currents gather at the inner end of the plunger due to the skin effect of the solid steel stator, and this makes flux in the stator go to the tip of the slot tooth. Thus most flux passes through the plunger at its end. In order to preclude this possibility, a laminated stator model is considered in following discussion.

1. The Laminated Stator Model with Nearly Closed Slot Mouth

A laminated stator model is displayed at the right hand top corner in Fig.

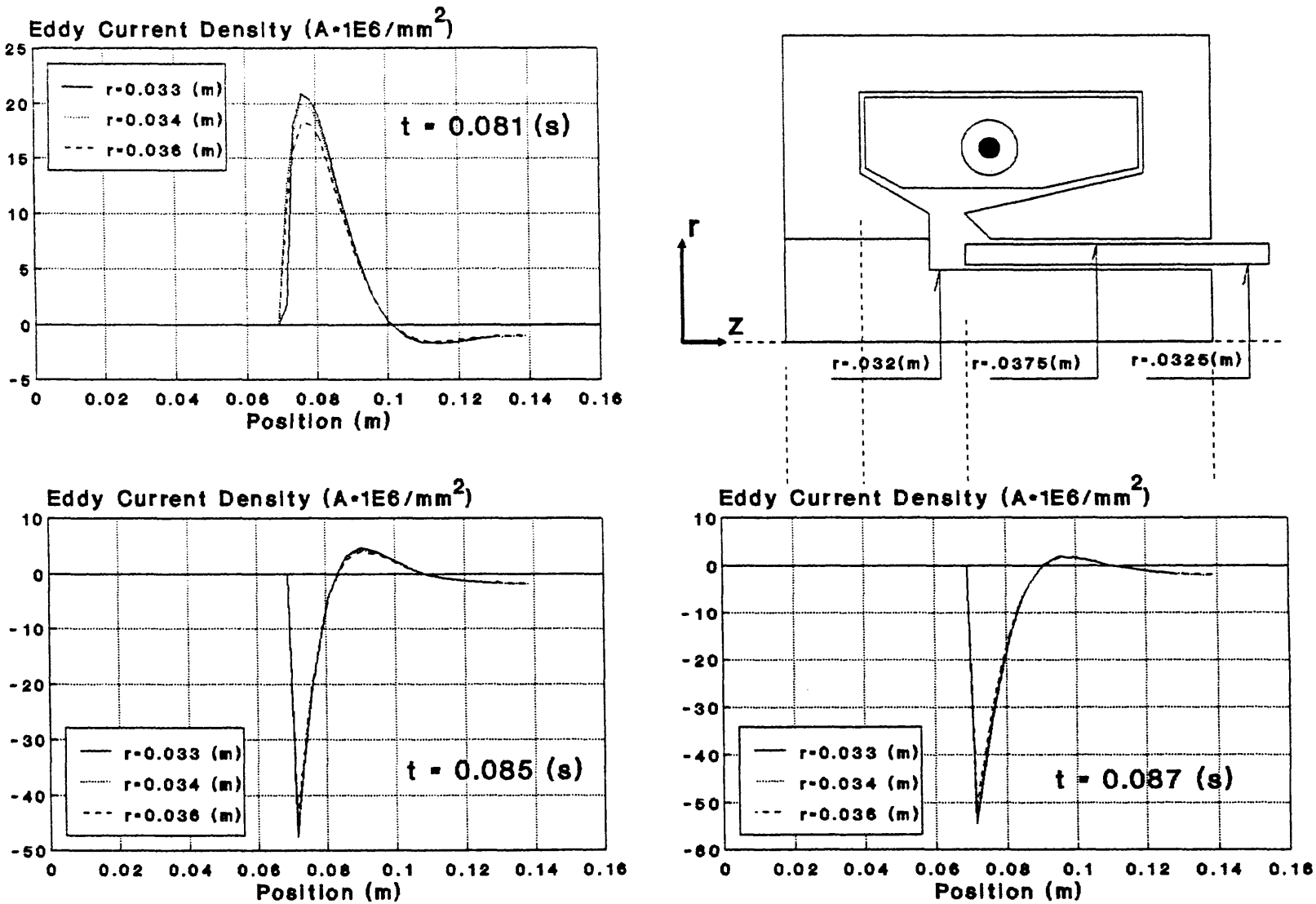

Fig. 5.17-1 Eddy Current Density in the Plunger

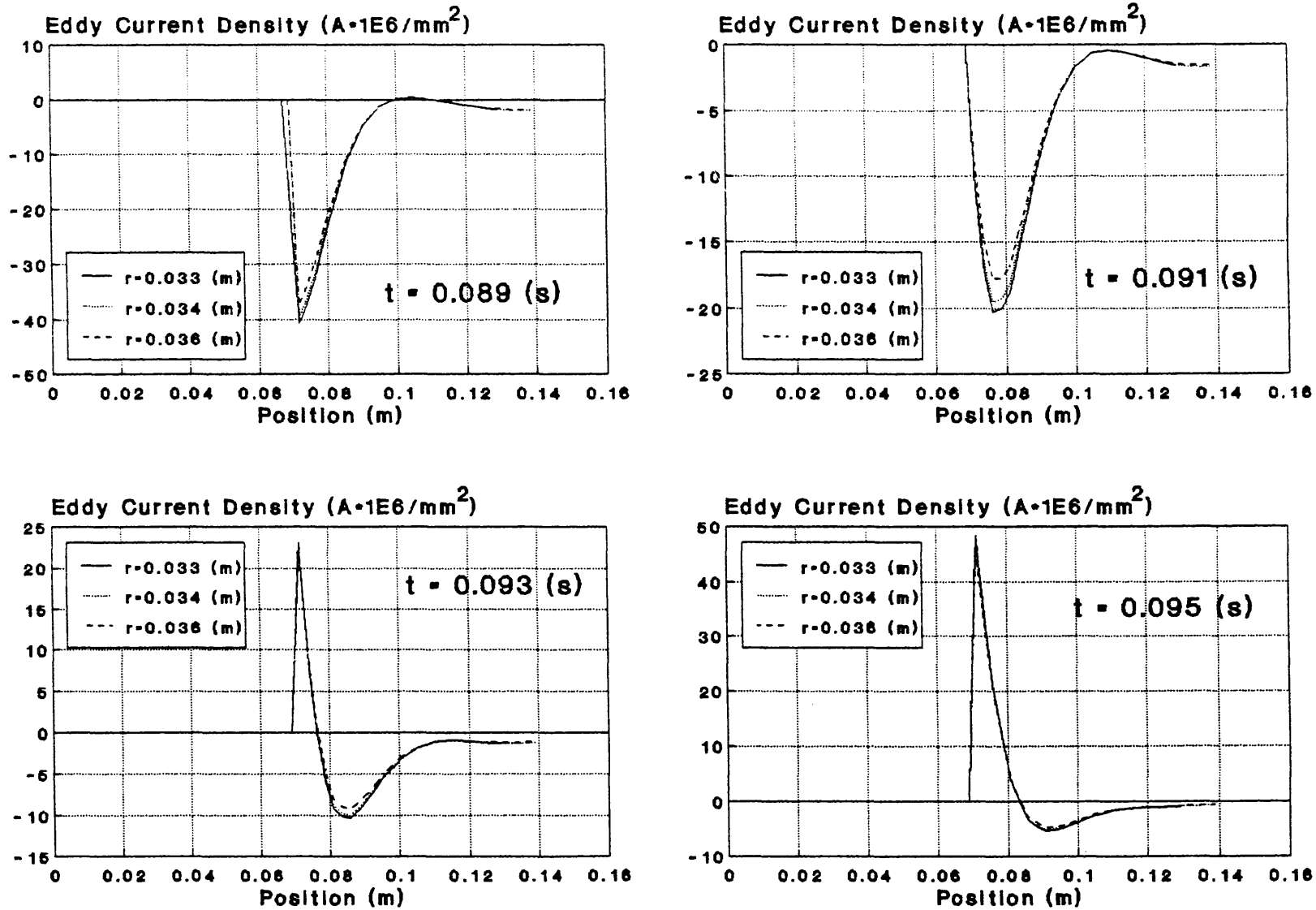

Fig. 5.17-2 Eddy Current Density in the Plunger

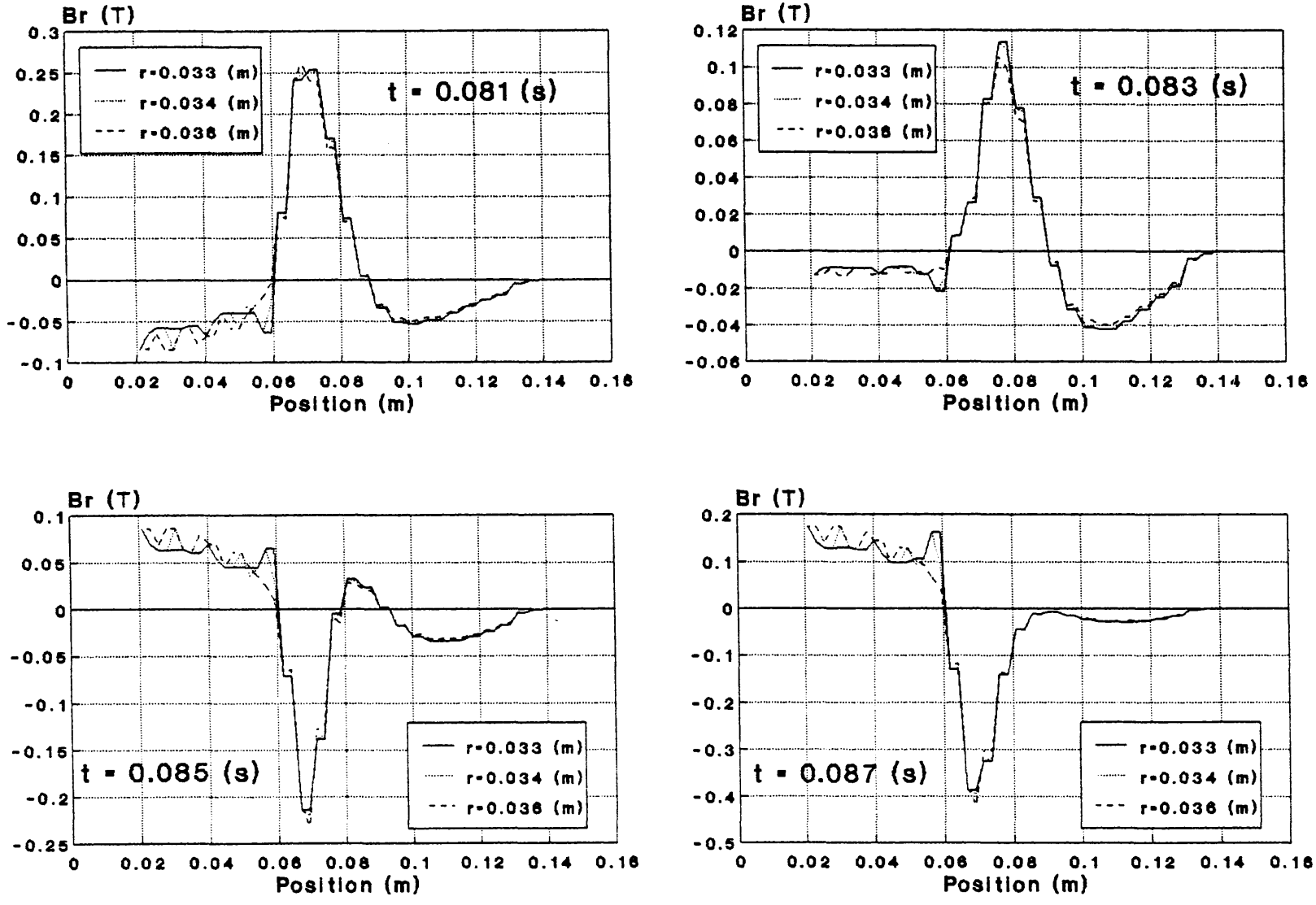

Fig. 5.18-1 Flux Density Distribution in the Plunger

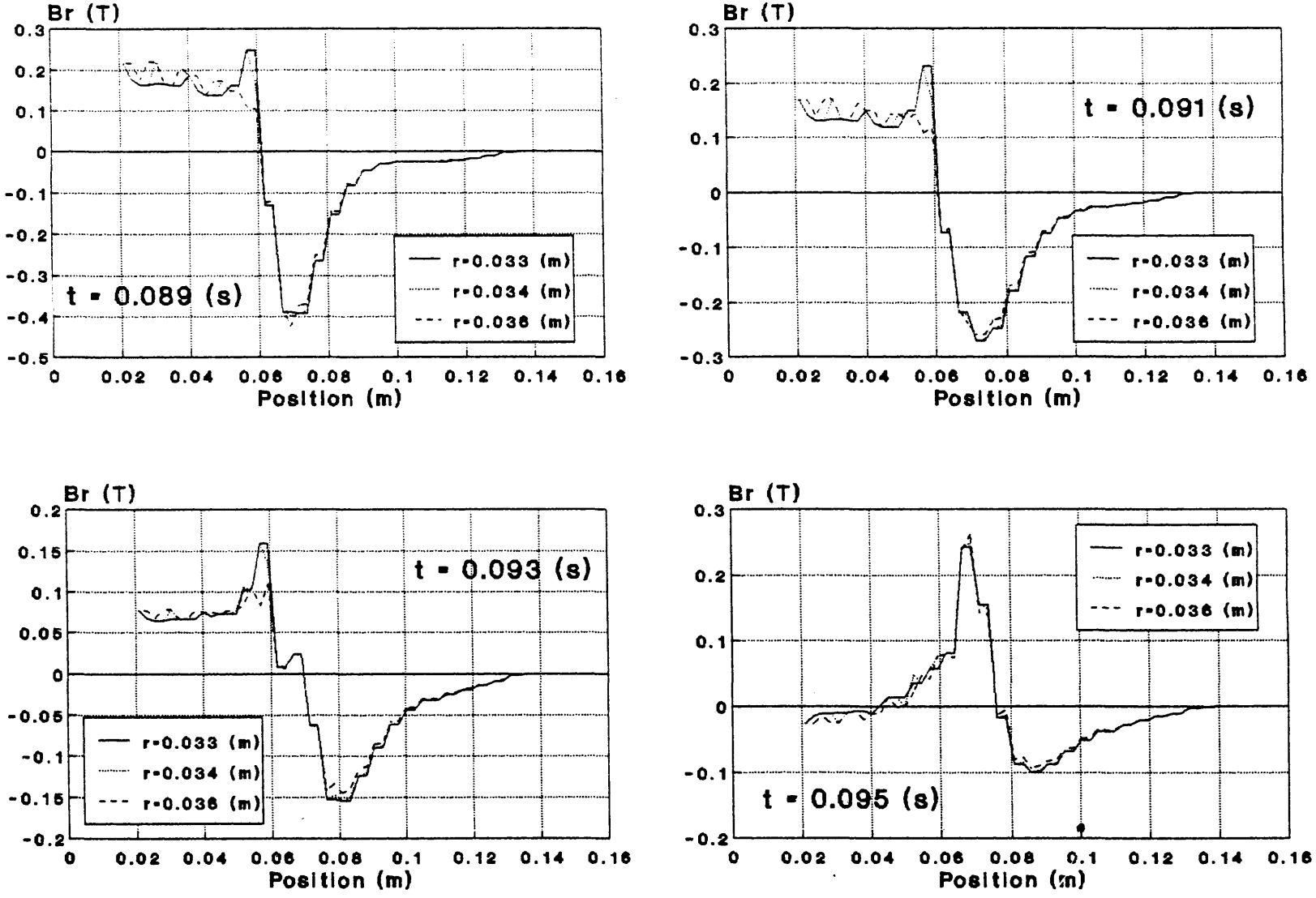

Fig. 5.18-2 Flux Density Distribution in the Plunger

5.17-1. Its slot mouth is nearly closed. The rest of its geometry and materials remain unchanged. Its stator winding is of 500 turns which is excited by 213 volts, 50 Hz sine wave while the plunger is blocked at the displacement of D = 0.008 (m), *i.e.* the position of 0.068 (m) in the graph. Fig. 5.17 shows the eddy current distribution in the plunger from the time instant of 0.081 (s) to 0.095 (s) with 0.002 (s) interval. At the instant of 0.087 (s) eddy current reaches its maximum. Its peak value times e^{-1} is located at D = 0.021 (m), *i.e.* the position of 0.081 (m) in the graph. Therefore, its penetration depth is approximately equal to 0.013 (m). Eddy current in the plunger attenuates mainly in the axial direction. Each graph shows three curves representing the eddy current density distribution at three different radii. There is no obvious attenuation to be found in the radial direction.

The radial flux density distributions in the plunger along three lines at three different radii are shown in Fig. 5.18. Most radial flux penetrates the plunger at its inner end within the length of 20 (mm). Its peak value is about 0.4 Tesla. According to the concept of the 'goodness' factor, if the flux density increases, the output force will increase too and the eddy current losses can be reduced. Therefore the flux density value of 0.4 Tesla indicates that there is a large room to improve this model. Similar to the eddy current distribution, there is no flux density attenuation in the radial direction apparent. The flux will change directions along the three horizontal lines at their radii 0.033 (m), 0.034 (m) and 0.036 (m).

Fig. 5.19 shows flux plots corresponding to each time instant in Fig. 5.17 and Fig. 5.18. Compared with those in Fig. 5.12, the flux distribution in

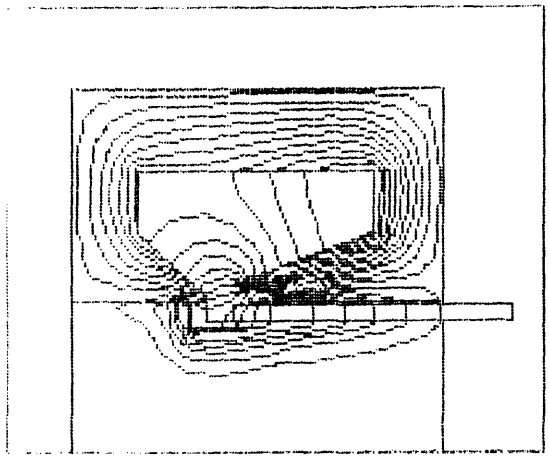

t = 81 (ms), I_1 = -4.01 (A)

I_e = 2175.0 (A), N_f = 9

F_z = 39.4 (N)

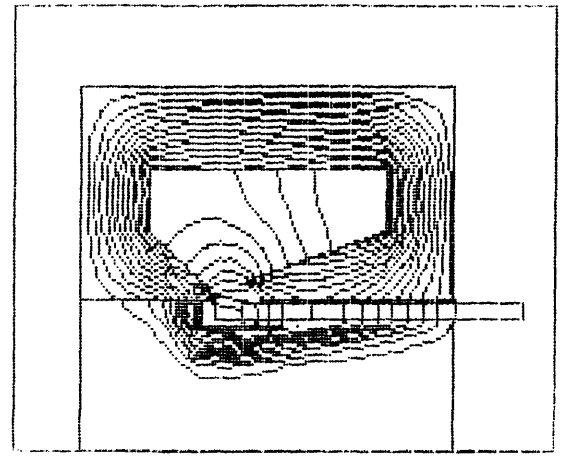

t = 83 (ms), I_1 = 0.11 (A)

I_e = 231.3 (A) N_f = 6

F_z = -1.28 (N)

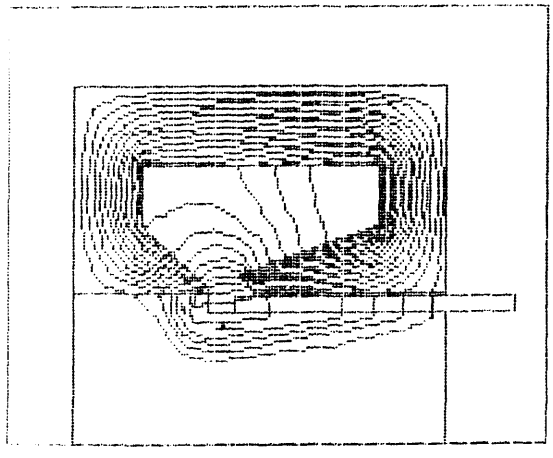

t = 85 (ms), I_1 = 4.34 (A)

I_e = -1798 (A), N_f = 5

F_z = 9.85 (N)

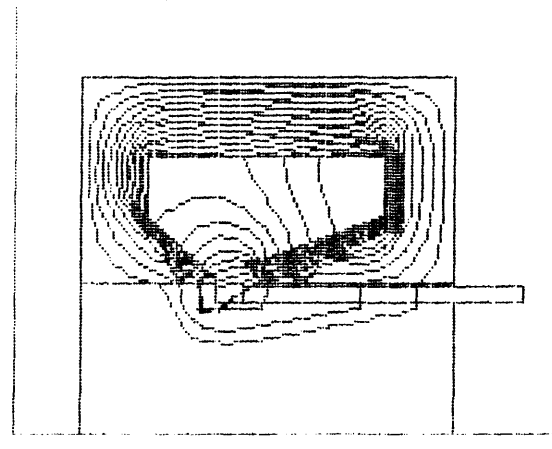

t = 87 (ms), I_1 = 7.01 (A)

I_e = -3033 (A) N_f = 4

F_z = 69.1 (N)

Fig. 5.19-1 The Flux Density Distribution for a Closed Slot TLIA

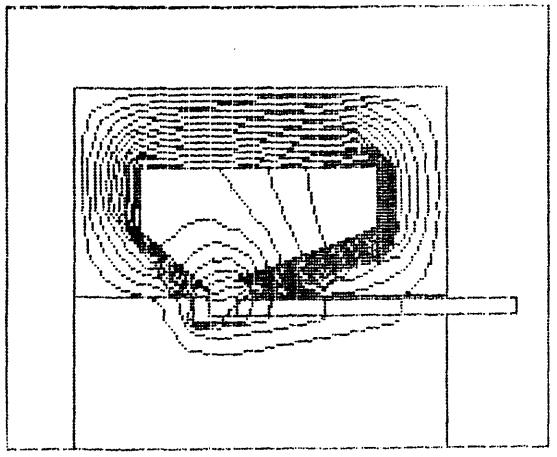

t = 89 (ms), I_1 = 7.19 (A)

I_e = -3053 (A), N_f = 4

F_z = 101.9 (N)

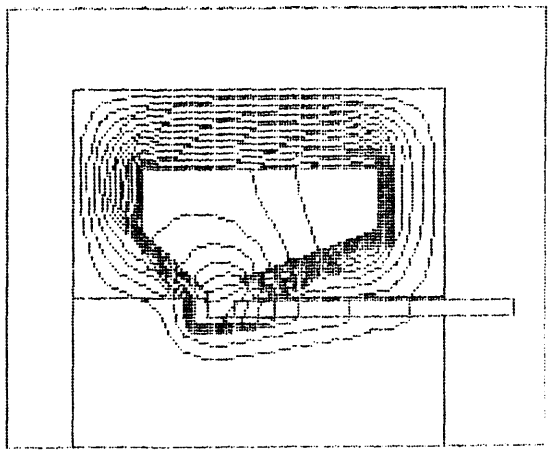

t = 91 (ms), I_1 = 4.78 (A)

I_e = -1902 (A) N_f = 7

F_z = 67.6 (N)

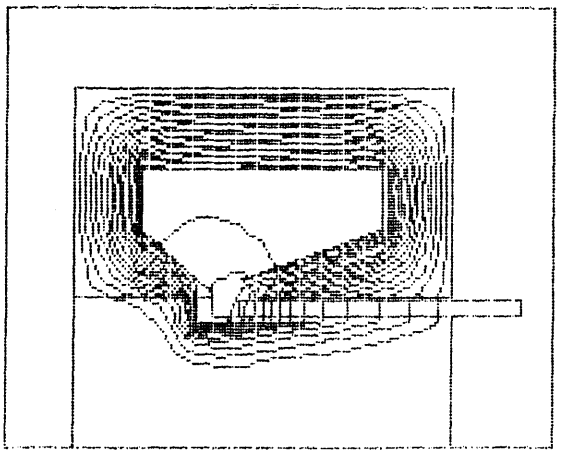

t = 93 (ms), I_1 = 0.7 (A)

I_e = 2.63 (A), N_f = 13

F_z = 8.38 (N)

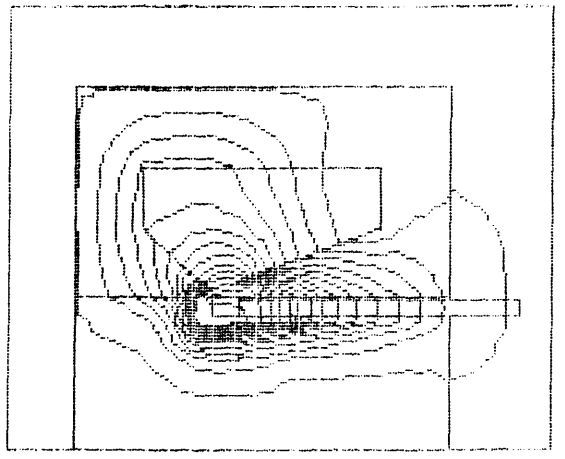

t = 95 (ms), I_1 = -3.55 (A)

I_e = 2027 (A) N_f = 15

F_z = -3.84 (N)

Fig. 5.19-2 The Flux Density Distribution for a Closed Slot TLIA

the stator seems to be 'usual' since the conductivity in the stator is set to zero. Of course, in the mandrel area, 'unusual' distribution still appears due to the induced eddy currents.

2. The Laminated Stator Model with an Open Slot Mouth

In the last section, it has already been found that the eddy current loss in the mandrel only occupies a small part of the total losses, as shown in Fig. 5.16. This means that some flux has not passed through the mandrel. There are two possible explanations to this phenomenon for the solid steel stator model with a closed slot. One is that the plunger has the shielding effect to prevent the flux from penetrating through. Another is that the closed slot provides the flux a short cut. In order to prove that the second possibility is not the main cause, an open slot model with a laminated stator is developed for the computer simulation. Except for the difference in the slot shape, all the other material and geometric sizes remain the same as in the model in Fig. 5.17-1. Its winding is of 500 turns and is excited by 213 volts, 50 Hz sine wave while the plunger is blocked at the displacement of D = 0.004 (m), *i.e.* the position of 0.064 (m).

Fig. 5.20 shows the simulated results in 12 flux density distribution graphs recorded at each simulating instant from 81 (ms) to 100 (ms) at 1 or 2 (ms) interval each. Under each graph, there is information about each transient instant, including the input current I_1, output force F_z, eddy current I_e and the number of flux density lines passing through the plunger.

The most striking feature of Fig. 5.20 is that in practice a considerable part of the flux lines does not go through the mandrel. Many of them

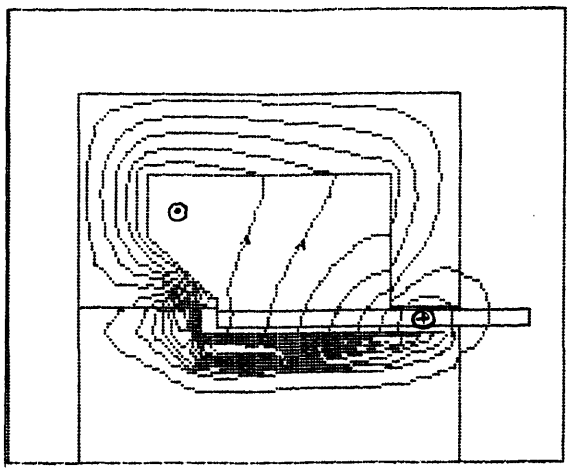

t = 182 (ms), I_1 = -0.92 (A)

I_e = 655.7 (A), N_f = 7

F_z = 1.92 (N)

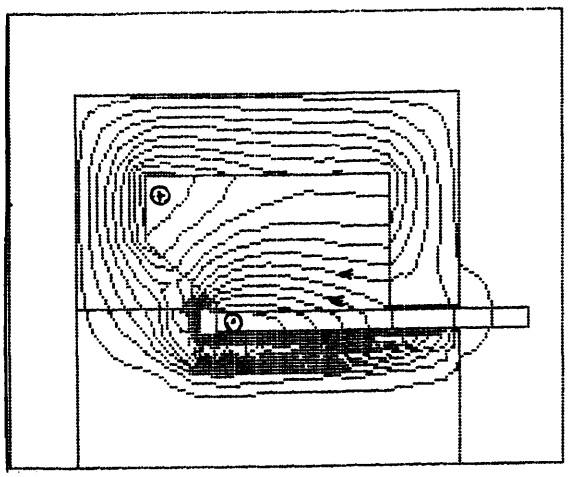

t = 183 (ms), I_1 = 3.99 (A)

I_e = -1997 (A) N_f = 6

F_z = -0.6 (N)

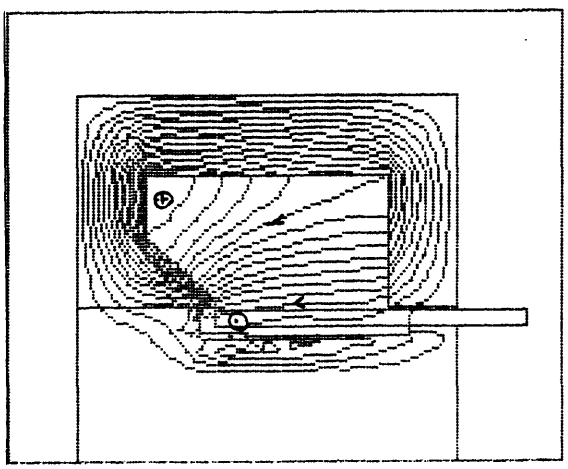

t = 185 (ms), I_1 = 12.27 (A)

I_e = -8479 (A), N_f = 3

F_z = 19.5 (N)

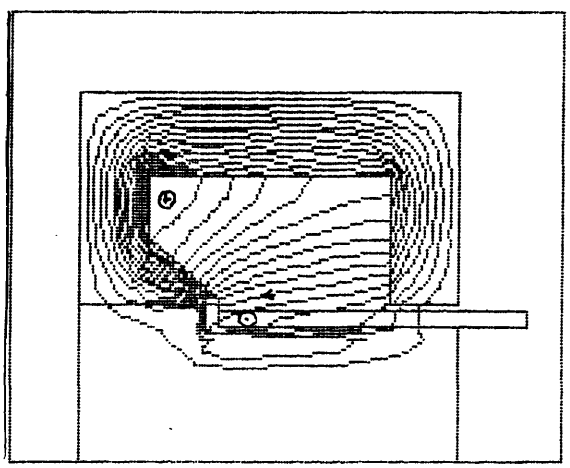

t = 187 (ms), I_1 = 15.99 (A)

I_e = -8355 (A) N_f = 5

F_z = 74.9 (N)

Fig. 5.20-1 The Flux Density Distribution for an Open Slot Model

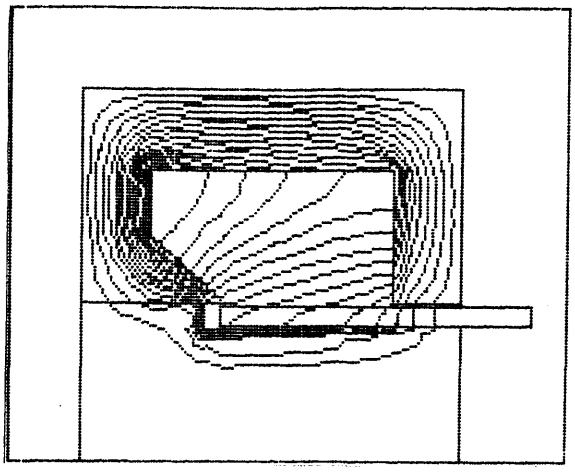

t = 189 (ms), I_1 = 13.75 (A)

I_e = -6968 (A), N_f = 7

F_z = 93.2 (N)

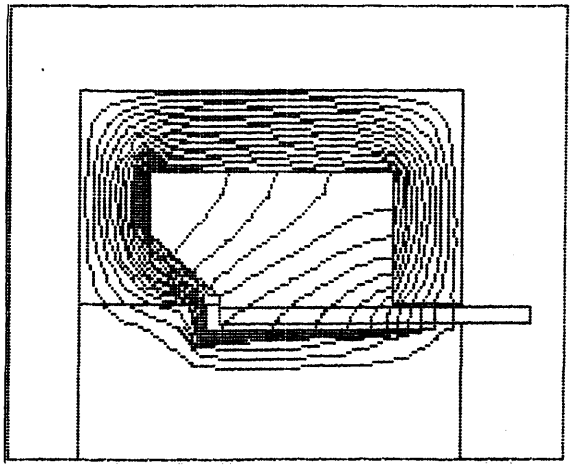

t = 191 (ms), I_1 = 6.38 (A)

I_e = -2908 (A) N_f = 11

F_z = 47.6 (N)

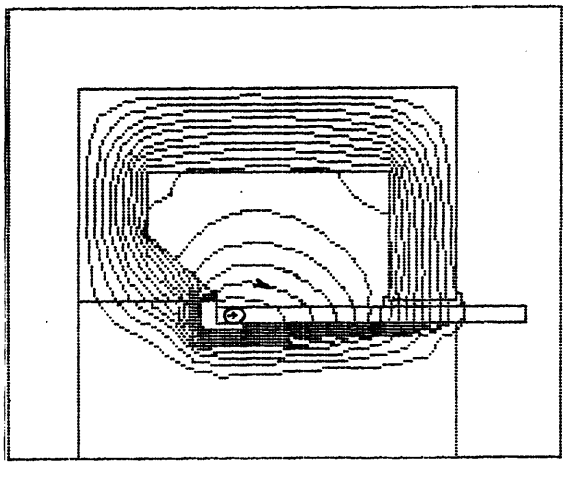

t = 193 (ms), I_1 = -3.32 (A)

I_e = 2319 (A), N_f = 15

F_z = -11.5 (N)

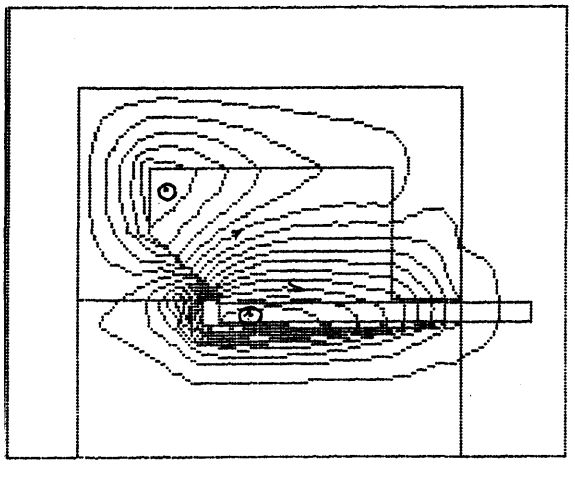

t = 195 (ms), I_1 = -11.6 (A)

I_e = 6795 (A) N_f = 7

F_z = -19.3 (N)

Fig. 5.20-2 The Flux Density Distribution for an Open Slot Model

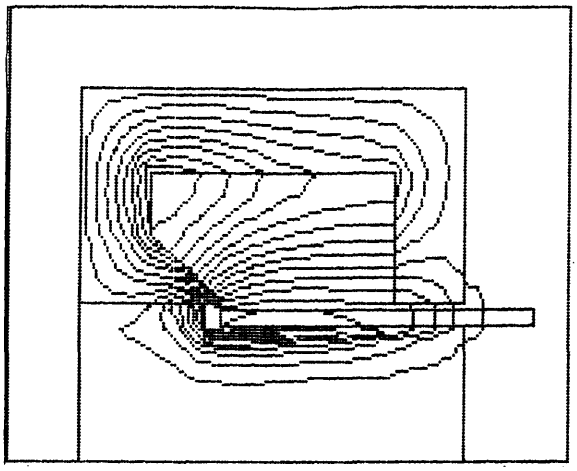

t = 196 (ms), I_1 = -14.2 (A)

I_e = 8132 (A), N_f = 4

F_z = -2.24 (N)

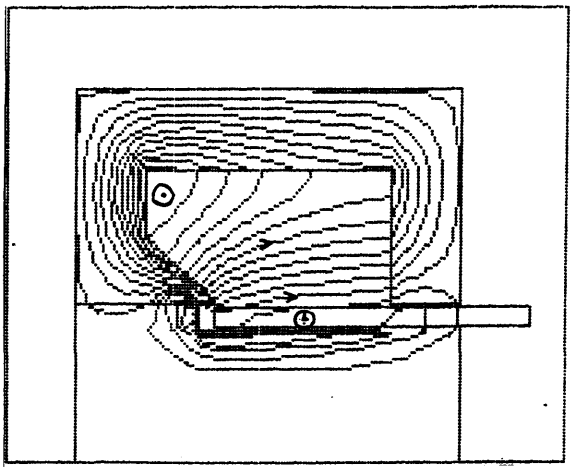

t = 198 (ms), I_1 = -14.99 (A)

I_e = 8371 (A) N_f = 4

F_z = 35.9 (N)

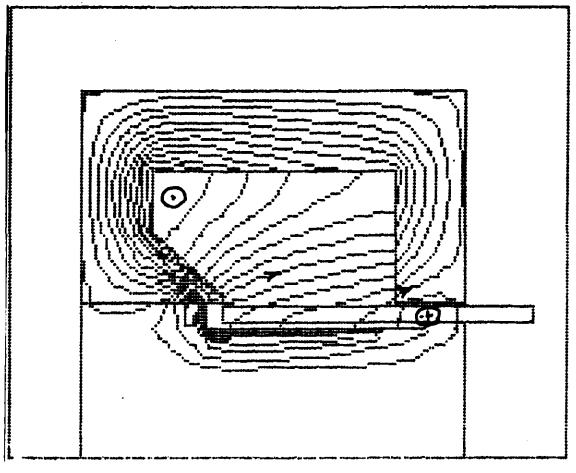

t = 200 (ms), I_1 = -9.95 (A)

I_e = 5506 (A), N_f = 5

F_z = 35.0 (N)

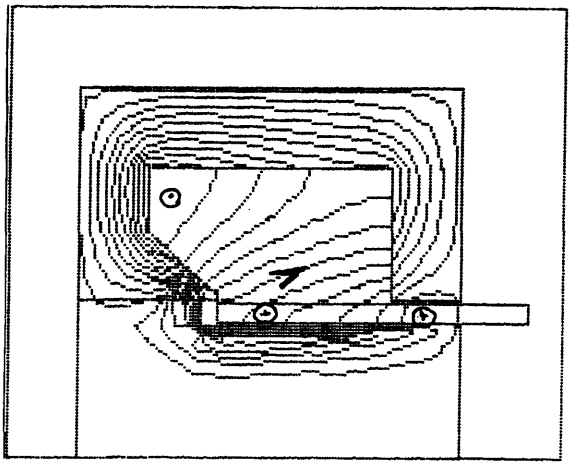

t = 201 (ms), I_1 = -5.76 (A)

I_e = 3219 (A) N_f = 6

F_z = 19.6 (N)

Fig. 5.20-3 The Flux Density Distribution for an Open Slot Model

change their directions to the other side of the stator and become leakage flux. Counting the number of flux lines which go through the plunger, we find that only 4 to 7 out of 15 lines are in the main magnetic circuit in most of the plots. This is strong evidence that the conducting plunger does have the shielding function. Therefore, it is extremely difficult to determine which is the main flux path and which is the leakage flux path by the magnetic circuit approach.

In general, almost all magnets, solenoids and electric motors, whether conventional or special, are analysed based on their main flux path, *i.e.* a main magnetic circuit which should couple both the moving and stationary parts. The additional meaning of the so called main flux path is that the major part of the flux, say more than 80%, should go through it. After the determination of this path, various leakage flux paths can be easily established. Then all the parameters such as slot leakage reactance, winding end leakage reactance, *etc.* can be estimated by the local electromagnetic field analysis. After being modified by knowledge arising from experimental results, these parameters will be used for both design and performance analysis. This procedure is routine in conventional design.

There are several kinds of electromagnetic devices which use the solid conductor as their secondary windings such as solid steel rotor induction motors, linear induction motors with a secondary plate or a conducting sheet backed by a ferromagnetic material, *etc.* However, the flux paths in these devices are very clear. Most of the flux will penetrate the conducting sheet under each pole pitch. Hence we can use a magnetic circuit to model the stator yoke, stator tooth, airgap and rotor yoke and

then determine the parameters of the equivalent circuit. This is why the equivalent circuit of the normal induction motor can be used for the linear induction motor with the solid secondary conducting plate, although the method of calculating the parameters is not the same.

What and where is the main flux path of the TLIA? Obviously, this main flux should couple both stator winding and the plunger. The original idea proposed in Chapter 1 is that the main flux will follow a dotted line illustrated in Fig. 1.2a. This flux interacting with the eddy currents induced in the plunger will produce the output force required. However, the analysis both in Chapter 1 and 2 leads to different answers based on the shielding effect and the inner end effect. For the TLIA, it is difficult to separate the leakage flux and the main flux linking the stator winding. Therefore, the classical method of estimating parameters first and then calculating the performance by means of an equivalent circuit is not suitable to this case. The only alternative method is to use numerical analysis. The finite element program COUPV developed has been proved to be a very effective tool.

3. Comparison between Open and Nearly Closed Slot Mouth Models

The locked state characteristics of this open slot model and its comparison with those of the closed slot model are shown in Fig. 5.21. Its axial output F_z increases significantly within the displacement from 10 (mm) to 40 (mm). It is about 10 times more than that of the previous solid steel stator machine. However, it should be noticed that the input current is almost doubled. Obviously, this is caused by the open slot mouth similar to the case introduced in Chapter 2. When the slot is half or almost

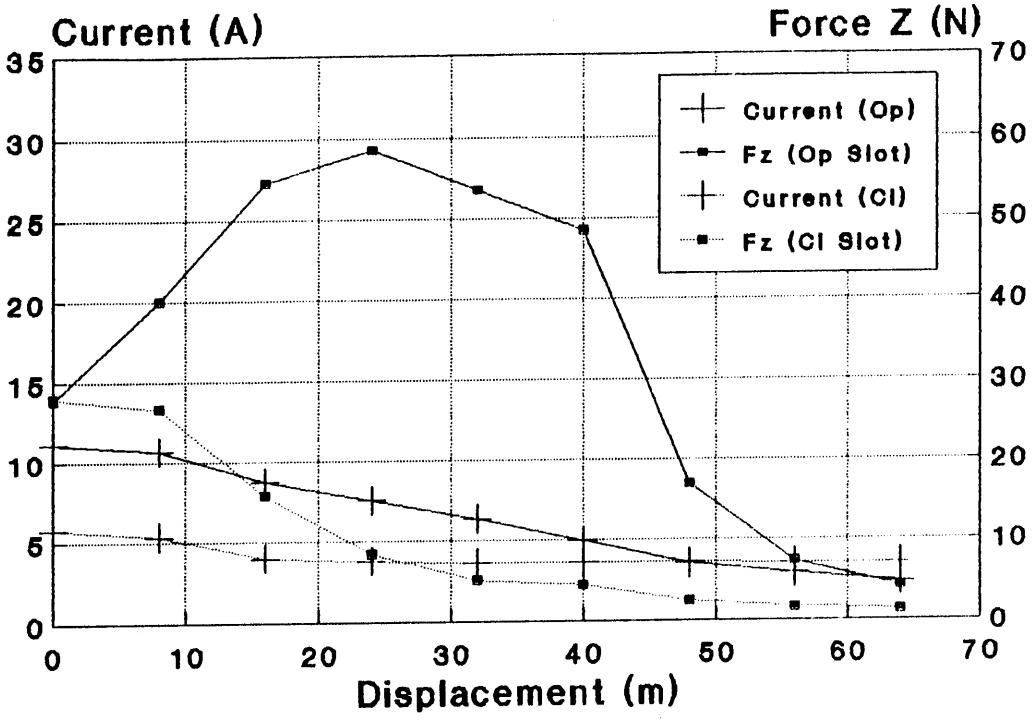

(a) Comparison of Current & Axial Force of Closed Slot Model

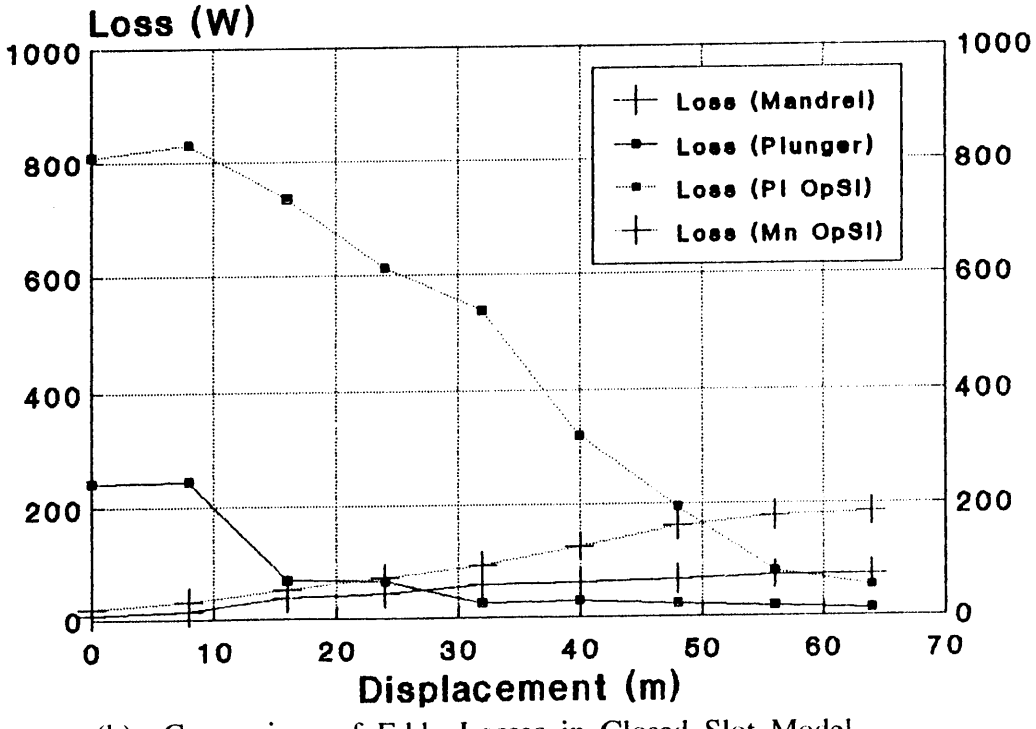

(b) Comparison of Eddy Losses in Closed Slot Model

Fig. 5.21 Steady State Characteristics of the Open Slot Model

closed, the leakage reactance of the stator winding is quite large because the steel tooth supplies a leakage flux path with high permeability. After the slot has been opened, instead of going through the ferromagnetic path, the leakage flux must go through the air direct. Its leakage reactance will greatly decrease. When the plunger is blocked, the TLIA works like a transformer with its secondary winding short circuited. Therefore, the input current is mainly determined by the short-circuit impedance. This is why the input current increases significantly. The loss in the mandrel is further evidence of the shielding effect. In Fig. 5.21b, it is noticeable that eddy current losses of the mandrel in the TLIA with an open slot will increase considerably as the plunger moves out. This means that when the plunger is located near the inner end of the TLIA, there is not much flux passing through the mandrel. When the plunger is located near the outer end of the TLIA or after it has moved out, most of the flux goes through the mandrel. The plunger obviously plays the role of shielding the flux path.

To reduce the input current in the blocked state the only possible way is to increase its leakage reactance. It is very clear however that use of a closed slot is not a choice because it will reduce the output force when the plunger moves under the tooth of the closed slot. An alternative choice will be given in the next chapter in which the input current is reduced while the output force remains almost unchanged.

5.4.3 Excited by a Square Wave Voltage

Nowadays, more and more electric motors and actuators are driven or controlled by various sorts of static converters. A common method of analysis and calculation is to use 'harmonic resolution'. However, since most machines are operated under non-linear conditions, this method can only supply approximate results in the steady state.

The time-stepping finite element method is a powerful tool to tackle this problem. It treats the time discretised forms of different waveforms of power supplies in the same way in its calculating procedure. Therefore, it can deal with various waveforms easily. It provides the information directly such as the transient current, force, power losses and their time variations. In this section the COUPV is used to simulate the solid steel stator TLIA which was used in the last section with its stator winding of 500 turns and the plunger blocked at D = 0.004 (m) but this time it is fed by an A.C. motor speed controller which can supply square wave with its frequency and peak voltage adjustable. Fig. 5.22. shows a square waveform used in the following experiment which can be expressed by the step function as follows,

$$U_s(t) = U_m \cdot \sum_{n=0,\ 2,\ 4,\ \ldots}^{\infty} \Big\{ [s(t - n\cdot T_1) - s(t - n\cdot T_1 - n\cdot T_e)] - s[t - (n+1)\cdot T_1] + s[t - (n+1)\cdot T_1 - (n+1)\cdot T_e] \Big\} \quad \cdots\cdots\cdots (5.7)$$

where U_m is voltage amplitude, $s(t)$ is the step function, T_e is the energising time and T_1 is the period of a half cycle. In Fig. 5.22, its peak voltage is 285 volts. The turn-on and turn-off time are 3 (ms) and 6

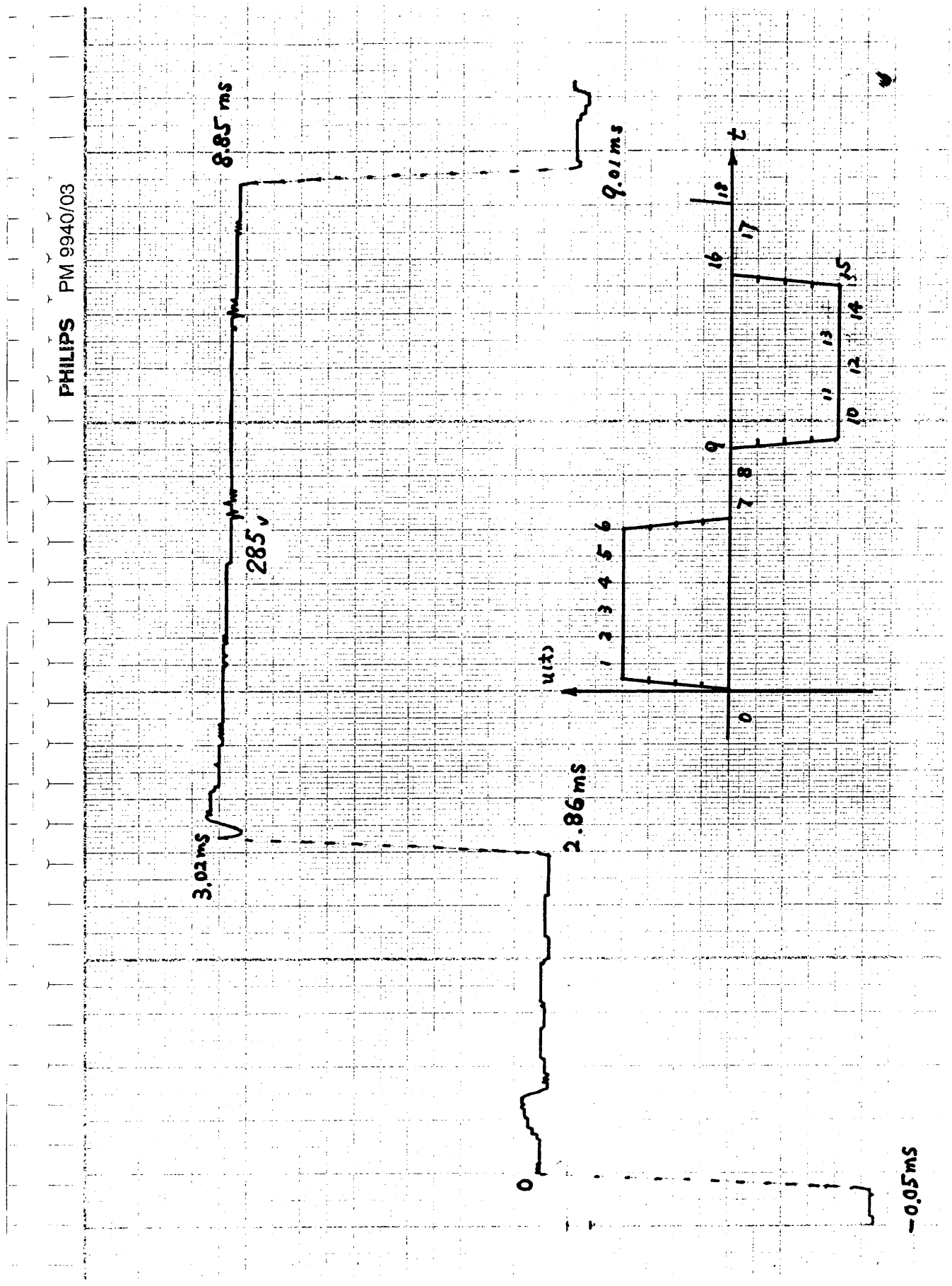

Fig. 5.22 Square Wave Voltage Supply for Locked State Experiment

(ms) respectively. In this example the simulating time step selected for the COUPV is equal to 1 (ms) so that we can simulate its turn-on period within 6 time steps and turn-off period within 3 time steps, and a total of 9 time steps in half a cycle. When the supply voltage jumps form 0 volts to positive or negative peak voltage or *vice versa*, a special treatment should be applied to avoid divergence. In Fig. 5.22 the voltage rise time and decay time is equal to 0.16 (ms) as measured by experiment. This figure will be fed into the COUPV and be divided into 3 or 4 smaller time intervals with smaller voltage jumps associated with each. The treatment of this example is shown at the bottom of Fig. 5.22. The rise or decay times are divided into 4 intervals. Therefore, the first two simulation steps are carried out under the conditions listed in Table 5.5,

nth time step	$V_{(n)}$ (V)	$t_{(n)}$(ms)	*nth time step*	$V_{(n)}$ (V)	$t_{(n)}$(ms)
1	71.25	0.04	10	285	6.0
2	142.5	0.08	11	213.75	6.04
3	213.75	0.12	12	142.5	6.08
4	285	0.16	13	71.25	6.12
5	285	1.0	14	0.0	6.16
6	285	2.0	15	0.0	7.0
7	285	3.0	16	0.0	8.0
8	285	4.0	17	0.0	9.0
9	285	5.0	18	71.25	9.04

Table 5.5 Switch on and off Instants

Fig. 5.23 shows the input current waveform recorded by the digital storage oscilloscope when the actuator is energised by the square wave voltage shown in Fig. 5.22. The envelope of the current curve is similar to that in Fig. 5.7. It decays following an exponential curve. The waveform is

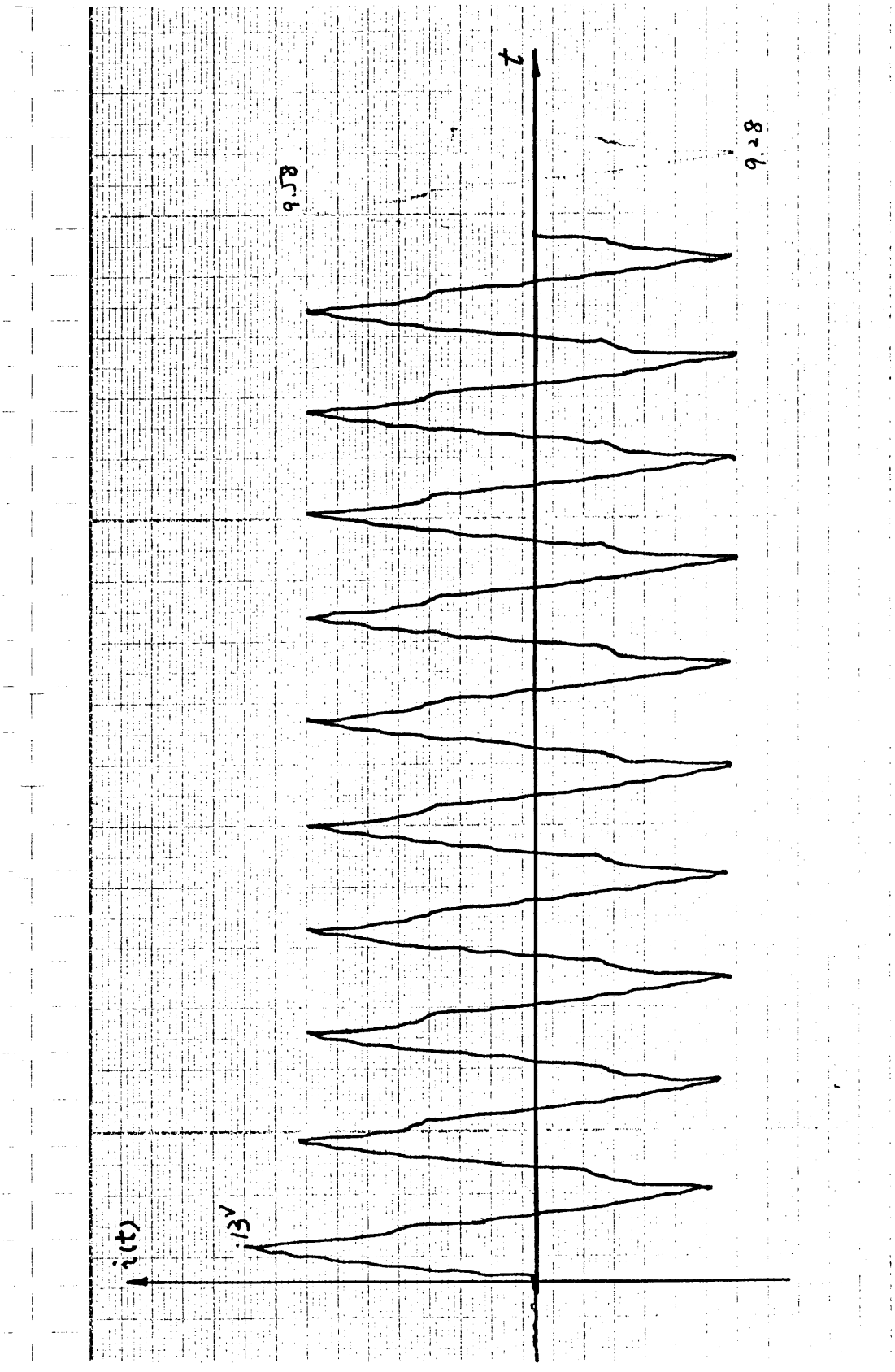

Fig. 5.23 Recorded Stator Current for Square Wave Excitation

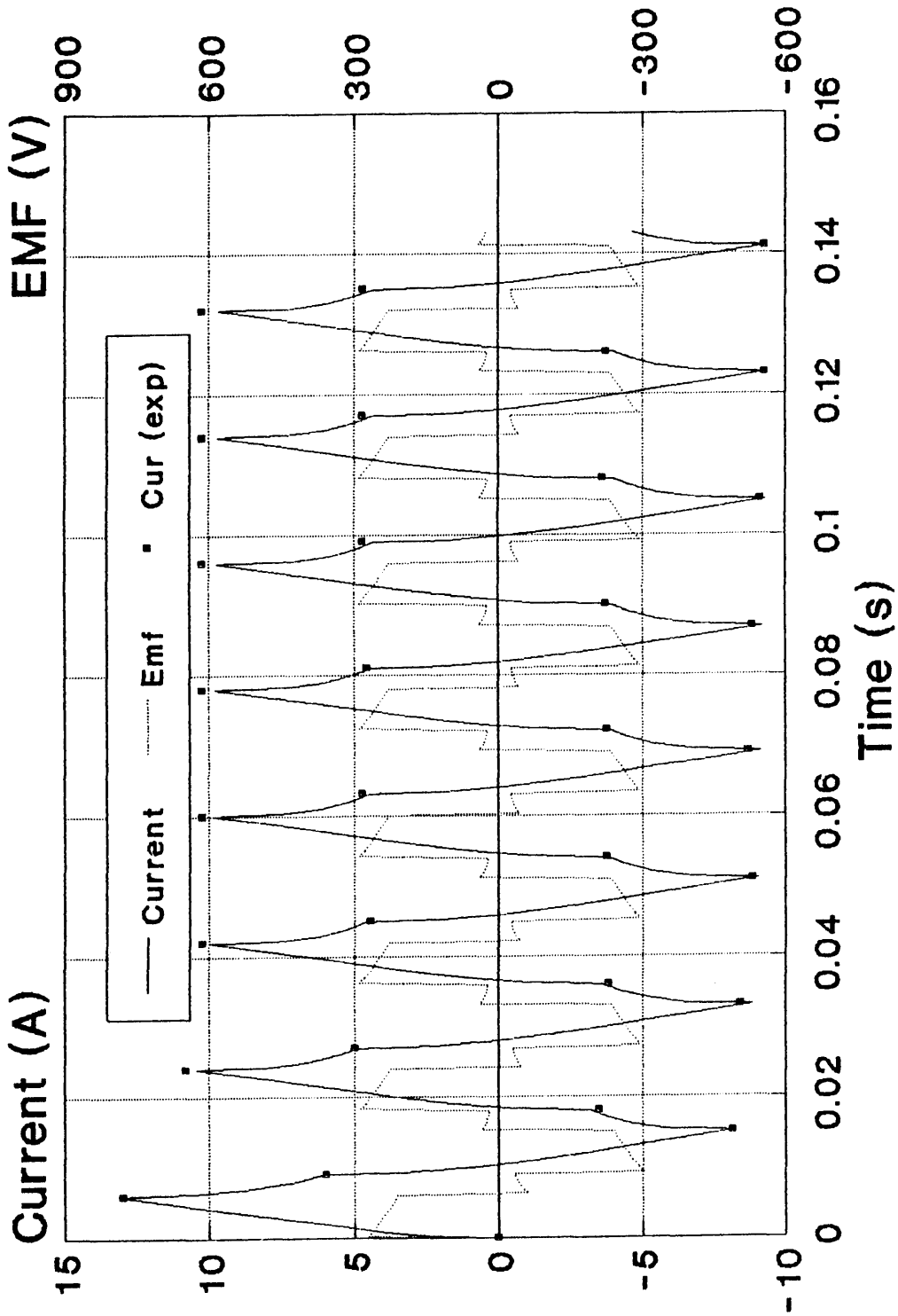

Fig. 5.24 Comparison between the Recorded & Simulated Results

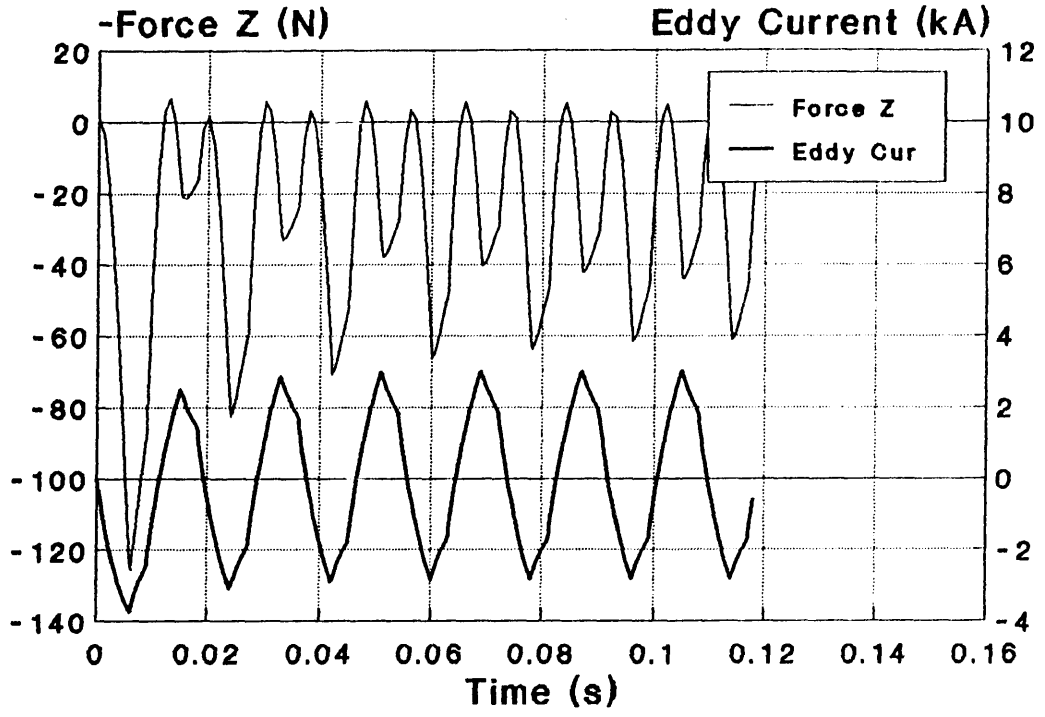

Fig. 5.25 Simulated Axial Force & Eddy Currents

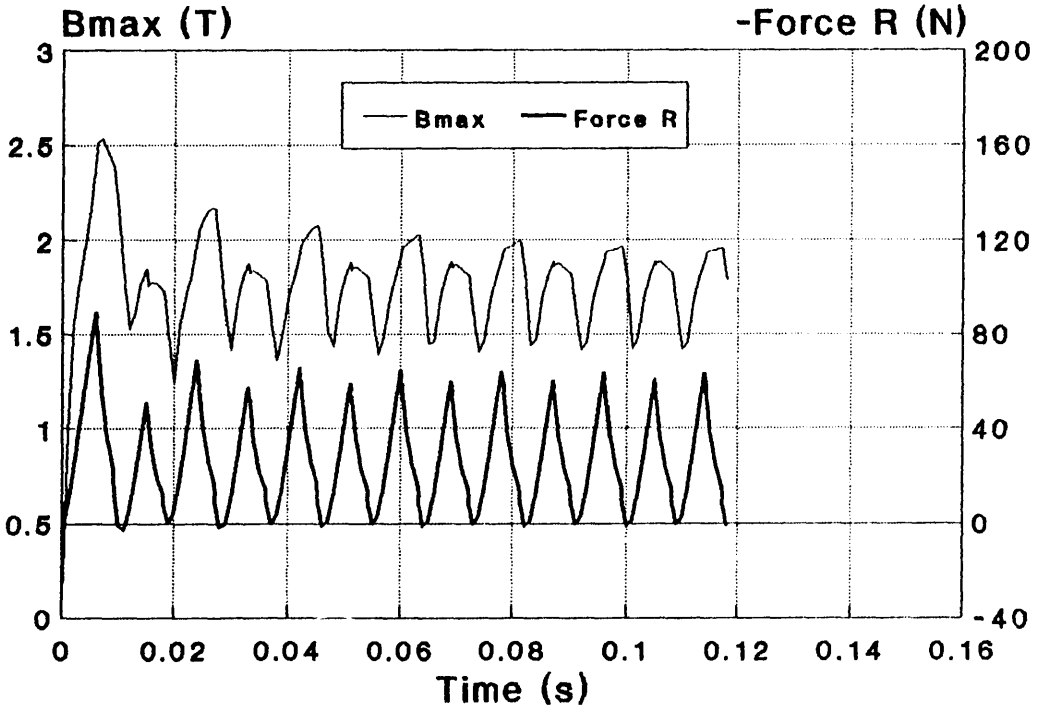

Fig. 5.26 Simulated Maximum Flux Density & Radial Force

also composed of exponentially decaying curves. This is easy to understand since the square wave can be regarded as the sum of many step functions described by (5.7) each with its own time shift. Since the locked state of this actuator can be expressed by a first order differential equation, its response to the step function is an exponential one. This results in the shape of current waveforms seen in both experiment and simulation.

The comparison of the experimental and simulation results is seen in Fig. 5.24. The small square dot '■' represents the current when the input voltage jumps from one voltage level to another. We observe that the simulation results are in quite good agreement with experiment. The *emf* variation is also shown in Fig. 5.24. The difference between the *emf* and the input voltage at each time step is the voltage drop on the winding resistance. Fig. 5.25 gives the time variations of the eddy current in the plunger and its output force in Z direction. As occurs when excited by a sine wave voltage, the output force contains a large amount of double frequency component in the case of square wave excitation too. Fig. 5.26 shows the maximum flux density and the radial force on the plunger wall in the r direction. As introduced in the section 5.4.1, the COUPV will calculate the r.m.s. current, mean output axial and radial force and mean power losses at the final simulation cycle according to the formulae of (5.3), (5.4) and (5.5). Obviously, the square wave power supply will produce considerable harmonic losses in the TLIA. However, this is the simplest way to control the TLIA with adjustable voltage and frequency which maintains the flux linkage a constant.

5.5 Dynamic Behavior & Experimental Verification

The most likely application for the TLIA is bang-bang movement or control. Like most solenoids and magnets, there are only two main operating states. One is the dynamic state while the plunger travels from its starting position to its destination. The other is the steady state after the plunger has reached its destination and remains blocked. The latter case has been investigated in the last section 5.4. The time elapse and response are two basic performance indicators for a fast-acting actuator. For example, when the solenoid is used as a fuel injector or as a relay, the most important thing is how fast it responds to the control commands and how long it takes to reach its target. A traditional analysis is based on the equivalent circuit. This enables the analysis to couple the external electric circuit directly. However this classical method is not adequate to analyse the TLIA as explained before.

The aim of this section is to check the accuracy of the COUPV when it is used for dynamic analysis. It predicts the dynamic characteristics of the TLIA before it reaches its destination. In order to show the versatility of the COUPV, the simulations and the experiments will be carried out under different conditions with different power supplies and different loads. In the section 5.5.1. the sine wave voltage power supply is used to energize the TLIA when it operates with no-load and a spring load. The section 5.5.2 gives the results of the TLIA with no-load and a weight load when excited by a square wave voltage. The simulated result compared with the experiment are quite satisfactory. Therefore, combined with the simulations in the locked state introduced in the last section, it can be concluded that the COUPV can be used to analyze the performances of actuators and motors, under transient and steady state.

5.5.1 Excited by a Sine Wave Voltage

In this section, both experiment and simulation are focused on the solid steel stator TLIA without the slit. The stator winding with 500 turns in series is connected to a switching point controller as shown in Fig. 5.3. The power supply with 213 volts, 50 Hz sine wave is controlled by the switching point controller and then fed to the TLIA. The mass of the copper plunger is 3.682 kg. Its initial displacement is 0 (m).

1. Operating in the No-load State:

Fig. 5.27 shows the transient input current waveform recorded by the digital storage oscilloscope. The pulse wave under the recorded current wave is obtained from the photo-transistor which emits infra light which is reflected by a white and black striped tape. One pulse represents the time required for 2 (mm) displacement of the plunger. From the graph, we can see that it takes 160 (ms) for the plunger to move 0.072 (m). The average speed is about 0.45 (m/s). Its comparison with the simulated results is shown in Fig. 5.28 and Fig. 5.29. The asterisk '*' is used to represent the amplitude of the current corresponding to that in Fig. 5.27. The small square dot '■' represents the displacement recorded by the measured pulse wave in Fig. 5.27. During the first 60 (ms) we see that the displacement obtained from both simulation and experiment are almost the same. Referring to Fig. 5.28 and Fig. 5.29 we find that this is during the time when the plunger is accelerating because the output axial force F_z is quite high. After 60 (ms), F_z decreases rapidly. The plunger still moves forward because of its inertia. During this period of time friction plays a key role so that the velocity goes down gradually. The velocity

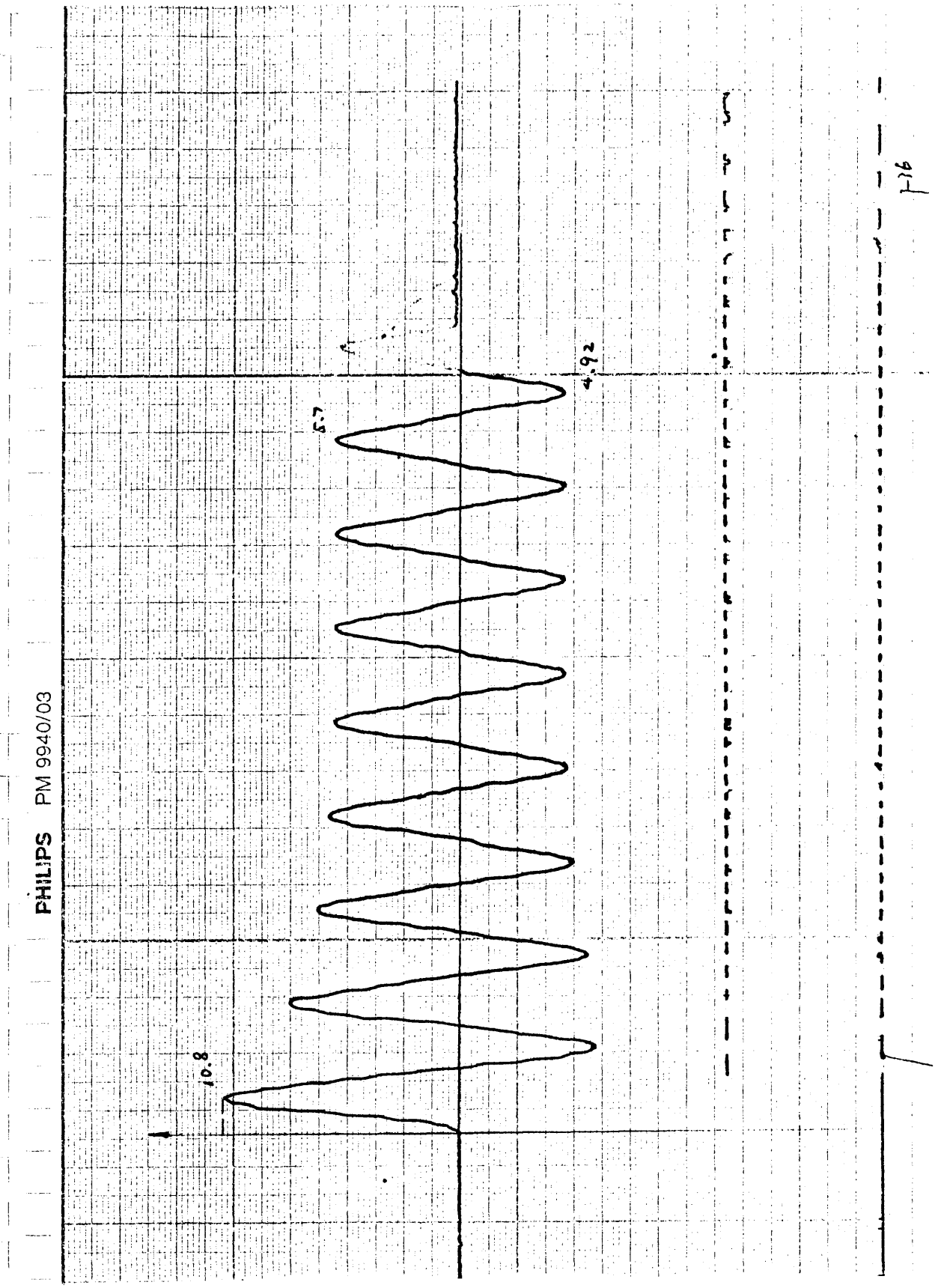

Fig. 5.27 Recorded No-load Current Excited by Sine Wave Voltage

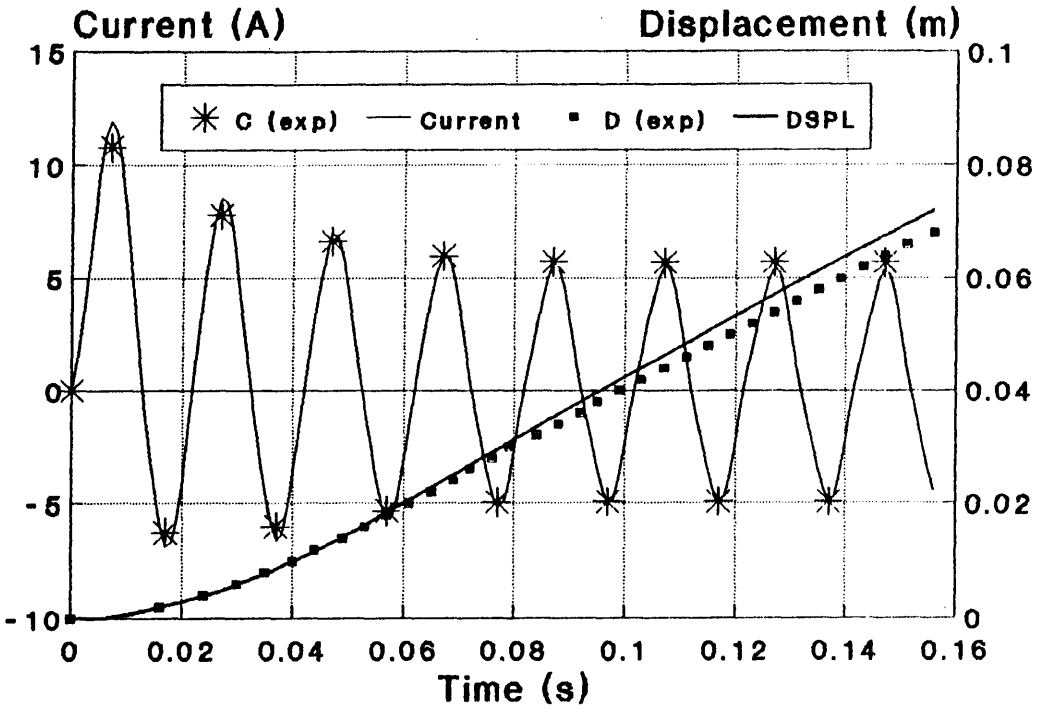

Fig. 5.28 Comparison between the Recorded & Simulated Results

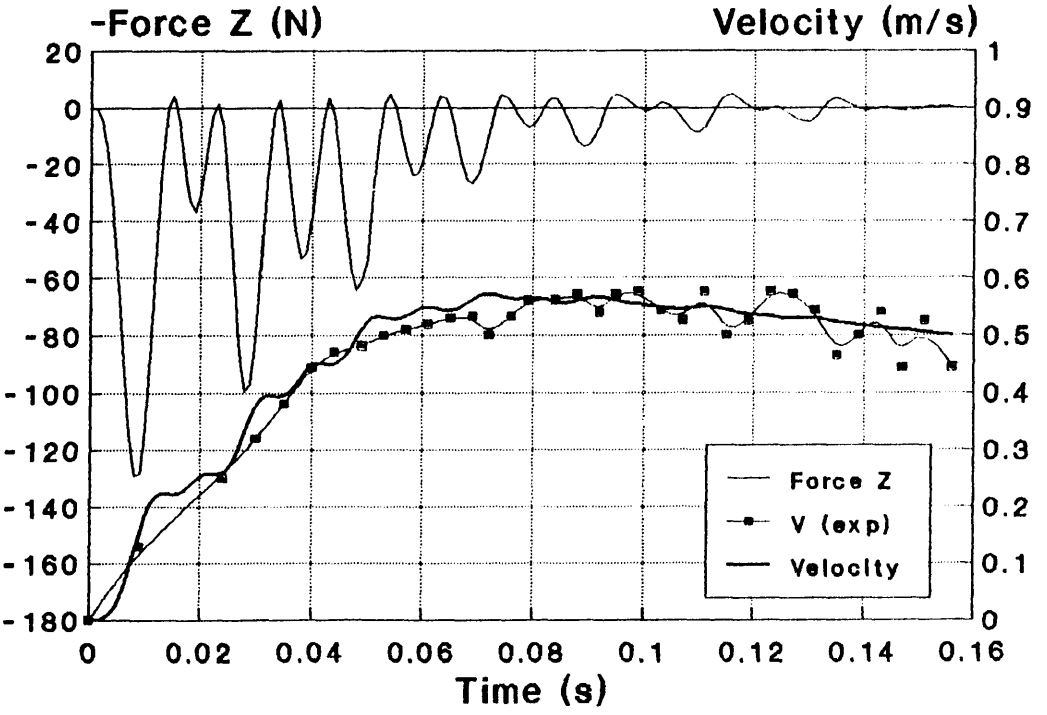

Fig. 5.29 Comparison of Dynamic Input Current & Displacement

indicated by those small square dots are calculated by the measured pulse in Fig. 5.27. As one pulse corresponds to the displacement of 2 (mm), the average speed while the plunger passes through one white and one black strip can be calculated by 2 (mm) divided by the time elapsed. However the accuracy of this method is not high. In Fig. 5.28 we can see that those small square dots are scatted around the simulated results. This can be explained in several ways. Firstly, because the white and black striped tape is stuck on a plate, it is difficult to ensure the smooth finish of the plate surface. Any uneveness will yield incorrect information which makes it difficult for the photo-transistor to distinguish the interface between the black and white strip properly. Secondly, when the plunger moves forward, it will vibrate because of the oscillation of the force, linear bearing, *etc.* This vibration not only happens in the axial direction but also in the radial direction. Therefore, it will influence the response of the photo-transistor. Thirdly, the interface between the white and black strip is not absolutely well defined. Tiny dust particles will lead to incorrect response of the photo-transistor. However, it is noticeable that the shape of the speed variations in Fig. 5.29 closely resembles the simulated result.

Fig. 5.30. illustrates the eddy current in the plunger and the back *emf* in the stator winding. The eddy current decreases a lot after 60 (ms). Referring to Fig. 5.29 it is found that at this moment the plunger has moved forward by about 0.02 (m). As described earlier, the flux in this solid steel stator always goes along the interior surface. Thus only a few flux lines go through beyond 0.02 (m) causing not much eddy currents. Hence not much force is produced too. The *emf* keeps constant during almost the whole dynamic state. It decreases slightly at start of motion because

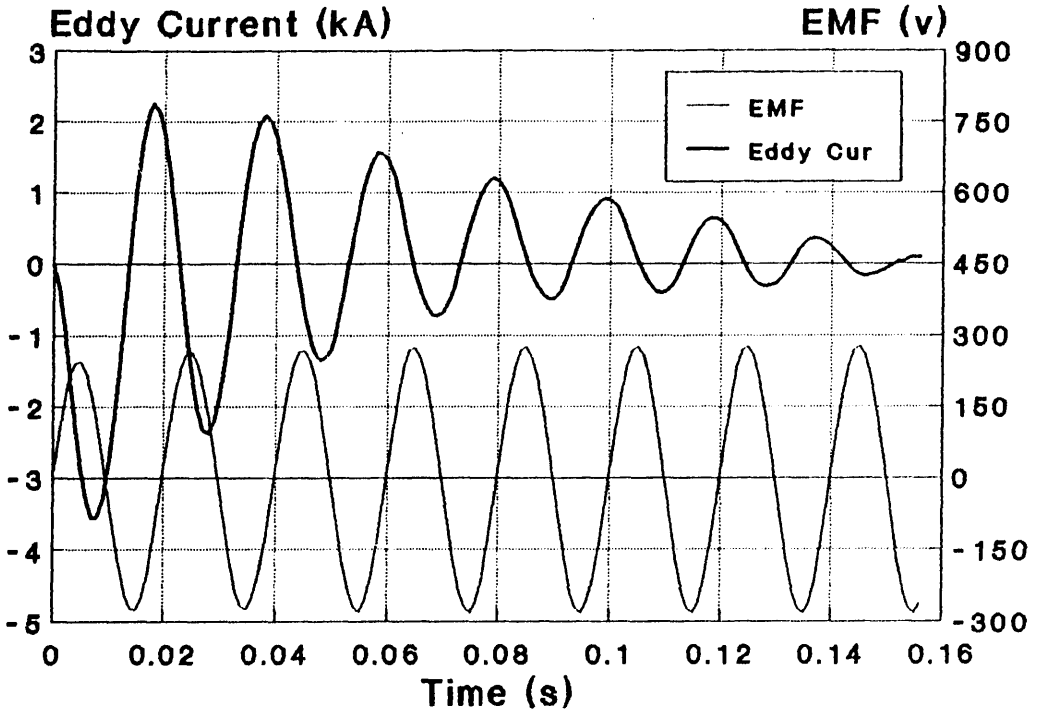

Fig. 5.30 Eddy Currents and EMF

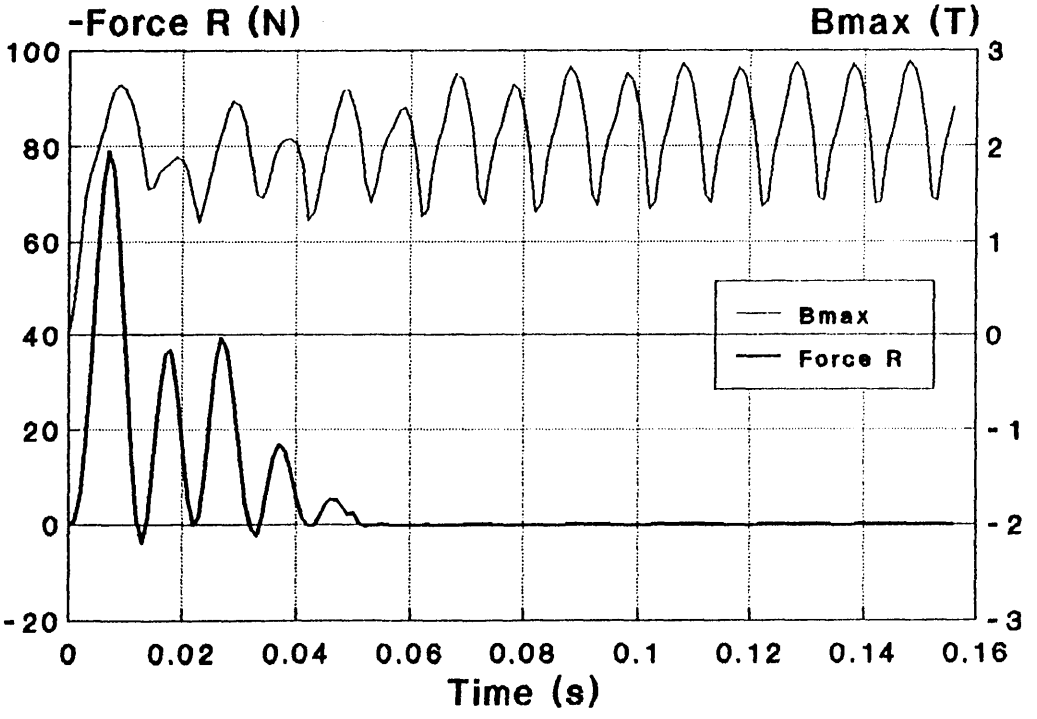

Fig. 5.31 Radial Force and Maximum Flux Density

there is a large transient current when the power is switched on. Fig. 5.31 shows both the maximum flux density and the radial force F_r, which is the product of B_z interacting with the eddy current density. After 60 (ms), it becomes zero. This means that there is almost no axial directed flux density B_z in the plunger. Most of the flux will pass through the slot tooth directly to the mandrel. Therefore, very little force will be produced on the plunger after it moves beyond 0.02 (m). The maximum flux density is around 2.0 Tesla at some local parts. According to the field plots in Fig. 5.12, these may occur in the tip of the slot tooth and the corner located near the connection between the stator and mandrel.

2. Operating with the Spring Load

Fig. 5.32 shows the measured current wave when a spring load is added. The spring coefficient is 100 (N/m). The other conditions remain the same as in the no-load experiment. The comparison between the experimental and simulated results are shown in Fig. 5.33 in which the asterisk '*' represents the current amplitude derived from Fig. 5.32. The small square dot '■' represents the displacement in Fig. 5.32. One pulse from the photo-transistor represents 2 (mm) displacement. Its width indicates the time elapsed for this 2 (mm) displacement.

Fig. 5.34 illustrates the output axial force F_z and the velocity. Unlike the velocity curve in Fig. 5.28, when the axial force F_z reduces to a very small value after the plunger has moved about 0.02 (m) at time instant 60 (ms), the velocity drops rapidly. In this case, the spring will try to pull the plunger back. The results of both the no load experiment and the spring loaded case in which the plunger reaches the position of D = 0.072 (m) are listed in the following table:

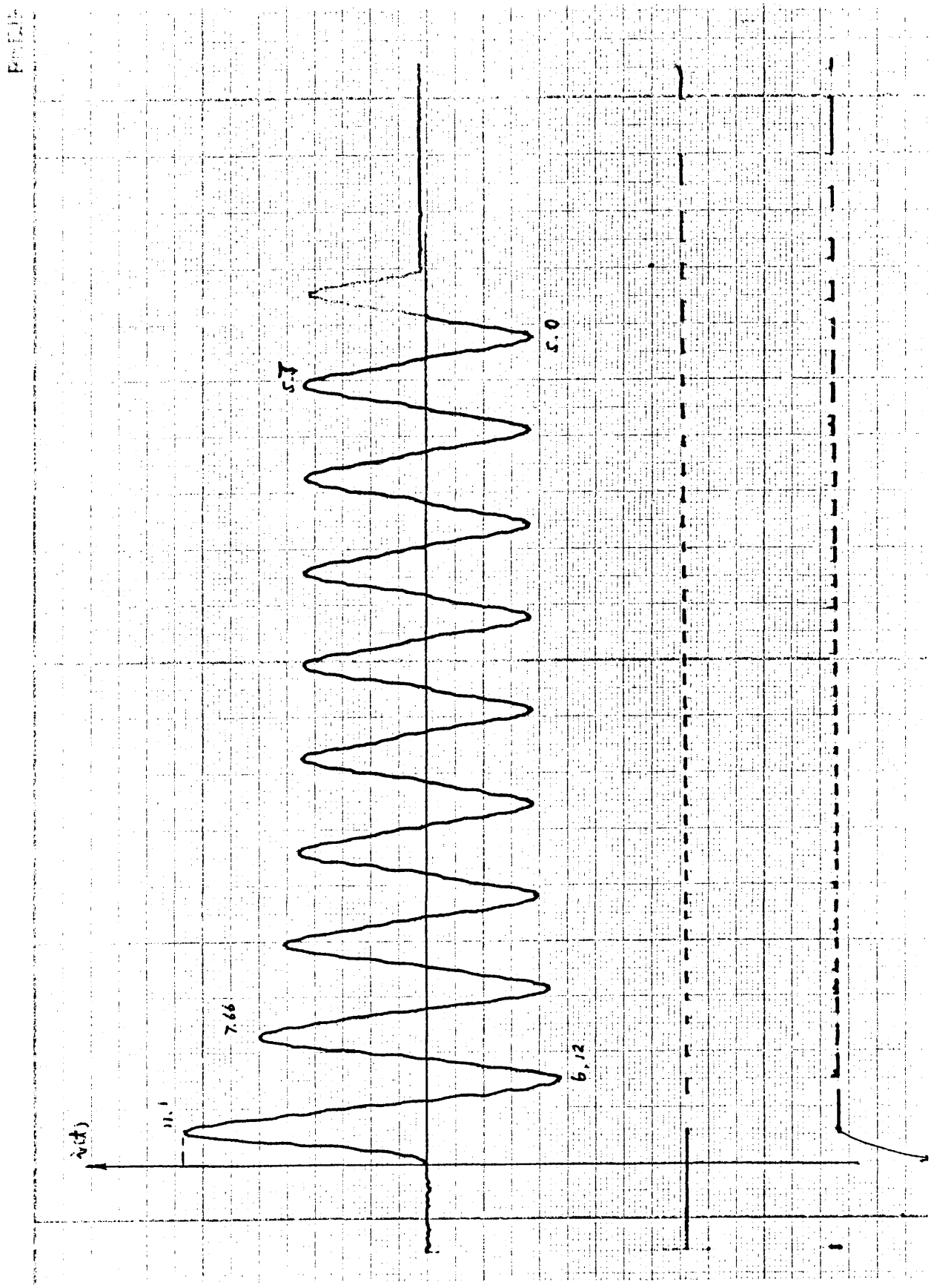

Fig. 5.32 Recorded Current with Spring-load Excited by Sine Wave Voltage

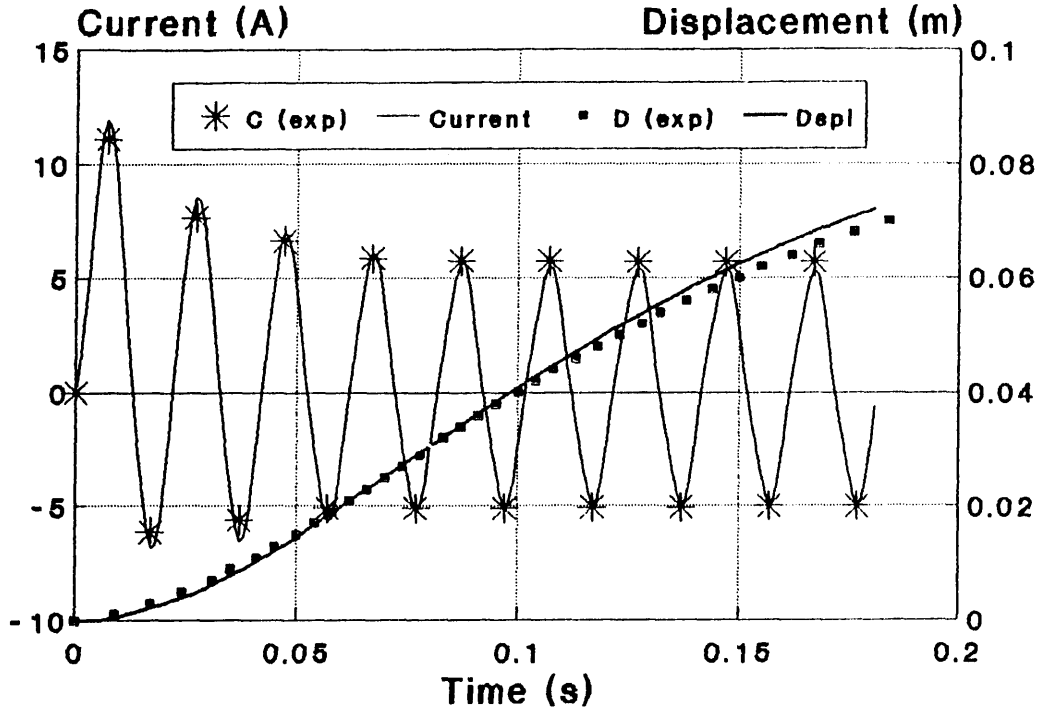

Fig. 5.33 Comparison between the Recorded & Simulated Results

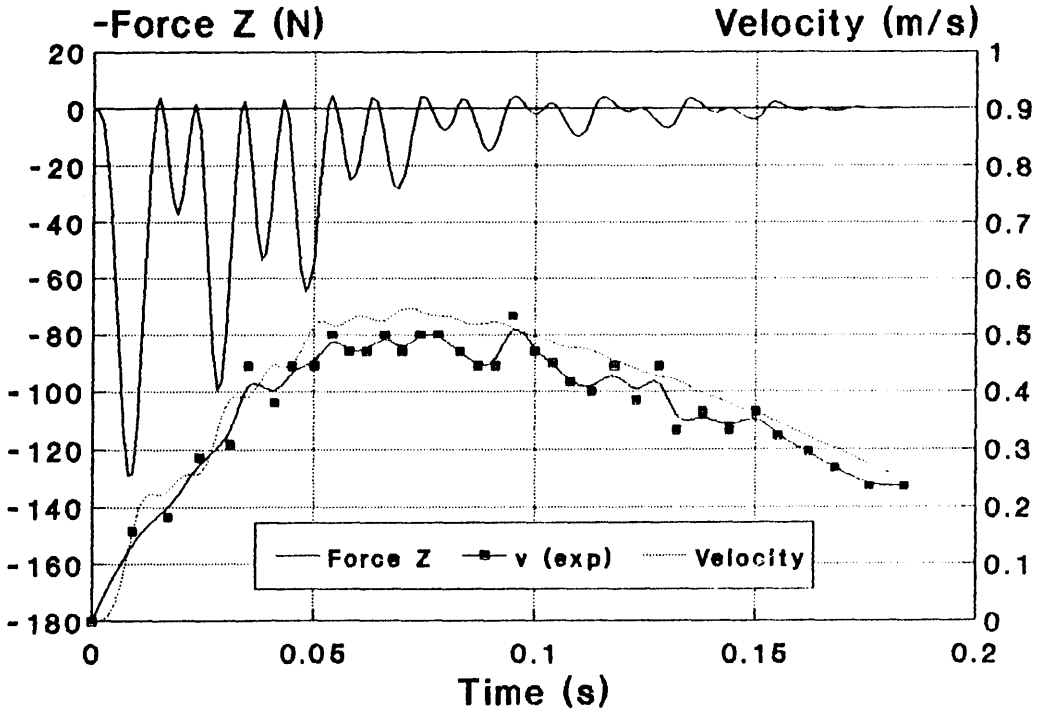

Fig. 5.34 Simulated Axial Force and Velocity

		No Load	Spring Load
Time (s)	Experiment	0.164 (s)	0.185 (s)
	Simulation	0.157 (s)	0.180 (s)
	Error	4.27%	2.7%
Velocity (m/s)	Experiment	0.48 (m/s)	0.24 (m/s)
	Simulation	0.50 (m/s)	0.25 (m/s)
	Error	4.17%	4.17%

Table 5.6 Comparison between Simulated & Experimental Results

Most solenoids, magnets and breakers use springs to pull back their moving parts. The spring, of course, will reduce the speed of the plunger and increase the response time. But it is believed to be the simplest way in bang-bang applications. The COUPV provides quite accurate results to simulate this performance. The maximum error is less than 5%.

5.5.2 Excited by a Square Wave Voltage

In section 5.5.1, the solid steel stator model without slits was excited by the sine wave voltage. In this section, the same machine energised by square wave voltage is investigated. In order to get faster response, only two coils in the stator totalling 340 turns in series are connected to the power supply. The square wave remains the same as shown in Fig. 5.22. The investigation is conducted with no-load and with a weight load.

1. Operating under No-load State

Fig. 5.35 shows the stator current waveform and the pulse waveform associated with the displacement, obtained from experiment. The total time elapsed for the displacement of 72 (mm) is 130.5 (ms). Their comparison with the the simulated results are given in Fig. 5.36 in which the asterisk '*' represents the values of current when the thyristors of the inverter are switched on or off. The small square dot '■'indicates the plunger displacement recorded by the digital storage oscilloscope in Fig. 5.35. They are in good agreement with each other. Fig. 5.37 gives the simulated results of the output axial force F_z and the plunger velocity.

2. Operating with a Weight Load

The experimental arrangement to attach weight loads has already been illustrated in Fig. 5.4. In this experiment, the weight pulled by the plunger is 1.5 (kg). It gives the plunger almost 15 (N) of constant retarding force. The other conditions remain the same as in the last case of no load. The mathematical model for the mechanical system used in the simulation is

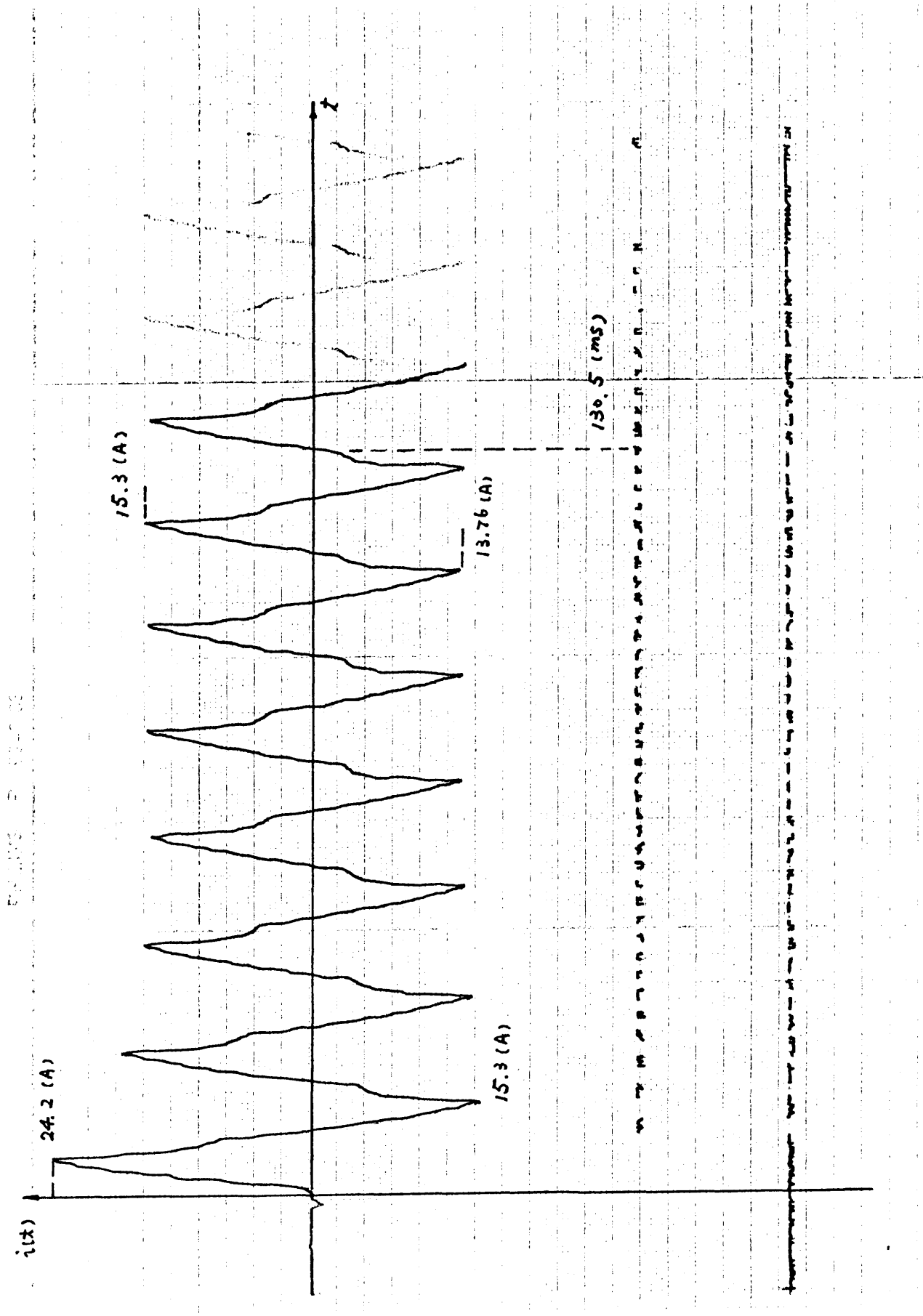

Fig. 5.35 Recorded No-load Performance Excited by Square Wave Voltage

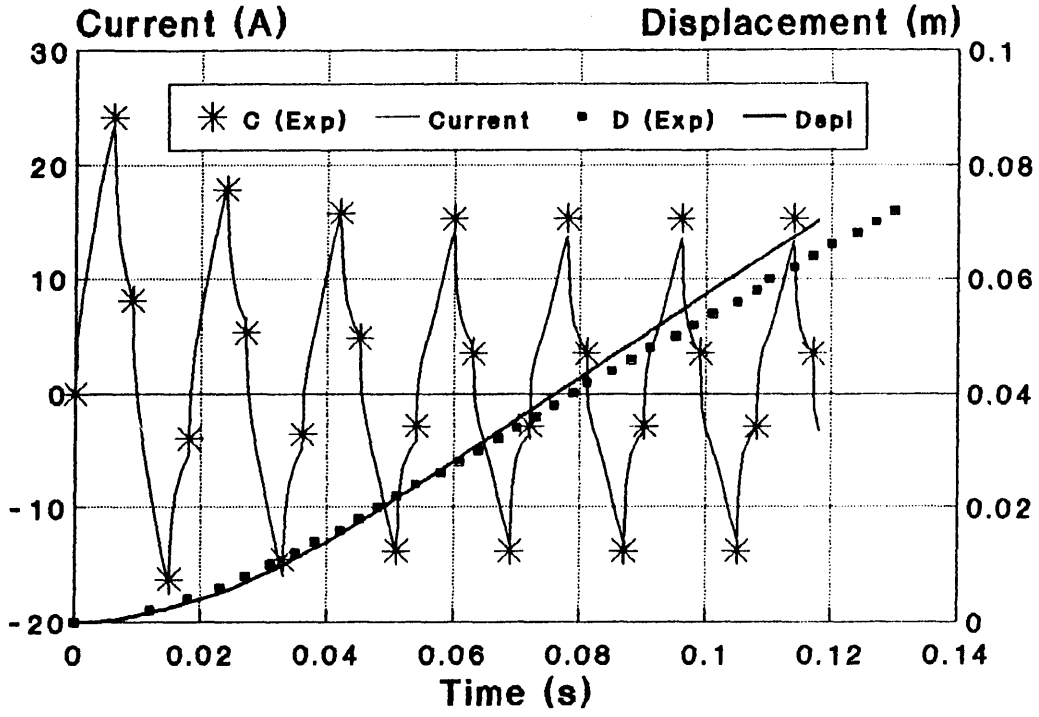

Fig. 5.36 Comparison between the Recorded & Simulated Results

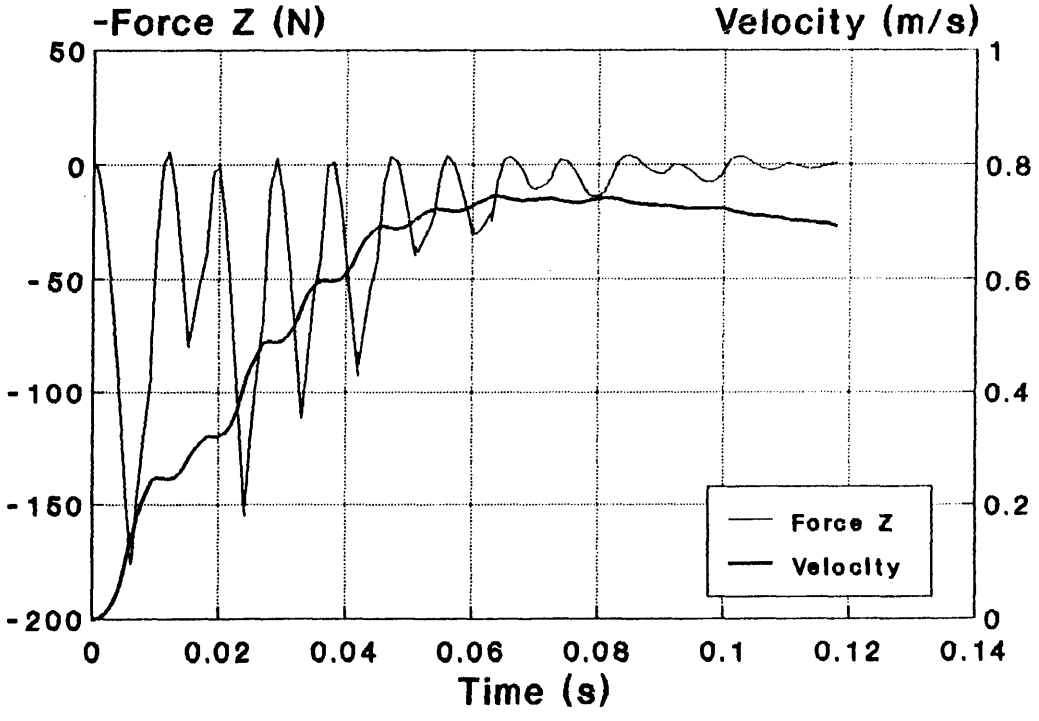

Fig. 5.37 Simulated Axial Force and Velocity

$$(m + m_1)\cdot\frac{d^2z}{dt^2} + D\cdot\frac{dz}{dt} + K\cdot z + m_1\cdot g = F_z \qquad \cdots(5.8)$$

where, m is the mass of the whole plunger,

m_1 is the mass of the weight and K=0 is the spring coefficient.

Fig. 5.38 shows the measured stator current wave and the pulse signal representing the movement of the plunger. Its comparison with the simulated results can be found in Fig. 5.39 and 5.40. In these two graphs, one can see two important characteristics of this solid steel stator TLIA. One is that the starting axial force F_z is quite large. The first amplitude of the force wave is more than 150 (N) which is 10 times more than the weight 1.5 (kg). Therefore, the starting characteristic is quite good. The plunger will start to move within a very short time. This is an advantage. The other is its shortcoming. After the plunger moves beyond 60 (mm), the axial output force F_z becomes very small and is too small to push the plunger forward. The weight will pull back the plunger until the output force balances the weight. Fig. 5.41 shows this balance obtained by the experiment.

The experiment has been carried out under the following conditions:

power supply ---- 123 (v) (sine wave);

switching ---- $\varphi = 0$ (controlled by the switching point controller as shown in Fig. 5.4);

and only one coil of 180 turns is connected to the power supply.

The choice of this combination is to obtain the largest output force with the permitted input current. The transient movement of the plunger with different weights is plotted in Fig. 5.41. When the 6 (kg) load is added

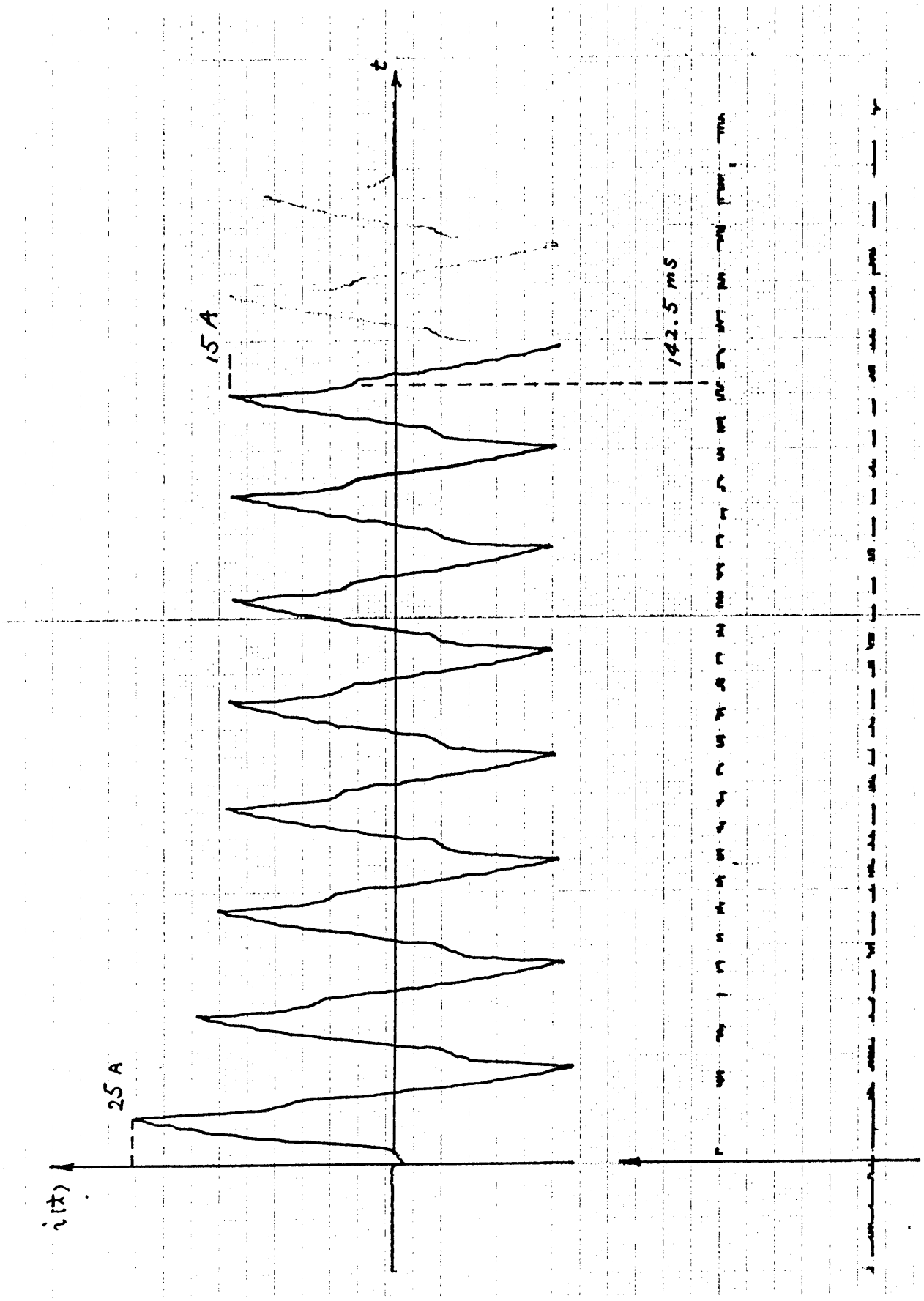

Fig. 5.38 Recorded Transient Performance with Weight-load

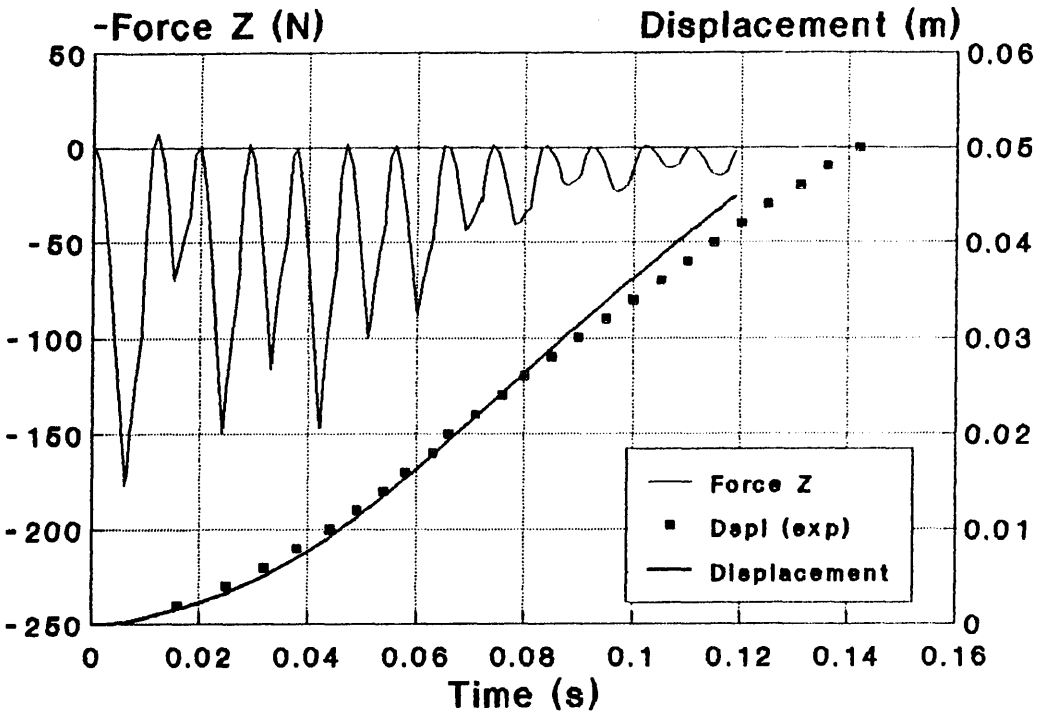

Fig. 5.39 Comparison between the Recorded & Simulated Results

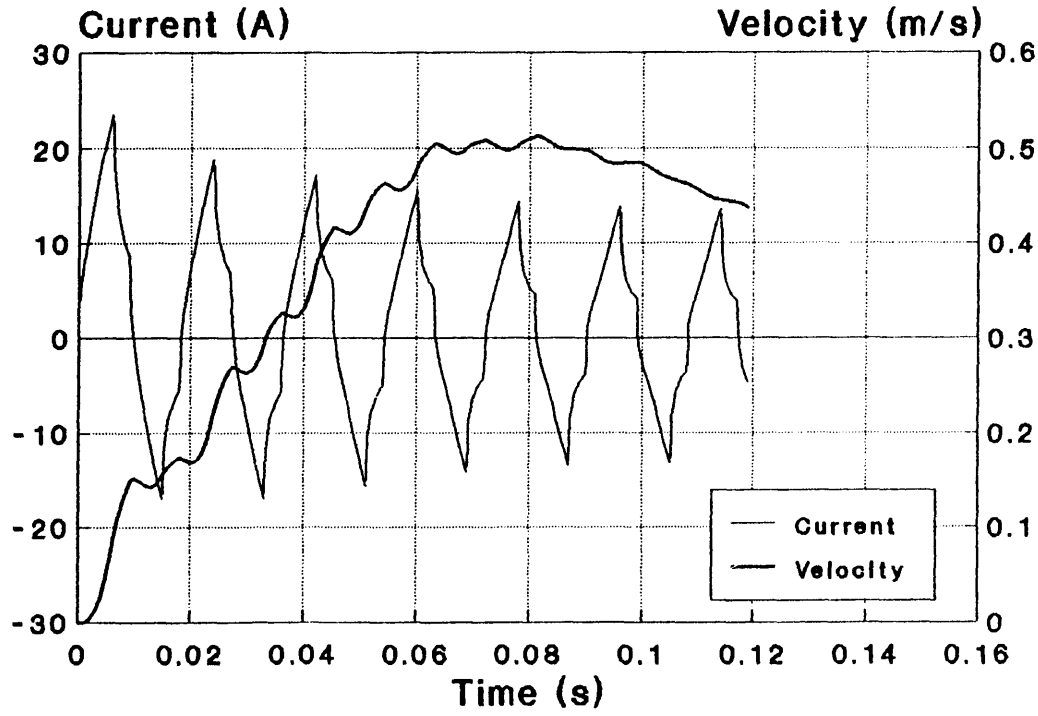

Fig. 5.40 Simulated Stator Current and Velocity

the plunger can only move 15 (mm). Then the plunger will be positioned at this point. This means the TLIA can be used in position control. If we increase the supply voltage, obviously the output force will increase and the equilibrium point will be more than the displacement of 15 (mm). This control characteristics will be discussed in the next chapter.

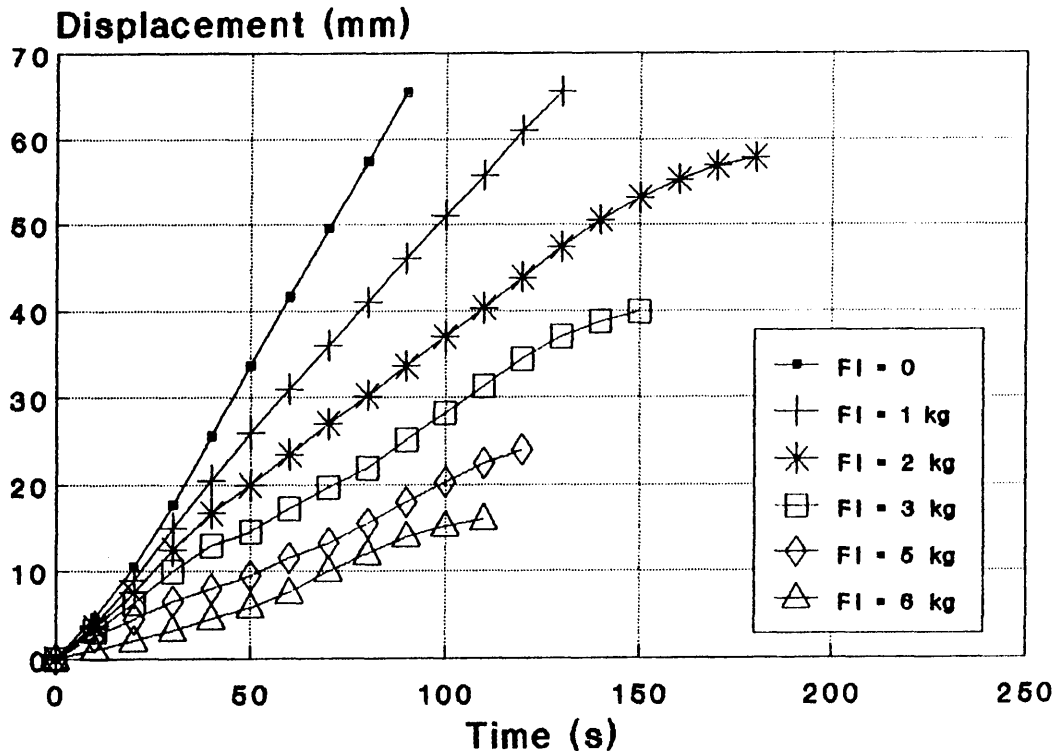

Fig. 5.41 Stroke versus Time with Pulling Weight

5.6 Two Stage TLIA

In Chapter 2, the steady state characteristics of the two stage TLIA was studied. Using proper control, *i.e.* switching on the TLIA one stage after another, the stroke can be increased. Its drawback is that between the two stages there is a concavity in which the output force is very low. If the load is heavy, the plunger may be stuck in the concavity. In fact, in this part, the TLIA loses its control. However, for a free plunger or a small load, this is a good way to extend the stroke. A very good example is the θ gun. The θ gun may be composed of several stages so that its projectile can be accelerated at each stage.

The purpose of this section is to ascertain if the COUPV is able to simulate the performance of the two-stage TLIA with reasonable accuracy. The experiment and simulation are conducted on the following model under the stated conditions. The experimental scheme can be seen Fig. 5.4. The plunger is in a free state with its initial displacement $D(0) = 0$ (m). The winding in the first stage with its two coils in series totalling 340 turns is connected to a closed switch of the relay. The winding in the second stage with its two coil in series totalling 320 turns is connected to an opened switch of the same relay. The relay is controlled by a photo-transistor which is mounted in the position of $D = 0.08$ (m). When the plunger passes this position the relay will turn off the power connected to the first stage and turn on the power to the second stage. The waveform of the power supply is illustrated in Fig. 5.42 which can be described by the formula (5.7) as follows:

$$U_s(t) = U_m \cdot \sum_{n=0,\ 1,\ 2,\ \ldots}^{\infty} \{[s(t - n \cdot T_1) - s(t - n \cdot T_1 - n \cdot T_e)]$$

$$- s[t - (n+1)\cdot T_1] + s[t - (n+1)\cdot T_1 - (n+1)\cdot T_e]\Big\}$$

$$= 350\cdot \sum_{n=0,\ 1,\ 2,\ ..}^{\infty} \Big\{[s(t - n\cdot 0.008) - s(t - n\cdot 0.008 - n\cdot 0.005)]$$

$$- s[t - (n+1)\cdot 0.008] + s[t - (n+1)\cdot 0.008 - (n+1)\cdot 0.005]\Big\}$$

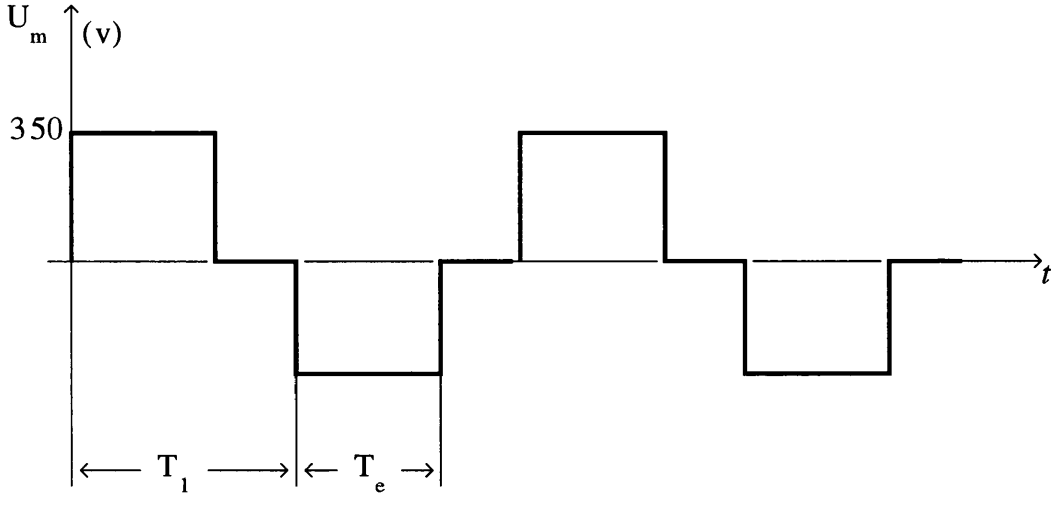

Fig. 5.42 The Supply Voltage for the Two Stage TLIA Experiment

Fig. 5.43 shows the recorded results from the experiment. The plunger takes 158 (ms) to move 0.118 (m). The comparison between the experiment and simulation is shown in Fig. 5.44. In the simulation, it takes 152 (ms) for the plunger to move 0.118 (m). The simulated current waveform and velocity are plotted in Fig. 5.45. Fig. 5.46 illustrates the flux density distribution during the time before and after the power supply connections change from the first stage to the second stage. The plots (a) and (b) give the flux density distribution just before the first stage is switched

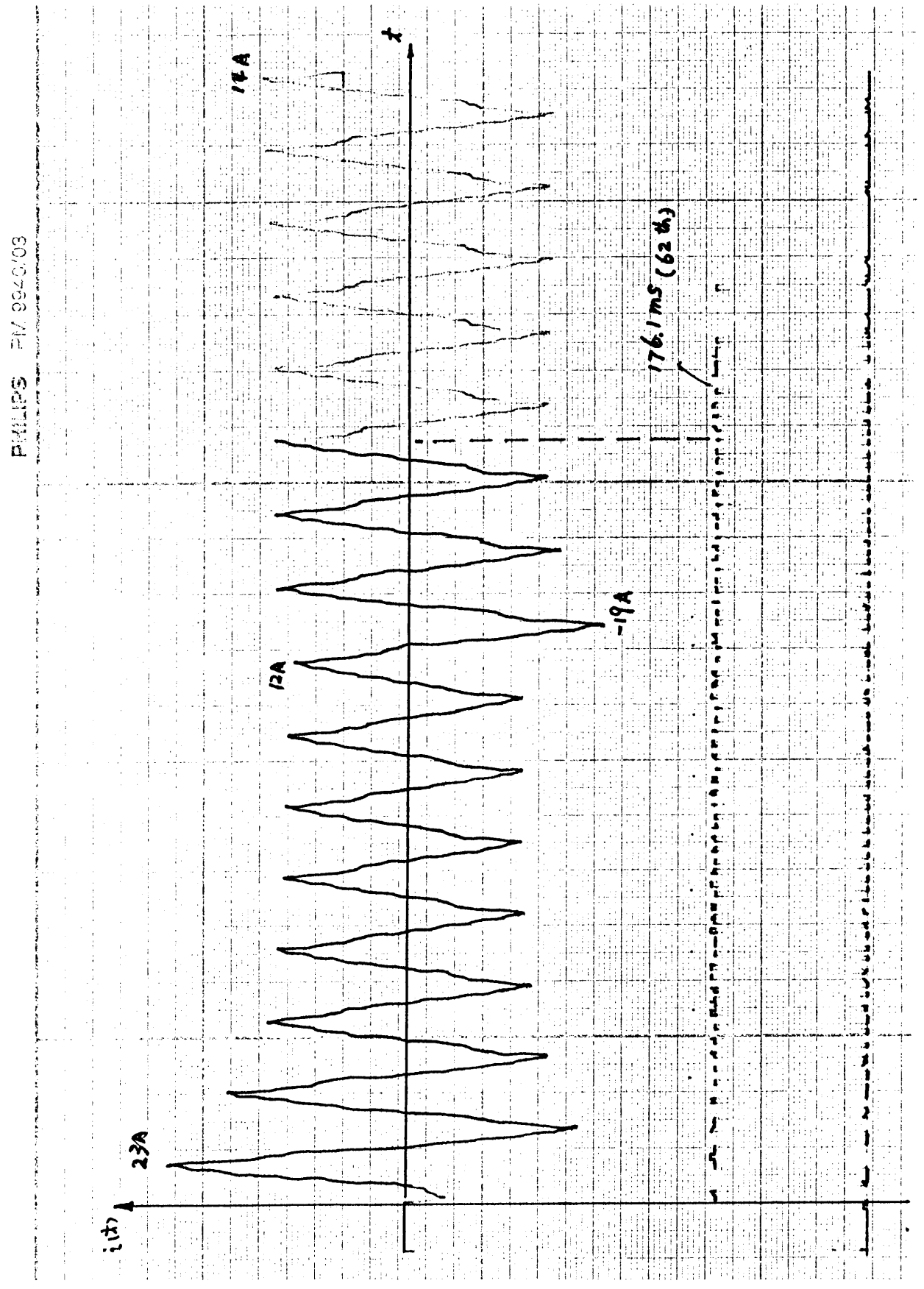

Fig. 5.43 Experimental Results of Current Wave & Displacement

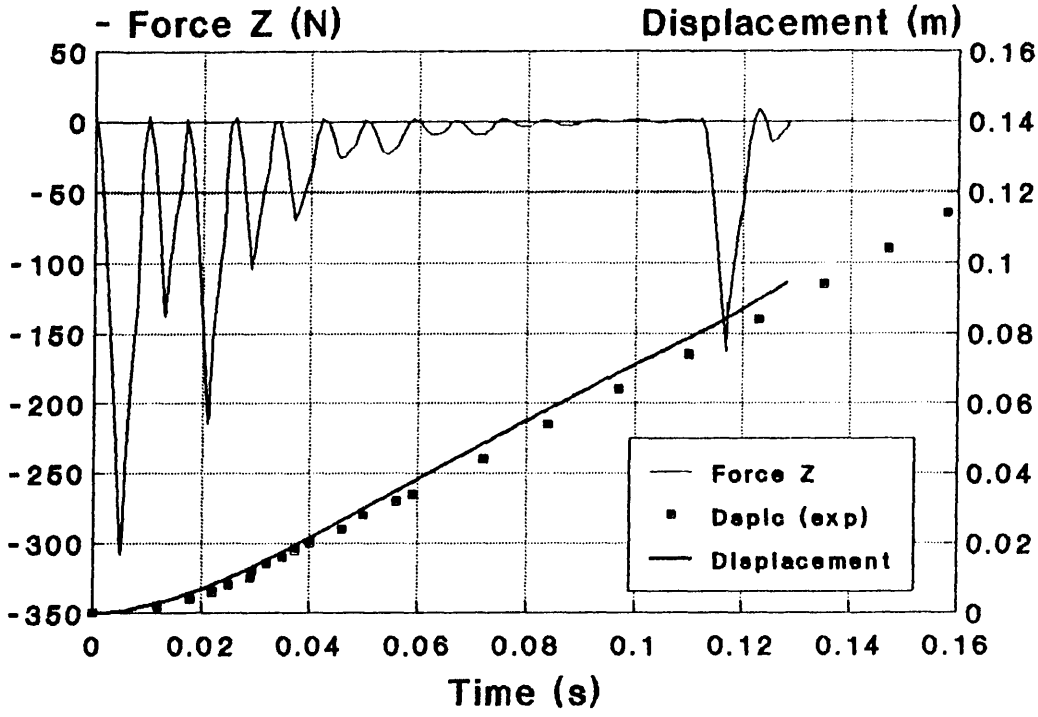

Fig. 5.44 Axial Force & Displacement Comparison

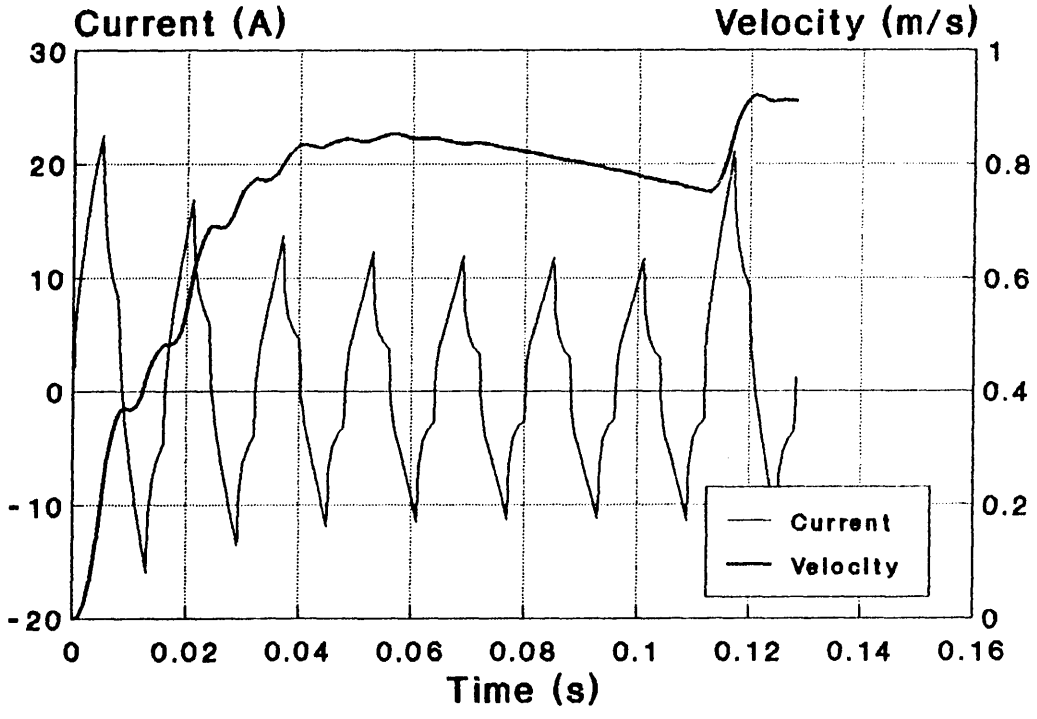

Fig. 5.45 Simulated Current Waveform & Velocity

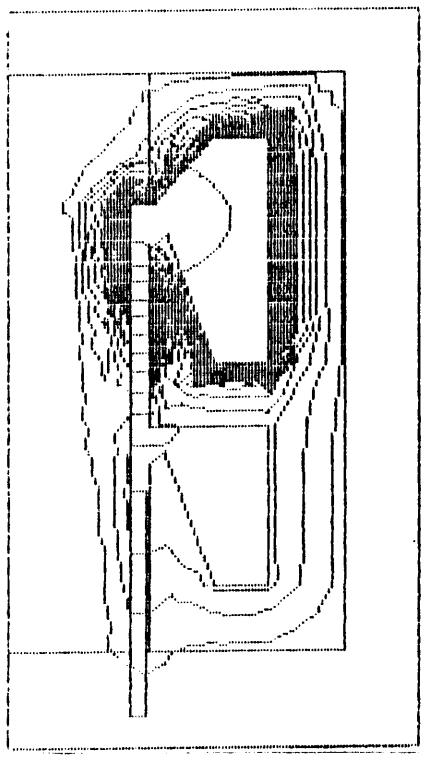

(a)

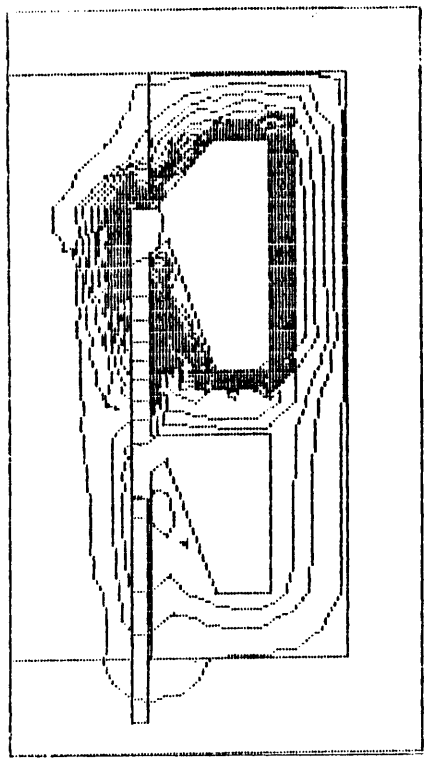

(b)

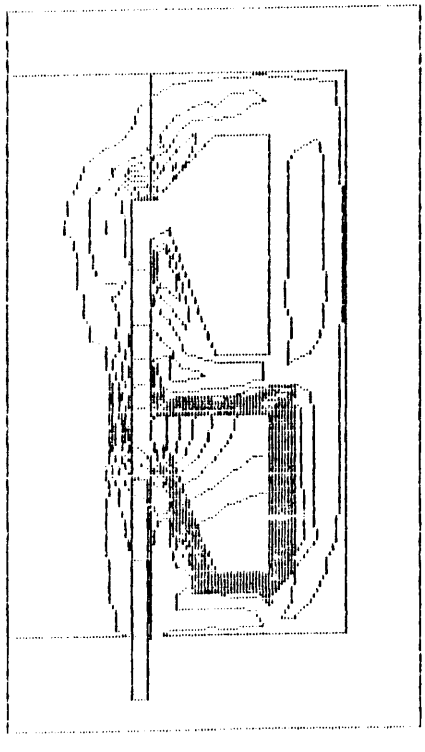

(c)

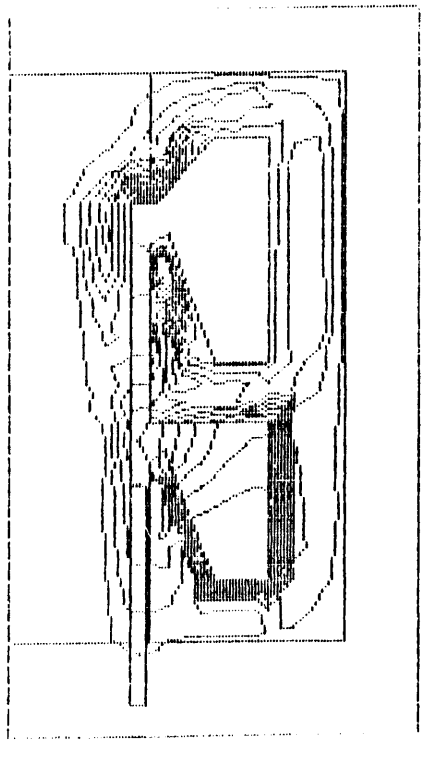

(d)

Fig. 5.46 Flux Density Distribution for Two Stage TLIA

off. The plots (c) and (d) give the flux density distribution just after the second stage is switched on. This switching instant in the experiment and simulation is chosen when the plunger is at a displacement of about 80 (mm). At that moment, the axial force produced by the first stage is almost equal to zero. The plunger moves forward due to its inertia. The second stage then gives the plunger another axial force and the plunger starts to accelerate again.

It is quite easy for the COUPV to simulate the procedure of changing the power connection from the first stage to the second stage. When the plunger reaches the switching position, the equation (4.1) and (4.2) will be applied to the second stage in which only resistance R, the number of the turns of the winding N_c and the section area A_s occupied by the stator winding need to be changed. In every time step, the COUPV will execute the procedure shown below until the power supply has been connected to the second stage.

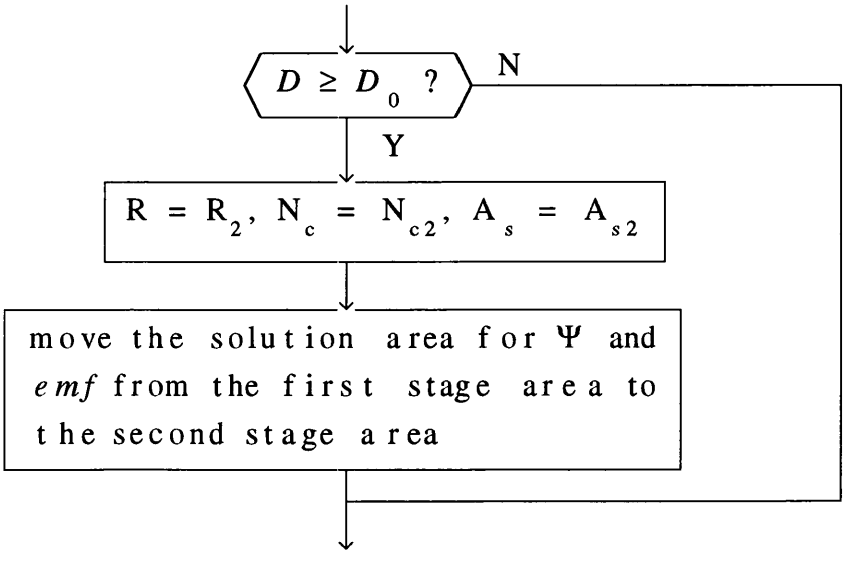

In the above flow chart, R_2, N_{c2} and A_{s2} are the resistance, winding turns and cross section area of the second stage.

5.7 Conclusions

In this chapter the validation of the COUPV has been carried out supported by experiments. Both experimental and numerical investigations are conducted under various conditions such as different power supplies including sine wave and square wave voltage excitations, different loads including no-load, springs and weights and different excitation arrangements including single stage and two stage excitation. In order to avoid uncertainty, a solid steel stator TLIA has been used since it is a real axisymmetric model. The results obtained from the experiment and simulation are in good agreement with each other.

The shielding effect and the inner end effect of the conducting plunger play a key role in the TLIA performance. They have been further confirmed in this chapter by the time-stepping FEM. These two effects also make it extremely difficult to use the traditional methods to analyze the TLIA. The simulation results confirm that the flux density distribution of the TLIA is quite unusual. It is very difficult to separate its leakage and main flux paths in the magnetic circuit. Therefore, the traditional methods of estimating the magnetising and leakage reactances is not suitable in this case.

The COUPV is believed to be a powerful and reliable tool for the CAD of various electromagnetic devices, which may include eddy currents, moving members and various voltage power supplies. It has demonstrated its abilities to predict and estimate both steady and dynamic state performances of the TLIA.

CHAPTER 6 STUDY OF EDDY CURRENTS IN SOLID STEEL TLIA

6.1 Introduction

Although the laminated stator construction is highly desirable for the TLIA, it is difficult to machine and assemble especially in small sizes. When a small TLIA is preferred, the solid steel stator construction is simpler and cheaper. Therefore, the study of a solid steel stator TLIA will not only provide verification of the COUPV but also provide useful information on a prototype.

In order to understand the eddy current effects in the solid steel stator, two search coils are used to observe the flux density distribution along the airgap and the mandrel. The function of the radial slits is also investigated. Evidently, these slits will reduce eddy current losses in the solid steel stator. Experiments are carried out for both stators with 8 and 16 slits. The presence of the slits makes the simulation more difficult as the problem becomes 3 dimensional. An equivalent conductivity is deduced so that the COUPV can be used directly. This approximate method proves to be quite effective and leads to reasonable accuracy of results.

As described in earlier chapters the main disadvantage of the TLIA is that its thrust falls quickly with displacement. The reason for this is that the conducting plunger shields the flux path. In order to let the flux go through the plunger directly, a model with an iron clad plunger is introduced. The simulated results show that this method greatly reduces the flux leakage and improves the force-stroke characteristics of the TLIA.

6.2 Flux Distribution in a Solid Steel Stator TLIA

If the TLIA is made of laminations then in the absence of the plunger, the flux density will be almost evenly distributed in the airgap under the laminated tooth, because the permeability of lamination is much larger than that of the airgap. Fig. 2.8 has confirmed this fact in which the plunger is locked near the exit end of the TLIA. Furthermore, it has been proved that flux density will not only evenly distribute in the air gap of the first stage but also in the second stage according to the formula (2.14) and Fig. 2.5c. Under such conditions the output axial force remains high over both the first and second stage regions, even though only the first stage is excited by a constant current source.

However, for a solid steel stator whether it has slits or not, it is impossible to have an evenly distributed flux density in the airgap. Fig. 5.12 shows the skin effect which makes flux gather at the interior surface of the stator against the winding. In order to confirm this conclusion, a search coil is used to measure the radial flux density along the airgap of the solid stator TLIA. The measurement is made with the winding carrying a constant A.C. current of 1.5 (A). Fig. 6.1 shows the results obtained from the measurements in which the *curve (1)* represents the case when only the first stage is fed by A.C. current of 1.5 (A). It declines very quickly along the axial direction. Only a very small amount of flux density exists in the second stage region. Most of the flux just circles round the first stage. The *curve (2)* represents the flux density distribution when only the second stage winding is energized by A.C. current of 1.5 (A). The maximum flux density appears near the slot mouth of the second stage. Flux density declines in the directions toward both sides. All these results confirm

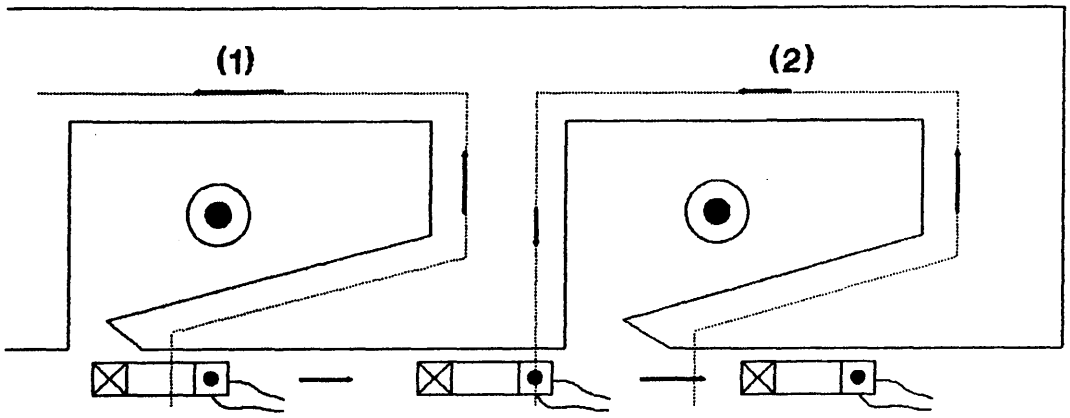

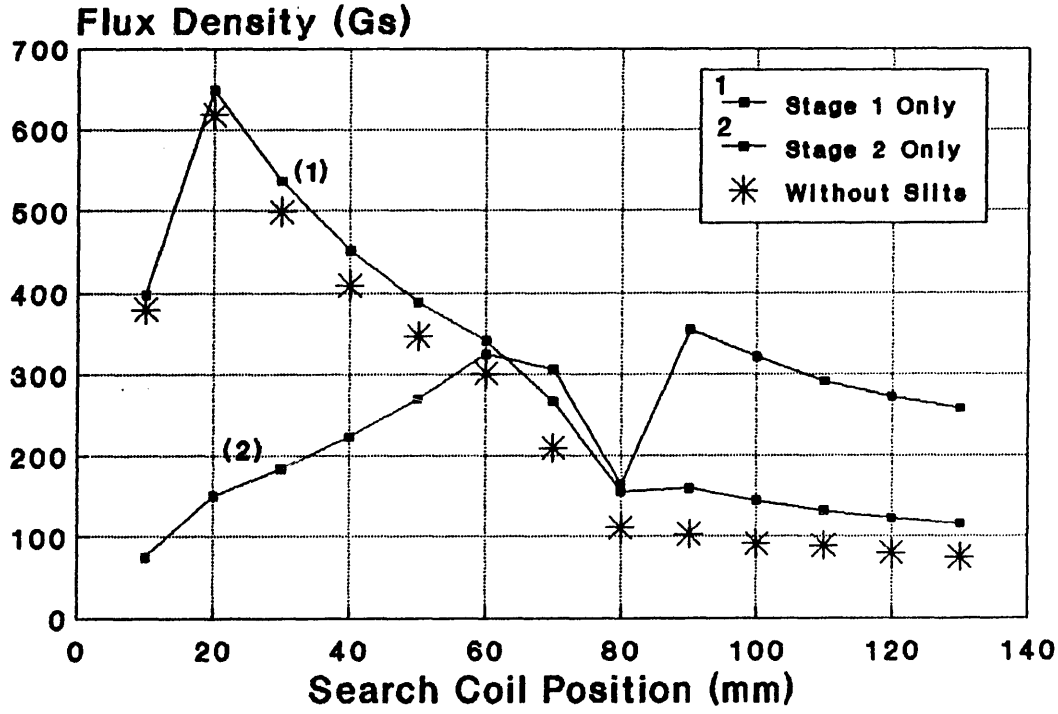

Fig. 6.1 Flux Density Distribution Measured by Search Coil

(Single Stage Energisation only)

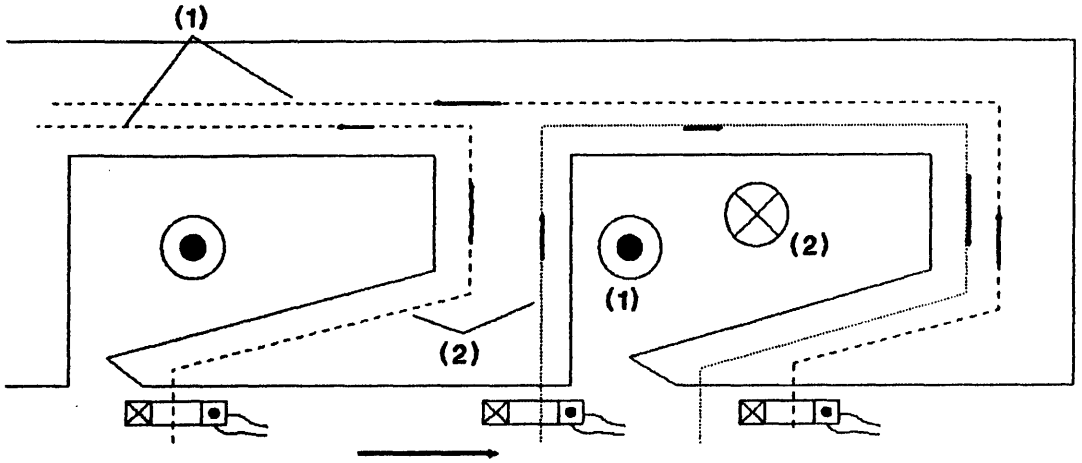

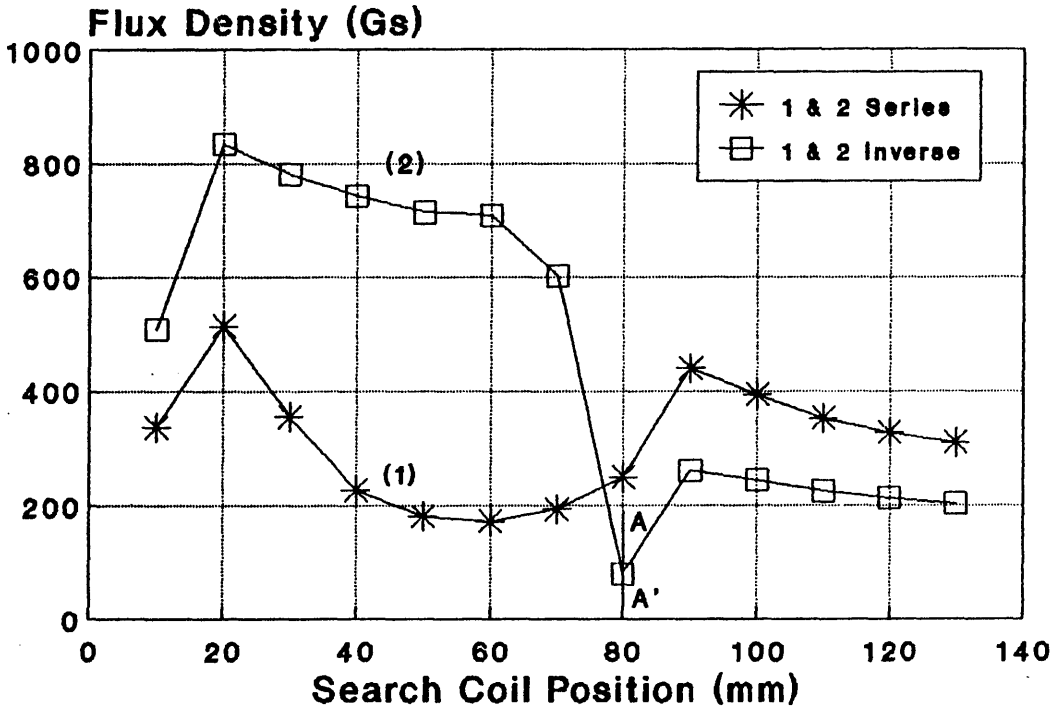

Fig. 6.2 Flux Density Distribution Measured by Search Coil

(Two Stage Energisation in Series)

that flux is concentrated along the interior surface of the solid steel stator. Therefore, besides causing eddy current losses, another disadvantage is that the thrust will decline along the axial direction very sharply in a closed slot solid steel stator TLIA.

Additional properties can be found from the experiment when two windings in two different stages are connected in series either with the same or opposite magnetic polarities. Fig. 6.2 shows these two cases. When the magnetic polarities of the windings are opposite to each other, there will be higher flux density under the first stage tooth, seen in the *curve (2)* of Fig. 6.2. However, the radial flux density under the second stage tooth will have an opposite direction. Although this can not be seen in the flux density curves as it is excited by an A.C. power supply, it is easy to visualise it with a pre-determined positive direction. In Fig. 6.2 the flux represented by the *curve (2)* to the right of the vertical line AA' has an opposite direction to the flux on the left side. When the polarities of the windings are the same, the flux distribution will have the shape of *curve (1)*. In Chapter 2 it was mentioned that no advantage was to be found by exciting two windings of the two stage TLIA together. Here, it is confirmed further with the solid steel stator model.

Fig. 6.3 gives the measured results when a second search coil is moved along the mandrel to obtain the back *emf* induced in it, which obviously is proportional to the axial flux density in the mandrel. Therefore, the curves in Fig. 6.3 also represent the axial flux density distribution. The *curve (1)* shows the results when only the first stage is excited by 1.5 (A) A.C. current. Most flux flows to the tip of the tooth and into the mandrel so that the measured *emf* declines very quickly as the search

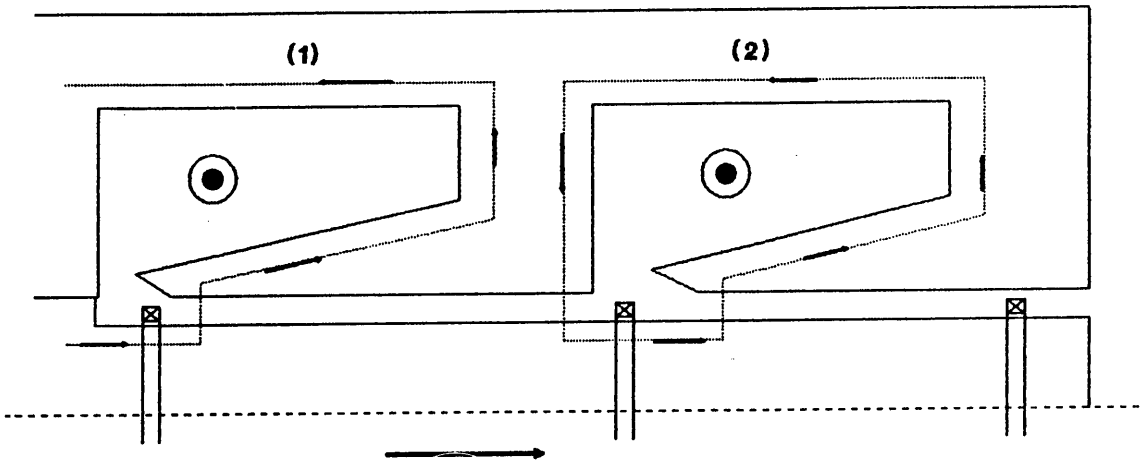

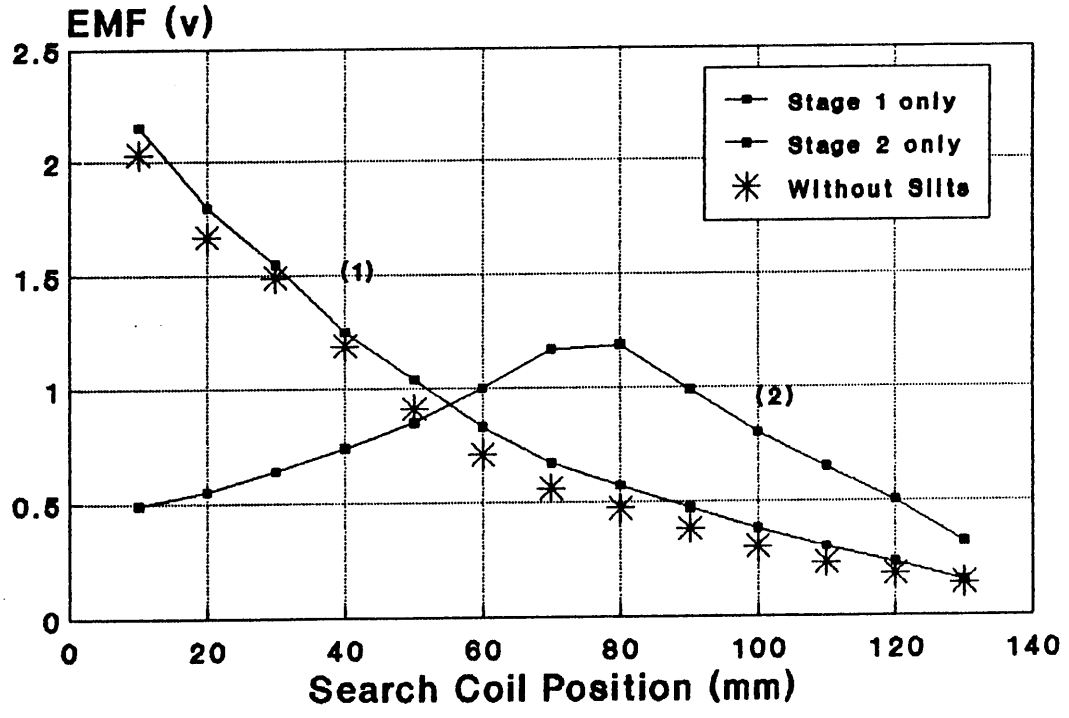

Fig. 6.3 Axial Flux Density in the Mandrel

coil moves outwards. The *curve (2)* gives the *emf* versus the search coil position when only the second stage is fed by 1.5 (A) A.C. current. In this case, the maximum *emf* occurs when the search coil is under the second slot mouth region. The measured *emf* decreases on either side in the axial directions.

In both Fig. 6.1 and Fig. 6.3, the small asterisk '*' represents the case when the first stage is replaced by a solid one without slits. When the coils are excited by 1.5 (A) A.C. current, the only difference is that the measured radial flux or *emf* decreases slightly. Their distributions are similar in shape to the TLIA in which both stages have the radial slits.

From the above measurements, one can arrive at three major conclusions:

(1) A major difference between the laminated and the solid steel stator is that the skin effect plays an important role in the latter. It makes the flux distribution in the airgap uneven when the TLIA has a nearly closed slot mouth. Most of the flux just gathers near the slot mouth. Therefore, its is impossible to obtain uniform thrust throughout the whole stroke.

(2) The phenomenon indicates that the closed slot mouth is not suitable for the solid steel stator. Furthermore, because the flux produced by each stage mainly circles its own stage, to energise both two stages at the same time is not desirable.

(3) Not much difference has been found in the flux distribution between the solid steel stator TLIAs with and without the slits since the measured flux distribution curves have similar shapes.

6.3. Radial Slits for Suppressing Eddy Losses

In Fig. 5.2 a solid steel stator with eight radial slits has been introduced for the purpose of reducing eddy currents and eddy current losses. Further investigations of the effects of the slits by increasing the number of radial slits to 16 is conducted in this section.

Fig. 6.4, 6.5 and 6.6 show the experimental results when three types of solid steel stator TLIAs are energized by 215 volts 50 Hz sine wave power supply. Except the slits, the other conditions remain the same as shown in Fig. 5.1. There are three main findings:

(1) The model without slits requires more input current than the models with slits. However, the difference between the model with 8 slits and one with 16 slits is quite small. Both of them require almost the same amount of input current;

(2) Although the input currents required by the 3 models are different, there is not much difference in their output axial forces. This means that the main effect of the solid steel is to increase eddy currents.

(3) The eddy current losses in the models have the same characteristics as the input current. Fig. 6.6 shows that the average eddy current losses in the whole stroke of the model without slits is about 550 (W) while the model with slits is only about 300 (W).

The conclusions from the above experiment are important in two aspects. First, the slits do suppress the eddy currents. Second, the number of slits does not affect the eddy currents and losses significantly, if l_s and l_t are much more than the penetration depth Δ in which l_s is the arc length of one section of the stator and l_t is the thickness of the stator wall as

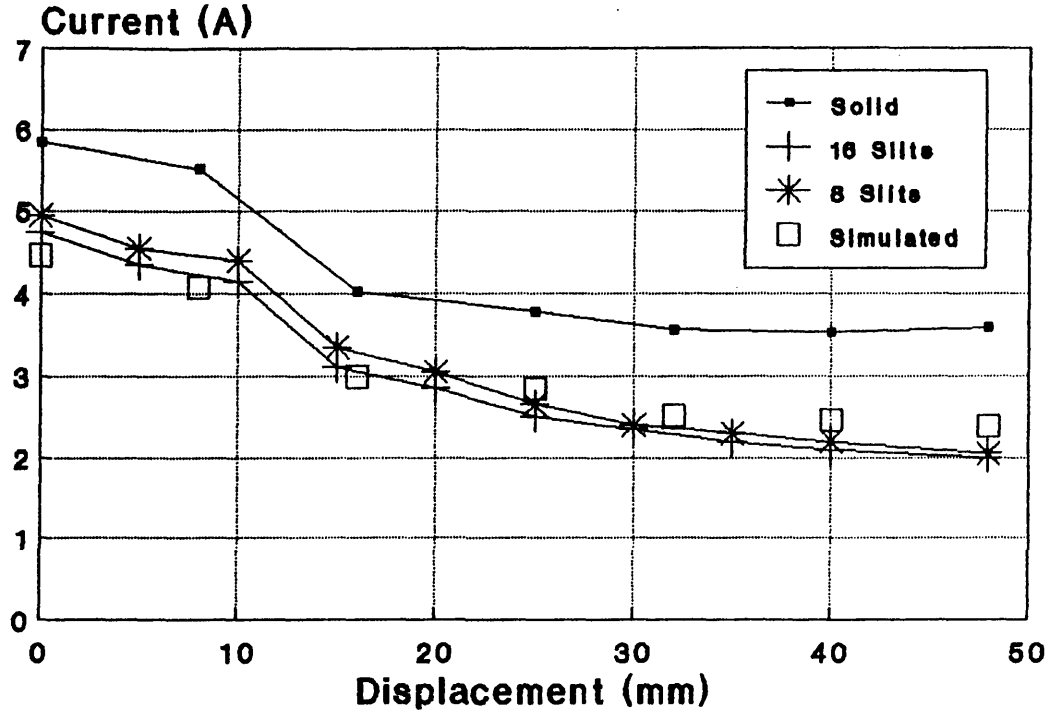

Fig. 6.4 Comparison of Input Currents between Three TLIAs

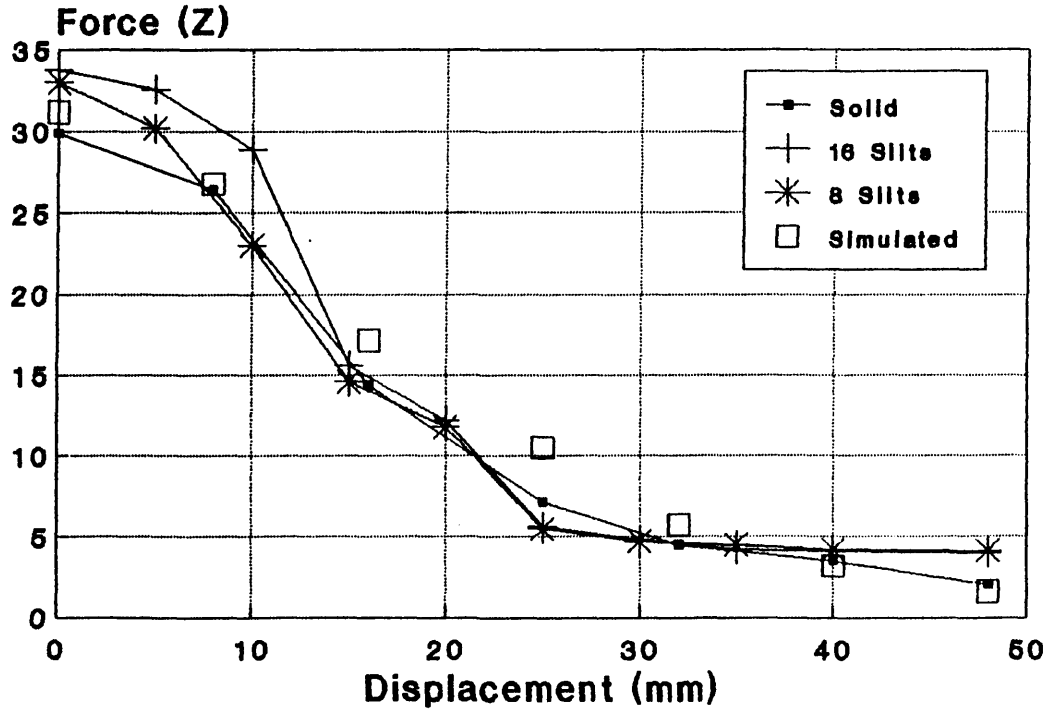

Fig. 6.5 Comparison of Output Forces between Three TLIAs

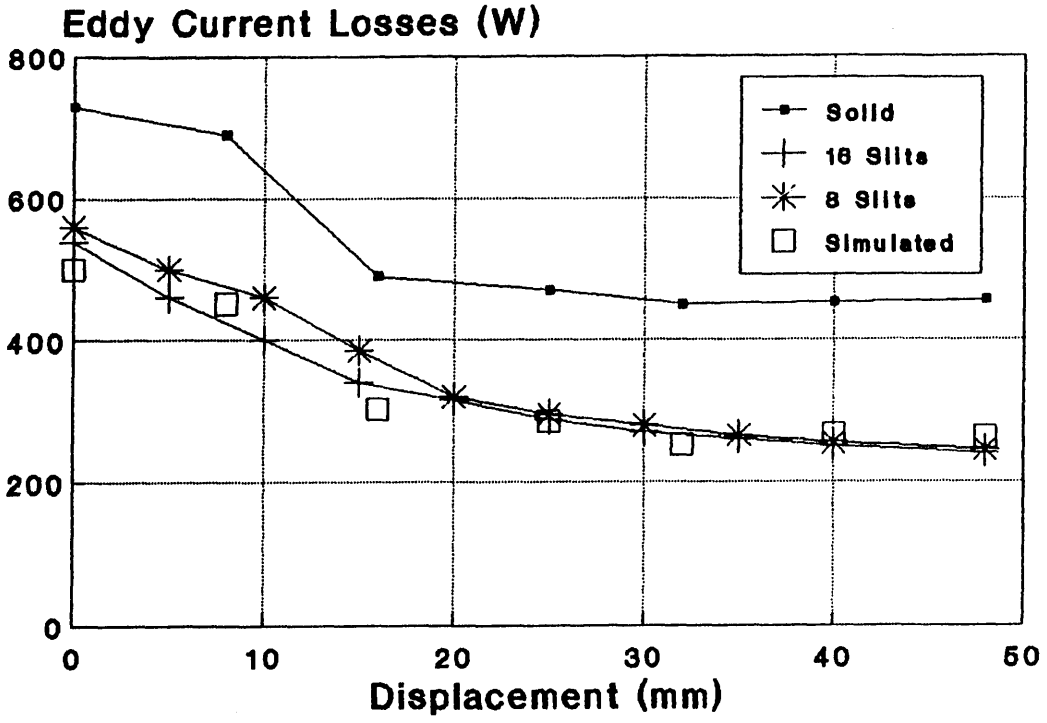

Fig. 6.6 Comparison of Eddy Current Losses between Three TLIAs

shown in Fig. 6.7b.

The results obtained from measurement confirm that the flux is confined to the interior surface. Therefore, we assume that the flux and induced eddy currents will flow through the path as shown in Fig. 6.7a and 6.7b. The main difference between the models without slits and with slits is that in the former the induced eddy current will circle round the whole stator while in the latter the eddy current can only circle in the each section split by the slits as shown in Fig. 6.7b. Obviously, to simulate the former case is easy by means of the COUPV but the latter is difficult as it is a three dimensional problem. A simple model will be introduced in the next section.

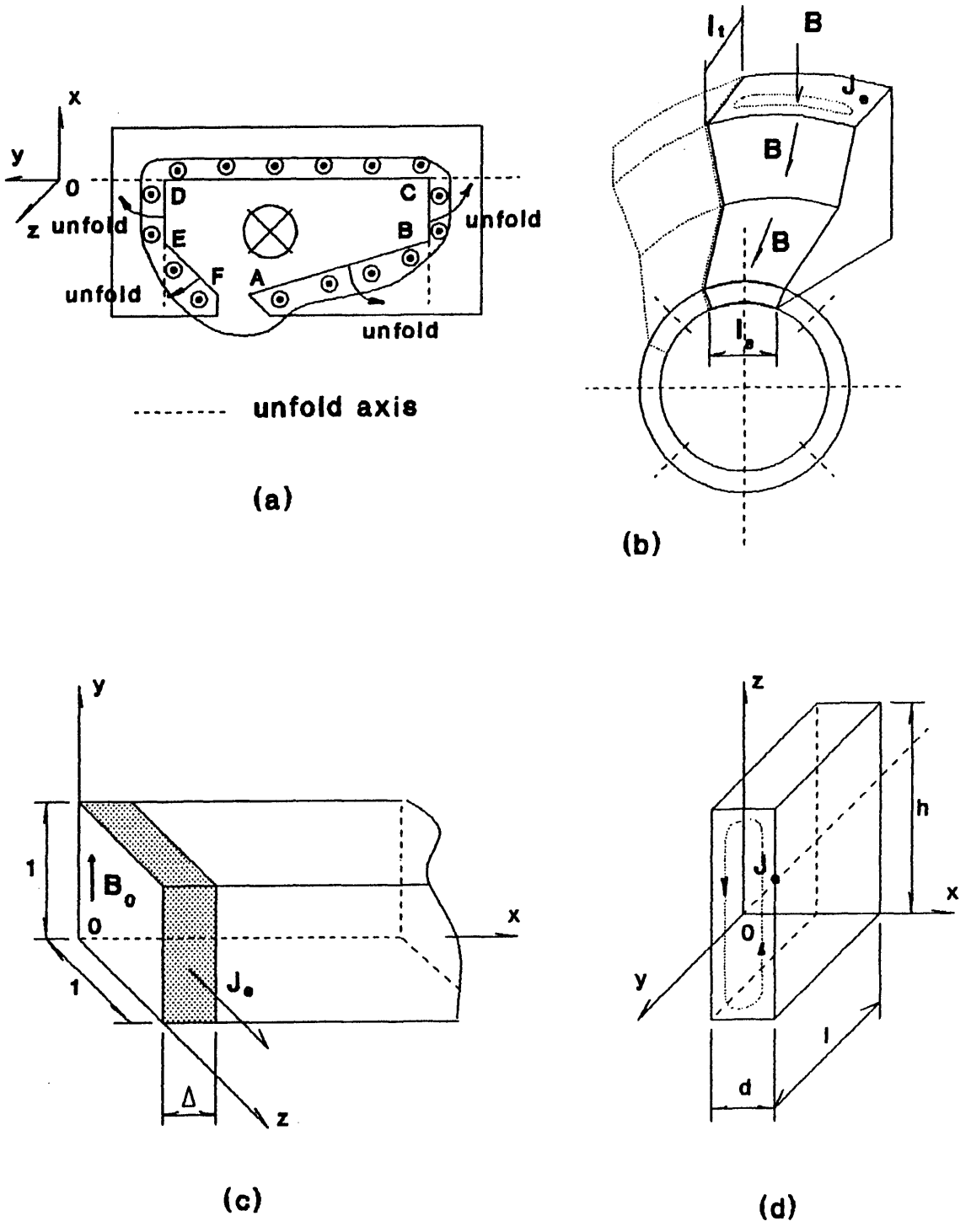

Fig. 6.7 Models for Equivalent Conductivity

6.4. An One Dimensional Model to Estimate the Slit Effect

As has been pointed out in the last section, the TLIA with slits in its solid steel stator makes its analysis much more complicated because it becomes a three dimensional problem. However, if the arc length l_s between two adjacent slits is much larger than the penetration depth Δ, *i.e.* $l_s \gg \Delta$ and the thickness of the solid steel stator wall l_t is also much larger than Δ, *i.e.* $l_t \gg \Delta$, then the problem can be tackled by a one dimensional model. An equivalent conductivity σ' is deduced in this way so that the COUPV can simulate the dynamic behaviour of a TLIA with radial slits.

This deduction is based on two fundamental facts relating to the solid steel stator TLIA. First, flux in a solid steel stator will flow along the interior surface whether it has slits or not. This has been confirmed by the flux density distributions of Fig. 6.1 and 6.3. Both solid steel stator with and without slits have similar flux density distributions. This means that the slit does not affect the flux path seriously but totally changes the path of the eddy current. In Chapter 5, a semi-infinite slab model was used to analyze the solid steel stator model. For a solid steel stator with slits, an infinite thin sheet model[44] will be used to analyze it. The function of the slits is to modify the path of the eddy current flowing along the circumference and into a number of smaller loops as shown in Fig. 6.7b. Accordingly, we assume that the eddy current circulates within a limited thickness of d as shown in Fig. 6.7d. The total flux produced by the windings of both stators with and without slits is almost the same. This is easy to understand as both stators have the same windings and fed by the same voltage. The main difference is the voltage drop in the winding resistance but this is very small compared with

the supplied voltage because the winding resistance is small. Two fundamental facts aid the following analysis. One is that the paths of the eddy current in both models differ from each other so that a semi-infinite slab model[45] is used to simplify the problem of the stator without slits and a thin sheet model to simplify the problem of the stator with slits. Another is that the total flux in both models is equal enabling the derivation of an equivalent conductivity.

In order to create a simple model, let us unfold the interior surface of the stator along the broken line ABCDEF and lay it out on a plane. Because the skin depth Δ is very small compared with the thickness l_t of the stator wall, the whole stator without slits can be considered a semi-infinite slab as shown in Fig. 6.7c. In the stator with slits, the flux is assumed to circulate within the depth of *d*. Therefore, an infinite thin sheet model is used as shown in Fig. 6.7d.

1. TLIA without Slits and Its Semi-infinite Slab Model

A semi-infinite slab model is a well known problem which can be investigated by an analytical method in one dimension. If the equation (5.1) is written in a complex form, the mathematical model of the semi-infinite slab will be

$$\begin{cases} \dfrac{\partial^2 \dot{B}_y}{\partial x^2} = j\omega \cdot \mu \cdot \sigma_y \dot{B} \\ \dot{B}_y \Big|_{x=0} = B_0 \cdot \cos \omega t \end{cases} \qquad \cdots\cdots(6.1)$$

in which B_0 is a boundary value at x=0.

Its well known solution is

$$\dot{B}_y = B_0 \cdot exp[-(1+j)\cdot\frac{x}{\Delta})] \qquad \text{or}$$

$$B_y = B_0 \cdot exp(-\frac{x}{\Delta})\cdot\cos(\omega t - \frac{x}{\Delta}) \qquad \cdots\cdots(6.2)$$

Because there is only eddy current in the area of interest, *curl* $\mathbf{H} = \mathbf{J}_e$ and $\mathbf{J}_e = J_{ez}\cdot\alpha_z$. Therefore,

$$\dot{J}_{ez} = -\frac{\partial \dot{H}_y}{\partial x} = -\frac{B_0\cdot(1+j)}{\mu\cdot\Delta}\cdot exp[-(1+j)\cdot\frac{x}{\Delta})]$$

$$= -\frac{\sqrt{2}\cdot B_0}{\mu\cdot\Delta}\cdot exp(-\frac{x}{\Delta})\cdot exp[-(\frac{x}{\Delta} - 45^\circ)]$$

$$= J_0\cdot exp(-\frac{x}{\Delta})\cdot exp[-j(\frac{x}{\Delta} - 45^\circ)]$$

or $$J_{ez} = -J_0\cdot exp(-\frac{x}{\Delta})\cdot cos(\omega t - \frac{x}{\Delta} + 45^\circ) \qquad \cdots\cdots(6.3)$$

where $$J_0 = \frac{\sqrt{2}\cdot B_0}{\mu\cdot\Delta} \qquad \cdots\cdots(6.4)$$

Eddy current loss in the volume of a unit area with x ranging from 0 to ∞ becomes

$$P_i = \frac{1}{2}\cdot\int_0^\infty \frac{|J_z|^2}{\sigma}\cdot dx = \frac{1}{2}\cdot\rho\cdot\int_0^\infty \left[J_0\cdot exp(-\frac{x}{\Delta})\right]^2\cdot dx$$

$$= \frac{1}{4}\cdot\rho\cdot J_0^2\cdot\Delta = \frac{1}{2}\cdot\frac{\rho\cdot B_0^2}{\mu^2\cdot\Delta} \qquad \cdots\cdots(6.5)$$

Flux in the unit area A_i as shown in Fig. 6.7c will be

$$\phi_i = \int_0^\infty B_0\cdot exp(-\frac{x}{\Delta})\cdot dx = B_0\cdot\Delta \qquad \cdots\cdots(6.6)$$

2. TLIA with Slits and Its Infinite Thin Sheet Model

As shown in Fig. 6.7c and d, the only difference between two models is their boundary conditions. For the infinite thin sheet the mathematical model is

$$\begin{cases} \dfrac{\partial^2 \dot{B}_y}{\partial x^2} = j\omega\cdot\mu\cdot\sigma_y\cdot\dot{B} \\ \dot{B}_y\Big|_{x=\pm\frac{d}{2}} = B_0'\cdot\cos\ \omega t \end{cases} \qquad \cdots\cdots(6.7)$$

where, B_0' is the boundary value of the infinite thin sheet model.

Its solution is

$$\dot{B}_y = \dot{K}_1\cdot sh[(1+j)\cdot\frac{x}{\Delta}] + \dot{K}_2\cdot ch[(1+j)\cdot\frac{x}{\Delta}] \qquad \cdots\cdots(6.8)$$

in which $\dot{K}_1$ and $\dot{K}_2$ are arbitrary complex constants.

According to the boundary condition they will be

$$\begin{cases} \dot{K}_1 = 0 \\ \dot{K}_2 = \dfrac{B_0'}{\frac{d}{2}\cdot ch\left(\frac{1+j}{\Delta}\right)} \end{cases} \qquad \cdots\cdots(6.9)$$

Thus flux can be obtained by

$$\dot{\phi}_s = \int_{-d/2}^{d/2} \dot{B}_y\cdot dx = \sqrt{2}\cdot B_0\cdot\Delta\cdot exp(-j45^\circ)\cdot th\left[(1+j)\cdot k\cdot\frac{d}{2}\right] \qquad \cdots\cdots(6.10)$$

where, $k = \dfrac{1}{\Delta}$.

$$\phi_s = |\dot{\phi}_s| = \sqrt{2}\cdot B_0'\cdot\Delta\cdot\left|\cdot th\left[(1+j)\cdot k\cdot\frac{d}{2}\right]\right| = \sqrt{2}\cdot B_0'\cdot\Delta\sqrt{\frac{ch\xi\ -\ cos\xi}{ch\xi\ +\ cos\xi}} \qquad \cdots\cdots(6.11)$$

in which $\xi = k\cdot d$

Average flux density in the thin sheet is

$$\bar{B}_s = \frac{\phi_s}{d} = \sqrt{2}\cdot B_0' \cdot \left(\frac{1}{\xi}\sqrt{\frac{ch\xi - cos\xi}{ch\xi + cos\xi}} \right) \qquad \cdots\cdots(6.12)$$

Eddy current density $\dot{J}_{ez}$ is

$$\dot{J}_{ez} = -\frac{\partial \dot{H}_y}{\partial x} = -\frac{B_0' \cdot (1+j)}{\mu \cdot \Delta} \cdot \frac{sh[(1+j)\cdot kx]}{ch\left[(1+j)\cdot\frac{k\cdot d}{2}\right]}$$

$$= -\frac{B_0' \cdot (1+j)}{\mu \cdot \Delta} \cdot th\left[(1+j)\cdot\frac{k\cdot d}{2}\right] \cdot \frac{sh[(1+j)\cdot kx]}{sh\left[(1+j)\cdot\frac{k\cdot d}{2}\right]}$$

$$= \dot{J}_0 \cdot \frac{sh[(1+j)\cdot kx]}{sh\left[(1+j)\cdot\frac{k\cdot d}{2}\right]} \qquad \cdots\cdots(6.13)$$

where $\dot{J}_0$ is the eddy current density at $x=\pm\frac{d}{2}$, which is equal to

$$\dot{J}_0 = -\frac{B_0' \cdot (1+j)}{\mu \cdot \Delta} \cdot th\left[(1+j)\cdot\frac{k\cdot d}{2}\right]$$

The eddy current losses in a unit volume is

$$\frac{P_s}{V} = \frac{\frac{1}{2}\cdot l\cdot h\cdot \int_{-d/2}^{d/2} \frac{J_z^2}{\sigma}\cdot dx}{l\cdot h\cdot d}$$

$$= \left(\frac{B_0}{\mu}\right)^2 \cdot \frac{1}{\mu\cdot\sigma\cdot\Delta^2}\cdot\left(\frac{1}{ch\xi + cos\xi}\right)\cdot\int_{-d/2}^{d/2}[ch(2k\cdot x) - cos(2k\cdot x)]\cdot dx$$

$$= \left(\frac{B_0}{\mu}\right)^2 \cdot \frac{\rho}{d\cdot\Delta}\cdot\left(\frac{sh\xi - sin\xi}{ch\xi + cos\xi}\right) = \left(\frac{\bar{B}_s}{\mu}\right)^2 \cdot \frac{\rho\cdot\xi^2}{2\cdot d\cdot\Delta}\cdot\left(\frac{sh\xi - sin\xi}{ch\xi + cos\xi}\right)$$

$$= 0.1602\cdot\left(\frac{\bar{B}_s}{\mu}\right)^2 \cdot \frac{\rho}{d\cdot\Delta} \qquad \cdots\cdots(6.14)$$

3. Equivalent Conductivity for TLIA with Slits

Whether the model has slits or not, the total flux passing through the stator section should be the same. Therefore,

$$\phi_i = B_0 \cdot \Delta = \bar{B}_s \cdot d = \phi_s \qquad \cdots\cdots(6.15)$$

In view of the measured results in Fig. 6.1 and 6.3, we assume that in both cases the average flux is calculated within the penetration depth, *i.e.* d=Δ. So the flux densities in the two models are equal, *i.e.*

$$B_0 = \bar{B}_s$$

If we use the model without slits instead of the one with slits, in order to ensure that they have the same eddy current losses, according to the equation (6.5) and (6.14),

$$P_i = 0.5 \cdot \frac{\rho_i \cdot B_0^2}{\mu^2 \cdot \Delta} \cdot h \cdot l = 0.1602 \cdot \left(\frac{\bar{B}_s}{\mu}\right)^2 \cdot \frac{\rho_s}{d \cdot \Delta} \cdot \Delta \cdot h \cdot l = P_s \qquad \cdots\cdot(6.16)$$

This leads to the following results:

$$\rho_i = 0.3204 \cdot \rho_s \quad \text{or} \quad \sigma_s = 0.3204 \cdot \sigma_i \qquad \cdots\cdot(6.17)$$

The physical meaning of the formula (6.17) is very clear. When slits are machined in the solid stator TLIA, the new eddy current path will be longer than the old one. In order to accommodate this fact, we increase the resistivity of the path instead of increasing the length.

4. Experimental Verification

Although the above method is only an approximate one, it proves quite effective in practice. Fig. 6.8 shows the measured current waveform when the TLIA with 16 slits is excited by 215 volts, 50 Hz sine wave. Its

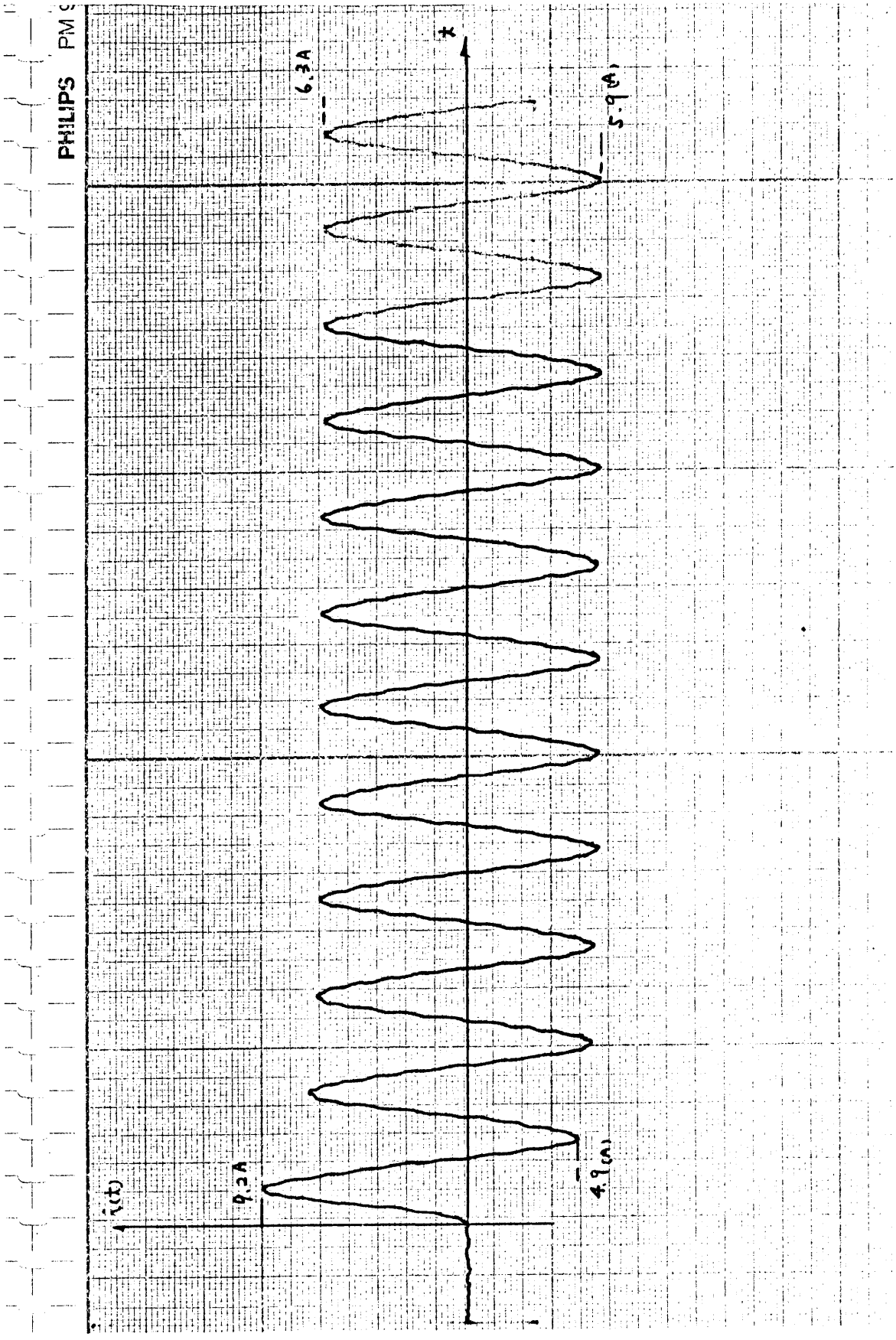

Fig. 6.8 Recorded Current Waveform in the Locked State

plunger is blocked at the displacement of D=5 (mm). Fig. 6.9 shows the simulated results of above case by the COUPV when the equivalent conductivity given blow is used.

$$\sigma' = 0.3204 \cdot \sigma = 0.3204 \times 0.33 \times 10^{-7} = 0.106 \times 10^{-7} \ (\Omega \cdot m)^{-1}$$

The simulated current waveform is similar to the one in Fig. 6.8. Both have almost the same amplitude. In Fig. 6.4, 6.5 and 6.6, the symbol '□' is used to represent the simulated results using the above equivalent conductivity. It is noticeable that in those graphs, the simulated input current, output axial force and power losses are quite close to the experimental results. Therefore, the COUPV can be directly used to simulate a TLIA with slits. Fig. 6.10 gives the eddy current losses in a solid steel stator with slits compared to one without slits. Both are obtained by simulation by the COUPV. In the former case the equivalent conductivity is used. The simulation reveals that the slits succeed in reducing eddy currents by more than half. The average eddy current losses in the stator without slits is about 250 (W) while it is only about 110 (W) in the one with slits. In both cases, the losses in the plunger are almost the same.

Both measured and simulated transient characteristics are shown in Fig. 6.11 and Fig. 6.12 respectively. The TLIA is excited by 215 volts, 50 Hz sine wave. Its plunger is in the free state. The time elapse during its movement from D=0 to D=72 (mm) is 160.1 (ms) by measurement. In Fig. 6.12, it is noticeable that for a displacement of 72 (mm) it takes 156 (ms). The current waveforms of Fig. 6.11 and Fig. 6.12 are also similar.

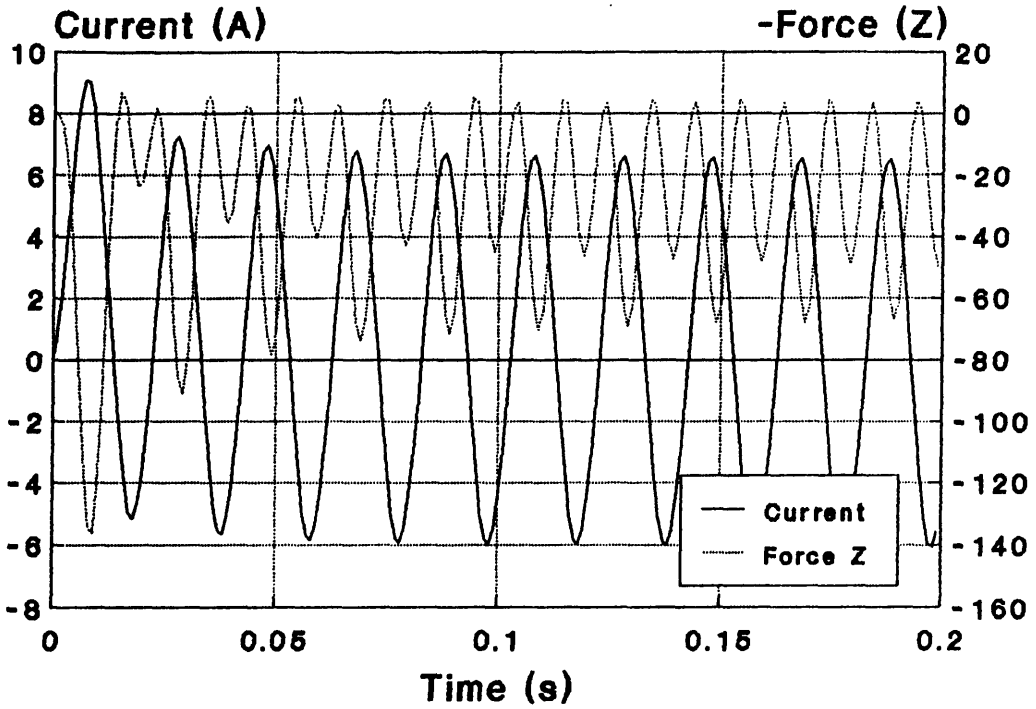

Fig. 6.9 Simulated Current and Axial Force in the Locked State

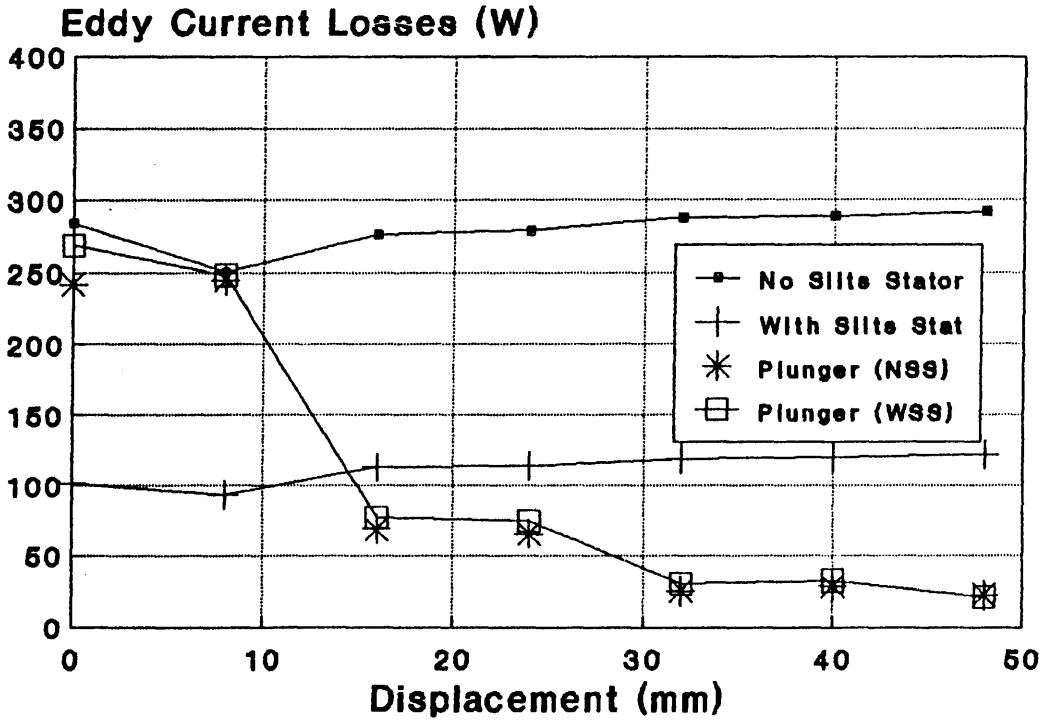

Fig. 6.10 Comparison of Eddy Current Losses in Slit & Non-slit Cases

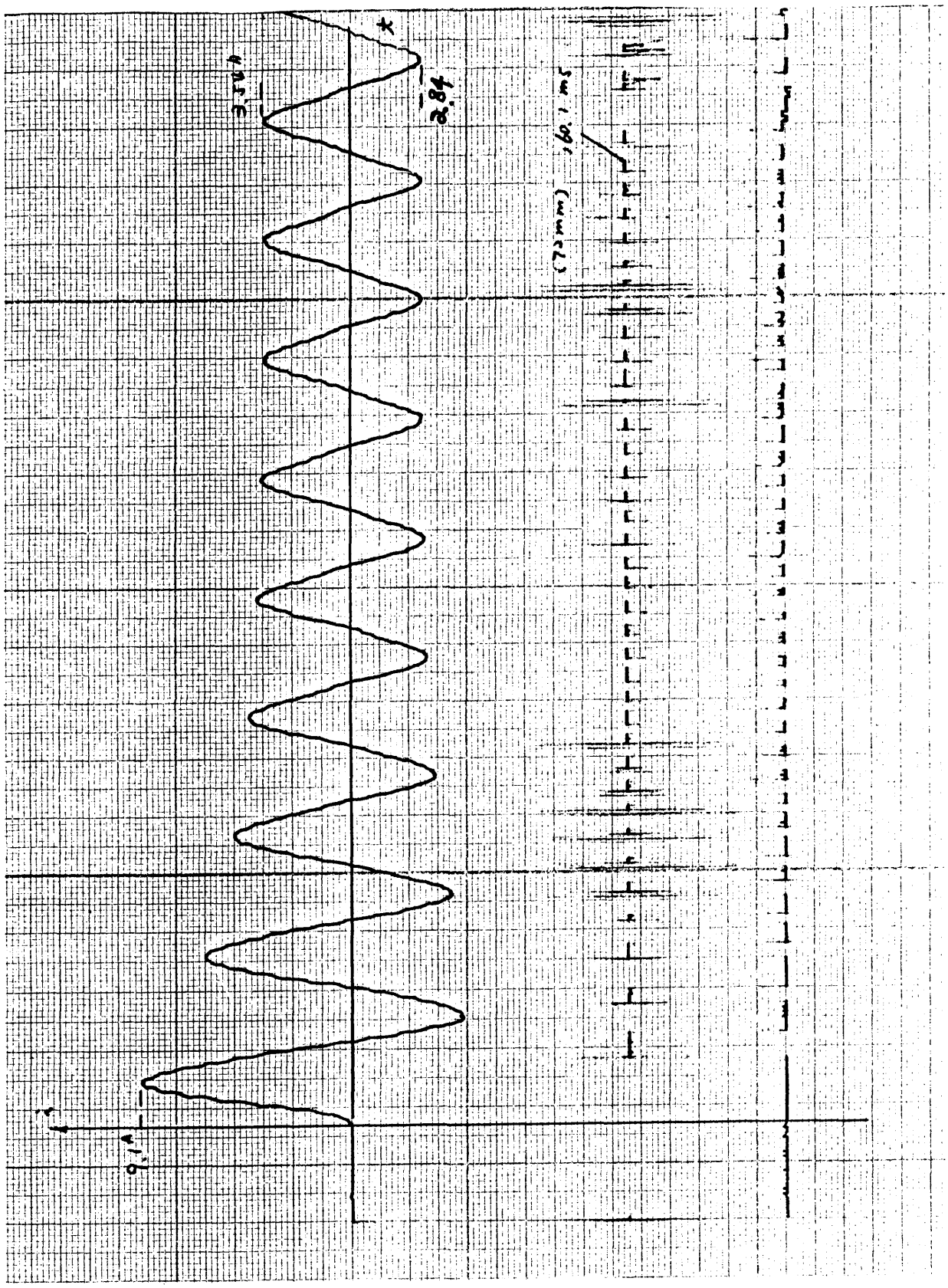

Fig. 6.11 Recorded Current & Displacement in Transient State

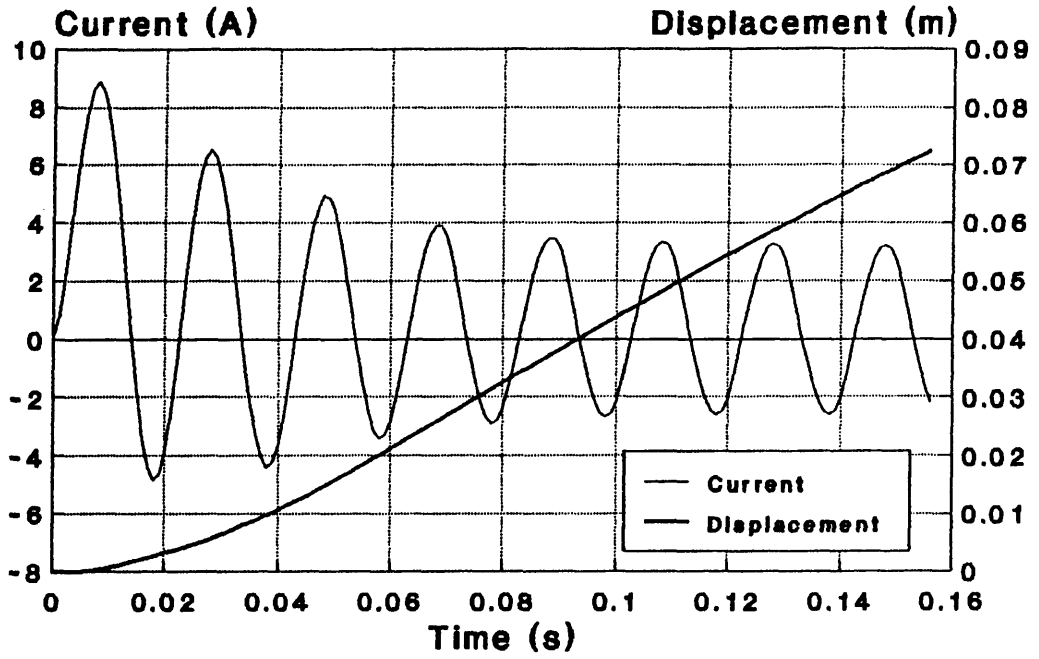

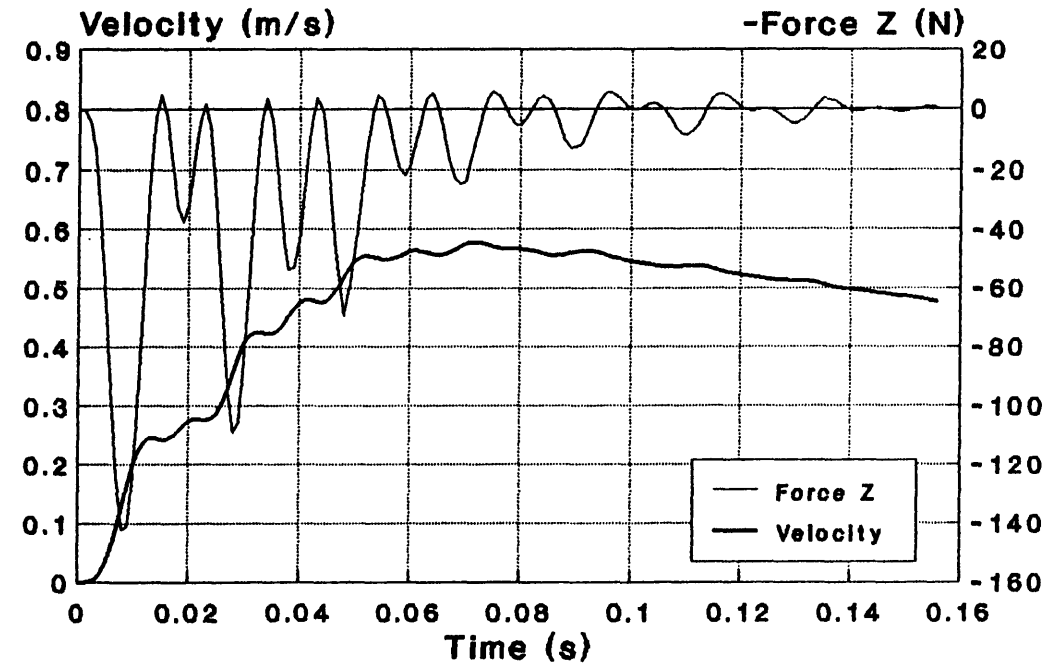

Fig. 6.12 Simulated Results in Transient State

6.5 Improvement of Force-stroke Characteristics

All the TLIA's studied so far have the common shortcoming of a fast declining force-stroke characteristics. For example, in Fig. 6.5, the force-stroke curves of three different types of solid steel stator TLIAs indicate that the force at the displacement of 20 (mm) is only equal to one third of the value at the displacement of 5 (mm). This is due to the shielding effect and the inner end effect pushing the flux back. Most of the flux becomes leakage which will not interact with the induced eddy current to produce useful force.

In Chapter 5 an open slot TLIA has been tried. Although the thrust-stroke characteristic is improved, it must pay the price of a larger input current and higher eddy current losses in the plunger as shown in Fig. 5.21. Obviously, this is because the open slot greatly reduces the leakage reactance associated with the magnetic circuit. In this section a numerical experiment is carried out on an iron clad plunger model[46] as shown in Fig. 6.13. Except for the plunger material and construction, all other geometric and electrical parameters remain the same as in the open slot model of section 5.4.2.

Fig. 6.14 shows a significant improvement of the force-stroke characteristics of the TLIA in which the axial output force remains high for most of the stroke as shown by the *curve (4).* This ensures that the TLIA can be used not only to push a free projectile but also to pull a heavy load such as a weight shown in Fig. 1.8. The time elapse of the plunger stroke will greatly decrease since the plunger will be accelerated all the time until it reaches to its destination.

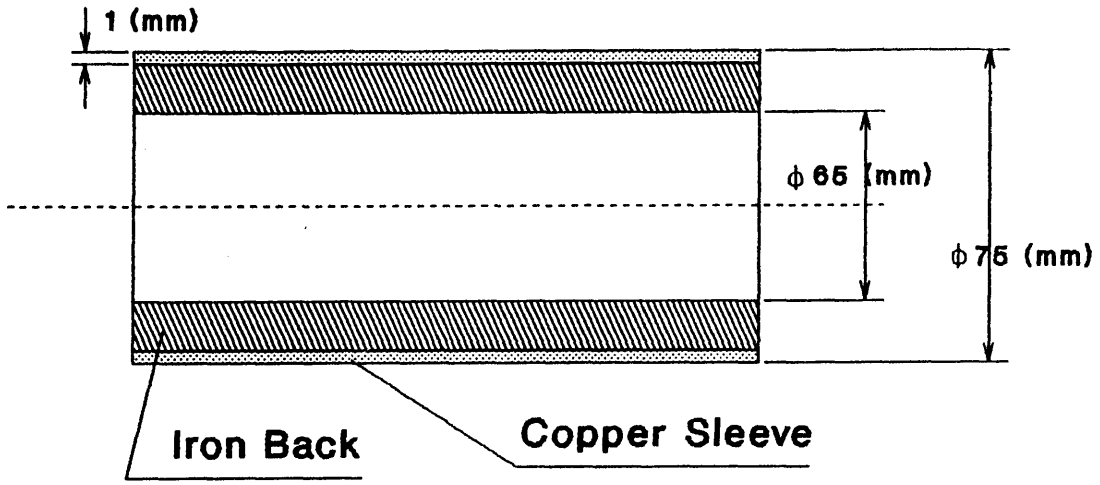

Fig. 6.13 Construction of the Clad Plunger

For the same stator, the clad plunger TLIA has a better force-stroke output curve, lower input current and lower power losses than the TLIA with a copper plunger. In Fig. 6.14, although the output force represented by *curve (3)* of the copper plunger is quite high, at least half of its force-stroke curve is in the unstable region as shown in the graph. We call it an unstable region because although the maximum output force is near 60 (N) it does not mean that it can push an object forward if only 40 (N) force is required. For example, if 30 (N) force is needed to push a load, the plunger and load will not move at all. On the other hand, the unstable area of the *curve (4)* is only less than half that in *curve (3).* It is clear that for a load requiring 30 (N) force to move it, the *curve (4)* is appropriate because of the nett force available at start. In addition to the output force, the input current will be greatly reduced for the clad plunger TLIA. It is shown by the *curve (2).* Compared with the

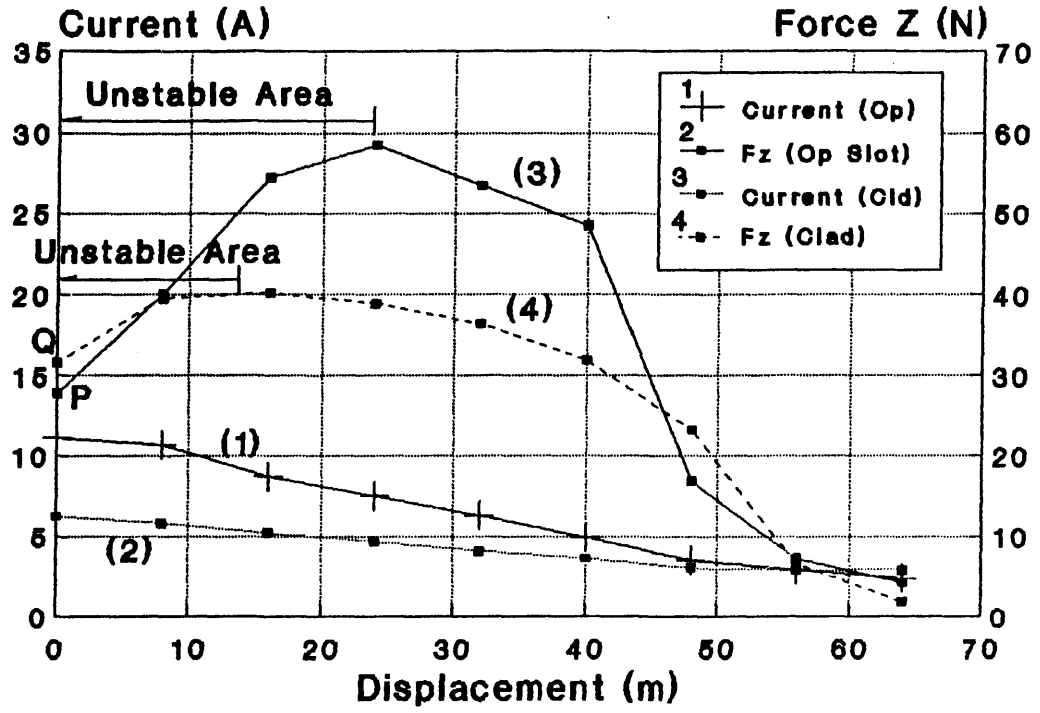

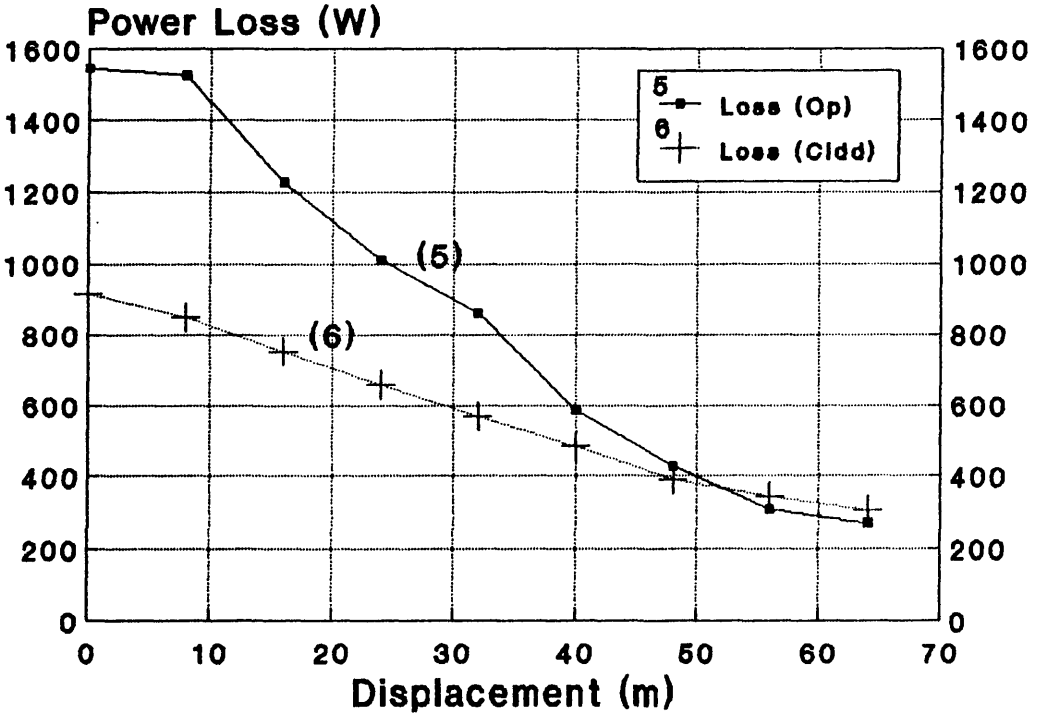

Fig. 6.14 Performance of the Clad Plunger Model

input current variation shown by the *curve (1)*, the former is almost only half the latter at strokes ranging from D=0 to D=25 (mm). This directly leads to the reduction of the eddy current losses in the former as shown by the *curve (6)* for the TLIA with a clad plunger and *curve (5)* for the unclad plunger TLIA.

The reason that the clad plunger improves the performance of the TLIA can be explained by the field plots of Fig. 6.15. There are six plots from 0.081 (s) to 0.097 (s) at intervals of 3 (ms) each. It is noticeable that the flux density is high in this clad plunger all the time. Moreover, it is seen by comparing Fig. 6.15 with Fig. 5.12, 5.19 and 5.20 that leakage flux is greatly reduced with a clad plunger. It is these two results that improve the TLIA performance.

As explained in Chapter 2, a high flux density leads to a high goodness factor. In conventional electric motors, the goodness factor is mainly determined by the resistance of its electric circuit and the reluctance of its magnetic circuit. The designer always tries to find an optimal structure to make the above two parameters smaller for a given *emf* and *mmf*. However, for a TLIA design, this is not enough. In general, the leakage flux forms a small part of the total flux in an electric motor. But because of the existence of the shielding effect, the leakage flux is not negligible in the TLIA. It can be as much as half the total flux. This phenomenon has already been confirmed in Fig. 5.20 in which the number of flux lines which pass through the plunger were counted. As has been discussed in the previous chapters, the shielding effect prevents the flux passing through the copper plunger. Even though there is very high eddy current density in the plunger, the output force is still very low due to

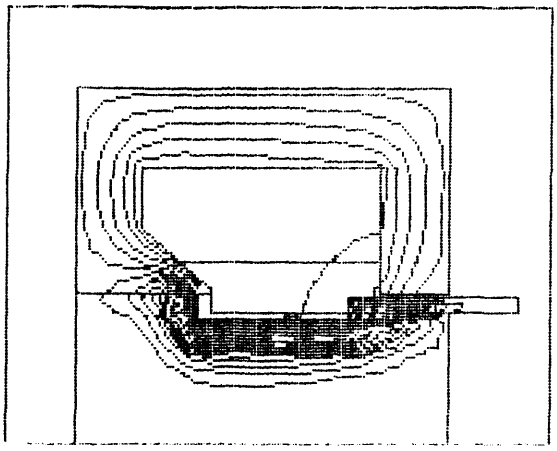

t = 81 (ms)

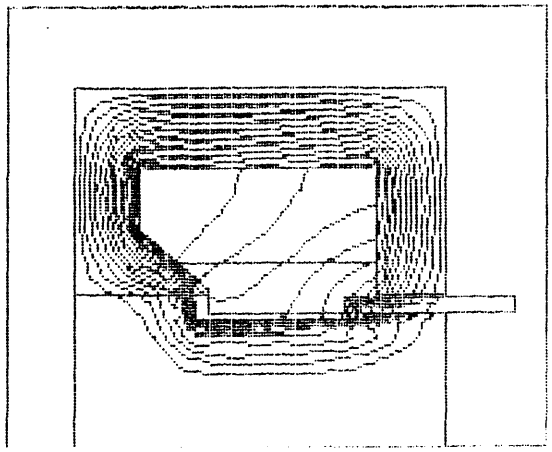

t = 84 (ms)

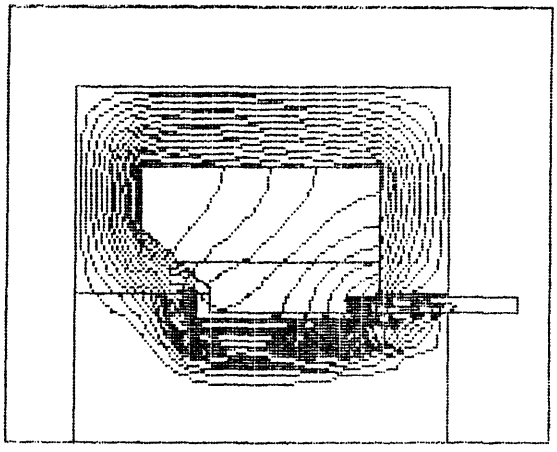

t = 87 (ms)

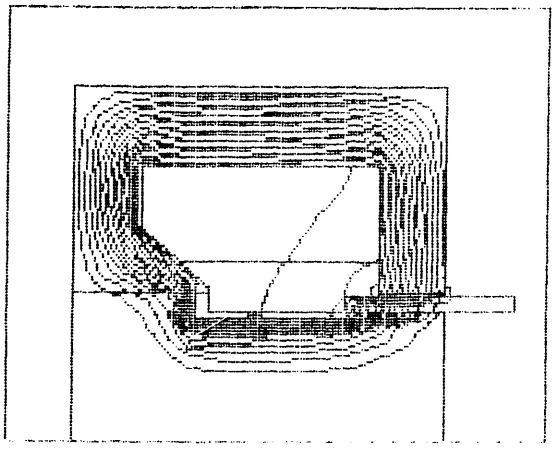

t = 91 (ms)

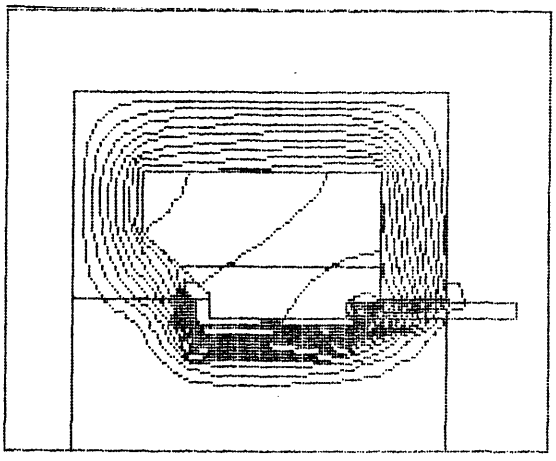

t = 94 (ms)

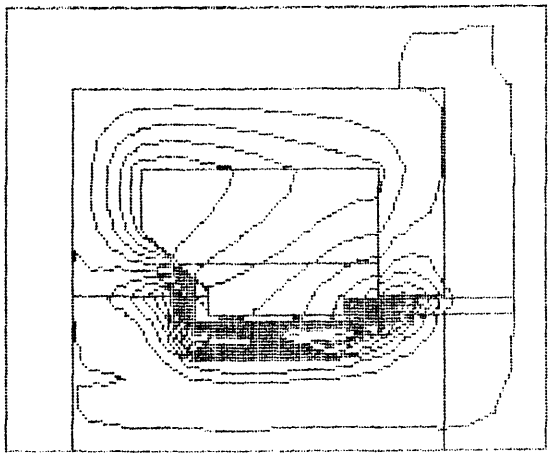

t = 97 (ms)

Fig. 6.15 Flux Density Distribution in a Clad Plunger Model

low flux density.

A clad plunger proves to be very effective in solving the above problems, and has three basic functions. Firstly, the iron back will obviously reduce the total reluctance of the magnetic circuit and attract the flux to go through the plunger. Secondly, using a thin copper plunger with iron back instead of a thick copper plunger will weaken the shielding effect. This reduces the leakage flux of the stator winding too. In other words, it increases the equivalent reactance X_e. When the TLIA is at standstill, its input current is mainly dependent on this equivalent reactance. Increasing the equivalent reactance means reducing the input current and thus the eddy current losses. Thirdly, because the iron back moves with the plunger all the time and it has a much higher permeability than the copper and air, the reluctance of the main magnetic circuit will not change significantly when the plunger is at different positions. This leads to an output force with flat shape as shown in Fig. 6-14, *curve (4).* In contrast, the pure copper plunger will change its main magnetic circuit significantly during its movement. This can be found in Chapter 2, where the equivalent reluctance X_e varies with different plunger positions as shown in Fig. 2.4b, 2.10b and 2.22a.

In order to estimate the forces produced by a TLIA with a clad plunger, the Maxwell stress method should be applied because of the participation of the iron back within the plunger. In the COUPV, both methods of calculating the forces by $\mathbf{J}\times\mathbf{B}$ and Maxwell stress can be chosen according to the requirement. The verification of the Maxwell stress method used by the COUPV is seen in Fig. 6.16. It shows the results when both methods are used to predict the output forces for the same TLIA with an unclad plunger.

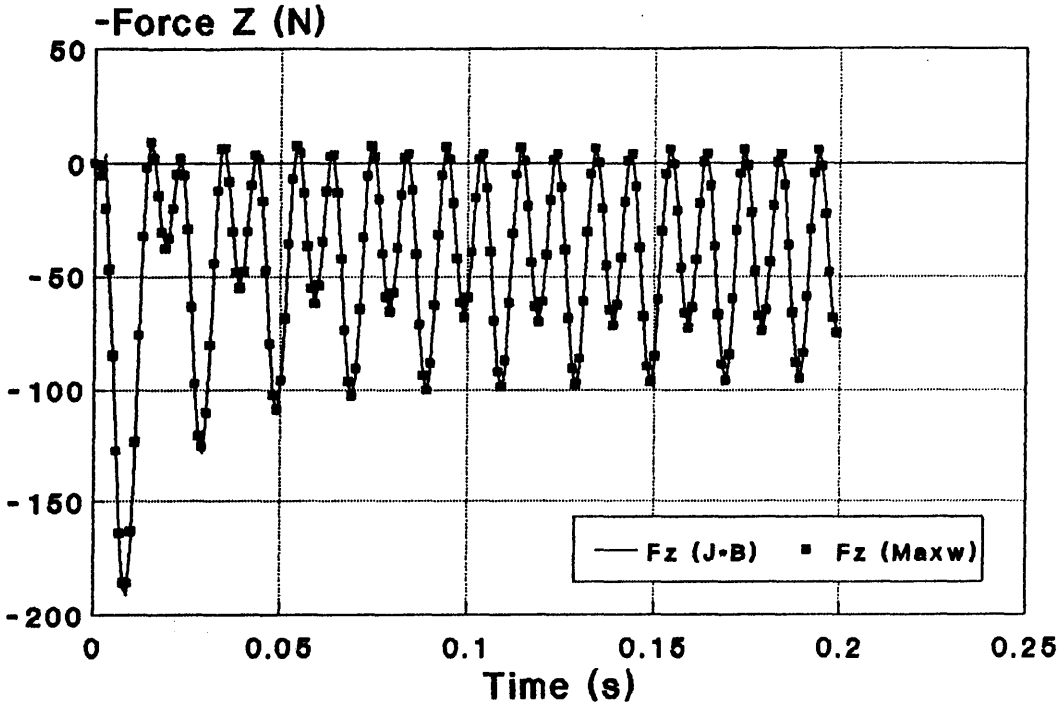

(a) The Axial Output Forces

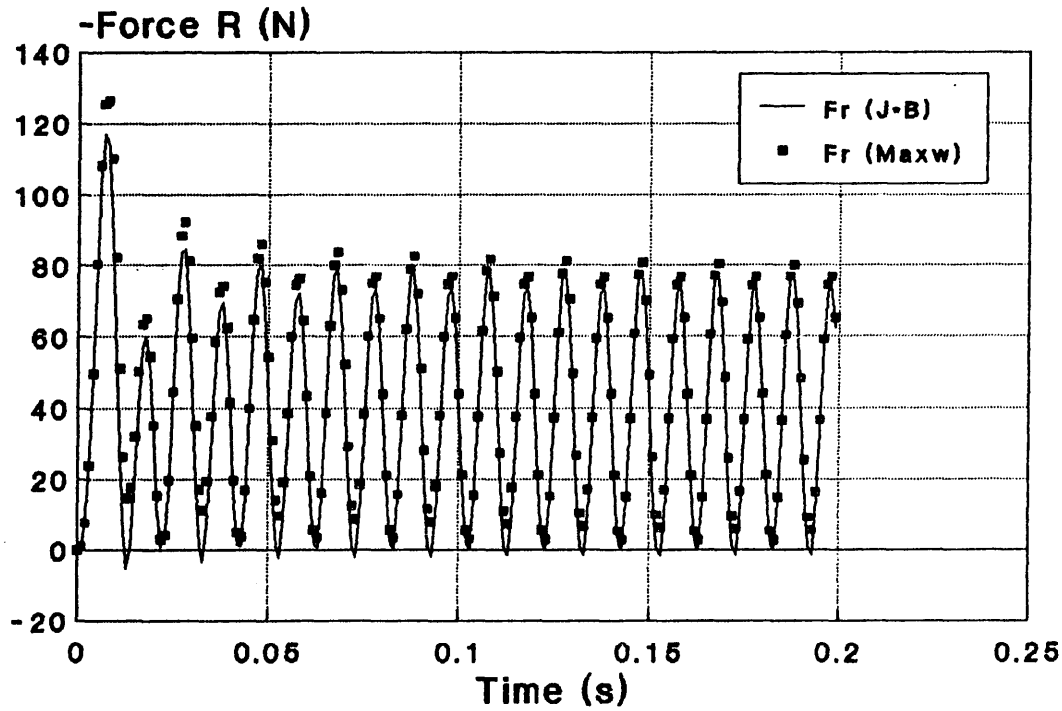

(b) The Radial Output Forces

Fig. 6.16 Comparison of the Forces Predicted by Two Methods

6.6 Conclusions

The eddy current effect in the TLIA has been examined in this chapter. Flux distributions in TLIAs with and without slits is measured by two different search coils. One is used to measure the flux distribution along the airgap and the other is used to measure the one in the mandrel. The results indicate that the flux distributions in the TLIAs with and without slits are similar. This leads to the use of two well known models to deduce an equivalent conductivity for the COUPV. They are a semi-infinite slab model and an infinite thin sheet model. This method has been proved to be very simple to deal with the solid steel stator with slits. The simulated results are reasonably accurate to satisfy the requirement in engineering design.

The shielding and inner end effects of the plunger introduced in previous chapters result in a big disadvantage in its performance, *i.e.* fast decline of force-stroke characteristics. Use of a clad plunger instead of a simple copper plunger proves to be a simple and effective method of overcoming this shortcoming.

CHAPTER 7 CONTROL OF THE TLIA

7.1 Introduction

The actuator is normally used as an executive component in an automatic control system. In general, most magnets, solenoids and relays can only be used for the bang-bang control, *i.e.* two position control under open loop control conditions. Unlike them, the TLIA has different force-stroke characteristics as aforementioned in Chapter 1. Thus it can find applications in both bang-bang and position control. The purpose of this chapter is to introduce its several features with regard to the control aspects that are special to the TLIA.

Before discussing and studying its control properties and strategies, the velocity influence in the simulation is investigated by the COUPV. Although the maximum speed of the plunger is only about 1 or 2 (m/s) in the existing prototypes, the 'motional' eddy current in the plunger occupies a considerable part of the total induced eddy current. Then the bang-bang control is studied examining its time response as it is affected by the number of stator winding turns and initial switching angles. It is easy to achieve position control with the TLIA. These control properties are investigated experimentally when it is controlled by an A.C. motor controller. The simplest and cheapest position control may use a Triac voltage controller to adjust the supply voltage. Therefore, its dynamic behaviour simulated by the COUPV will be valuable. In the final section the simulated results when the TLIA is controlled by a Triac voltage controller are presented.

7.2 Velocity Influence in the Simulation

In order to simulate the transient characteristics of the TLIA, the velocity term $\sigma \cdot V_z \cdot \frac{\partial A}{\partial z}$ must be included in the mathematical model as expressed by the equation:

$$\frac{\partial}{\partial z}\left(\nu \cdot \frac{\partial A}{\partial z}\right) + \frac{\partial}{\partial r}\left(\frac{\nu}{r} \cdot \frac{\partial (r \cdot A)}{\partial r}\right) = -J_c + \sigma \cdot \frac{\partial A}{\partial t} + \sigma \cdot V_z \cdot \frac{\partial A}{\partial z} \qquad \cdots\cdots(7.1)$$

This term has the same dimensions as current density. It results from the movement of the conducting plunger interacting with the existing radial magnetic field.

With the help of the COUPV, it is easy to examine its features and estimate it as a percentage of the total eddy currents induced in the plunger. Fig. 7.1 demonstrates the simulated results when a 500 turn winding of the solid stator TLIA with closed slot mouth is connected to 240 volts, 50 Hz sine wave. The total eddy current in the plunger can be found in graph (a), in which it attenuates with time, *i.e.* when the plunger reaches the outer end of the TLIA, there is no significant eddy current induced in the plunger. The graph (b) shows that the 'motional' induced eddy current forms a considerable percentage of the total eddy current in the plunger. During the time period from 0 to 0.03 (s), it increases as

(1) the plunger is being accelerated to a high speed as shown in the graph (c); and

(2) It can also be seen in the graph (c) that at the instant of 0.03 (s) the plunger has a displacement of about 15 (mm). This means that the plunger is still under the slot mouth region and with high flux density passing through it.

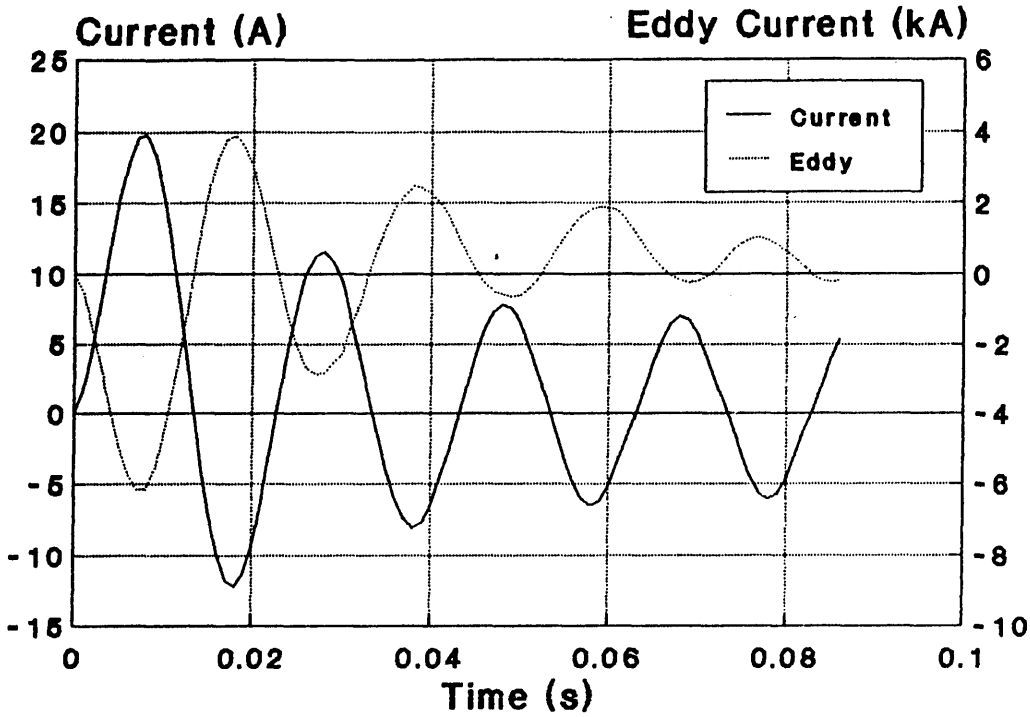

(a) Input Current & Total Eddy Current in the Plunger

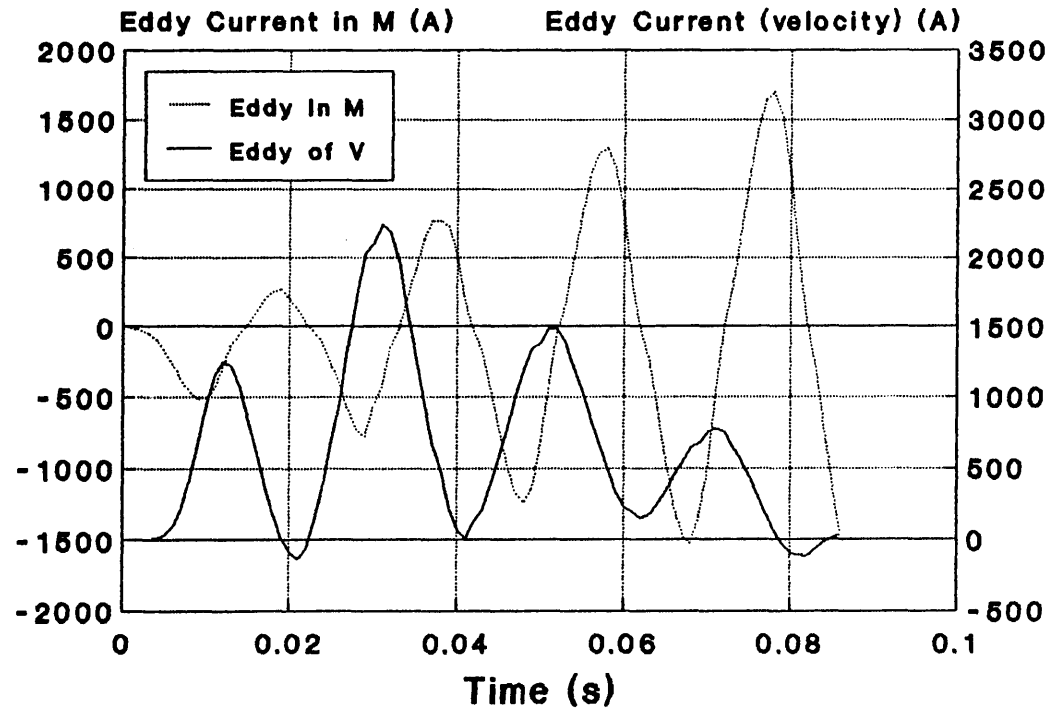

(b) Eddy Current in Mandrel & Eddy Current due to Velocity in Plunger

Fig. 7-1 Velocity Effects to Eddy Current in the Plunger

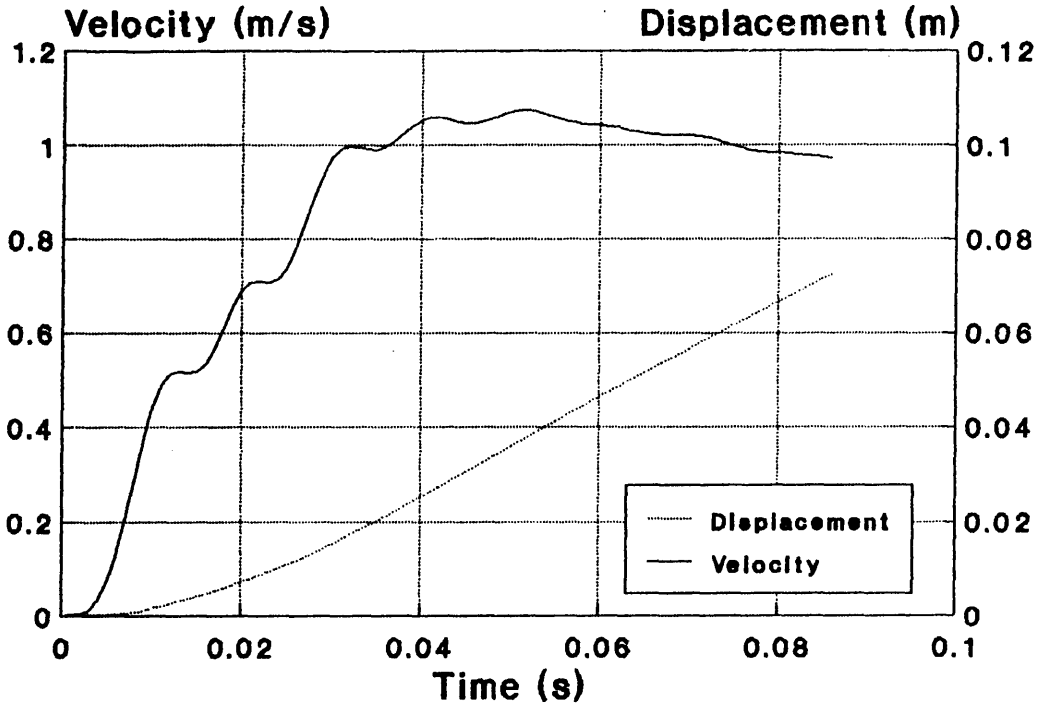

(c) Velocity & Displacement of the Plunger

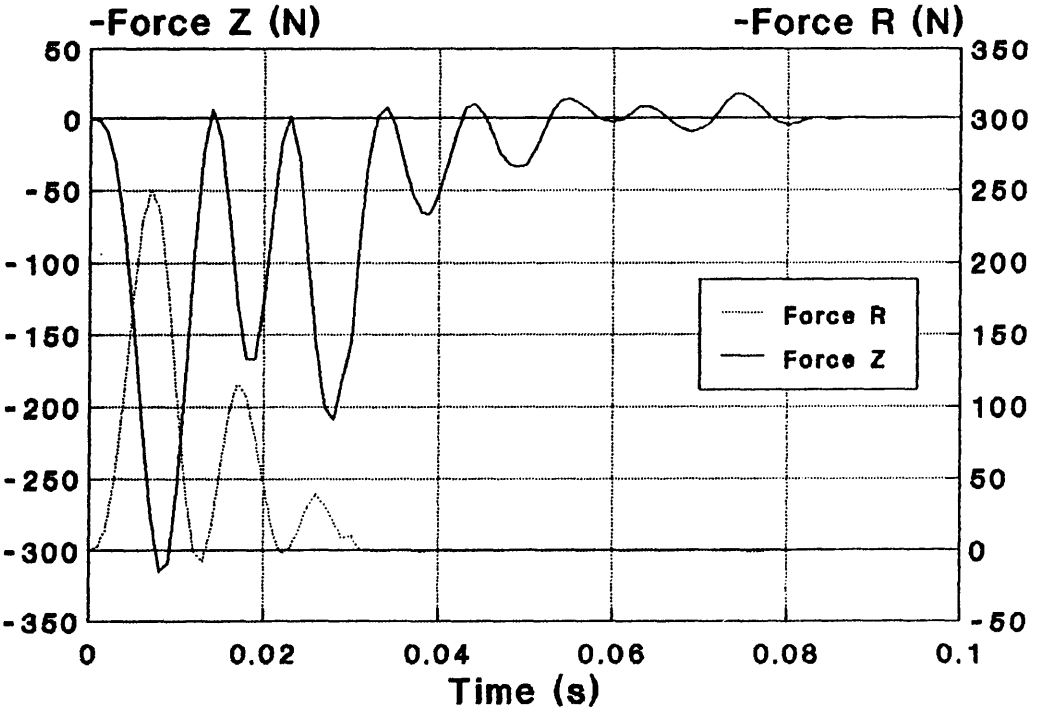

(d) Axial Force & Radial Force Produced in Plunger

Fig. 7-1 Velocity Effects in the Plunger

After the plunger moves under the slot tooth, although the velocity remains almost constant at about 1(m/s), the motional eddy current apparently declines. This is easily explained by the shielding effect. Under the slot tooth, most of the flux will no longer pass through the plunger. Therefore, the motional eddy current $\mathbf{J}_v$, which is given by

$$\mathbf{J}_v = \sigma \cdot (\mathbf{V} \times \mathbf{B}) \qquad \cdots\cdots(7.2)$$

will be greatly reduced as the flux density decreases.

From the above numerical experiment, we can conclude that the velocity term is a very important factor influencing the transient characteristics of the actuator. Even though the actuator is not in high speed, for instance in the above case it is only about 1 (m/s), in order to obtain high accuracy it must be taken into account. For a fast actuator, especially for the θ gun, in which the projectile may reach 3 (km/s) at the end of its barrel[47], the motional eddy current will be much higher than the induced eddy current due to the transformer *emf*.

So far, most papers[48,49] which have considered the velocity effect assume that the velocity remains constant during movement. This is only suitable for estimating the steady state operation. As most actuators always work in the transient state, using average speed to simulate its dynamic behaviour will result in unacceptable error. In Fig. 7.1b, one can see the motional eddy current variation with time.

7.3 Bang-bang Control

Most of the magnets, solenoids and relays are used in bang-bang control systems, *i.e.* two position control. The TLIA has similar control prospects. For example, it can be used as a very simple component in an automatic product line to push a work piece into a certain position. In such applications the time response is an important specification connected directly to productivity. In addition, the initial point on wave switching will influence its transient response. How serious is this influence? Is it large enough to affect its normal operation? This section will address these by either experiment or numerical investigation.

7.3.1. Time Response

Time response is a key index of the actuator. Two major factors affecting its time response are the total mass of the plunger plus its load and the output axial force of the TLIA. Fig. 7.2 shows the experimental results of the solid steel stator TLIA with 8 slits shown in Fig. 5.2. It was excited by 123 volts, 50 Hz sine wave controlled by the switching point controller so that the switching-on phase angle can be adjusted to remain at zero. As there are three coils in the first stage, the number of turns of the winding can be changed during the experiment. The TLIA is experimented under no-load condition but with two different plungers. One is made of copper with its mass of 3.682 (kg) and the other is made of aluminum with a mass of 1.378 (kg). For a stroke of 70 (mm), the total time of travel is shown by the curves of Fig. 7.2. Obviously, the lighter the mass, the less will be the time of travel. Under constant output force, the response time for the different masses travelling over the same distance can be evaluated by

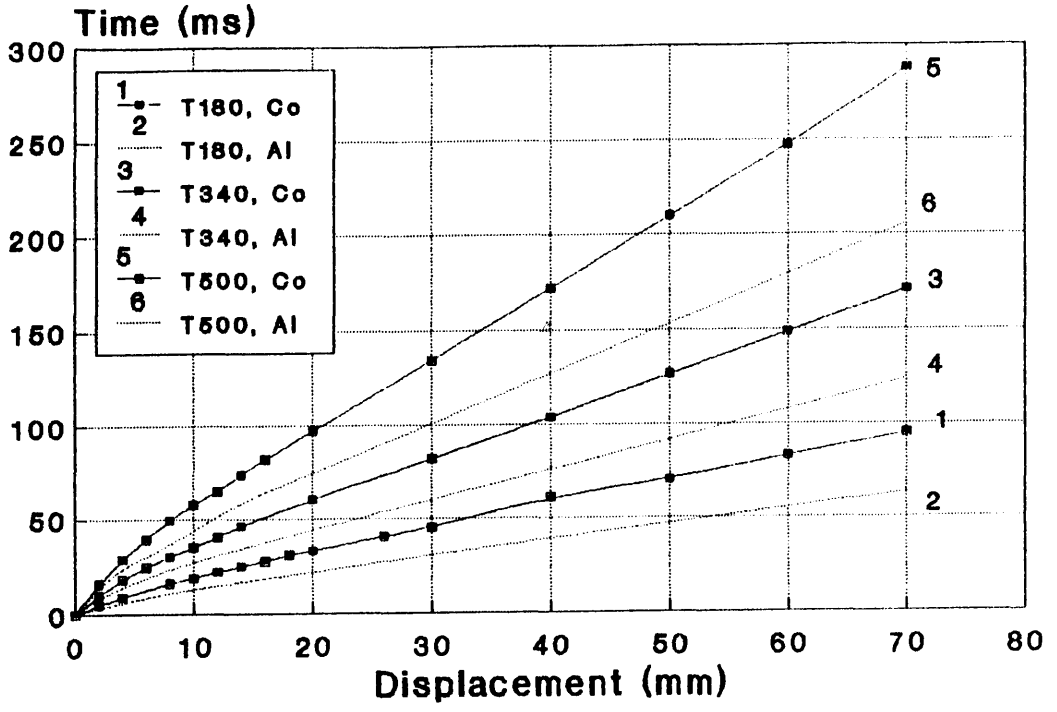

Fig. 7.2 Time Response with Different Masses & Number of Coil Turns

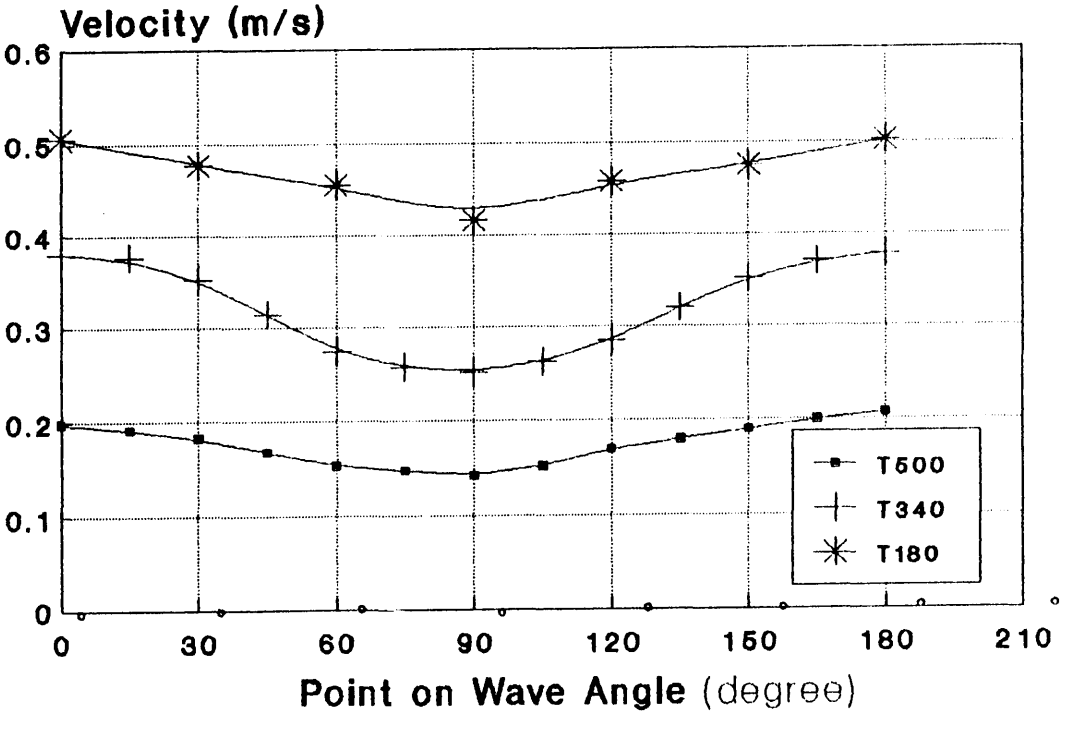

Fig. 7.3 Average Speed of Copper Plunger in Initial 2 (mm) Displacement

$$\frac{t_1}{t_2} = \sqrt{\frac{m_1}{m_2}} \qquad \cdots\cdots(7.3)$$

Varying the number of turns of the winding is the same as changing the exciting voltage, because for an electromagnetic induction device,

$$|\dot{U}| \approx |\dot{E}| = \omega \cdot N_c \cdot |\dot{\phi}| \qquad \cdots\cdots(7.4)$$

Under constant voltage, reducing N_c means increasing total flux. If the input current is controlled within permitted limits, and the magnetic circuit is under reasonable saturation, changing N_c is a simple way to change the time response of the TLIA.

In practice, N_c is a major parameter which must be determined during the design. From the expression (7.4), one can see that it directly affects the flux $|\dot{\phi}|$ in the machine. In a conventional electric motor, it is easy to choose $|\dot{\phi}|$ according to B_a, the required flux density in the airgap, and A_a the area corresponding to each pole pitch. However, it is difficult to estimate A_a in the TLIA since the distribution of the flux density is unknown due to the eddy current in the plunger. Therefore, the optimal value of N_c must be investigated by the use of an electromagnetic field analysis tool such as the COUPV.

Fig. 7.2 shows the experimental results when the number of turns of the exciting coil changes from 180 to 340 and 500 turns. With the same input voltage of 123 volts, decreasing the number of coil turns means increasing the flux in the magnetic circuit and also increasing the input current. There will be larger force produced and faster time response achieved.

7.3.2 Point on Wave Switching

When the TLIA is energized by a sine wave supply, the switching-on instant will obviously affect the time response of the stator current, output force and plunger velocity. Fig. 7.3 shows the experimental results which show the average speed of a copper plunger starting from an initial displacement of 2 (mm). The TLIA used in the last subsection 7.3.1 is excited by 123 volt, 50 Hz sine wave whose switching point is controlled by a point on wave switching controller. From Fig. 7.3, it is noticeable that in order to achieve maximum initial acceleration, the switching-on instant of the supply should be zero. The speed variation ζ from a maximum to a minimum when the switching angle is 90° is defined as

$$\zeta = \frac{\text{maximum speed - minimum speed}}{\text{maximum speed}} \times 100\%$$

In Fig. 7.3 it is found that when the 500 turns winding is connected to the supply, ζ is about 27%. In general, because this influence only lasts during the first few energising cycles, it will not lead to significant differences in the total time elapsed when the plunger has a long stroke. However, for a TLIA requiring only a very short stroke or very fast action this factor must be considered.

7.4 Position Control

One advantage of the TLIA compared with solenoid actuators is that it is easy for the TLIA to function as a position controller under open loop conditions. Fig. 7.4 shows the experimental results when the solid steel stator TLIA with 8 slits is excited by the A.C. motor speed controller. There are four force-stroke curves in Fig. 7.4a. Every curve is obtained by connecting the TLIA to a square wave with different voltage and frequencies as shown in the Fig. 7.4b. If there is a load with a constant resisting force of 13 (N) as shown by a horizontal line, the plunger can be easily controlled between two positions *A* and *B* by adjusting the voltage from 380 (V) to 138 (V).

From Fig. 7.4a, it is noticeable that the control range for this solid steel stator TLIA is quite small. Under a constant load of 13 (N) resisting force, the plunger can only move along the straight line *AB* within a displacement of 20 (mm). It is easy to understand that this is due to its sharply declining force-stroke characteristics. If a laminated stator model with an open slot and clad plunger is used as introduced in section 6.5, its position control range can be significantly expanded. This can be seen from the force-stroke curve (4) in Fig. 6.14. If its power supply is adjustable and if it carries a constant load of 15 (N) force, then its control range can be expanded to more than 40 (mm). This is about twice the control range of the solid steel stator TLIA with a closed slot mouth. The suitability of the TLIA for use in position control may widen its application area. For example, it can be used to control a valve not only in two states, either open or close, but also in any position to adjust the rate of flow.

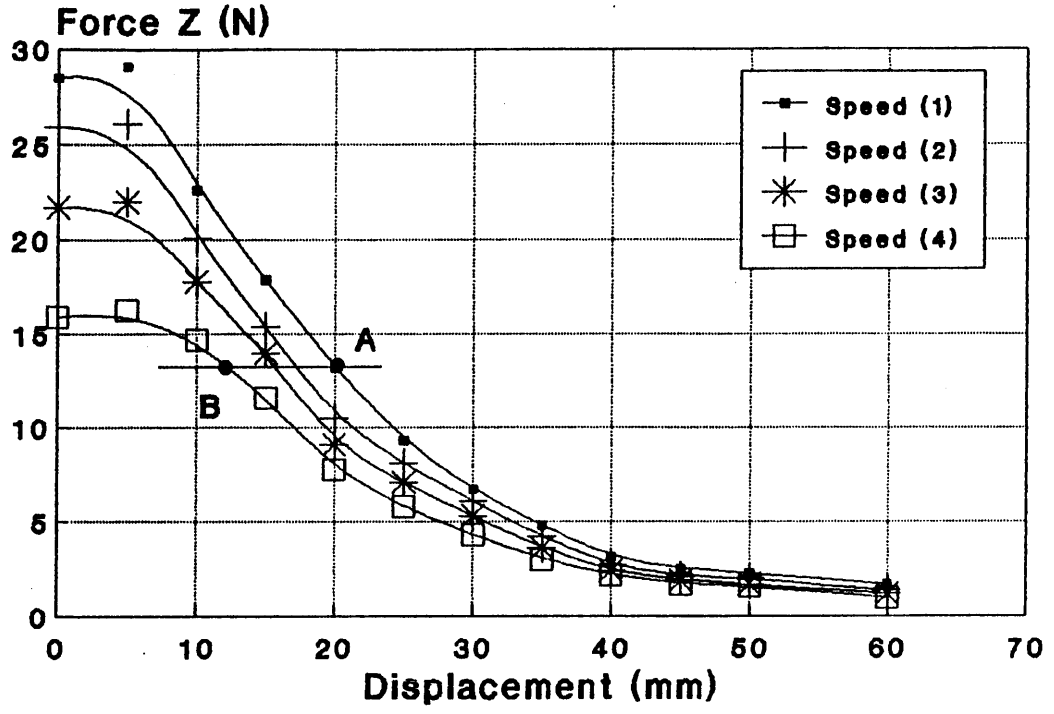

(a) Force-stroke Behaviour under Adjustable Supplies

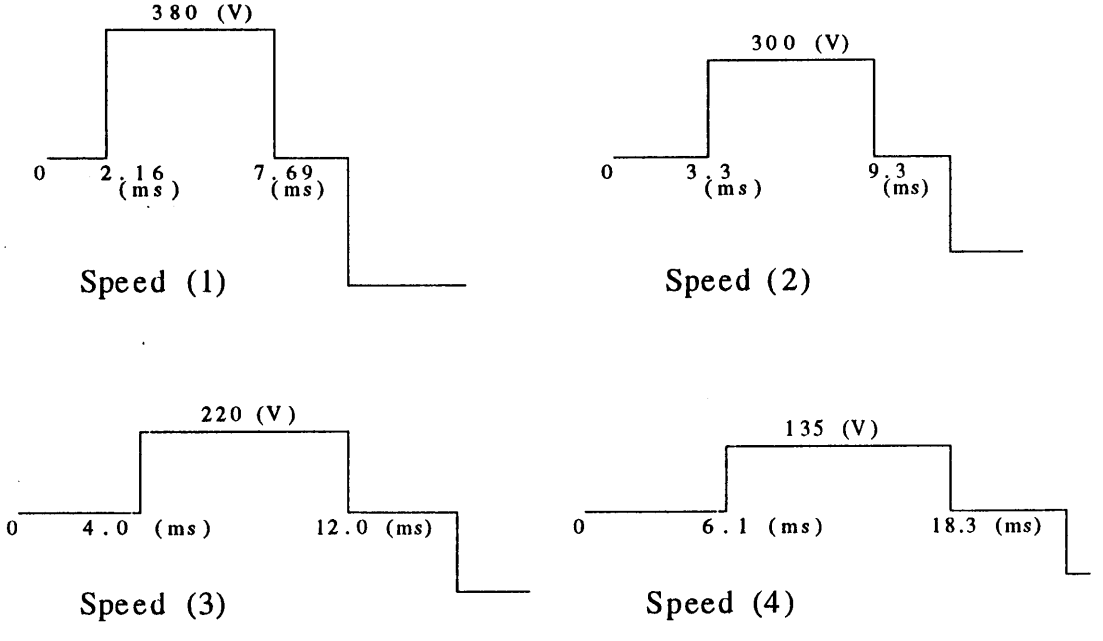

(b) Waveforms of Four Different Excitation

Fig. 7.4 Position Control

7.5 Simulation of a TLIA Connected to a Phase-angle Controller

The simplest way to adjust the output force, plunger speed and position may be to use a Triac or a pair of thyristors connected in anti-parallel as shown in Fig. 7.5.

These phase-angle controllers have already found wide applications in adjusting the output voltage for lights, small fans, *etc.* Although it can only control the *r.m.s.* value of its output voltage, it is very simple and cheap. Compared with the A.C. motor speed controller used in the last section it may only be 10% of the price of the former.

The performance of the phase-angle converter is well known[50]. If it carries a resistive load, its current waveform will have the same shape as its voltage waveforms as shown in Fig. 7.5c. However, when it carries an inductive load especially with non-linear materials, its current wave will be non-sinusoidal and discontinuous as shown in Fig. 7.5d. At present, no literature is available covering the simulation of an electromagnetic device controlled by a phase-angle controller by the finite element method. This section tries to introduce this function of the COUPV.

As the TLIA is an inductive device, its performance can be expected to be similar to Fig. 7.5d. Since the Triac or thyristor can not be switched off until its current falls to zero, when the sine wave voltage reaches zero, there are currents still in the TLIA. This delay can be represented by a phase angle φ which means the current is lagging the voltage. The control angle α must be larger than φ to ensure proper operation. In general, the input current wave is not a continuous one.

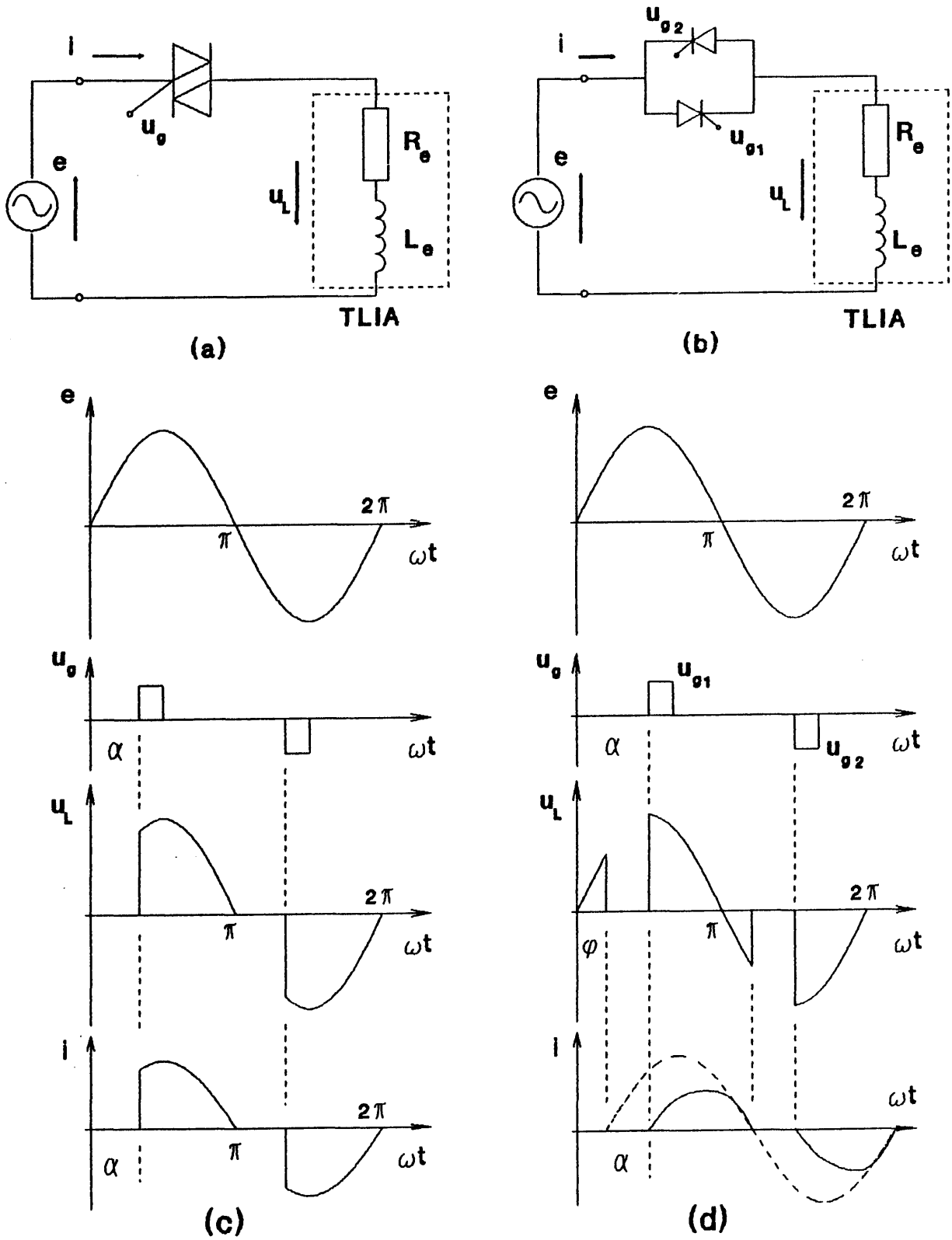

Fig. 7.5 Phase-angle Controller and Its Output Waveforms

Fig. 7.6 shows the simulated results by the COUPV. A model used in section 6.5 is adopted, *i.e.* a laminated stator TLIA with open slot and clad plunger. The excitation is a 240 volts, 50 Hz sine wave. Its triggering angle is controlled at $\alpha = 90^{\circ}$. The plunger is blocked at a displacement of 32 (mm). The current waveform is obviously a non-sinusoidal one. When it reaches zero, the triac or thyristor will be turned off automatically until the next triggering signal arrives. Meanwhile, there is residual electromagnetic energy left in the TLIA. This can be found from an *emf* curve in Fig. 7.6a and eddy current in the plunger from Fig. 7.6b. Although the TLIA has been disconnected from the power supply, there is a considerable amount of eddy current in the conducting plunger. This results in an axial force shown in Fig. 7.6b which tends to pull the plunger backward.

In order to verify the COUPV when it is used to simulate a Triac controlled TLIA, an experiment is carried out by connecting the solid steel stator TLIA to a Triac voltage controller. Fig. 7.7 gives the simulated results when the phase angle is adjusted from 72° to 126°. Corresponding experimental results are shown in Fig. 7.8. The results are in quite good agreement.

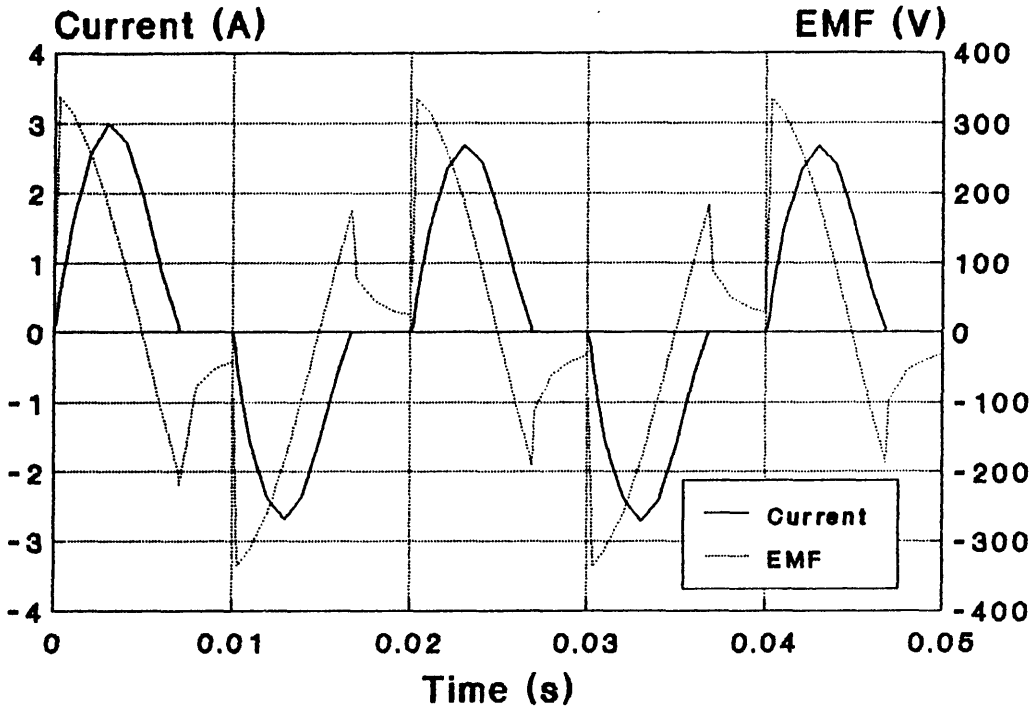

(a) Input Current & Back EMF in the Stator Winding

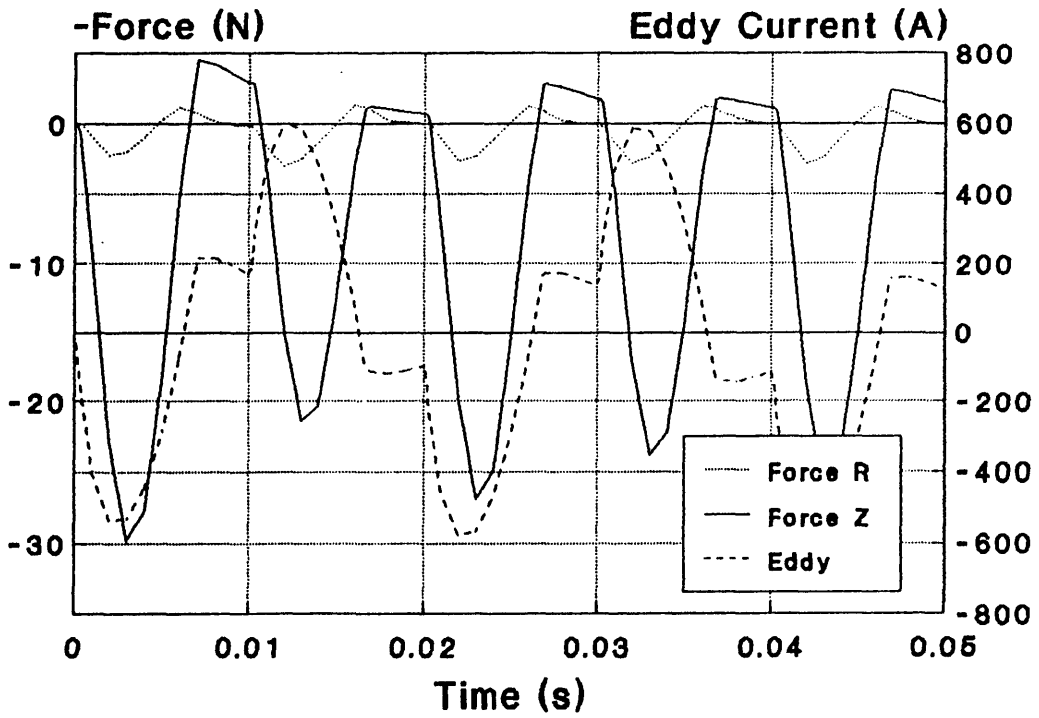

(b) Forces & Eddy Current in the Plunger

Fig. 7.6 Performance of a TLIA Connected to a Triac Voltage Controller

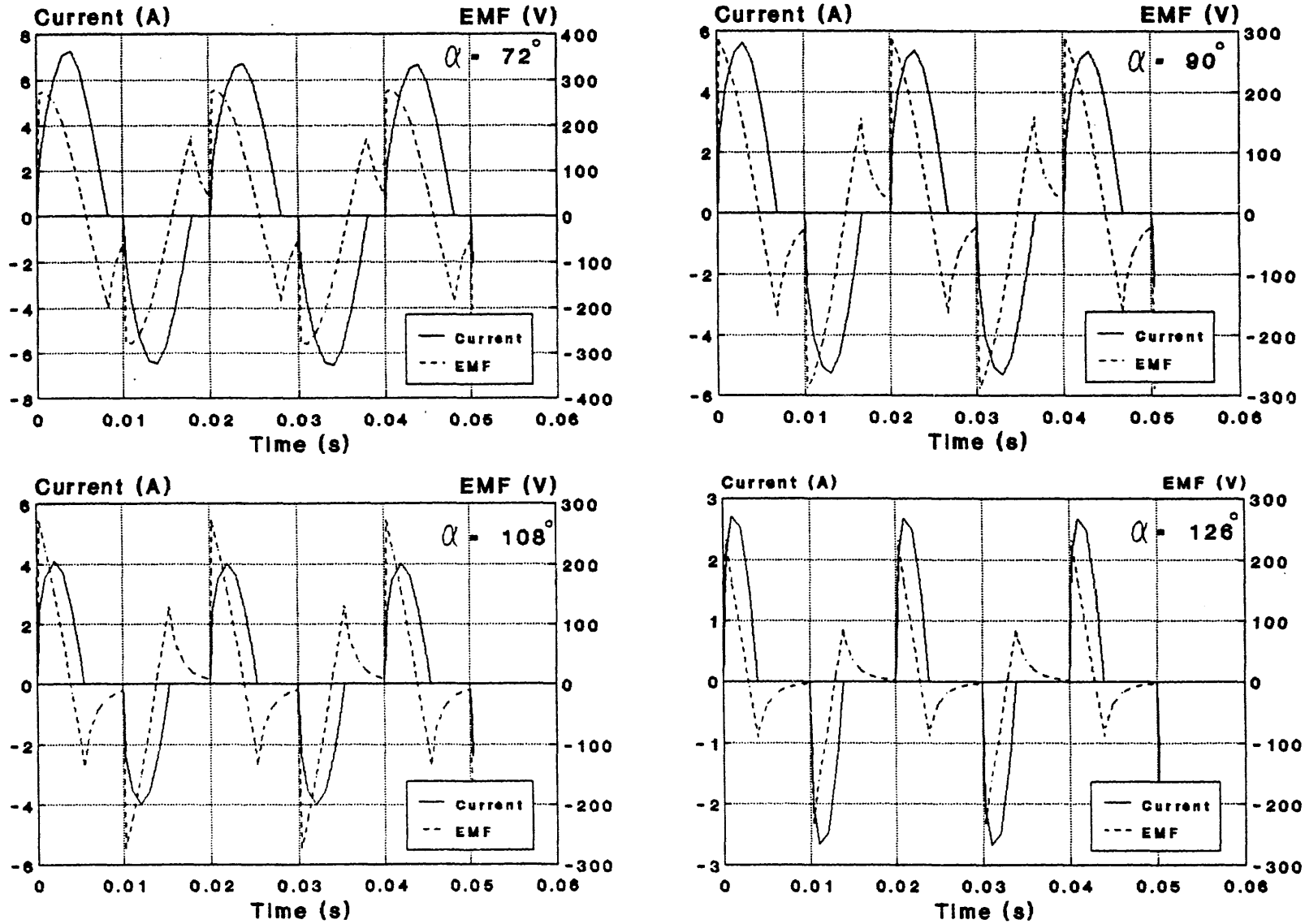

Fig. 7.7 Performance with Changing Phase Angle

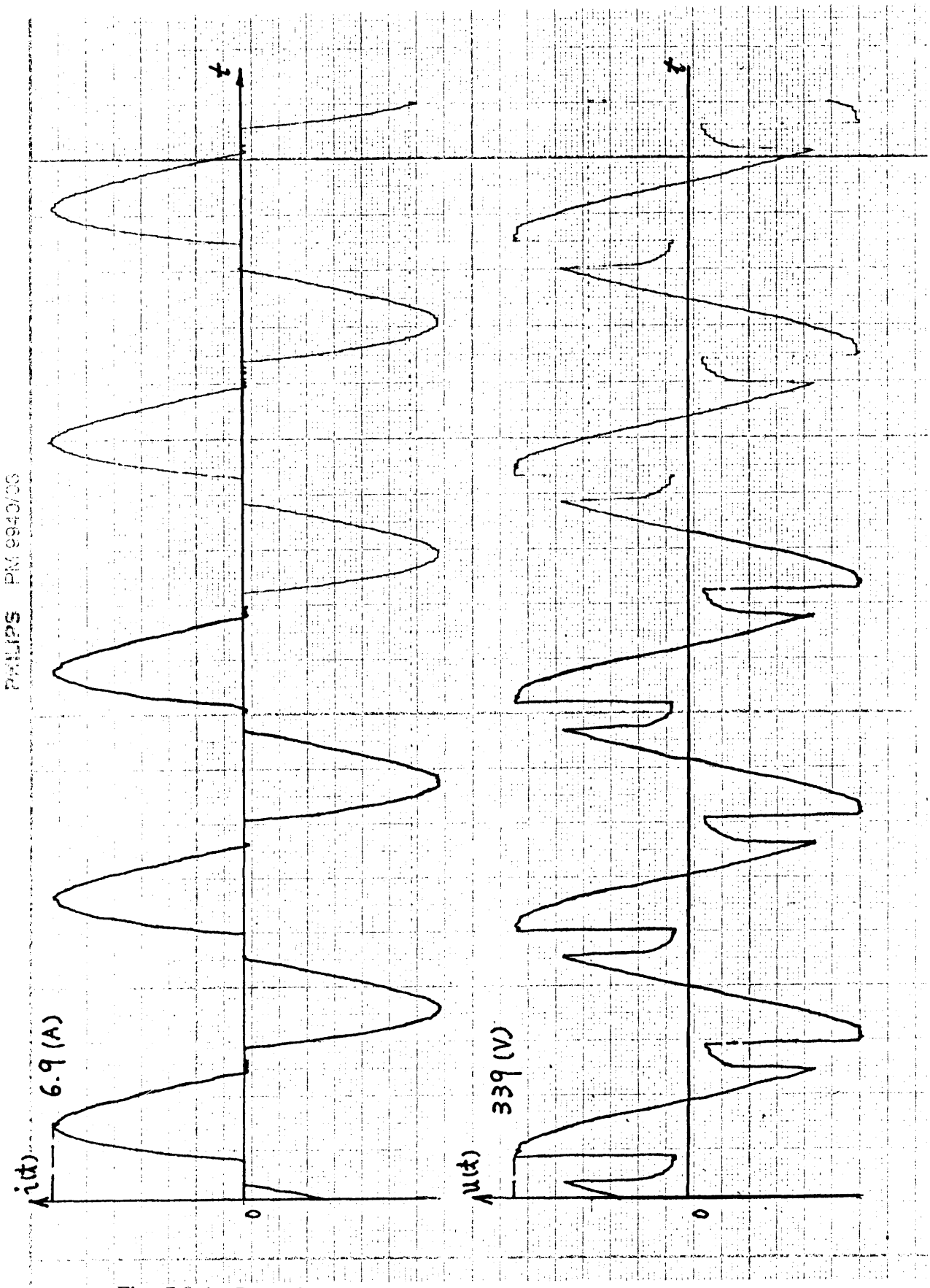

Fig. 7.8-1 Recorded Results of the TLIA Controlled by a Triac ($\alpha = 72^{\circ}$)

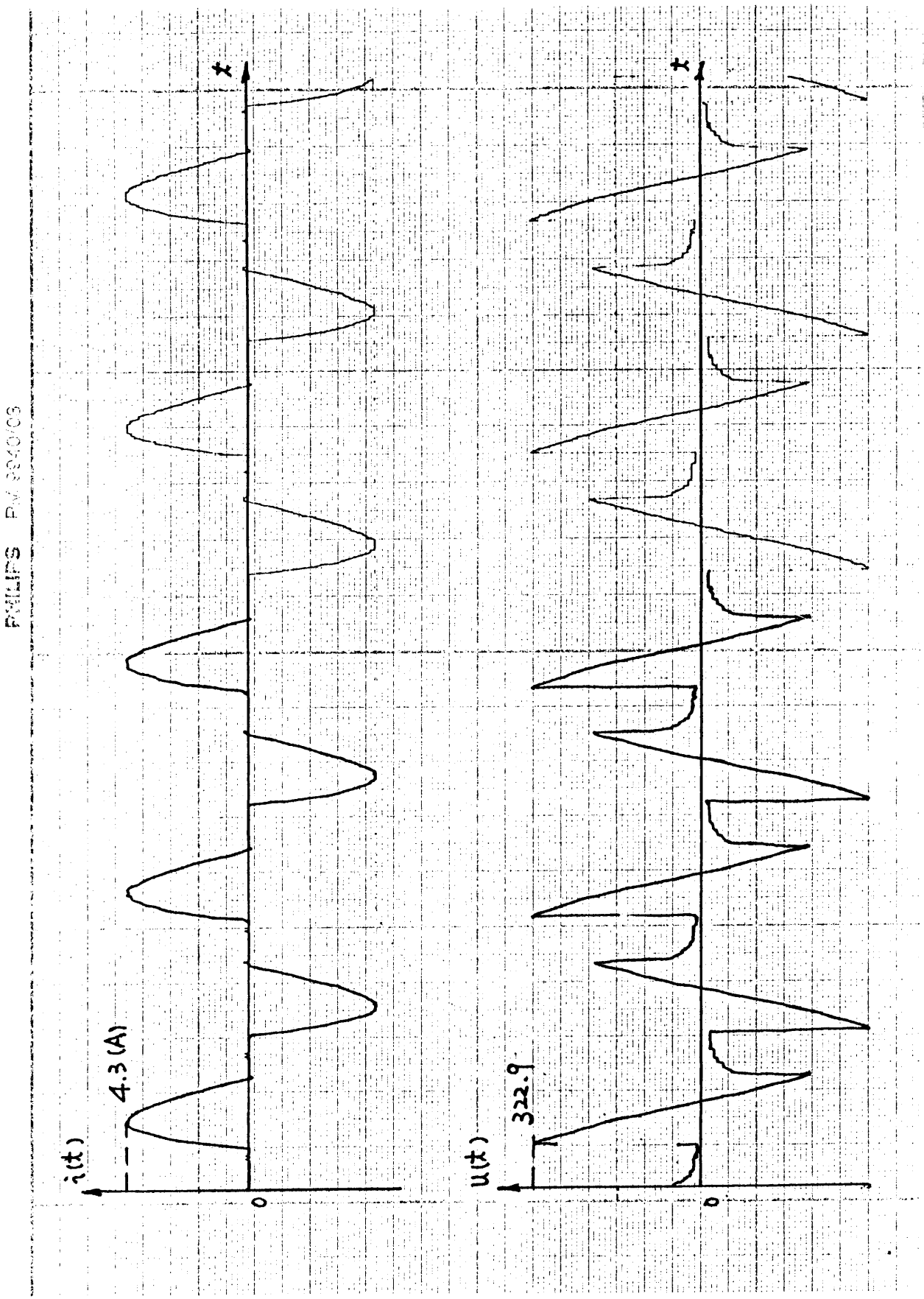

Fig. 7.8-2 Recorded Results of the TLIA Controlled by a Triac

($\alpha = 108^{\circ}$)

7.6 Conclusions

The COUPV is useful both in investigating the internal electromagnetic phenomenon and external characteristics when the TLIA is connected to various power supplies. It shows that the 'motional' eddy current in the plunger occupies a considerable part of the total induced eddy current. Therefore, the velocity effect of the moving part should be carefully considered. Neglecting this part or simply assuming it as a constant may lead to inaccurate result for the transient analysis of the actuator.

Bang-bang control is a basic operation of the solenoid and the TLIA. As they are energised by A.C. power supply, the initial switching-on instant will affect their performance. The experimental results show that this factor must be taken into account when the TLIA is used for a very short strokes. In addition to the bang-bang control, the TLIA can find application in position control. This is because it possesses different force-stroke characteristics from the solenoid. This will widen its application area.

The simplest way to control the TLIA by the Triac is investigated by both experiment and simulation. Again, the results provide the evidence that the COUPV is very effective in simulating the TLIA fed by any kind of exciting voltage waveforms.

CHAPTER 8 CONCLUSIONS AND FURTHER WORK

The work described in this thesis was aimed at introducing a novel actuator and developing computational methods to enable designers to investigate its basic principles, properties and performance. There are four major areas in the thesis, (1) eddy currents; (2) moving conductors; (3) coupling external power supplies that include power electronic components and (4) design improvement.

1. Eddy Current Problems

The TLIA is an example of utilising eddy currents to produce useful thrust. Therefore, it is impossible to neglect the eddy currents or use a simplified method of analysis as one must know exactly how these eddy currents distribute themselves in the conducting areas first. In normal similar eddy current devices such as solid steel rotor motors and solid secondary linear motors, no matter what positions the rotors are in, their main magnetic circuits are fixed and remain almost unchanged throughout. This enables the use of equivalent circuits to calculate their performances. However, in the TLIA, the different positions of the plunger lead to the variations of its main magnetic circuit. The main cause of this phenomenon are two unique features. One is called the shielding effect and the other is the inner end effect. Because of these two effects, it is necessary to analyze its inherent characteristics by field theory rather than circuit approaches. Both harmonic and time-stepping finite element methods have been used to study those two effects. The shielding effect referred to is the tendency of the conducting plunger to push flux backwards to the stator side. Especially when a two-stage TLIA is modelled, the inserted plunger isolates the magnetic interaction between

the two stages. Under closed slot conditions, the end effect conforms to the penetration depth law in the plunger's axial direction. To reduce and weaken those two effects, an iron clad copper plunger is proved to be effective. The iron back supplies a magnetic path which greatly reduces the reluctance of the main magnetic circuit and flux leakage. From the simulated results it is evident that most of the flux is able to pass through the thin copper sleeve into the iron backing. An additional important function is that it reduces the variations in the reluctance of the main magnetic circuit. Therefore, the force-stroke characteristics are improved significantly.

Since it was difficult to machine and construct a four limbed laminated stator, a solid steel stator TLIA was manufactured instead. Although it is not an ideal machine, it serves as an accurate model to validate the developed program COUPV. It also offers an opportunity to study the skin effect and the function of the slit in reducing the induced eddy currents. A simple method combining a semi-infinite slab model with an infinite thin sheet model to estimate the function of the slit has been proposed. This has proved to have reasonable accuracy.

2. Moving Conductors

The inclusion of a moving conductor leads to two main difficulties in developing a computer program. One is that the velocity term in the integro- differential equations makes the final global stiffness matrix asymmetric. The other is that at each time step, its mesh configuration must be changed in accordance with the movement of the plunger. As the TLIA is an inherently transient device, the steady-state force-stroke curves can only give information concerning its steady state properties.

In order to investigate its dynamic behaviour, transient analysis is indispensable.

Starting from the original Maxwell equations, the thesis has deduced the whole finite element procedure by means of the Galerkin Residual Method. Although there are several papers available with studies involving velocity, most of them consider the velocity being constant and few details are given. From the simulated results it has been found that the 'motional' eddy current caused by the movement of the conductor forms a considerable part of total induced eddy currents even though the plunger speed is only around 1 m/s. With the help of the COUPV, all the dynamic performance indices such as its time response, velocity and position variations versus time, axial and radial force variations versus time and effects of the switching-on angles, *etc.* can be studied.

3. The Treatment of the Coupling Problem

Most electromagnetic devices are excited by a voltage rather than a current source. Therefore, machine designers and researchers are keen on having a simulation package to deal with the former case directly. The thesis has developed a hybrid strategy combining a modified secant method with a curve fitting technique to couple the internal electromagnetic field with the external electric circuit. At each time step, this strategy is able to determine the current to balance both circuit and field equations within 3 to 4 iterations. A 'fish-bone' storage method has been used in the COUPV to store all the elements of the asymmetric global stiffness matrix. This nearly doubles the total memory required. The mesh modification during the plunger movement has been treated by a simple method based on a special numbering sequence of the elements within the moving area. All the

techniques used in the COUPV are validated by the experimental results. Nowadays, many actuators are controlled by power electronics. Their power supplies are neither sinusoidal A.C. sources nor pure D.C. sources. The COUPV can be applied to any of them. The thesis gives examples when the TLIA is controlled by a square waveform inverter and a Triac voltage controller.

4. Design Improvement

As this is a new machine and there are no similar machines which can be used for a reference, the study must start from its basic constructions, operating principles and performance. The investigation includes its single and two stage models, its slot shape, the selection of plunger materials, power supply frequencies and the position control. Use of two or more than two stage is a method to extend the stroke. Because of two special effects in the TLIA, it is found that the best way to control the multi-stage TLIA is to switch each stage in sequence one after the other. This strategy has been used for θ gun.[4] However, for the TLIA carrying a heavy load, there are two main disadvantages. One is that there are marked drops in force between the stages. The other is that only one stage operates at any time. This means the utilization ratio of the coil is quite low. As the TLIA is an eddy current device, its eddy current losses in the plunger is a very important performance index. High conductivity and thickness of the conducting plunger will obviously reduce the losses. The former depends on the material. If a superconductor is used, there will be no losses at all. In terms of the 'goodness' factor, one might prefer to increase flux density rather than eddy current density to increase the output thrust. An iron clad plunger was presented. Its flux distribution shows that it greatly reduces both the shielding effect and the inner end

effect. So, it possesses a 'hard' force-stroke characteristics.

It is hoped that the work described in this thesis forms a contribution to the current knowledge in the area of actuators and the simulation technique developed may make numerical methods more readily acceptable to the designers. Certainly, for this new machine, there is a lot of further work to do.

1. Optimal Shape Design

The COUPV developed in the thesis provides a CAD tool for the TLIA. It follows the classic design procedure[51]: *Device -- Analysis -- Performance.* First, the designer should design a device based on his own experience. Then CAD tool will help to calculate its performance. If the results agree with required specification, the design is fulfilled. If not, the designer should modify the related parts of the geometry of the device until it produces the desired performance. Recent interests in CAD have moved towards 'shape optimization design' or 'inverse problem'[52] which can be described as: *Performance--Design--Device.* Up to date, most inverse problems are limited to considerations of the static-state analysis. Therefore, it will be a big challenge to deal with time-dependent problems such as that of the TLIA.

2. Improving the Thrust Variations

Similar to the A.C. solenoid, there is inevitable oscillations contained in the output thrust, with double power supply frequency. A well known method to suppress it is to add a shading coil. For the model with a closed slot it is difficult to determine where best to locate it. For an open slot model it can be fixed at the same position as the conventional solenoid.

3. Material Selection

To limit the eddy currents in the stator, it is usually laminated. However, it is not easy to manufacture a laminated stator in small sizes. Soft ferrites[53] may be an alternative choice. Although its B-H characteristics is not as good as mild steel in the low frequency range, its eddy current losses will be greatly reduced.

4. Strategies for Dealing with the Coupling Problem

The COUPV couples the circuits and fields by the 'indirect' method which finds the unknown current by iteration method. This gives a clear physical meaning. In addition, in each time step, the COUPV only takes 3 to 4 iterations to reach the solution. However, it is difficult to use an iteration method to solve a multi-input problem as it becomes a 2 or 3 dimensional search problem. Therefore, for some special problems, for example, asymmetric operation of a 3-phase induction motor, capacitor induction motor and so on, it is better to use a 'direct' method.[54]

To fulfill the above further tasks requires proper equipment and enough financial support.

REFERENCES

[1] D.C. Greenwood, 'Manual of Electromechanical Devices', McGraw-Hill Book Co. New York, 1965.

[2] C.B. Rajanathan & G. Hu, 'A Novel Tubular Linear Induction Actuator', *Proceeding of ICEM'92,* Inter. Conf. on Electrical Machines', Manchester, U.K. 15-17 Sept. 1992, pp. 137-140.

[3] C.B. Rajanathan, D.A. Lowther & E.M. Freeman, 'Stability Characteristics of the Xi-core', *Proc. of IEE, Pt. A. 133*, 1986, pp. 89-93.

[4] T.J. Burgess, E.C. Cnare, W.L. Oberkamf, S.G. Beard and M. Cowan, 'The electromagnetic θ gun and Tubular Projectiles', *IEEE Trans. on Magnetics,* Vol. 18, No.1, Jan. 1982, pp. 46-59.

[5] E.R. Laithwaite, 'Linear Electric Motors', Mills & Boon Ltd, London, 1971.

[6] C.W. Trowbridge, 'Electromagnetic Computing: The Way Ahead?', *IEEE Trans. on Magnetics,* Vol. 24, No.1, Jan. 1988, pp. 13 -- 18.

[7] B. Burais, A. Foggia, A. Nicolas, J.P. Pascal and J.C. Sabonnadiere, 'Numerical Solution of Eddy Currents Problems Including Moving Conducting Parts', *IEEE Trans. on Magnetics, Vol. 20.* No. 5, Sept. 1984. pp. 1995 -- 1997.

[8] D. Rodger, T. Karagular & P.J. Leonard, 'A Formulation for 3D Moving Conductor Eddy Current Problems', *IEEE Trans. on Mag.* Vol. 25, No.5, Sept. 1989, pp. 4147 -- 4149.

[9] D. Rodger and J.F. Eastham, 'Characteristics of a Linear Induction Tachometer -- A 3D Moving Conductor Eddy Current Problem', *ibid,* pp. 2412 -- 2415.

[10] C.B. Rajanathan & G. Hu, 'Electromechnaical Transient characteristics

of an Induction Actuator by Finite Element Analysis' (invited paper), *The 5th IEEE BIENNIAL conf. on Electromagnetic Field computation,* Claremont, California, U.S.A. 3rd-5th Aug. 1992.

[11] C.B. Rajanathan, 'FEM2D', Dundee Institute of Technology, 1987.

[12] H.C. Roters, 'Electromagnetic Devices', John Wiley & Son, Inc. 1941.

[13] O.C. Zienkiewicz and R.L. Taylor, 'The Finite Element Method', McGraw-Hill Book Company (UK) Ltd, 1989.

[14] P.E. Allaire, 'Basics of the Finite Element Method', Wm. C. Brown Publishers, USA, 1985.

[15] C.T.A. Johnk, 'Engineering Electromagnetic Fields and Waves', John Wiley & Sons, Inc. 1975.

[16] J. Sabonnadiere and J. Coulomb, 'Finite Element Methods in CAD', North Oxford Academic, 1987.

[17] F. Bouillaut and A. Razek, 'Dynamic Model for Eddy Current Calculation in Saturate Electric Machines', *IEEE Trans on Magnetics,* Vol. 19, No. 6, Nov. 1983, pp. 1639 -- 2642.

[18] M.V.K. Chari, 'Finite Element Analysis', *Computer Aided Design of Electromagnetic Devices,* Imperial College, 5-7th, Sept. 1983.

[19] S.R.H. Hoole, 'Computer-Aided Analysis and Design of Electromagnetic Devices', Elsevier Science Publishing Co., Inc. New York, 1989.

[20] P. Silvester, H.S. Cabayan and B.T. Browne, 'Efficient Techniques for Finite Element Analysis of Electric Machines', *IEEE Trans. on PAS,* Vol. 92, No. 4, July-Aug. 1973, pp. 1274 -- 1281.

[21] E. Cuthill and J. McKee, 'Reducing the Bandwidth of Sparse Symmetric Matrices', Proc. of National Conf. Association for Computing Machinery', ACM Publication P-69, August 26-28, 1969, pp. 157-172.

[22] C.B. Rajanathan, 'Pre-processor', Dundee Institute of Technology, 1987.

[23] B.K. Bose, 'Power Electronics -- An Emerging Technology', *IEEE Trans.*

on Industrial Electronics, Vol. *36.* No. 3, 1989, pp. 403 -- 413.

[24] Song Zhi-ming, Xie De-xin and Hou Cheng-qian, 'The Finite Element Solution of Transient Axisymmetrical Nonlinear Eddy-current Field Problems', *IEEE Trans. on Magnetics, Vol. 21,* No. 6, Nov. 1985, pp. 2303 -- 2036.

[25] G. Hu, and B.C. Rajanathan, 'Dynamic Analysis of Voltage Excited Tubular Linear Induction Actuators', Proc. to *IEE International Conf. on Computation in Electromangetics,* London, U.K. 25-27 Nov. 1991, pp. 319--322.

[26] E.G. Strangas, 'Coupling the Circuit Equations to the Non-linear Time Dependent Field Solution in Inverter Driven Induction Motors', *IEEE Trans. on Magnetics, Vol. 21,* No. 6, Nov. 1985, pp. 2408 -- 2411.

[27] D. Shen, G. Meunier, J.L. Coulomb and J.C. Sabonnadiere, 'Solution of Magnetic Fields and Electrical Circuits Combined Problems', *ibid, Vol. 21,* No. 6, NOv. 1990, pp. 2288 -- 2291.

[28] F. Piriou and A. Razek, 'Coupling of Saturated Electromagnetic Systems to Non-linear Power Electronic Devices', *ibid, Vol. 24,* No. 1 Jan. 1988, pp. 274 -- 277.

[29] J.A MacBain, 'Magnetic Field Simulation form a Voltage Sourced', *ibid, Vol. 19,* 1983, pp. 2180 -- 2182.

[30] A.M. Pawlak and T.W. Nehl, 'Transient Finite Element Modeling of Solenoid Actuators: The Coupled Power Electronics, Mechanical and Magnetic Field Problem', *IEEE Trans. on Magnetics Vol. 24,* pp. 270 -- 273.

[31] K. Yuan and K. Chen, 'A New Algorithm for Coupled Solutions of Electric, Magnetic, and Mechanical Systems in Dynamic Simulation of Solenoid Actuators', *ibid, Vol. 26,* No. 3, May, 1990, pp. 1189 -- 97.

[32] T.E. Stern, 'Theory of Nonlinear Networks and Systems: An

Introduction', Addis on-Wesley, 1965.

[33] M.J. Mar son and R.J. Lopez, 'Numerical Analysis --- A Practical Approach', Wadsworth Publishing Company, U.S.A. 1991.

[34] D. Rodger, P.J. Leonard and J.F. Eastham, 'Modeling Electromagnetic Launchers at Speed Using 3D Finite Elements', *The 5th Symposium of Electromagnetic Launch Technology,* 2nd April, 1990.

[35] J. Bison, J.C. Sabonnadiere and J.L. Coulomb, 'Finite Element Analysis of an electromagnetic Brake', *IEEE Trans. on Magnetics, Vol. 19,* No. 6, Nov. 1983, pp. 2632-2634.

[36] S.R.H. Hoole, 'Rotor Motion in the Dynamic Finite Element Analysis of Rotating Electrical Machinery', *ibid,* pp. 2292 -- 2295.

[37] B. Davat, Z. Ren and M. Lauoie-Mazenc, 'The Movement in Field Modelling', *ibid, Vol. 21,* No. 6, Nov. 1985, pp. 2296 -- 1199.

[38] D. Rodger, P.J. Leonard and T. Karagular, 'An Optimal Formulation for 3D Moving Conductor Eddy Current Problems with Smooth Rotors', *IEEE Trans. on Magnetics,* Vol. 26, No. 5, Sept. 1990, pp. 2359 -- 2363.

[39] D. Rodger, T. Karaguler & P.J. Leonard, 'A Formulation for 3D Moving Conductor Eddy Current Problems', *IEEE Trans. on Mag.* Vol. 25, No.5, Sept. 1989, pp. 4147 -- 4149.

[40] H.R. Bolton, 'Electric Actuators for Rotary Drive and Shake-testing Applications', *Proceedings of Actuator Update Conference, Institute of Physics,* London, 1988, pp. 21 -- 38.

[41] P. Hammond, 'Applied Electromagnetism', Pergamon Press, 1978.

[42] B. Aldefeld, 'A Numerical Solution of Transient Nonlinear Eddy Current Problems Including Moving Iron Parts', *IEEE Trans. on Magnetics, Vol. 14,* No. 5, Sept. 1978, pp. 371 -- 373.

[43] J. A. MacBain, 'Magnetic Field Simulation form a Voltage Source', *ibid, Vol. 19,* No. 5, Sept. 1990, pp. 2180 -- 2182.

[44] R.L. Stoll, 'The Analysis of Eddy Currents', Clarendon P. 1974.

[45] B.V. Jayawant, 'Induction Machines', McGraw-Hill, London, 1968.

[46] S.A. Nasar and I. Boldea, 'Linear Motion Electric Machines', Wiley, 1976.

[47] F.C. Moon, 'Magneto-Solid Mechanics', John Wiley & Sons, New York, 1984.

[48] C.G. Hong and G.J. Hwang, 'Nonlinear Complex Finite Element Analysis of Squirrel Cage Induction Motor Performance', *IEE Proc. B,* Vol. 138, No. 5, Sept. 1991, pp. 277 -- 284.

[49] Y. Marechal and G. Meunier, 'Computation of 2D and 3D Eddy Current in Moving Conductors of Electromagnetic Retarders', *IEEE Trans. on Magnetics,* Vol. 26, No. 5. Sept. 1990, pp. 2382 -- 2384.

[50] W. Shepherd and L.H. Hulley, 'Power Electronics and Motor Control', *Cambridge University Press,* Cambridge, 1987.

[51] S.R.H. Hoole, 'Inverse Problems: Finite Elements in Hop-stepping to Speed up', *International Journal of Applied Electromagnetics in Materials,* 1990, pp. 255 -- 261.

[52] S.J. Salon and B. Istfan, 'Inverse Non-linear Finite Element Problems,' *IEEE Trans. on Magnetics,* Vol. 22, No.5, Sept. 1986, pp. 817 -- 818.

[53] E.C. Snelling, 'Soft Ferrites Properties and Application', Butterworth & Co. Ltd., 1988

[54] T. Nakata and N. Takahashi, 'Direct Finite Element Analysis of Flux and Current Distributions under Specified Conditions', *IEEE Trans. on Magnetics,* Vol. 18, No.2, March, 1982, pp. 325 -- 330.

[55] K.J. Binns, P.J. Lawrenson and C.W. Trowbridge, 'The Analytical and Numerical Solution of Electrical and Magnetic Fields', John Wiley & Sons, 1992.

APPENDIX I NUMERICAL INTEGRATION IN TRIANGULAR ELEMENTS

In order to evaluate an element matrix, the area coordinates are often used instead of the rectangular coordinates since in the former the quadrature procedure of the shape function is simple:

$$\iint_{\Delta} \zeta_1^i \cdot \zeta_2^j \cdot \zeta_3^k \cdot dxdy = \frac{i! \cdot j! \cdot k! \cdot 2 \cdot \Delta}{(i + j + k + 2)!} \tag{A-1}$$

in which

$$\begin{cases} \zeta_1 = \frac{1}{2 \cdot \Delta}(a_1 + b_1 \cdot x + c_1 \cdot y) \\ \zeta_2 = \frac{1}{2 \cdot \Delta}(a_2 + b_2 \cdot x + c_2 \cdot y) \\ \zeta_{2 \cdot \bar{\Delta}} \frac{1}{3}(a_3 + b \cdot x_3 + c \cdot y) \end{cases}$$

This is similar to (3.14) in the *z-r* coordinate system.

A formal proof of the formula (A-1) can be found in the Ref. [9]. In general, a polynomial $F(\zeta_1, \zeta_2, \zeta_3)$ needs to be integrated in a triangular area and the numerical integration will make the procedure much easier. In this case, the integration can be written by the formula:

$$\iint_{\Delta} F(\zeta_1, \zeta_2, \zeta_3) \cdot dxdy = \Delta \cdot \sum_{n=1}^{m} \rho^{(n)} \cdot F(\zeta_1^{(n)}, \zeta_2^{(n)}, \zeta_3^{(n)}) \tag{A-2}$$

in which m is the number of the points chosen in the triangle, $(\zeta_1^{(n)}, \zeta_2^{(n)}, \zeta_3^{(n)})$ is the area coordinates of the point, $F(\zeta_1^{(n)}, \zeta_2^{(n)}, \zeta_3^{(n)})$ is the numerical integral outcome of the corresponding point and $\rho^{(n)}$ is a corresponding weight. They can be consulted in Ref. [55] and are called the Gauss quadrature for triangles as shown in Table A-1.

With the aid of the Table A-1, the deduction of the formulae in the page

Quadrature Points and Weights

Order	Points	Area Coordinates	Weight
Linear $O(h^2)$	1	$\zeta_1 = \frac{1}{3}\cdot(1, 1, 1)$	1
Quadratic $O(h^3)$	3	$\zeta_1 = \frac{1}{2}\cdot(1, 1, 0)$ $\zeta_2 = \frac{1}{2}\cdot(0, 1, 1)$ $\zeta_3 = \frac{1}{2}\cdot(1, 0, 1)$	$\frac{1}{3}$

Table A-1 Gauss Quadrature for Triangles

100 becomes very simple. For example, the integration $\iint \frac{1}{r}\cdot drdz$ can be expressed by

$$\iint_{\Delta} \frac{1}{r}\cdot drdz = \iint_{\Delta} \frac{1}{N_i\cdot r_i + N_j\cdot r_j + N_k\cdot r_k}\cdot drdz$$

$$= \Delta\cdot \sum_{n=1}^{m} \rho^{(n)}\cdot F(\zeta_1^{(n)}, \zeta_2^{(n)}, \zeta_3^{(n)}) \qquad \text{(A-3)}$$

According to Table A-1, choosing the second order approximation, one obtains

$$\iint_{\Delta} \frac{1}{r}\cdot drdz = \Delta\cdot\left[\frac{1}{3}\cdot\left(\frac{1}{\frac{1}{2}\cdot r_j + \frac{1}{2}\cdot r_k} + \frac{1}{\frac{1}{2}\cdot r_j + \frac{1}{2}\cdot r_k} + \frac{1}{\frac{1}{2}\cdot r_j + \frac{1}{2}\cdot r_k}\right)\right]$$

$$= \frac{2\cdot\Delta}{3}\cdot\left(\frac{1}{r_j + r_k} + \frac{1}{r_j + r_k} + \frac{1}{r_j + r_k}\right)$$

in which the weight ρ is equal to 3 and three points are chosen in the triangular element.

APPENDIX II B-H CURVE OF THE SOLID STEEL

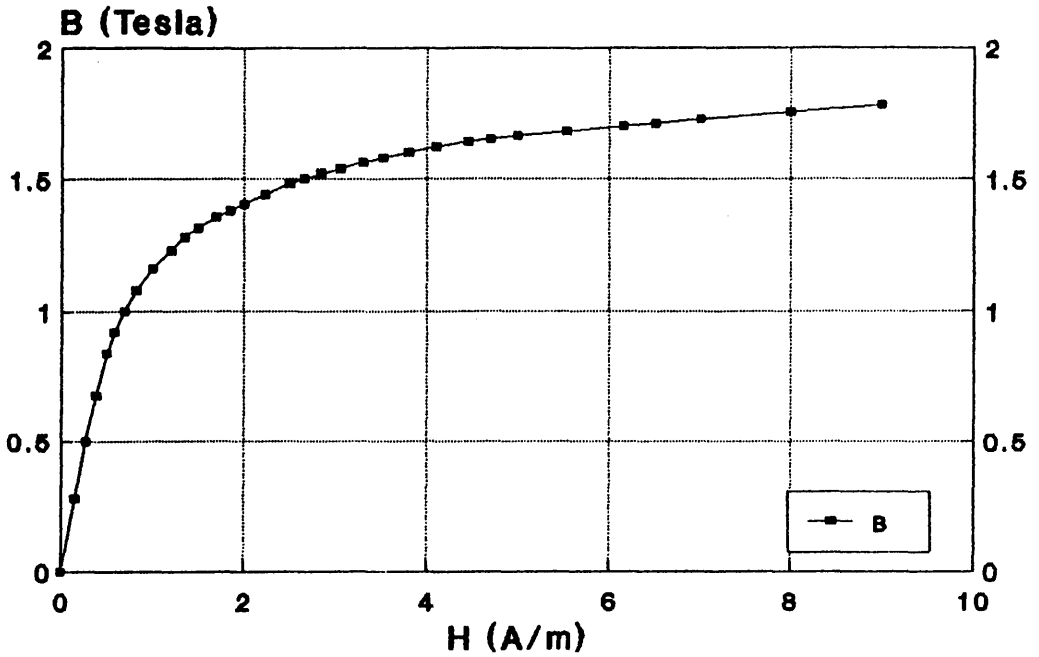

APPENDIX III B-H CURVE OF THE LAMINATION M6